EARTHQUAKE RESEARCH AND NETWORK OPERATIONS IN THE INTERMOUNTAIN SEISMIC BELT - WASATCH FRONT

Robert B. Smith
and
Walter J. Arabasz

Department of Geology and Geophysics
University of Utah
Salt Lake City, Utah 84112

USGS CONTRACT NO. 14-08-0001-16725
Supported by the EARTHQUAKE HAZARDS REDUCTION PROGRAM

OPEN-FILE NO.81-290

CONTENTS

List of Figures

Final Technical Report

Period: April 1, 1980 through September 30, 1980

Introduction

During the six months of this report period, our contractual efforts were devoted chiefly to: (1) implementation of a USGS-supplied computer system for network operations and research, (2) on-going research on several topics (outlined below) related to earthquake hazard evaluation and earthquake prediction in the Wasatch Front area, and (3) long-term planning (FY81-83) and final negotiation of support (FY-81) for continued earthquake research in the Wasatch Front area.

Scientific accomplishments achieved during the current contract year have been summarized during the last six months in five new manuscripts--including three student theses. Accordingly, complete manuscripts are included in this report as attachments and make up most of the relevant technical discussion.

Two manuscripts have just been submitted for publication. The first, entitled "Earthquake prediction in the Intermountain seismic belt -- an intraplate extensional regime" by W. J. Arabasz and R. B. Smith, was submitted September 26, 1980, for inclusion in the Proceedings of the Third Maurice Ewing Symposium -- Earthquake Prediction. The manuscript summarizes important observations to date from earthquake prediction studies in the Utah region -- particularly relating to changes in space-time seismicity patterns -- and it assesses inherent problems for predicting moderate to large earthquakes in the Intermountain seismic belt. The second manuscript,

entitled "Simultaneous inversion for hypocenters and lateral velocity variations: An iterative solution with a layered model" by B. W. Hawley, G. Zandt, and R. B. Smith, was submitted October 2, 1980, for publication in the Journal of Geophysical Research. These two manuscripts appear as Attachments No. 1 and No. 2, respectively, in this report.

Three M.S. theses completed at the University of Utah under the auspices of this contract during the last six months include the following:

Griscom, M. (1980). Space-time seismicity changes in the Utah region and an evaluation of local magnitude as the basis of a uniform earthquake catalog, 134 pp. (Five copies forwarded to USGS Government Technical Officer July 29, 1980, accompanying Quarterly Management Report.)

Doser, D. I. (1980). Earthquake recurrence rates from seismic moment rates in Utah, 164 pp. (Attachment No. 3 in this report.)

Owens, T. J. (1980). Flexure and normal faulting in lithospheric plates with application to the Wasatch Front, Utah, 65 pp. (Attachment No. 4 in this report.)

Results of some current research have also been summarized in two abstracts submitted during September 1980 for presentation at the Fall Annual Meeting of the American Geophysical Union, December 8-12, 1980, in San Francisco:

Doser, D. I.: Source parameters of Utah earthquakes.

Owens, T. J.: Flexure and normal faulting in an elastic-perfectly plastic plate.

Detailed Seismicity Along the Wasatch Front
April 1 - September 30, 1980

Epicenter maps of earthquake activity in the Wasatch Front study area during the six months of this report period are shown in Figures 1 and 2. During this period, 255 earthquakes were located ($M_L \leq 4.4$); notable seismicity shown in Figures 1 and 2, from N to S, includes the following:

a) On-going small-magnitude earthquakes ($M_L < 3.0$) in the Idaho-Utah border area, SW of Malad City, including aftershock seismicity within Pocatello Valley and microseismicity extending SE into Blue Creek Valley and SW into Hansel Valley. Several shocks in the magnitude range 2.0 to 3.5 intermittently occurred during the report period beneath the Newfoundland and Hogup Mountains (~41.4°N, 113.1°W) -- on a SW extension of current seismicity in Hansel Valley.

b) Five small earthquakes, including a magnitude 2.1 event (September 17, 1980), located on the Wasatch fault 15 to 20 km N of Brigham City. Significantly, this locality marks one of the few areas along the entire course of the Wasatch fault where accurately located microearthquakes can be associated with the fault.

c) Two felt earthquakes, both of magnitude 2.9, that occurred 10-15 km SE of Logan on August 15 and September 16, 1980. Both shocks were accompanied by smaller earthquakes.

d) Continued low-level seismicity ($M_L < 2.5$) near Magna in the NW part of the Salt Lake Valley.

e) Concentrated activity 25 km W of Manti near Fayette at the southern end of the Wasatch fault. Earthquakes occurred sporadically either as

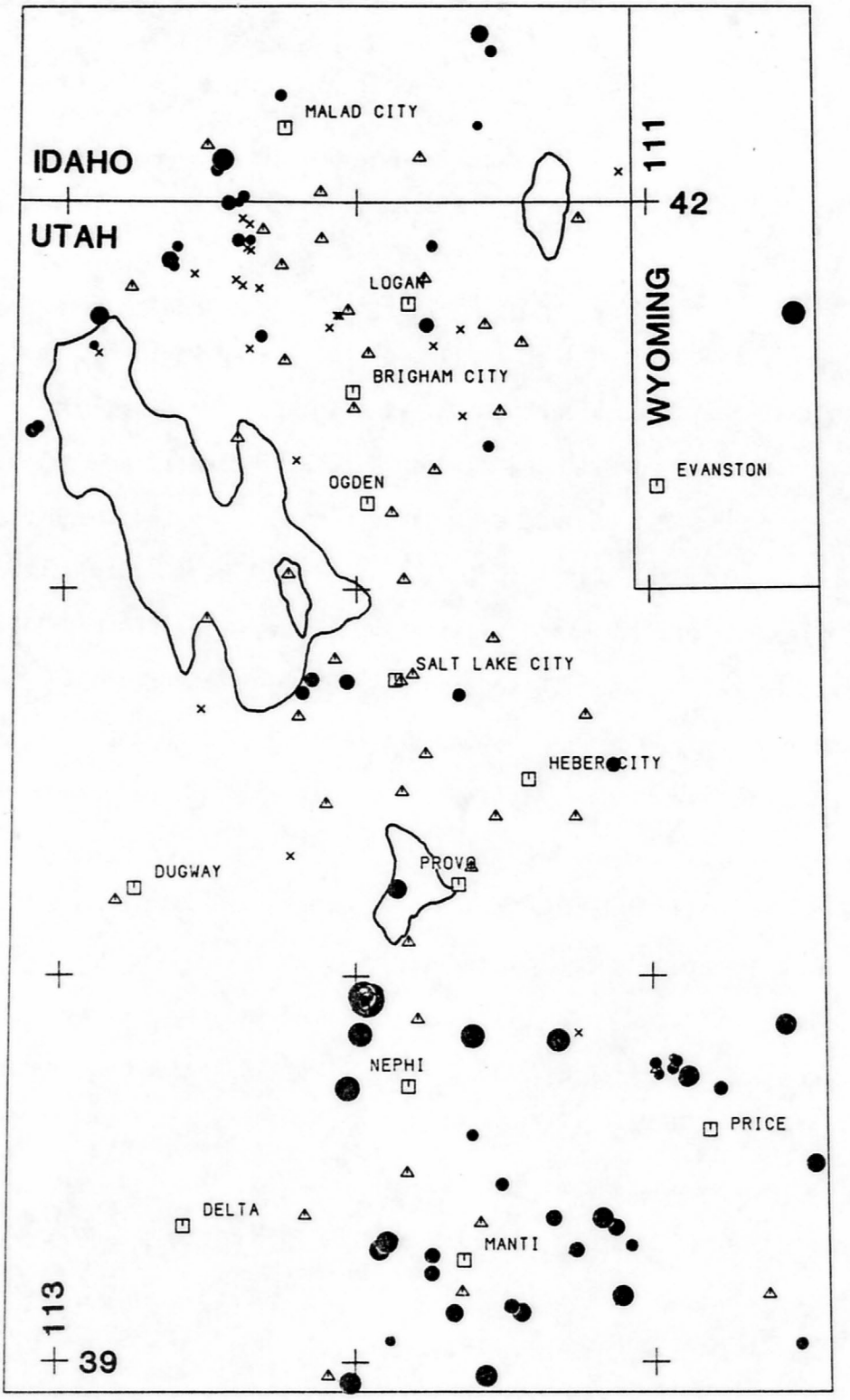

WASATCH FRONT EQ'S: APR - JUNE, 1980

MAGNITUDE SCALE (ML):

6 4 2 1 < 1.0

△ SEISMOGRAPH STATION

0 50 100 KM

Figure 1

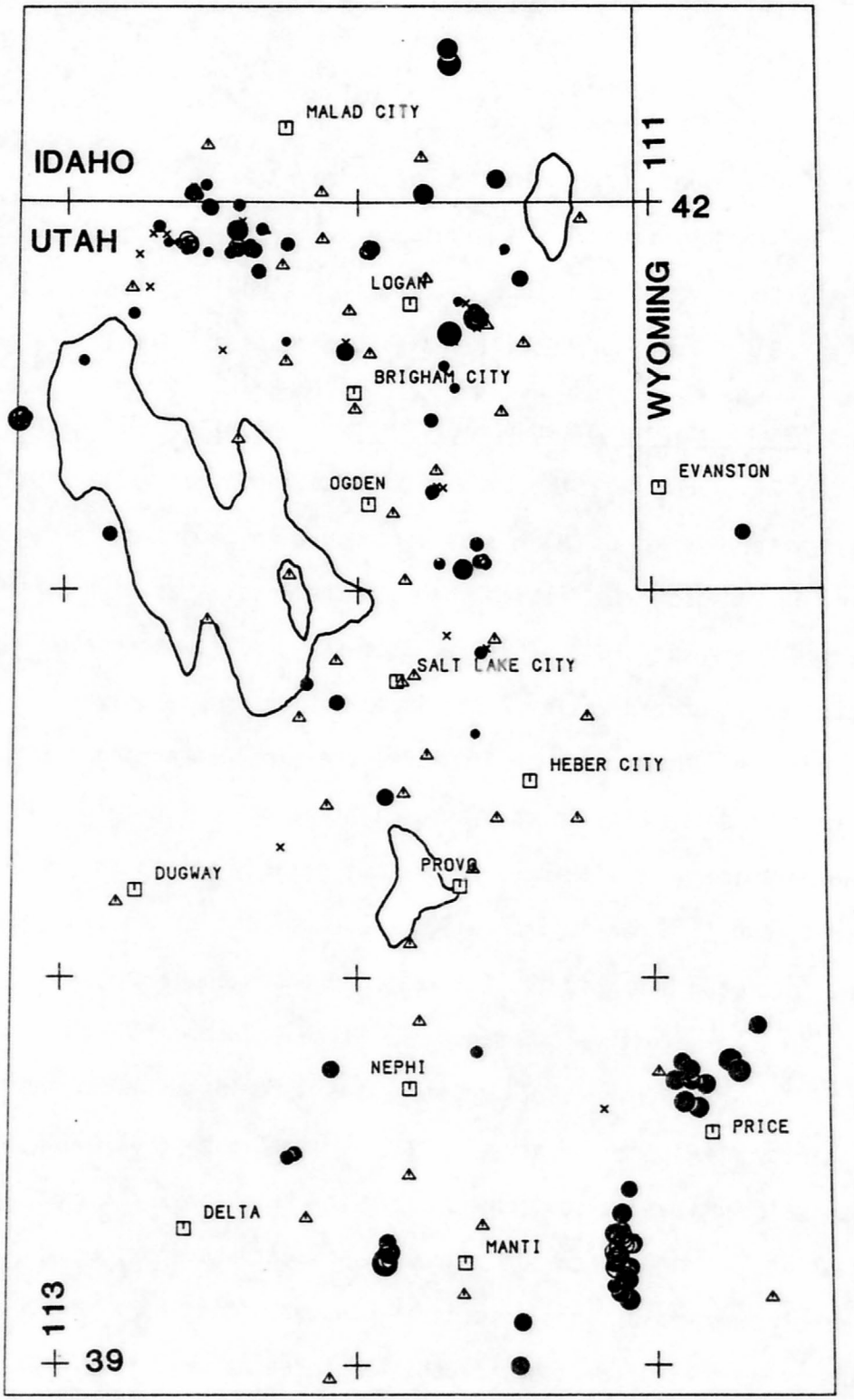

WASATCH FRONT EQ'S: JULY - SEPT, 1980

MAGNITUDE SCALE (ML):

6 4 2 1 < 1.0

SEISMOGRAPH STATION

0 50 100 KM

Figure 2

single events or as clusters of 10 to 30 earthquakes (not all locatable). The largest shock was a magnitude 3.1 event on July 5, 1980.

f) Earthquakes of magnitude 3.8 (April 6, 1980) and magnitude 4.4 (May 24, 1980) 30 km NW of Nephi (Figure 1, discussed below).

Seismicity in Goshen Valley, Utah. A magnitude 4.4 earthquake occurred on May 24, 1980, near the town of Elberta in Goshen Valley, Utah, forty-eight days after a smaller (M_L = 3.8) earthquake in the same hypocentral area. The May 24 shock was felt strongly in the local area with a maximum epicentral intensity (MM) of V-VI. Because episodic microseismicity has been detected in Goshen Valley since installation of the University of Utah's telemetered seismic network in 1974, these recent earthquakes prompted concern that seismicity in this area might be premonitory to a larger shock. The seismicity is within 15 km of (but clearly separated from) the Wasatch fault, and it occurs within a 300 x 100-km-long anomalously quiet sector of the Intermountain seismic belt that had experienced only one mainshock larger than magnitude 3.5 since 1967 (see Attachment No. 1 in this report).

Four MEQ-800 portable seismographs were installed in the general vicinity of Elberta on May 24, 1980 -- immediately following the magnitude 4.4 mainshock -- to complement our fixed telemetry stations. The temporary stations were operated for four days. Twenty-seven aftershocks (M_L<2.0) were located in a tight epicentral cluster within 5 km radial distance of the town of Elberta; focal depths clustered at 7-10 km. Focal mechanisms for the April 6 shock, the May 24 shock, and for aftershocks following the latter event, all indicate a predominance of normal faulting on NNW-to-NNE trending nodal planes. Correlation with a specific fault, however, is not unambiguous. We have no evidence that the May 24 earthquake was anything but a culminating event within Goshen Valley, rather than part of

a preparatory process for a larger shock. More complete details of this study form part of an M.S. thesis in preparation.

Implementation of USGS-Supplied Computer System

A major accomplishment during this 6-month reporting period was the implementation of the PDP-11/34 and 11/70 computer systems supplied by the USGS for automated recording and semi-automatic processing of earthquake data. During the period April 1 to September 30, 1980, we received final shipments of hardware, implemented UNIX system software on the 11/70 and RSX-11M on the 11/34, converted 50 stations to on-line recording on the 11/34, and initiated analysis of the earthquake data on the 11/70.

Final Shipments of Hardware. Partial shipments of computer hardware started arriving on February 12, 1980, and receipts of shipments are documented up to April 10 in our Semi-Annual Technical Report (14-08-0001-16725). A Tektronix 4014-1 CRT terminal was received on May 22, 1980, and installed. Shipment of a second TE16 and card reader for the 11/70, plus the LPA hardware for the 11/34, arrived in mid-June. Complete installation of all 11/34 hardware in the USGS-specified configuration was completed July 31, 1980. All 11/70 hardware installation (including the DH11-AD) was completed by August 1, 1980

System Software Implementation. Edition 7 of the UNIX operating system was brought up on the 11/70 on May 13, 1970, and is operating currently. RSX-11M (version 3.2) was built on the 11/34 on June 10, 1980; however, further progress on implementing 11/34 recording was not possible due to delayed shipment of the LPA hardware.

PDP 11/34 Recording. On September 10, 1980, signals from eighteen stations were wired into the 11/34 to test the triggering and recording

program. The software was provided by the University of Washington and was written by Carl Johnson (USGS) and Alex Bittenbinder (U. of Washington). By September 19, 50 channels (49 stations and IRIG time code) of data were wired into the 11/34; however a problem in the trigger software prevented recording. The problem was found (see 'Problems Encountered' section) and removed on September 23 and computer recording of earthquake data was initiated on September 24, 1980. During the next several weeks, the trigger parameters were tweaked and subarray configurations were varied to find the optional parameters and configuration for our array. We are currently running twelve subarrays with the trigger short/long term ratio set at 3/2. The system records about 20 events per tape (70-150 second record durations) and a tape lasts from one to two days. The false start rate is 20 to 50%. Preliminary comparisons with Develocorder analysis of the same data indicate all locatable earthquakes were recorded by the automatic system. Figure 3 shows stations available for on-line recording on the 11/34.

Analysis Procedure. Analysis of the computer-recorded data is performed on the Tektronix CRT using the "ping" program written by Steve Malone (U. of Washington). After picking the seismograms unusable records are discarded, and the analyzed seismic data are stored on an archive tape. For the month of October the earthquakes are analyzed from both computer-recorded tapes and Develocorder film. This comparison will provide a data base for evaluating the computer recording and analysis procedure.

Accounting. An accounting system based on a version operating on the CIRES and St. Louis University PDP-11/70's will be implemented as soon as possible. See Management Report for further details.

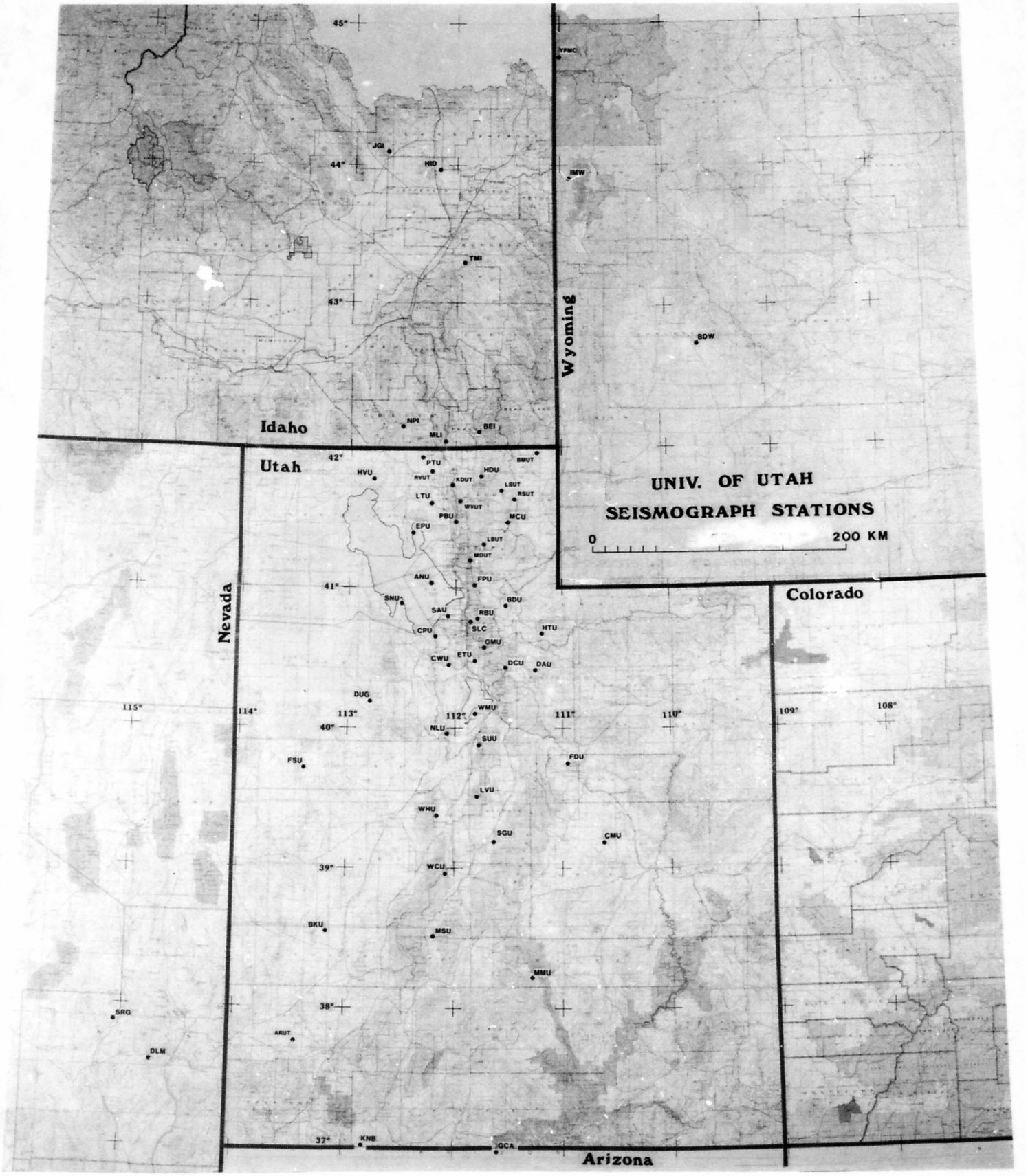
UNIV. OF UTAH
SEISMOGRAPH STATIONS
0
200 KM
Idaho
Wyoming
Utah
Nevada
Colorado
Arizona
45°
44°
43°
42°
41°
40°
39°
38°
37°
115°
114°
113°
112°
111°
110°
109°
108°
YPMC
IMW
JGI
HID
TMI
BDW
NPI
BEI
MLI
BMUT
HVU
PTU
HDU
RVUT
KDUT
LSUT
RSUT
LTU
WVUT
PBU
MCU
EPU
LBUT
MOUT
ANU
FPU
SNU
BDU
SAU
RBU
CPU
SLC
HTU
GMU
CWU
ETU
DCU
DAU
DUG
WMU
NLU
SUU
FSU
FDU
LVU
WHU
SGU
CMU
WCU
BKU
MSU
MMU
SRG
ARUT
DLM
KNB
GCA

Figure 3

Problems Encountered. The staggered delivery schedule of hardware delayed implementation of the computer recording system. Once all hardware was delivered and installed, the implementation went relatively smoothly--aided by the experience gained by personnel at other installations of the system. Especially helpful were Steve Malone and Alex Bittenbinder at the University of Washington and Carl Johnson of the USGS at Cal Tech where similar systems are in operation.

One problem encountered was mentioned briefly in the "PDP 11/34 Recording" section. The trigger program was written for RSX-11M version 3.1. The program needed slight modification to run correctly under version 3.2. A modified version of the program that works under version 3.2 is available from us upon request.

Inadequate disc storage space is another problem affecting data analysis. The RP04 does not have enough space to allow demultiplexing of one entire tape; hence, partial demultiplexing, analysis, and archiving is necessary on an almost daily basis. This significantly slows down the speed of analysis with only one CRT available for picking. With the present procedure we are barely able to maintain the 1 to 2 day delay in analysis for normal background seismicity.

Other problems with the analysis procedure are determination of hypocenters and magnitudes of local earthquakes. The former problem should be solved with the delivery of the program HYP080 written by the USGS for the 11/70. Magnitudes from duration of computer-recorded data are complicated by the triggering algorithm, which sometimes truncates larger events. This may require an amplitude or envelope magnitude calculation and will be investigated in the future.

A major hardware problem we are facing currently is the introduction of excessive electronic noise into data channels 17-64. These data channels have a high amplitude (~10x greater than seismic noise) high-frequency carrier, which is introduced somewhere in the multiplexer or A/D converter. This problem also complicates the duration magnitude problem. We are working with DEC personnel to eliminate this problem.

Implementation of Research Software

Concurrently with the implementation of the analysis software we have started implementation of seismic research software that we require in order to pursue our research objectives. To avoid unnecessary duplication of programming we will borrow standard programs already programmed for the 11/70. However, we are developing several programs on our own. These include programs for: the simultaneous inversion of local earthquake data for hypocenters and velocity structure, time-series analyses for seismic moment calculations (spectral calculations, instrument corrections, etc.), teleseismic P-wave travel time analyses, FM-digital conversion algorithms, joint-hypocenter algorithms, and analyses of refraction data. Details of these programs and their applications will be presented in future reports.

ATTACHMENT No. 1

EARTHQUAKE PREDICTION IN THE INTERMOUNTAIN SEISMIC BELT-- AN INTRAPLATE EXTENSIONAL REGIME

Walter J. Arabasz and Robert B. Smith

Department of Geology and Geophysics
University of Utah
Salt Lake City, Utah 84112

ABSTRACT

The Intermountain seismic belt (ISB) is characterized by late Quaternary normal faulting, diffuse shallow seismicity, and episodic scarp-forming earthquakes ($6\frac{1}{2} \leq M \leq 7\frac{1}{2}$) associated with the complex interaction of subplates within the western North American plate. Because of the intraplate setting, predominantly extensional stress regime, and relatively low strain rates, earthquake prediction studies in this area provide a useful complement to similar studies along active plate margins and in areas of intraplate compression. A master catalog of earthquakes since 1850 in the Utah region has been systematically examined for foreshock occurrence, precursory quiescence and clustering, migration of mainshocks, and seismicity gaps. Precursory quiescence is common and quiescent periods before the largest historical mainshocks appear to scale in duration with mainshock size. Well-documented studies indicate precursory quiescence and clustering before the 1975 Pocatello Valley earthquake (M_L=6.0) and monotonically increasing seismicity before four of its late aftershocks ($M_L \leq 3.6$). Since 1967 there has been a 300 km by 100 km N-S trending seismicity gap ($M_L \geq 3.5$) along the main axis of the ISB that is anomalous with respect to long-term rates of seismic energy release. No earthquake larger than M_L $5\frac{1}{2}$ has occurred in this zone since 1914.

This same zone envelops two 70-km-long microseismicity gaps along the Wasatch fault zone that coincide with segments that have ruptured repeatedly in Holocene but not historical time. Data are inadequate to conclude whether any of these seismicity gaps are precursory. Extensive quarry-blast monitoring throughout the Wasatch Front area, on a weekly basis since 1974, has revealed no significant velocity variations with time; no shocks greater than M_L 3.6, however, have occurred close to any ray path. Problems for earthquake prediction in the ISB include: (1) a lack of understanding of the seismic cycle on major normal faults; (2) relatively low seismic flux, which makes the detection of precursory seismicity changes difficult; and (3) uncertainty in the mechanism of normal faulting, which may be listric (i.e., flattening with depth) -- causing variations in dynamic source parameters not now accounted for in models of normal faulting.

INTRODUCTION

The Intermountain seismic belt (ISB) is an extensive zone of intraplate deformation within the western United States (Figure 1) that is characterized by late Quaternary normal faulting, diffuse shallow seismicity, and episodic scarp-forming earthquakes ($6\frac{1}{2}<M<7\frac{1}{2}$) associated with the complex interaction of subplates within the western North American plate [e.g., Smith and Sbar, 1974; Smith, 1978]. Because of the intraplate setting, the predominantly extensional stress regime, and relatively low strain rates, earthquake prediction studies in this area provide a useful complement to similar studies along active plate margins and in areas of intraplate compression. Our objectives here are: (1) to characterize the ISB and assess inherent problems for predicting major earthquakes in such an area, and (2) to present observations from preliminary earthquake prediction studies in the Utah region as probably representative of the ISB.

Characteristics of ISB

Detailed descriptions of the regional seismicity and contemporary tectonics of the ISB are summarized by Smith [1978] for the ISB, by Arabasz et al. [1980] for the Wasatch Front area of north-central Utah, and in a summary volume edited by Arabasz et al. [1979] for the Utah region as a whole. Some notable features of the ISB are: (1) its length (>1300 km) and breadth (100-200 km); (2) its segmentation into several sectors with divergent trends; (3) the diffuseness of seismicity, with focal depths

almost exclusively shallower than 15-20 km, and weak correlation with major active faults (based on dense-network monitoring with both portable and fixed microearthquake networks); (4) a general predominance of normal faulting reflecting an extensional stress regime, but with spatially rapid changes in stress orientation in some areas; (5) the common occurrence of swarm sequences at various localities throughout the ISB; (6) relatively low rates of crustal strain (~10^{-8}/yr or less) compared to those at active plate boundaries; (7) moderate background seismic flux, which, for comparison, is lower by a factor of 4-6 than that in the California-Nevada seismic Zone [Algermissen, 1969]; (8) apparent stresses that are within the range of values (0.01-100 bar) computed similarly for intraplate earthquakes elsewhere [Doser, 1980]; (9) relatively long (>1000 yr) recurrence intervals for surface faulting (excepting parts of the Wasatch fault) [Swan et al., 1980; Wallace, 1980]; and (10) a historical paucity of large (M>7.0) surface-faulting earthquakes -- despite abundant late Quaternary and Holocene fault scarps throughout the ISB [e.g., Bucknam et al., 1980; Swan et al., 1980; Witkind, 1975].

Along most of its length, the ISB follows the boundary between thin weak lithosphere of the Basin and Range Province and thicker more stable lithosphere of the Rocky Mountains and the Colorado Plateau [e.g., Thompson and Zoback, 1979]. Significantly, the ISB coincides with a preexisting zone of weakness in the North American continent along which differential crustal movement occurred during the Paleozoic and early Mesozoic, and which also defined where eastward-moving thrust plates broke to the surface during a late Cretaceous-early Tertiary orogeny [Stokes, 1976]. We return to this point later because these preexisting thrust faults appear to have had a fundamental influence on Cenozoic normal faulting.

Contemporary Deformation

Contemporary W- to NW-oriented horizontal extension characterizes most of the ISB as well as the Great Basin itself -- apparently reflecting sources of stress both beneath and at the boundaries of the involved subplates [Smith, 1978; Zoback and Zoback, 1980]. Recent estimates of rates of crustal deformation in parts of the ISB include: (1) uplift rates of the Wasatch Mountains east of the Wasatch fault from fission-track dating of 0.012 mm/yr, for the period 90 m.y. to 10 m.y., and 0.4 mm/yr for 10 m.y. to present [Naser et al., 1980]; (2) Holocene rates of dip-slip on segments of the Wasatch fault of ~1-2 mm/yr from geological trenching studies [Swan et al., 1980]; and (3) estimates of extensional strain rates (from seismic moment rates) across the ISB between about 36°N and 42°N that range from 2-7 x 10^{-9}/yr [Doser, 1980] to 1-5 x 10^{-8}/yr [Greensfelder et al., 1980] -- both compatible with geological rates of Late Quaternary extension.

With regard to geodetically-measured horizontal strain, Prescott et al., [1979] have reported data for 1972 to 1978 that show an "apparently reversed strain field" north of Salt Lake City. Their data imply ENE-WSW compression of 0.17 ±0.05 μstrain/yr across the Wasatch fault near Ogden, rather than general E-W extension expected from normal faulting and exhibited by focal mechanisms in the area. A regional strain tensor computed by Doser [1980] from 18 earthquakes in the Utah region indicates a maximum principal strain component oriented N79°E that is extensional and approximately equal to the amount of near-vertical compressional strain.

Seismicity and Recurrence

Since 1850 at least 15 independent earthquakes (i.e., mainshocks or the largest event of a swarm) within the ISB have had an estimated magnitude

of 6.0 or greater (Figure 1). There are two documented cases of historical surface fault displacement. Normal fault scarps with maximum surface displacements of 6.7 m and 0.5 m, respectively, were produced by the M=7.1 Hebgen Lake, Montana, earthquake of August 1959 and by the M=6.6 Hansel Valley (Kosmo), Utah, earthquake of March 1934. Regional instrumental monitoring of earthquakes in the ISB dates from about 1950, systematic computerized locations from the early 1960's, and monitoring with telemetered seismic networks since the early to mid-1970's.

As apparent in Figure 1, the ISB comprises at least four major zigzag segments, with many of the largest historical shocks tending to occur where there are pronounced changes in trend of the ISB. North of 42°N, seismicity appears to "wrap around" the leading edge of the NE-propagating Snake River Plain, perhaps reflecting a stress field influenced by the development of the volcanogenic Snake River Plain along a lithospheric zone of weakness [Smith et al., 1977; Furlong, 1979]. Yellowstone Park, at the apex of the Snake River Plain, marks the apparent convergence of three seismic zones trending E-W, NE-SW, and NW-SE.

The epicenter maps in Figure 2 illustrate the problem of correlating accurately-located earthquakes with active faults in the ISB. Figure 2a shows a 5.5-yr sample of earthquakes in the Wasatch Front area located with a 43-station telemetry network [Arabasz et al., 1980]. The most striking feature of Figure 2a is the paucity of small-magnitude earthquakes along most of the 370-km-long Wasatch fault, despite the fact that this major normal fault zone has been the most active locus of surface faulting in the eastern Great Basin during Holocene time [Bucknam et al., 1980; Wallace, 1980]. The seismicity pattern shown in Figure 2a, including anomalously low seismicity along the Wasatch fault, diffuse seismicity

throughout the Wasatch Front area, and abundant microseismicity a few tens of kilometers east and west of the Wasatch fault has been generally observed since systematic instrumental monitoring began in the area in 1962 [Arabasz et al., 1980]. Another major normal fault shown in Figure 2a is the East Cache fault that forms the eastern boundary of the Cache Valley graben. Abundant seismicity occurs to the east of the fault, beneath the Bear River Range, precluding correlation with the East Cache fault itself. Figure 2c shows the results of extensive microearthquake monitoring by the University of Utah in southeastern Idaho and western Wyoming. Here too the predominance of earthquake locations away from the traces of major active faults such as the Teton fault and the bounding faults of Swan Valley, Star Valley, and Bear Lake Valley, is striking. Microearthquake monitoring during the 1970's in the vicinity of the Red Canyon and Hebgen faults that ruptured during the 1959 Hebgen Lake earthquake sequence shows a similar result (Figure 2b).

There is accumulating evidence that the repeat time (at a particular location) for large displacement events on faults in the ISB is significantly longer than 1000 years [e.g., Wallace, 1980], with the apparent exception of the Wasatch fault. Swan et al. [1980] demonstrate that the two most recent scarp-forming earthquakes on the Wasatch fault near Kaysville, Utah, occurred within the past 1580 ±150 years; further, they estimate that the recurrence interval for a magnitude 6½ to 7½ earthquake along the entire Wasatch fault zone may be 50 to 430 years. A maximum magnitude of ~7½ is generally assumed from the historical experience of Basin and Range faulting in the western United States. Seismic moment rates predict a recurrence interval for an earthquake of magnitude 7.0 to 7.5 in the Wasatch Front area (Figure 2a) as short as 120 to 280 years [Doser, 1980], and

extrapolating the historical seismicity leads to a recurrence interval of 200 years for the same area and magnitude range [Arabasz et al., 1980].

EARTHQUAKE PREDICTION-RELATED OBSERVATIONS

Three areas of earthquake prediction research that have been most actively pursued in the Utah region include: (1) long-term monitoring of local quarry blasts for temporal variation in P-wave velocities before local earthquakes, (2) analysis of space-time patterns of Utah seismicity for general forecasting, and (3) rheological modeling of crustal flexure (and predicted stress fields) associated with major normal faulting -- as a means of discerning stages of a seismic cycle on segments of the Wasatch fault zone. We will briefly summarize topic (1) and elaborate on topic (2); topic (3) is discussed by Zandt and Owens [1980].

Temporal Monitoring of Seismic Velocities

The feasibility of detecting temporal changes in P-wave velocities along the Wasatch Front has been investigated by Smith et al. [1980]. Quarry blasts averaging 40,000 lb of explosives at the Kennecott Bingham Canyon copper mine, 25 km SW of Salt Lake City, were used as timed sources. From October 1974 through June 1978, several thousand P-wave arrival measurements were made at 24 selected stations of the Wasatch Front seismic network. Standard deviations of source-corrected travel times averaged ±0.1 s (with that at only one station larger than ±0.14 s). Computed velocities showed remarkable stability for the observation period, and no significant variations in velocity greater than one standard deviation, which ranged from 1 to 4 percent, were interpreted as meaningful. However, during the observation period no earthquakes larger than M_L = 3.6 occurred

close to any sampled ray path. Short-term ($\leq$60 d) velocity anomalies were identified at 14 stations, but none correlated convincingly with earthquake activity. Measurable velocity variations with time were not found in two cases of special interest: (1) for several sampled ray paths that passed through the hypocentral region of an earthquake swarm ($M_L \leq 3.3$) near Magna, Utah, less than 20 km from the Bingham Canyon copper mine; and (2) for ray paths through a source region in Pocatello Valley in which seismicity changes occurred before late aftershocks ($M_L \leq 3.6$) of an earthquake of $M_L = 6.0$ (see Figure 4). Monitoring local blasts, even on daily to weekly basis, is not encouraging for the prediction of small earthquakes ($M_L \leq 3.5$) in the Wasatch Front area. However, a meaningful test of this prediction technique for moderate to large earthquakes in the ISB has yet to be made.

Space-Time Seismicity

Major efforts were recently made at the University of Utah to compile a master catalog of all locatable earthquakes in the Utah region (Figure 3) since 1850 [see Arabasz et al., 1979]. The catalog comprises revised historical and instrumental data sets corresponding to periods before and after July 1962, respectively, and now contains more than 5000 earthquakes, including 413 in the historical data set. The catalog has been systematically examined for foreshock occurrence, precursory quiescence and clustering, migration of mainshocks and seismicity gaps [Arabasz and Griscom, 1978; Griscom and Arabasz, 1979; Griscom, 1980]. Figure 3 gives an overview of cumulative seismicity in the defined region; the earthquake record is most complete for the elongate polygonal subarea, designated the sample area, along the main axis of the seismic belt.

Foreshocks. Prominent foreshocks preceded two magnitude 6 earthquakes near Elsinore, Utah, in 1921 [Pack, 1921] and the 1975 Pocatello Valley earthquake of M_L=6.0 near the Idaho-Utah border [Arabasz et al., 1981]. From a systematic study of foreshocks in the Utah region, Griscom [1980] found the following: (1) Defining foreshocks to be smaller prior earthquakes occurring within 40 days [Jones and Molnar, 1979] and 50 km of a mainshock, identifiable foreshocks have preceded 12% of all historical mainshocks of Modified Mercali epicentral intensity (I_o) IV or greater, and 43% of all instrumental mainshocks of $M_L \geq 3.5$ in the Utah region. (2) Observed foreshock activity is variable and does not simply characterize any definable geographic region. (3) Examining prior seismicity within 100 days and 50 km of all mainshocks of $M_L \geq 3.5$ in the Utah region, the probability of earthquake occurrence is roughly constant for $10<t_p<100$, where t_p is the time preceding the mainshock in days, and increases by about a factor of 2 for $t_p<10$ (peaking during the last 6 hours). (4) The percentage of foreshocks located within 15 km of the mainshock epicenter increases as t_p decreases.

For the best locally recorded foreshock sequence to date, that for the 1975 Pocatello Valley earthquake, an accelerated increase in rate of foreshocks occurrence postulated by Jones and Molnar [1979] was not observed [Arabasz et al., 1981]. A foreshock of M_L=4.2 occurred abruptly 22 hours before the mainshock of M_L=6.0, followed by 156 smaller shocks that behaved as aftershocks of the M_L=4.2 event. Systematic increases in frequency of occurrence were observed by Arabasz and Richins [1976] before four late aftershocks (M_L=3.4-3.6) occurring 4.7 to 14.5 months after the Pocatello Valley mainshock. Figure 4 shows their data, which consists of counts of

earthquakes (S-P<2.5 s), complete above a magnitude threshold for each case, for overlapping 12-hr time windows with 4 counts per day. The increase in rate of occurrence before each culminating event is roughly linear.

Precursory quiescence and clustering. Arabasz and Griscom [1978] observed that before the largest historical earthquakes in the Utah region there were unusually long periods marked by the absence of felt shocks in the epicentral area, despite proximity to towns that had a long earlier history of reporting small shocks. Hundreds of small towns were distributed throughout the active earthquake belt in Utah by the 1870's [see Griscom, 1980]. To test an hypothesis of precursory quiescence, the following simple experiment was devised. For all pre-instrumental mainshocks of $I_o \geq V$ in the sample area (Figure 3) during 1900-1959, t_p was measured for the first preceding felt shock located within 75 km of the mainshock. Immediate foreshocks (t_p<40 days) were excluded. Also, data points were rejected for which t_p was greater than 2/3 the interval time to the last earthquake of equal or greater size. There are obvious uncertainties in the completeness and accuracy of the earthquake locations; however, the catalog for the selected time period contains 224 small shocks ($I_o \leq IV$) whose locations are fairly well constrained by felt reports. Figure 5 shows the measured values of t_p for cutoff distances of 50 km and 75 km plotted as a function of mainshock size. In terms of models of precursory quiescence and/or clustering [e.g., Wyss et al., 1978], t_p here might reflect the timing either of a precursory burst of seismicity or the onset of a decrease in seismicity.

The results (Figure 5) shows the tendency for t_p to increase with size of mainshock. As a check, the observations were tested by assuming

that the occurrence of felt earthquakes was a Poisson arrival process with mean rate of occurrence λ. From historical data summarized in Arabasz et al. [1979], λ for 210 independent felt earthquakes in the sample area, 1870 to 1959, is 2.6×10^{-2} per year per 1000 km^2. (Average recurrence for the Wasatch Front area predicts $\lambda = 2.3$ earthquakes ($I_o \geq$IV) per year per 1000 km^2.) The probability of no felt earthquake in any interval of time or length t is simply $e^{-\lambda t}$, for which values corresponding to circular areas of radius 50 km and 75 km, respectively, are indicated in Figure 5. For the 50-km-cutoff area, for example, it can be seen that all seven data points for earthquakes of $I_o \geq$VII have values of t_p corresponding to probabilities less than 0.5, and two have corresponding probabilities less than 0.15. An estimate of the $(1-\alpha)$ 100 percent upper confidence interval on the proportion of interval times greater than t_o can be made [e.g., Benjamin and Cornell, 1970] as $\exp[-\lambda t_o/(1+k_\alpha\sqrt{1/n})]$, where k_α is that value of a standard normal vairable that will be exceeded with probability α, and n is the sample size. Noting for the 50-km case that all seven data points for $I_o \geq$VII have $t_p >$1350 days, we can state with 95 percent confidence that the expected proportion should be less than 0.51 for a Poisson process; with identical confidence, the proportion of interval times greater than 750 days for the 75-km case should be less than 0.40, rather than the observed 6/7 for $I_o \geq$VII. If t_p in Figure 5 does indeed reflect a precursory time interval, and one that scales with mainshock magnitude, it appears that precursory time intervals for seismicity changes in the ISB may be significantly longer than equivalent times observed elsewhere [Kristy and Simpson, 1980; Wyss et al., 1978], which approximately follow the scale of Scholz et al. [1973] shown in Figure 5 for reference.

For post-July 1962 instrumental recording, seismicity prior to the M_L=6.0 Pocatello Valley earthquake forms the most complete data set in the Utah catalog and shows evident changes (Figures 6 and 7). Figure 6 shows a space-time plot of seismicity within 100 km epicentral distance (Δ) of the March 28, 1975 mainshock. For Δ<50 km, a period of relative quiescence began 6.4 years (t_p = 2327 d) before the mainshock and lasted for 4.4 years until April 14, 1973 (t_p = 712 d) when an earthquake of M_L = 4.2 occurred at Δ = 9 km. During the following 200 days, small-magnitude shocks clustered at $\Delta \leq 25$ km. During the 450 days preceding the mainshock there is a weak suggestion of a few small shocks migrating toward the mainshock focus. Recall that a foreshock of M_L=4.2 (Δ = 1 km) occurred 22 hours before the mainshock. Epicentral patterns corresponding to periods of interest in Figure 6 are shown in Figure 7. A general precursory model involving a significant decrease in background seismicity, interrupted by a burst of earthquakes clustered in the source region, is a reasonable one for the Pocatello Valley earthquake. Let us examine the prior seismicity more critically, again by assuming a Poisson process.

The circular area of 50-km radius centered on the Pocatello Valley earthquake experienced 12 independent earthquakes between July 1, 1962 and the time of the March 28, 1975 mainshock (12.75 years) that were of $M_L \geq$ 2.5 -- the catalog's threshold for completeness in the Wasatch Front area. Accordingly, λ = 0.94 events per year. For comparison, the rate predicted from 129 years of seismicity in the Wasatch Front area [Arabasz et al., 1980] is 1.27 events per year. For a Poisson process the probability of the observed 4.4-year period of quiescence would be 0.015, and at the 95 percent confidence level, the proportion of interval times greater

than 4.0 years would be less than 0.08. It is noteworthy that the onset of the long quiescence at t_p = 2327 days is consistent with the historical data of Figure 5 for a mainshock of magnitude 6.0, while the onset of the precursory burst of seismicity at t_p = 712 days is close to the time scale of Scholz et al. [1973]. Griscom [1980] has systematically analyzed seismicity prior to other mainshocks in the Utah instrumental catalog and found additional evidence of precursory quiescence and clustering, but inadequate numbers of sampled earthquakes make conclusions tentative.

Seismicity gaps. Spatial gaps in the distribution of the largest earthquakes in a seismic belt and temporal decreases in seismicity before larger earthquakes now have a widely recognized significance for earthquake prediction. These two cases of "missing" earthquakes have been termed seismic gaps of the first kind and second kind, respectively, by Mogi [1979]. Seismic gaps of the first kind can be recognized in some intra-plate areas. Can any be recognized in the ISB? In general, the historical record in the ISB is simply inadequate to define any repetitive cycles of major strain-energy release throughout the belt. There is, however, a 300-km-long segment of the ISB between 38.9°N and 41.5°N that has had a conspicuous absence of historical earthquakes larger than magnitude 5½. This segment, if any, might be considered a gap of the first kind because it encompasses 80 percent of the Wasatch fault zone, which has yet to rupture in historical time. Also, studies of the Utah earthquake catalog have recently called attention to a significant decrease in seismicity along this same segment of the ISB beginning in the late 1960's that might be interpreted as some form of a seismic gap of the second kind [Griscom

and Arabasz, 1979; Griscom, 1980]. This is illustrated in Figure 8, a space-time plot of independent mainshocks ($I_o \geq$IV) within the sample area of Figure 3. The hachured space-time compartment in Figure 8 points out that within a 300 km x 100 km N-S trending zone along the ISB, only one mainshock of $M_L \geq 3.5$ occurred from 1968 through March 1980 -- despite background microseismicity (Figure 2a). And along this same zone, no mainshock larger than intensity VII or about magnitude 5½ has occurred since 1914. In contrast, the sectors of the ISB immediately north and south of this zone have shown more uniform seismic flux since the late 19th century. Moderate-size earthquakes at each end of the zone have occurred roughly every 20-25 years with a tendency to alternate north and south. (Application of the technique of Kasahara [1978] to test for migration showed no significant trend for all grouped mainshocks in either the Utah region or the sample area.)

What is the significance of the 300-km-long seismicity gap? From instrumental seismicity recorded since 1962, the mean rate of occurrence of independent mainshocks of $M_L \geq 3.5$ throughout the main seismic belt in Utah is ~3×10^{-2} events per yr per 1000 km^2, which predicts 0.9 shocks per year ($M_L \geq 3.5$) for the hachured space compartment in Figure 8. By any measure, the absence of all but one such event during a 12.25-yr period is statistically significant (e.g., the probability assuming a Poisson process is less than 0.01). Figure 8 shows that relative quiescence appears in the same space compartment during 1923-1938, prior to a period of normal seismicity during 1939-1963. The earthquake record is admittedly incomplete prior to 1938, but there probably was a real reduction in seismicity -- based on observations in temporally earlier and spatially

adjacent space-time compartments. If true, the 1968-1979 seismicity gap may be one of a series of quiescent periods reflecting progressive stress concentration, and may not itself culminate in a large earthquake [e.g., Ishida and Kanamori, 1980].

The 300-km-long seismicity gap for $M_L \geq 3.5$ envelops two 70-km-long seismicity gaps along the Wasatch Front (see Figure 2a) that have been quiet down to the microearthquake level since at least 1962 [Arabasz et al., 1980]. Evidence of recurrent Holocene surface faulting along these quiet segments of the Wasatch fault argues convincingly for large ($6\frac{1}{2}<M<7\frac{1}{2}$) prehistoric earthquakes [Swan et al., 1980] and against long-term aseismicity. Uncertainties discussed by Swan et al. [1980] regarding the timing of the last surface-faulting event and the variation of inter-event times at sites within the microseismicity gaps are such that one cannot confidently determine whether the corresponding segments of the Wasatch fault are in the initial or later stages of a seismic cycle. Thus the microseismicity gaps are not necessarily gaps of the second kind. Whether or not the anomalous segment of the ISB between 38.9°N and 41.5°N is in a late preparatory stage for a large earthquake remains to be determined. But the space-time seismicity suggests at least that it is one of the most likely candidate areas for future earthquakes of moderate size ($5 \leq M \leq 6\frac{1}{2}$).

PROBLEMS FOR PREDICTION

No area of the ISB has yet been targeted for any multifaceted earthquake prediction experiment. Consequently, prediction studies to date in the ISB have relied almost exclusively on variations in seismic characteristics, and -- for the foreseeable future -- geodetic data, additional data on ages of faulting, and subsurface structural data from petroleum exploration will likely provide the only supplemental infomation. With this in mind, let us summarize some significant problems for predicting major earthquakes in the ISB.

Perhaps the foresmost problem is a lack of understanding of the seismic cycle on a major normal fault and whether specific segments of active faults are in the initial or later stages of a strain accumulation cycle. This problem is paramount for the Wasatch fault but applies as well to seismically quiet faults with equally spectacular Holocene scarps such as the Teton fault south of Yellowstone Park. Preliminary data on apparent stress and stress drops in the ISB [Doser, 1980] are consistent with arguments of Raleigh and Evernden [1980] that intraplate earthquakes in the western U.S. should reflect low mean stress similar to that at the plate boundary in California. If true, the implications are that precursory changes in rock properties, such as seismic velocity, may be very localized, and sites of potentially damaging earthquakes will likely be characterized by low ambient stress, extensive fracturing, and high fluid pressure [Raleigh and Evernden, 1980].

We assume that the sites of earthquakes of M≥7.0 may be reasonably anticipated from the Late Quaternary geology. It is of course a moot point whether the sporadic occurrence of large scarp-forming earthquakes outside the bounds of the main seismic belt -- such as prehistoric faulting on the Fish Springs fault in western Utah [Bucknam et al., 1980] or along the Howe and Arco faults NW of the Snake River Plain [see Witkind, 1975] -- can be anticipated unless there is premonitory seismicity. Within the main seismic belt, the problematical correlation of seismicity with geological structure suggests that candidate sties for moderate size shocks as large as M=6½ may not be targeted. For example, the location and structural complexity of the 1975 Pocatello Valley earthquake would not have been expected from the surface geology [Arabasz, et al., 1981].

Another key problem regarding the correlation of seismicity with geological structure is that of listric of "sledge-runner" normal faults that flatten with depth, rather than maintaining moderate to steep dips of 45°-70°, as classically interpreted for Basin and Range faulting. New seismic reflection data from petroleum exploration in the overthrust belt of Wyoming, Idaho, and Utah show that many normal faults in the eastern part of the ISB become listric at depth merging into a single sole or decollement fault that originally formed as a low-angle thrust in an earlier period of horizontal compression [e.g., Royse et al., 1975; MacDonald, 1976]. The role and extent of listric faulting as an earthquake generating mechanism in the ISB is unknown but may be of considerable importance. For example, does diffuse seismicity between major faults reflect slip on listric faults or on steeply-dipping fractures within basement rocks? Predicted stress levels would differ greatly.

Three models of normal and listric faulting are shown in Figure 9, all of which depict normal faulting with Holocene surface displacement. In the right-hand model, of particular interest, subsurface structure is controlled by seismic reflection and drilling information and shows late Cretaceous-early Tertiary crustal shortening on imbricate thrust faults [Royse et al., 1975]. Relaxation of the horizontal compression in Cenozoic time and the predominance of horizontal extension has led to the development of secondary normal faults as antithetic slip planes forming a surficial graben that relieves extensional strain. The center model in Figure 9 suggests that normal faults developing under crustal extension may become curved at depth, either because of variation of the coefficient of internal friction or increasing effect of anelasticity; the left-hand model illustrates a classical interpretation of subsurface structure associated with Basin and Range faulting.

In the listric fault models the slip surfaces eventually merge with a flat zone of decoupling where horizontal displacement is accommodated. The speculative boundary between an overlying layer of brittle deformation and a decoupled extending plastic layer lies near the top of a distinct crustal low-velocity zone in the Intermountain area [Smith et al., 1975], close to the maximum depth of earthquakes in the ISB. Whether the low-velocity layer indeed is a layer of low shear strength is unknown, but high ambient temperature in the Basin and Range and the presence of stacked thrust sheets of marine sedimentary rocks as a source of pore fluid make it reasonable. If listric faulting is a plausible seismogenic mechanism, then such parameters as fault zone friction along reactivated zones of weakness, configuration and depth extent of slip surfaces, and

variation of stress with slip length will be critical for the predictability of earthquakes in the ISB.

Finally, for statistical analysis of space-time seismicity patterns in the ISB, a serious problem results from the relatively low seismic flux and short historical record. Adequate numbers of earthquakes above a magnitude threshold are typically unavailable for rigorous time-series analysis. Results presented in this paper, however, are encouraging for the detection of significant precursory changes in space-time seismicity patterns -- and the possibility of longer precursor times in the ISB could be distinctly advantageous.

ACKNOWLEDGMENTS

This paper benefited from ideas developed in conversations and joint research with George Zandt, Melinda Griscom, and Diane I. Doser. We thank George Zandt for critically reviewing the manuscript. Support from the following sources is gratefully acknowledged: U.S. Department of the Interior, Geological Survey, Contract 14-08-0001-16725; Division of Earth Sciences, National Science Foundation, NSF Grant EAR 77-23706; and the state of Utah.

REFERENCES

Algermissen, S. T., Seismic risk studies in the United States, Proc. Fourth World Conf. on Earthquake Engineering, 1, 14-27, 1969.

Arabasz, W. J., and M. Griscom, Precursory seismicity patterns in the Utah region: Can regional variations in the precursor time scale be large? (abstract), Eos Trans. AGU, 59, 1126, 1978.

Arabasz. W. J., and W. D. Richins, Late aftershocks -- a search for premonitory seismic changes (abstract), Eos Trans. AGU, 57, 68, 1976.

Arabasz, W. J. W. D. Richins, and C. J. Langer, The Pocatello Valley (Idaho-Utah border) earthquake sequence of March-April 1975, Bull. Seismol. Soc. Amer. (in press), 1981.

Arabasz, W. J., R. B. Smith, and W. D. Richins (Eds.), Earthquake Studies in Utah, 1850 to 1978, 552 pp., Special Publication, University of Utah, Salt Lake City, 1979.

Arabasz, W. J., R. B. Smith, and W. D. Richins, Earthquake studies along the Wasatch Front, Utah: network monitoring, seismicity, and seismic hazards, Bull. Seismol. Soc. Amer., 70, 1479-1499, 1980.

Benjamin, J. R., and C. A. Cornell, Probability, Statistics, and Decision for Civil Engineers, 684 pp. McGraw-Hill, New York, 1970.

Bones, D. G., and W. J. Arabasz, Seismicity of the Intermountain seismic belt in southeastern Idaho and western Wyoming, and tectonic implications (abstract), Earthquake Notes, 49(1), 1978.

Bucknam, R. C., S. T. Algermissen, and R. E. Anderson, Patterns of late Quaternary faulting in western Utah and an application in earthquake hazard evaluation, U.S. Geol. Surv. Open File Rep. 80-801, 299-314, 1980.

Doser, D. I., Earthquake recurrence rates from seismic moment rates in Utah, M.S. thesis, Univ. of Ut., Salt Lake City, 1980.

Furlong, K. P., An analytic stress model applied to the Snake River Plain (northern Basin and Range province, U.S.A.), Tectonophysics, 58, T11-T15, 1979.

Greensfelder, R. W., F. C. Kintzer, and M. R. Somerville, Seismotectonic regionalization of the Great Basin, and comparison of moment rates computed from Holocene strain and historic seismicity, U.S. Geol. Surv. Open File Rep. 80-801, 433-493, 1980.

Griscom, M., Space-time seismicity patterns in the Utah region and an evaluation of local magnitude as the basis of a uniform earthquake catalog, M.S. thesis, Univ. of Ut., Salt Lake City, 1980.

Griscom, M., and W. J. Arabasz, Space-time seismicity patterns in the Utah region: A 300-km-long seismicity gap in the Intermountain seismic belt (abstract), Earthquake Notes, 50(4), 69, 1979.

Ishida, M., and H. Kanamori, Temporal variation of seismicity and spectrum of small earthquakes preceding the 1952 Kern County, California earthquake, Bull. Seismol. Soc. Amer., 70, 509-527.

Jones, L. M., and P. Molnar, Some characteristics of foreshocks, J. Geophys. Res., 84, 3596-3608, 1979.

Kasahara, K., Statistical discrimination of migrating seismic activity, U.S. Geol. Surv. Open File Rep. 78-943, 335-350, 1978.

Kristy, M. J., and D. W. Simpson, Seismicity changes preceding two recent central Asian earthquakes, preprint, 1980.

MacDonald, R. E., Tertiary tectonics and sedimentary rocks along the transition, Basin and Range Province to Plateau and Thrust Belt Province, Utah, in Symposium on Geology of the Cordilleran Hingeline, edited by J. G. Hill, pp. 281-317, Rocky Mt. Assoc. Geol., 1976.

Mogi, K., Two kinds of seismic gaps, Pure Appl. Geophys., 117, 1172-1186, 1979.

Pack, F. J., The Elsinore earthquakes in central Utah, September 29 and October 1, 1921, Bull. Seismol. Soc. Amer., 11, 155-165, 1921.

Prescott, W. H., J. C. Savage, and W. T. Kinoshita, Strain accumulation rates in the western United States between 1970 and 1978, J. Geophys. Res., 84, 5423-5435.

Raleigh, C. B., and J. F. Evernden, The case for low deviatoric stress in the lithosphere, U.S. Geol. Surv. Open File Rep. 80-625, 1, 168-198, 1980.

Royse, F., M. A. Warner, and D. L. Reese, Thrust belt structural geometry and related stratigraphic problems, Wyoming-Idaho-northern Utah, in Symposium on Deep Drilling Frontiers in the Central Rocky Mountains, pp. 41-54, Rocky Mt. Assoc. Geol., 1975.

Scholz, C. H., L. R. Sykes, and Y. P. Aggarwal, Earthquake prediction: A physical basis, Science, 181, 803-810, 1973.

Smith, R. B., Seismicity, crustal structure, and intraplate tectonics of the interior of the western Cordillera, in Cenozoic Tectonics and Regional Geophysics of the Western Cordillera, edited by R. B. Smith and G. P. Eaton, pp. 111-144, Geol. Soc. Amer. Mem., 152, 1978.

Smith, R. B., L. Braile, and G. R. Keller, Crustal low velocity layers: Possible implications of high temperatures at the Basin Range-Colorado Plateau transition, Earth Planet. Sci. Lett., 28, 197-204, 1975.

Smith, R. B., and M. L. Sbar, Contemporary tectonics and seismicity of the western United States with emphasis on the Intermountain seismic belt, Geol. Soc. Amer. Bull., 85, 1205-1218, 1974.

Smith, R. B., J. R. Pelton, and D. L. Love, Seismicity and the possibility of earthquake related landslides in the Teton-Gros Ventre-Jackson Hole area, Wyoming, Wyoming Univ. Contr. Geol., 2, 57-64, 1976.

Smith, R. B., R. T. Shuey, J. R. Pelton, and J. T. Bailey, Yellowstone hot spot: Contemporary tectonics and crustal properties from new earthquake and aeromagnetic data: J. Geophys. Res., 82, 3665-2676, 1977.

Smith, R. B., G. Zandt, and J. E. Gaiser, Temporal monitoring of seismic velocity along the Wasatch Front using quarry blasts, Bull. Seismol. Soc. Amer., 70, 1527-1546, 1980.

Stokes, W. L., What is the Wasatch Line?, in Symposium on Geology of the Cordilleran Hingeline, edited by J. G. Hill, pp. 11-25, Rocky Mt. Assoc. Geol., 1976.

Swan, F. H., III, D. P. Schwartz, and L. S. Cluff, Recurrence of moderate-to-large magnitude earthquakes produced by surface faulting on the Wasatch fault zone, Bull. Seismol. Soc. Amer., 70, 1431-1462, 1980.

Thompson, G. A., and M. L. Zoback, Regional geophysics of the Colorado Plateau, Tectonophysics, 61, 149-181, 1979.

Wallace, R. E., Active faults, paleoseismology, and earthquake hazards, Proc. Seventh World Conf. on Earthquake Engineering, in press, 1980.

Witkind, I. J., Preliminary map showing known and suspected active faults in Idaho, U.S. Geol. Surv. Open File Rep. 75-278, 71 pp., 1975 [Open File Rep. 75-279 for Wyoming; Open File Rep. 75-285 for Montana.]

Wyss, M., R. E. Habermann, and A. C. Johnston, Long term percursory seismicity fluctuation, U.S. Geol. Surv. Open File Rep. 78-943, 869-894, 1978.

Zandt, G., and T. J. Owens, Crustal flexure associated with normal faulting and implications for seismicity along the Wasatch Front, Utah, Bull. Seism. Soc. Amer., 70, 1501-1530, 1980.

Zoback, M. L., and M. Zoback, State of stress in the conterminous United States, J. Geophys. Res. (in press), 1980.

FIGURE CAPTIONS

Figure 1. Index map of Intermountain seismic belt. Epicenters of historical mainshocks ($M \geq 6.0$) shown as large circles, NOAA epicenters through 1974 as smaller circles. Magnitudes (in parentheses) are estimated or measured values of M_L, except values for 1925-1959 (attributed to Pasadena), which are either m_b or M_S. Epicenter of 1966 shock (M_L 5.6, m_b 6.1) added for reference.

Figure 2. Diffuse upper-crustal seismicity in the Intermountain seismic belt showing lack of strong correlation with major active faults in (a) the Wasatch Front area [Arabasz et al., 1980], (b) the Hebgen Lake area [Smith et al., 1977], and (c) the Idaho-Wyoming border area [Bones and Arabasz, 1978; Smith et al., 1976]. Earthquakes in (b) and (c) are of $M_L \leq 3.0$. Large and small circles in (b) indicate focal depths greater than and less than 10 km, respectively. Elliptical areas in (a) outline seismicity gaps discussed in text.

Figure 3. Earthquakes ($M_L \geq 3.5$) in the Utah region, 1850-1979. Pre-instrumental shocks have Modified Mercalli epicentral intensities of IV or greater.

Figure 4. Frequency of occurrence versus time for time samples preceding four late aftershocks (M_L=3.4-3.6) of the March 28, 1975 Pocatello Valley earthquake (M_L=6.0). Positive linear trends have correlation coefficients of 0.7, 0.7, 0.3, and 0.5 for cases 1 to 4, respectively. [From Arabasz and Richins, 1976].

FIGURE CAPTIONS (continued)

Figure 5. Interval time of earthquake occurrence, as a function of mainshock magnitude, before all independent mainshocks ($I_o \geq V$) in the sample are in Figure 3. Time t_p is the interval between a mainshock and the last felt earthquake located either 50 or 75 km. P[0,t]is the probability of no shock occurring during a time interval corresponding to t_p, assuming a Poisson arrival process (see text).

Figure 6. The time t_p of earthquakes that occurred before the 1975 Pocatello Valley earthquake as a function of epicentral distance Δ from the mainshock. Time periods of interest are keyed to Figure 7.

Figure 7. Spatial distribution of seismicity ($M_L \geq 1.5$) preceding the 1975 Pocatello Valley earthquake during consecutive periods of interest outlined in Figure 6.

Figure 8. Space-time plot of earthquakes, in terms of Modified Mercalli epicentral intensity ($I_o \geq 4$), within the sample area of Figure 3 as a function of latitude. Vertical lines are time markers for sample completeness: $I_o \geq 7$ since 1896 and $I_o \geq 6$ since 1938; shocks of $I_o \geq 5$ are complete since 1950, and those of $I_o \geq 4$ or $M_L \geq 3.5$ since 1962 when instrumental monitoring begain. Hachured area and dashed lines outline space-time compartments discussed in text.

Figure 9. Idealized models of normal faulting in the Intermountain seismic belt. Histogram of focal depths from dense-network studies in Pocatello Valley, Idaho-Utah border, and Hansel Valley, Utah [Arabasz et al., 1980]. Crustal velocity from seismic refraction surveys in central Utah [Smith et al., 1975].

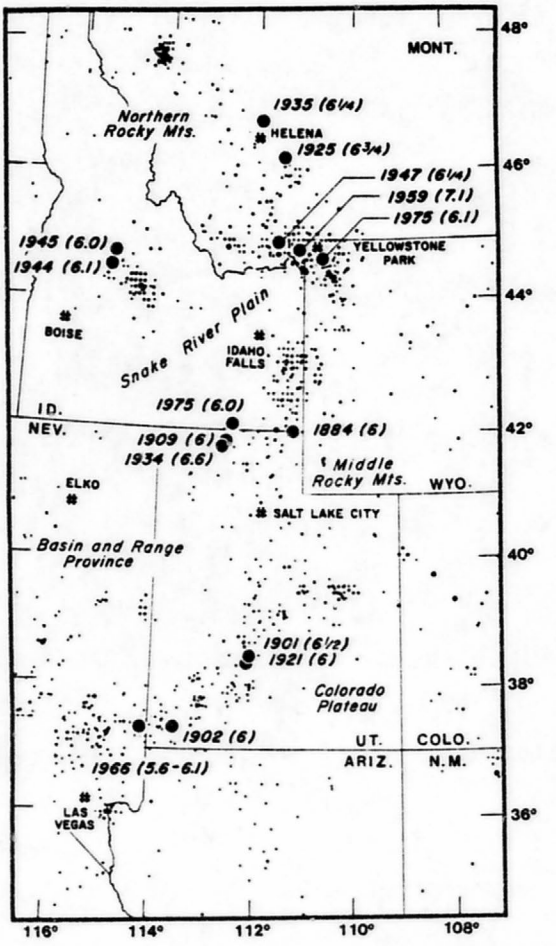
MONT.
1935 (6¼)
Northern Rocky Mts.
HELENA
1925 (6¾)
1947 (6¼)
1959 (7.1)
1975 (6.1)
1945 (6.0)
1944 (6.1)
YELLOWSTONE PARK
BOISE
Snake River Plain
IDAHO FALLS
ID.
NEV.
1975 (6.0)
1884 (6)
1909 (6)
1934 (6.6)
Middle Rocky Mts.
WYO.
ELKO
SALT LAKE CITY
Basin and Range Province
1901 (6½)
1921 (6)
Colorado Plateau
1902 (6)
UT.
COLO.
ARIZ.
N.M.
1966 (5.6-6.1)
LAS VEGAS
48°
46°
44°
42°
40°
38°
36°
116°
114°
112°
110°
108°

Figure 1.

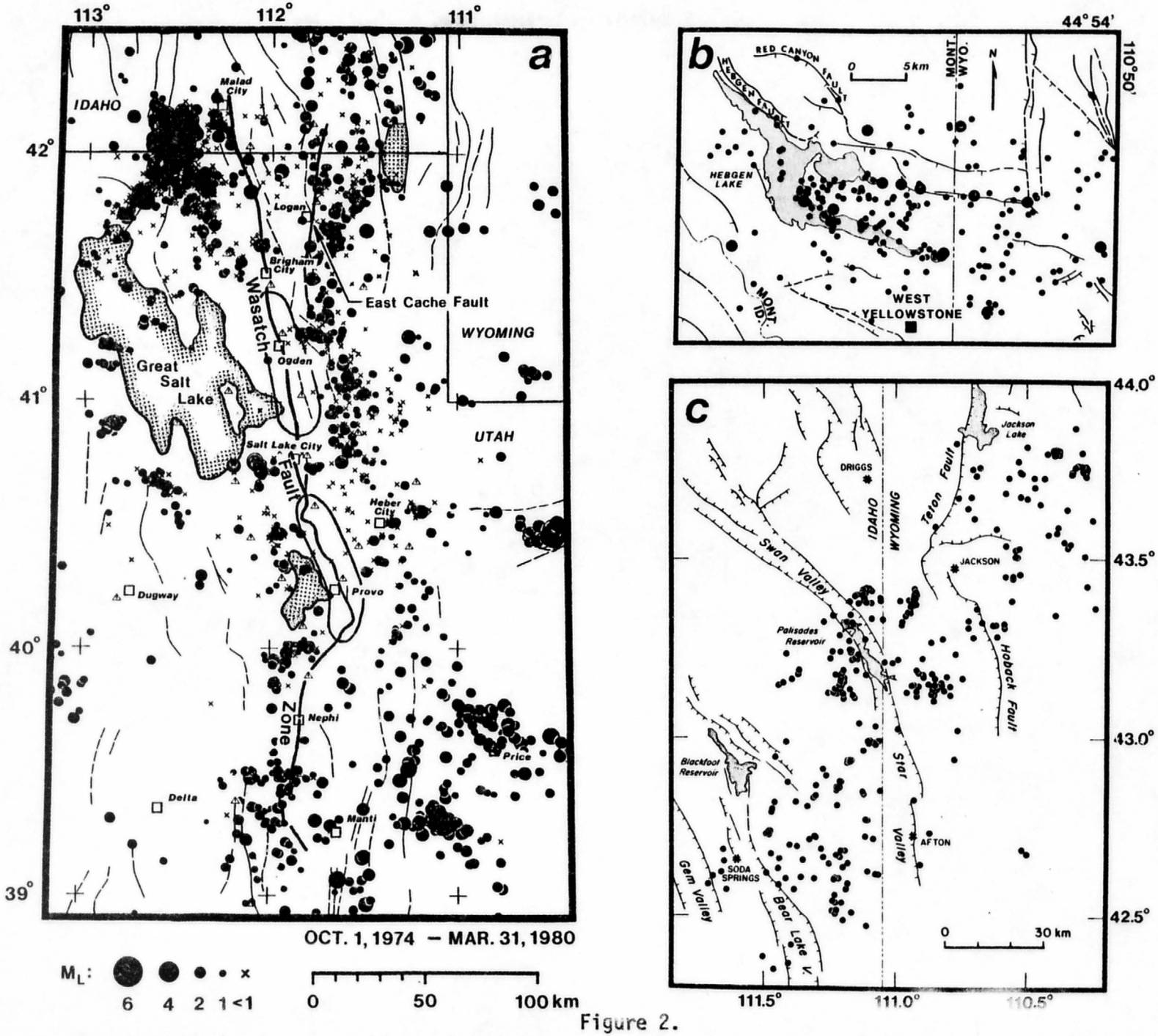
a
113°
112°
111°
42°
41°
40°
39°
IDAHO
WYOMING
UTAH
Malad City
Logan
Brigham City
Wasatch
East Cache Fault
Ogden
Great Salt Lake
Salt Lake City
Fault
Zone
Heber City
Provo
Dugway
Nephi
Price
Delta
Manti
OCT. 1, 1974 – MAR. 31, 1980
M_L:
6 4 2 1<1
0 50 100 km
b
44°54'
110°50'
RED CANYON FAULT
HEBGEN FAULT
0 5km
N
MONT.
WYO.
HEBGEN LAKE
MONT.
ID.
WEST YELLOWSTONE
c
44.0°
43.5°
43.0°
42.5°
111.5°
111.0°
110.5°
Jackson Lake
DRIGGS
IDAHO
WYOMING
Teton Fault
Swan Valley
JACKSON
Palisades Reservoir
Hoback Fault
Blackfoot Reservoir
Star Valley
AFTON
SODA SPRINGS
Gem Valley
Bear Lake V.
0 30 km

Figure 2.

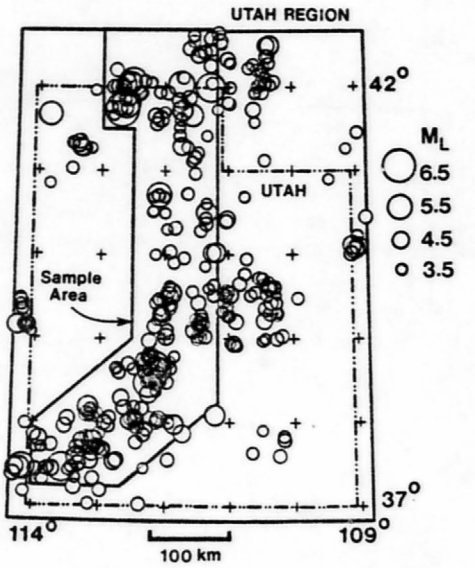

Figure 3.

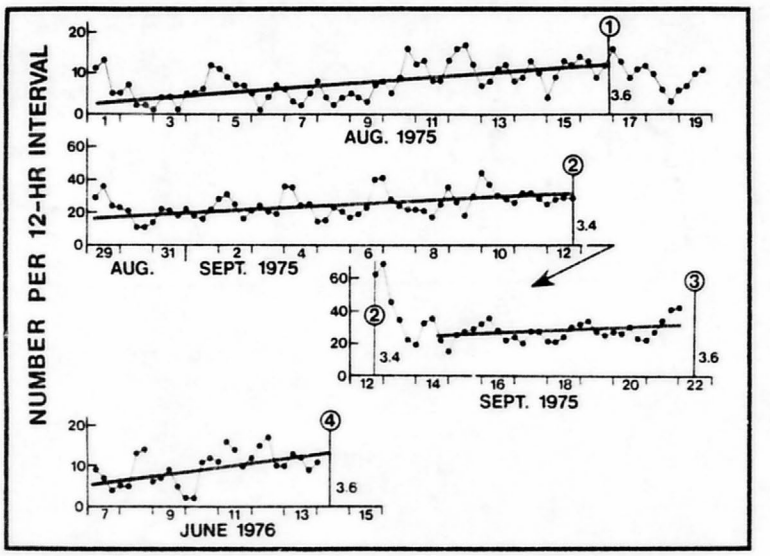
NUMBER PER 12-HR INTERVAL
AUG. 1975
AUG.
SEPT. 1975
SEPT. 1975
JUNE 1976
3.6
3.4
3.4
3.6
3.6

Figure 4.

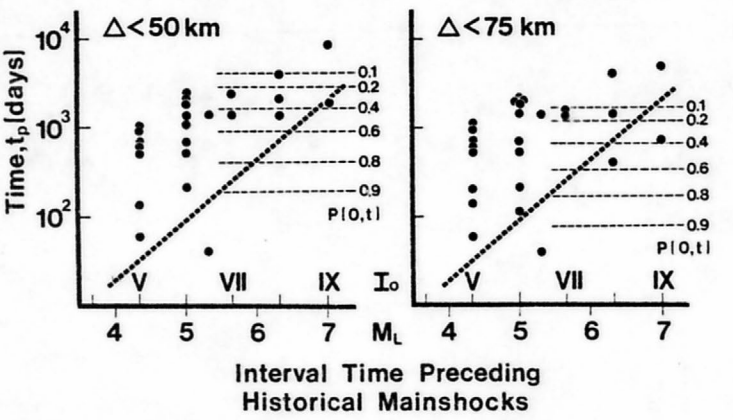
Δ<50 km
Δ<75 km
Time, t_p (days)
10^4
10^3
10^2
0.1
0.2
0.4
0.6
0.8
0.9
P(0,t)
V
VII
IX
I_o
4
5
6
7
M_L
Interval Time Preceding
Historical Mainshocks

Figure 5.

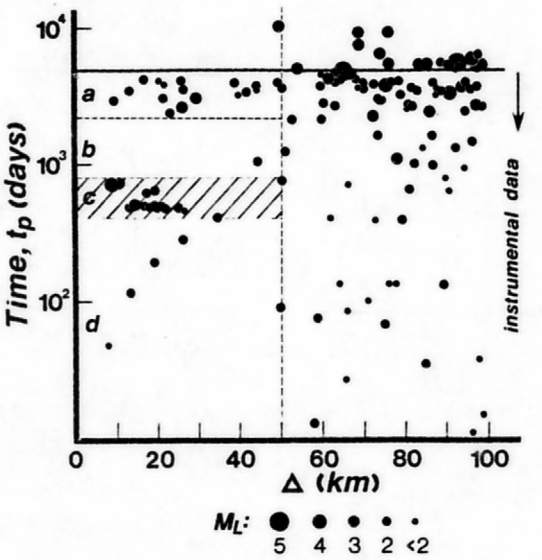
10^4
10^3
10^2
a
b
c
d
Time, t_p (days)
instrumental data
0
20
40
60
80
100
Δ (km)
M_L:
5
4
3
2
<2

Figure 6.

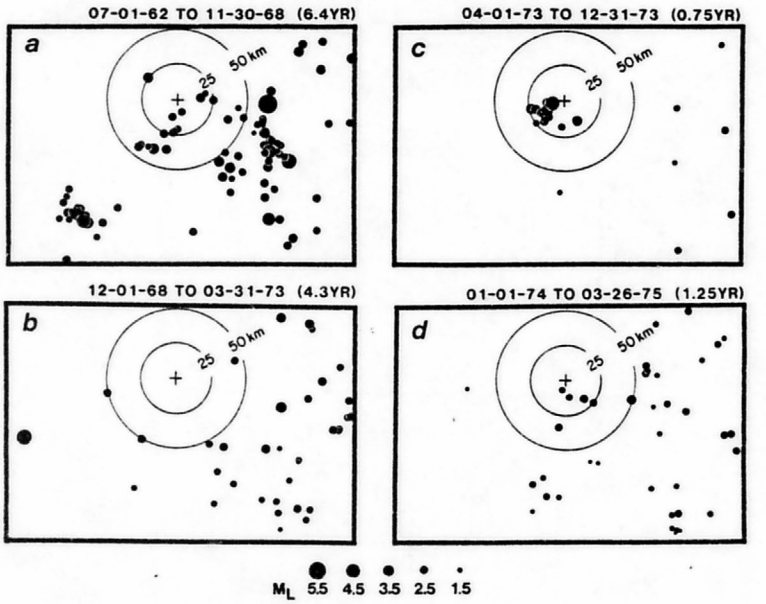
07-01-62 TO 11-30-68 (6.4YR)
a
50 km
25
04-01-73 TO 12-31-73 (0.75YR)
c
50 km
25
12-01-68 TO 03-31-73 (4.3YR)
b
50 km
25
01-01-74 TO 03-26-75 (1.25YR)
d
50 km
25
M_L 5.5 4.5 3.5 2.5 1.5

Figure 7.

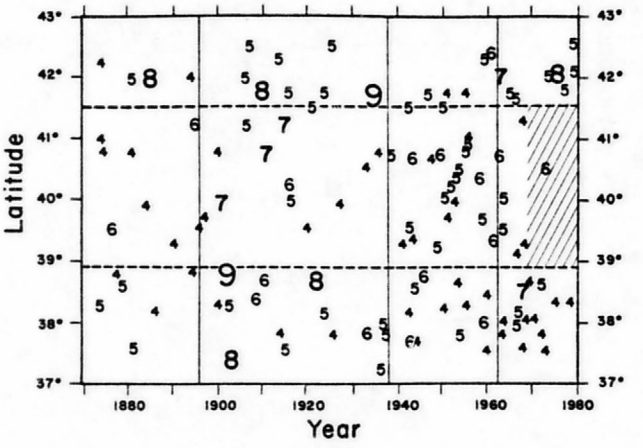
Latitude
Year
43°
42°
41°
40°
39°
38°
37°
1880
1900
1920
1940
1960
1980

Figure 8.

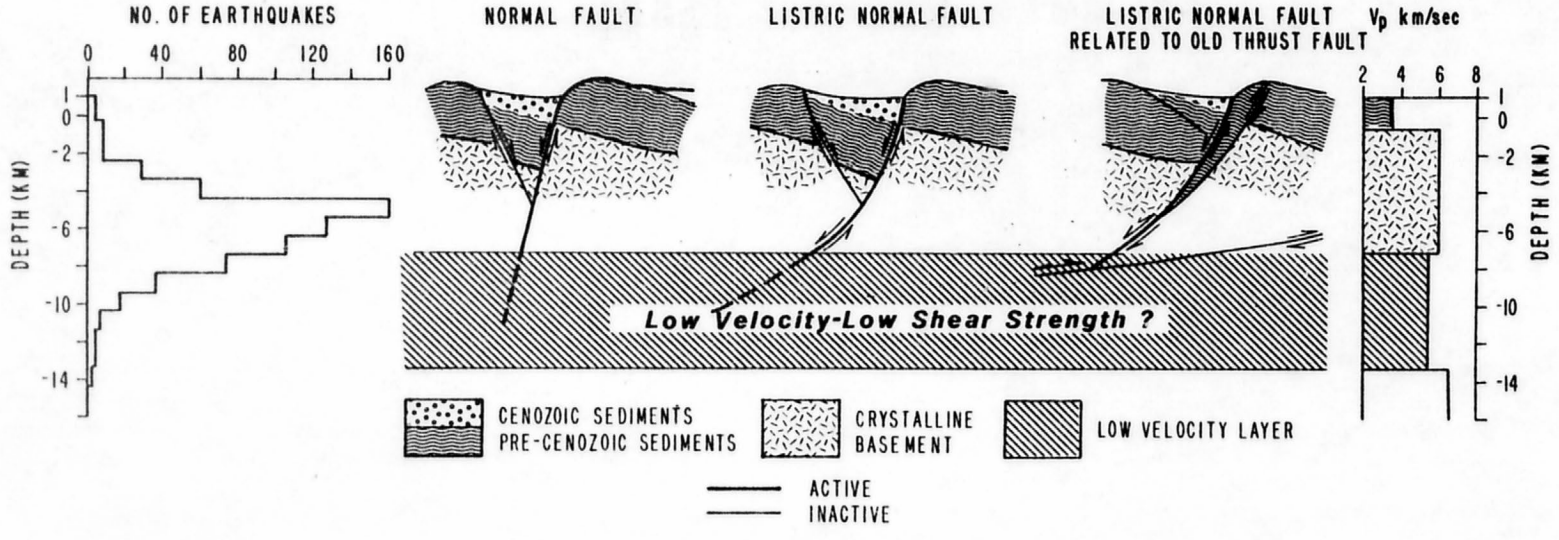
NO. OF EARTHQUAKES
0
40
80
120
160
DEPTH (KM)
1
0
-2
-6
-10
-14
NORMAL FAULT
LISTRIC NORMAL FAULT
LISTRIC NORMAL FAULT
RELATED TO OLD THRUST FAULT
Vp km/sec
2
4
6
8
Low Velocity-Low Shear Strength ?
CENOZOIC SEDIMENTS
PRE-CENOZOIC SEDIMENTS
CRYSTALLINE
BASEMENT
LOW VELOCITY LAYER
ACTIVE
INACTIVE

Figure 9.

ATTACHMENT No. 2

SIMULTANEOUS INVERSION FOR HYPOCENTERS AND LATERAL VELOCITY VARIATIONS: AN ITERATIVE SOLUTION WITH A LAYERED MODEL

B. W. Hawley, G. Zandt, and R. B. Smith

Department of Geology and Geophysics, University of Utah
Salt Lake City, Utah 84112

ABSTRACT

An iterative inversion technique has been developed that uses the direct P- and S-wave arrival times from local earthquakes to compute simultaneously a three-dimensional velocity structure and relocated hypocenters. Crustal structure is modeled by subdividing flat layers into rectangular blocks. An interpolation function is used to smoothly vary velocities between blocks, allowing ray trace calculations of travel-times in a three-dimensional medium. Tests using synthetic data from known models show that solutions are reasonably independent of block size and spatial distribution, but sensitive to the choice of layer thicknesses.

Application of the technique to observed earthquake data from north-central Utah shows the following: (1) lateral velocity variations in the crust as large as 7% occur over 30 km distances; (2) earthquake epicenters computed with the three-dimensional velocity structure were shifted an average of 3.0 km from locations determined assuming homogeneous flat layered models; and (3) the laterally varying velocity structure correlates with anomalous variations in the local gravity and aeromagnetic fields suggesting that the new velocity information can be valuable in acquiring a better understanding of crustal structure.

INTRODUCTION

Over the past decade many workers have used matrix-inversion techniques to extract hypocenter and velocity information from the arrival times of earthquakes and artificial seismic events. One important advantage of these inversion techniques is that existing arrival time data can be processed without modification. Following the deployment of modern seismograph networks with dense station spacing during the past decade, there is now ample data and a clear need for sophisticated techniques to exploit the rapidly increasing data base.

Generalized inverse solutions using homogeneous, layered velocity models were developed by Michaels (1973) and Crosson (1976) for use with both head-wave and direct-wave arrival time data from local earthquakes. Michaels allowed both layer velocities and layer boundaries to vary in his inversion scheme, that solved for velocity structure and hypocenters using a boot-strap procedure. Crosson fixed the layer boundaries but added station corrections in an effort to correct his model for laterally inhomogeneous structure.

A significant contribution on generalized modeling of three-dimensional velocity structure was made by Aki and Lee (1976), who subdivided flat layers into rectangular blocks, then solved for a constant velocity perturbation for each block. For simplicity they started with a homogeneous half-space as an initial model and inverted only once for their final solution. Their results showed that this type of one-step inversion is

limited, because without inverting iteratively, the final solution was highly dependent on the starting model.

In this paper we describe an iterative inversion technique that incorporates some of the important characteristics of the previous methods along with some new ideas. The technique described here uses direct P- and S-wave arrival times from local earthquakes to define, by simultaneous inversion, both a three-dimensional velocity structure and relocated hypocenters. We chose to use direct P- and S-wave arrivals because most first-arrivals from earthquakes in the distance range 0 to 100 km are from the direct wave branches. In addition, while refracted waves provide important information on average layer velocities, direct waves provide better information on lateral variations within a layer.

Formulation of the forward problem is a modification of Aki and Lee's (1976) method in which the restriction of the half-space initial model is removed and travel times are computed using three-dimensional ray tracing. Inversion is accomplished by using the singular-value decomposition algorithm of Golub and Kahan (1963) to compute the eigenvalues and eigenvectors of the system matrix from which the parameter adjustments are computed. The parameter adjustments are weighted using a diagonal parameter-weighting matrix (Jackson, 1972) and are damped using the "damped least squares" technique (Levenberg, 1944; Marquardt, 1963). Test cases are shown with theoretical data from known models as well as an application to observed earthquake data from the Wasatch Front in north-central Utah.

FORMULATION OF THE MATHEMATICAL MODELING

The traveltime equation is approximated using a Taylor series expansion to form a set of linear equations for the observed data in terms of the source and medium parameters. Given an initial estimate for the hypocenter and origin time for an event j, the equation for the observed first arrival at station i, T^o_{ij}, is written

$$T^o_{ij} = T^c_{ij} + \left(\frac{\partial T}{\partial X}\right)_{ij}\Delta X_j + \left(\frac{\partial T}{\partial Y}\right)_{ij}\Delta Y_j + \left(\frac{\partial T}{\partial Z}\right)_{ij}\Delta Z_j + \Delta OT_j + \sum_k \left(\frac{\partial T}{\partial C}\right)_k \left(\frac{\Delta C}{C}\right)_k \quad (1)$$

where higher order terms are ignored. T^c_{ij} is the calculated arrival time based on the initial model. The first three terms in paranthesis are the partial derivatives of the travel time with respect to the earthquake location coordinates X, Y, and Z. The terms ΔX_j, ΔY_j, ΔZ_j, and ΔOT are the unknown corrections to the initial earthquake hypocenter and origin time. The factors in the summation represent the medium parameters: C_k is the initial layer velocity and ΔC_k is the unknown velocity correction for the k^{th} segment of the ray path.

Crustal structure is modeled using flat-lying constant-thickness layers that are subdivided into rectangular blocks (Figure 1). The initial layered velocity model is based, if possible, on apriori information such as results of seismic refraction surveys. The models used here have a relatively thin (1 km), low-velocity (3.5 km/s) surface layer that represents the surficial, unconsolidated material. Note however, that the lack of earthquakes within this top layer precludes the determination of velocity

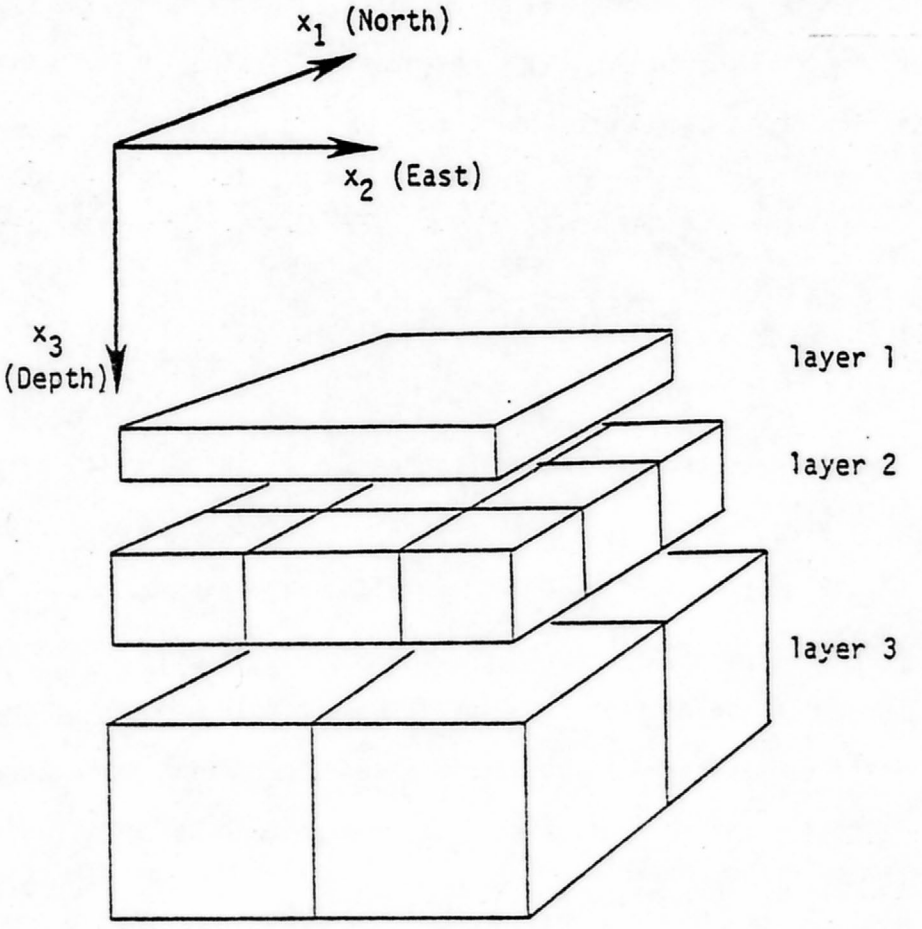

Figure 1 Basic three-layer velocity block model. Spacing between layers, only to better show block distributions.

variations within the layer. In order to account for surficial variations which undoubtedly exist in the top layer, station corrections can be applied to the data. Otherwise elevation corrections are unnecessary because the upper-surface of the top layer varies as a function of the station elevation.

Succeeding layers are subdivided into rectangular blocks. Within each of these layers an interpolation function is used to eliminate discontinuities in velocity between adjacent blocks. These discontinuities must be eliminated because they introduce unrealistic ray-path shadow zones at the surface.

The interpolation of the velocities (Figure 2) produces a single two-dimensional velocity function for each layer by smoothly varying the velocities between adjacent blocks within that layer. A set of n, two-dimensional velocity functions are then used to define the three-dimensional velocity structure for an n-layered model. Distinct layer boundaries corresponding to velocity discontinuities were maintained in this three-dimensional model because of evidence for head-wave arrivals on refraction profiles.

Interpolation is performed between velocity nodes that are defined explicitly along lines that pass vertically through the center of each block (see Figure 3a). The velocity, C, along a line L, inside a particular layer is given by the interpolation expression (Figure 3b):

$$C = f(r_1)[f(r_2)V_1 + f(1-r_2)V_2] + f(1-r_1)[f(r_2)V_3 + f(1-r_2)V_4] \qquad (2a)$$

where V_i, $i = 1, 2, 3, 4$, are the velocities at the four lines that surround L; $f(r_i)$ is an interpolation function that is proportional to the distance from L to the respective velocity nodes. Equation (2a) can be simplified to:

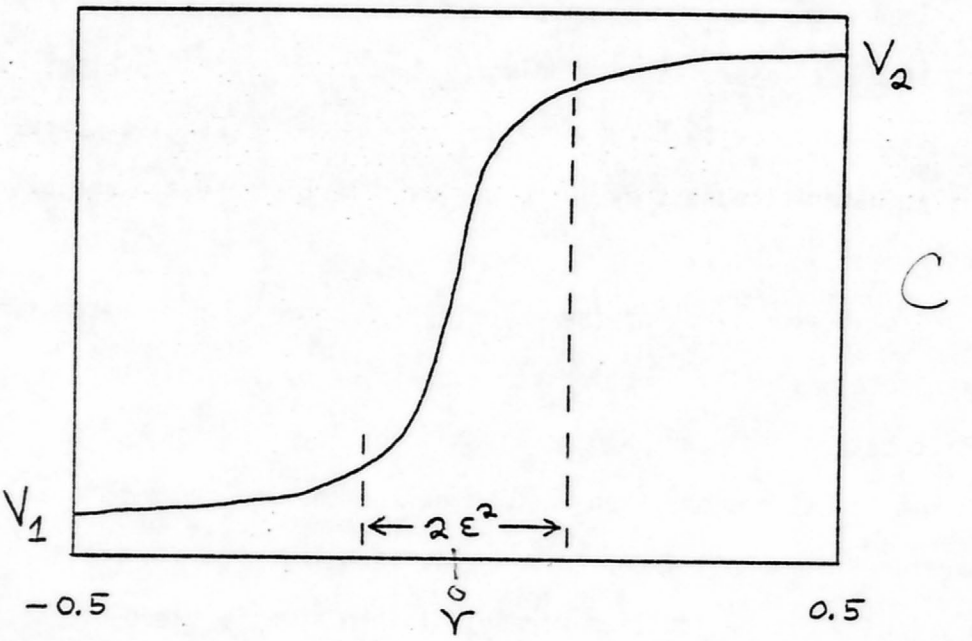

$$C = V_1 + f(r)\left(V_2 - V_1\right)$$

$$f(r) = 0.5 + \left[\frac{(0.5 + \varepsilon^2)\, r}{\varepsilon^2 + |r|}\right]$$

Figure 2 Adjustable bandwidth velocity interoplation function, shown in two-dimensions between two adjacent velocity line elements.

locations to velocity (avg = 0.2). This correlation showed that the errors in longitude were coupled to errors in velocity. This is confirmed by the final values of the velocities of the blocks adjacent to the fault in layer two. The velocities immediately west of the fault were slightly underestimated while those east were slightly overestimated, a pattern consistent with the slight, yet systematic mislocation of the epicenters. Despite this, the RMS velocity error in layer two was only 0.13 km/s (2.4%) in comparison to the 0.60 km/s (10.9%) total contrast across the fault. The velocity errors in layer three are again somewhat larger at 0.43 km/s (6.6%), yet the velocity contrast of 0.60 km/s (9.1%) across the fault was still discernable. Part of the reason for the worse velocity determination in this model is the location of all the hypocenters on the straight N-S fault. Data from events off the fault would provide better sampling and result in better determinations.

The computer program HYPOELLIPSE (Lahr, 1979) was then used to locate the same events with the same noise level of 0.05 sec. As expected, this resulted in a westward shift (negative longitudes) of all epicenters by 1.7 km (Table 3). The error ellipses given for the solutions consistently had their major axis oriented east-west, suggesting least control in that direction; however, no insight could be gained as to the cause of the poor control. The HYPOELLIPSE solution for the other source parameters is just as good as the simultaneous inversion solution. This is due to the very structured east-west heterogeneity of the San Andreas fault model.

Both the source and medium parameters have larger errors in this model than the equivalent (σ_n = .05) Wasatch Front model. The very restricted hypocenter distribution (linear) in the San Andreas model is probably the

Table 4

P-wave velocities (km/sec) computed by Simultaneous Inversion for idealized San Andreas fault model (Figure 7)

layer 2				layer 3	
5.80	5.80	5.20	5.20	6.90	6.30
5.80	5.80	5.20	5.20	6.90	6.30
5.80	5.80	5.20	5.20	6.90	6.30
5.80	5.80	5.20	5.20		

True Values

5.62	5.97	5.22	5.35	6.68	6.59
5.89	5.74	5.26	5.22	7.02	5.81
5.83	5.73	5.34	5.17		
5.60	5.47	5.25	5.24	7.17	7.12

Inversion Values for $\sigma_n = 0.05$

TABLE 3

Comparison of Hypocentral Parameters Computed by 3-D Inversion and HYPOELLIPSE for Idealized San Andreas Fault Model

Event No..	True Values	Inversion σ_n = 0.05	Hypoellipse σ_n = 0.05	Event No.	True Values	Inversion σ_n = 0.05	Hypoellipse σ_n = 0.05
		(latitude, km)*				(Depth, km)*	
1	22.00	21.36	21.24	1	14.00	14.23	13.47
2	13.00	12.86	12.82	2	8.00	8.00	7.78
3	4.00	4.13	4.19	3	10.00	10.13	9.86
4	- 4.00	- 4.00	- 4.02	4	7.00	8.04	7.86
5	-13.00	-13.16	-12.67	5	13.00	13.70	13.30
6	-22.00	-22.19	-22.34	6	12.00	12.30	11.80
7	24.00	23.89	24.04	7	20.00	20.93	19.91
8	12.00	11.54	11.97	8	17.00	17.39	17.36
9	0.00	0.19	0.20	9	19.00	19.19	18.65
10	-12.00	-13.31	-12.67	10	16.00	16.15	16.29
11	-24.00	-23.65	-23.63	11	18.00	17.29	17.54
avg. error	-----	0.33	0.28	avg. error	----	0.43	0.35
		(longitude, km)*				(Origin Time, sec)	
1	0.00	- 0.11	- 1.95	1	0.00	0.02	0.15
2	0.00	- 0.22	- 1.24	2	0.00	0.02	0.06
3	0.00	- 0.13	- 1.18	3	0.00	0.01	0.09
4	0.00	- 0.52	- 1.48	4	0.00	59.93 †	59.99
5	0.00	- 0.51	- 1.55	5	0.00	59.93	0.04
6	0.00	- 0.70	- 1.49	6	0.00	59.89	0.05
7	0.00	- 0.65	- 2.29	7	0.00	59.96	0.00
8	0.00	- 0.31	- 1.86	8	0.00	59.98	59.94
9	0.00	- 0.19	- 2.17	9	0.00	59.94	0.03
10	0.00	- 0.56	- 1.58	10	0.00	0.06	59.94
11	0.00	- 0.87	- 1.74	11	0.00	0.08	0.04
avg. error	----	0.43	1.68	avg. error	----	0.05	0.05

* In local Cartesian coordinate system

* Datum at mean sea level

† Refers to previous minute; ie -0.07 sec

and noise with a standard deviation of 0.10 sec was added to all arrival times. The RMS errors in latitude, longitude, depth, and origin time were 0.84 km, 1.04 km, 2.17 km, and 0.23 sec, respectively. The errors in source parameters are three to four times larger than the 3-D inversion with equivalent data sets (Table 1). The test also indiciates that final RMS residuals are not singley a good measure of the accuracy of hypocenter locations. The mean RMS for these HYPOELLIPSE locations was 0.11 sec which is very near the noise level of the data, implying excellent fit to the data. Nevertheless, the test shows that systematic lateral velocity variations on the order of less than 7% will degrade earthquake locations if a homogeneous layer velocity model is assumed. However, this assumption need not be made, and our tests indicate there is sufficient information in even average quality arrival time data to resolve more complex velocity models allowing better earthquake locations.

To evaluate the dependance of these tests on a particular model, similar tests were performed with the San Andreas fault data set; intially with σ_n = 0.05 sec. Using the same weighting factors and damping coefficients as before, the inversion reduced the RMS to 0.03 sec in seven iterations. At the start of the second iteration all events were located about 1.6 km west of the fault; however, the following five iterations were able to correct the locations by simultaneously adjusting the velocity model until the events were within an average of 0.4 km away from the fault (see Tables 3 and 4). The standard errors computed for longitude (0.05 km) gave no evidence that the events were located 0.4 km away from the fault, but the correlation matrix elements relating longitudes and velocities were consistently higher (avg = 0.4) than any of the other elements relating

The RMS errors in latitude, longitude, depth, and origin time were respectively 0.14 km, 0.19 km, 0.32 km, and 0.03 sec. The RMS error in velocity for layer 2 is 0.05 km/s (0.8%) in comparison to the 0.40 km/s (6.7%) contrast in velocity between the southwest and northeast corners of the layer. In layer 3, the RMS error was 0.13 km/s (1.6%) in comparison to the 0.30 km/s (4.7%) west-to-east velocity contrast. These results show that when random noise of σ_n = 0.05 sec is added to even a relatively sparse data set, reasonable results can be obtained.

Since earthquake data often have greater noise levels than the previous test an inversion was performed with a more realistic noise level of 0.10 sec standard-deviation. Using the same weighting and damping as before, the RMS was reduced to 0.07 sec after seven iterations. Generally, doubling the noise in the data doubled the errors. The RMS errors in latitude, longitude, depth, and origin time were 0.27 km, 0.30 km, 0.53 km, and 0.06 sec, respectively. The RMS velocity error in layer 2 increased to 0.09 km/s (1.4%) which is still small in comparison to the total 6.7% contrast. The RMS velocity error in layer 3 increased to 0.25 km/s (3.9%), this RMS error is approaching the total velocity contrast in layer 3 (4.7%); however, the errors are distributed such that the east-west contrast is still clearly visible (Table 2). More data from earthquakes in layer 3 would certainly improve these results. Overall the results (Tables 1 and 2), when compared to those of the last test, showed that the inversion technique remained stable with an increasing noise level in the data.

As a comparative test the same events were located using the program HYPOELLIPSE (Lahr, 1979) where average velocities were used for each layer

TABLE 2

P-wave velocities (km/sec) computed by Simultaneous Inversion for idealized Wasatch Front model (Figure 5)

layer 2				layer 3	
6.00	6.07	6.13	6.20	6.50	6.20
5.93	6.00	6.07	6.13	6.50	6.20
5.87	5.93	6.00	6.07	6.50	6.20
5.80	5.87	5.93	6.00		

True Values

6.04	6.12	6.16	6.21	6.54	6.16
6.00	6.01	6.03	6.22	6.31	6.05
5.91	5.92	5.99	6.06	6.57	6.38
5.88	5.87	6.00	6.06		

Inversion Values $\sigma_n = 0.05$

6.04	6.17	6.20	6.24	6.57	6.20
6.10	6.03	6.01	6.28	6.13	5.98
5.93	5.89	5.99	6.07	6.62	6.48
5.92	5.88	6.04	6.13		

Inversion Values $\sigma_n = 0.10$

TABLE 1

Comparison of Hypocentral Parameters Computed by 3-D Inversion and HYPOELLIPSE for idealized Wasatch Front Model

Event No.	True Values	Inversion σ_n = 0.05	Inversion σ_n = 0.10	Hypoellipse σ_n = 0.10
		(latitude, km)*		
1	40.00	39.95	39.88	40.73
2	35.00	34.76	34.57	35.02
3	25.00	25.03	24.85	22.61
4	10.00	10.20	10.01	10.98
5	5.00	5.13	5.33	5.29
6	-12.00	-11.85	-11.61	-10.98
7	- 8.00	- 7.89	- 7.81	- 7.32
8	-35.00	-34.99	-34.99	-35.96
9	-35.00	-35.05	-35.08	-35.05
10	-40.00	-39.97	-39.98	-40.38
11	40.00	40.29	40.48	41.43
12	30.00	30.19	30.43	30.53
13	5.00	4.76	4.40	6.05
14	5.00	5.07	5.22	4.42
15	-30.00	-29.91	-29.81	-30.68
16	-20.00	-19.58	-19.31	-19.24
avg. error	----	0.14	0.27	0.84
		(longitude, km)*		
1	-30.00	-29.94	-29.85	-29.20
2	0.00	0.37	0.71	0.64
3	30.00	30.09	30.18	29.84
4	-20.00	-19.85	-19.81	-18.96
5	15.00	14.79	14.77	16.54
6	-32.00	-31.80	-31.58	-31.67
7	-32.00	-11.93	-11.87	-11.10
8	-30.00	-30.24	-30.33	-29.13
9	5.00	4.93	4.88	7.23
10	30.00	30.29	30.51	30.00
11	-30.00	-30.02	-30.09	-29.44
12	20.00	19.87	19.85	20.40
13	-15.00	-14.52	-14.16	-13.25
14	25.00	25.17	25.38	27.18
15	-30.00	-30.47	-30.94	-27.46
16	20.00	20.05	19.91	19.41
avg. error	----	0.19	0.30	1.04

Event No.	True Values	Inversion σ_n = 0.05	Inversion σ_n = 0.10	Hypoellipse σ_n = 0.10
		(Depth, km)*		
1	12.00	12.10	12.07	10.63
2	11.00	11.70	12.05	8.50
3	7.00	7.15	7.05	3.50
4	8.00	9.04	9.89	11.30
5	6.00	5.65	5.19	4.47
6	9.00	8.68	8.52	10.83
7	8.00	7.85	7.75	9.99
8	10.00	9.09	8.48	12.60
9	9.00	8.84	8.80	6.66
10	12.00	12.22	12.69	7.37
11	18.00	17.87	17.65	16.60
12	21.00	21.19	21.53	19.46
13	20.00	19.80	19.67	20.86
14	17.00	17.31	17.51	16.73
15	19.00	18.77	18.34	20.91
16	22.00	21.97	21.94	20.00
avg. error	-----	0.32	0.53	2.17
		(Origin Time, sec)		
1	0.00	0.02	0.04	59.90
2	0.00	59.99†	0.02	59.90
3	0.00	0.02	0.07	0.20
4	0.00	59.96	59.93	59.60
5	0.00	0.06	0.13	59.70
6	0.00	0.05	0.08	59.80
7	0.00	0.02	0.02	59.00
8	0.00	0.09	0.15	59.70
9	0.00	0.02	0.01	59.80
10	0.00	59.98	59.94	59.90
11	0.00	0 02	0.04	59.70
12	0.00	59.94	59.90	59.90
13	0.00	59.97	59.93	59.80
14	0.00	59.97	59.94	59.90
15	0.00	0.00	0.00	59.80
16	0.00	0.06	0.11	0.10
avg. error	----	0.03	0.06	0.23

* In local Cartesian coordinate system centered 10 km South of Brigham City, Utah.

* Datum at mean sea level

† Refers to previous minute; ie -0.01 sec

theoretical arrival times. Simultaneous inversion, using the computer program 3-D INVERSE (Hawley, 1979) was then performed to calculate hypocenters and three-dimensional velocity structure. The starting model consisted of flat-lying homogeneous layers and all events were initially located at 12 km beneath the station with the earliest arrival time. During the inversion the damping coefficient, θ^2, was set at 0.05 for the first iteration then gradually decreased to 0.01 for the fifth and final iteration.

The elements of the weighting matrix were adjusted through successive iterations in an effort to maintain a normalized system equation (Equation 13). For the last two of the four iterations the optimum values for these weighting coefficients were:

$$\begin{aligned} W_x &= W_y = 1/1.0 \text{ km}^{-1} \\ W_z &= 1/0.33 \text{ km}^{-1} \\ W_T &= 1/0.15 \text{ sec}^{-1} \\ W_v &= 1/0.10 \text{ sec/km} \end{aligned} \tag{18}$$

While developing a systematic method for selecting these factors, the expected trade-off between resolution and variance was observed. Knowledge of this trade-off allowed the use of the resolution matrix and parameter standard errors to assist in the selection of the weighting factors.

For the Wasatch Front data, the inversion technique reduced RMS to a final value of 0.04 sec after five iterations. This final value was below the level of the noise and the solution was attempting to fit the noise. The computed source coordinates for the Wasatch Front are compared to their true values in Table 1 and the computed velocities are compared in Table 2.

Layer 1 velocity = 3.4 km/sec

5.80	5.80	5.20	5.20
5.80	5.80	5.20	5.20
5.80	5.80	5.20	5.20
5.80	5.80	5.20	5.20

layer 2

6.90	6.30
6.90	6.30
6.90	6.30

layer 3

P- wave velocities in km/sec

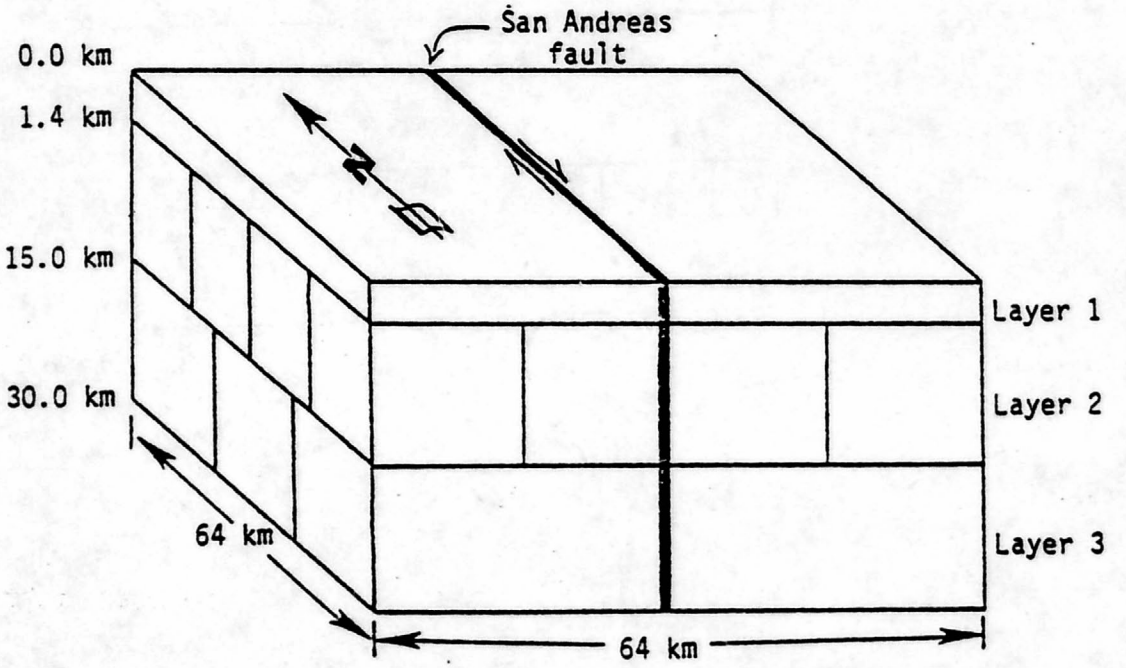

Figure 6 Idealized San Andreas fault zone velocity model, shown with fault location.

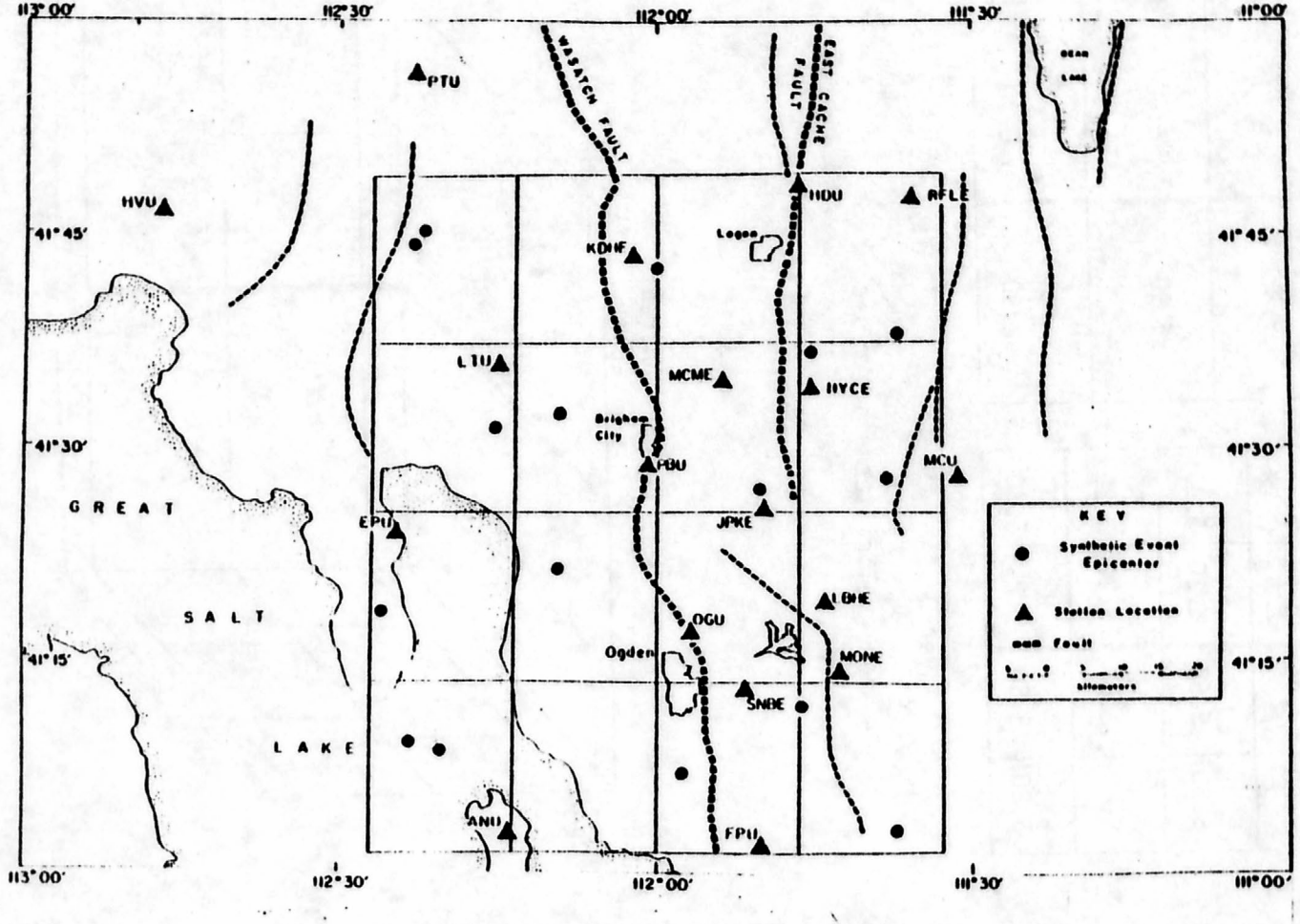

Figure 5 Map of station locations and synthetic-event epicenters used for idealized Wasatch Front model.

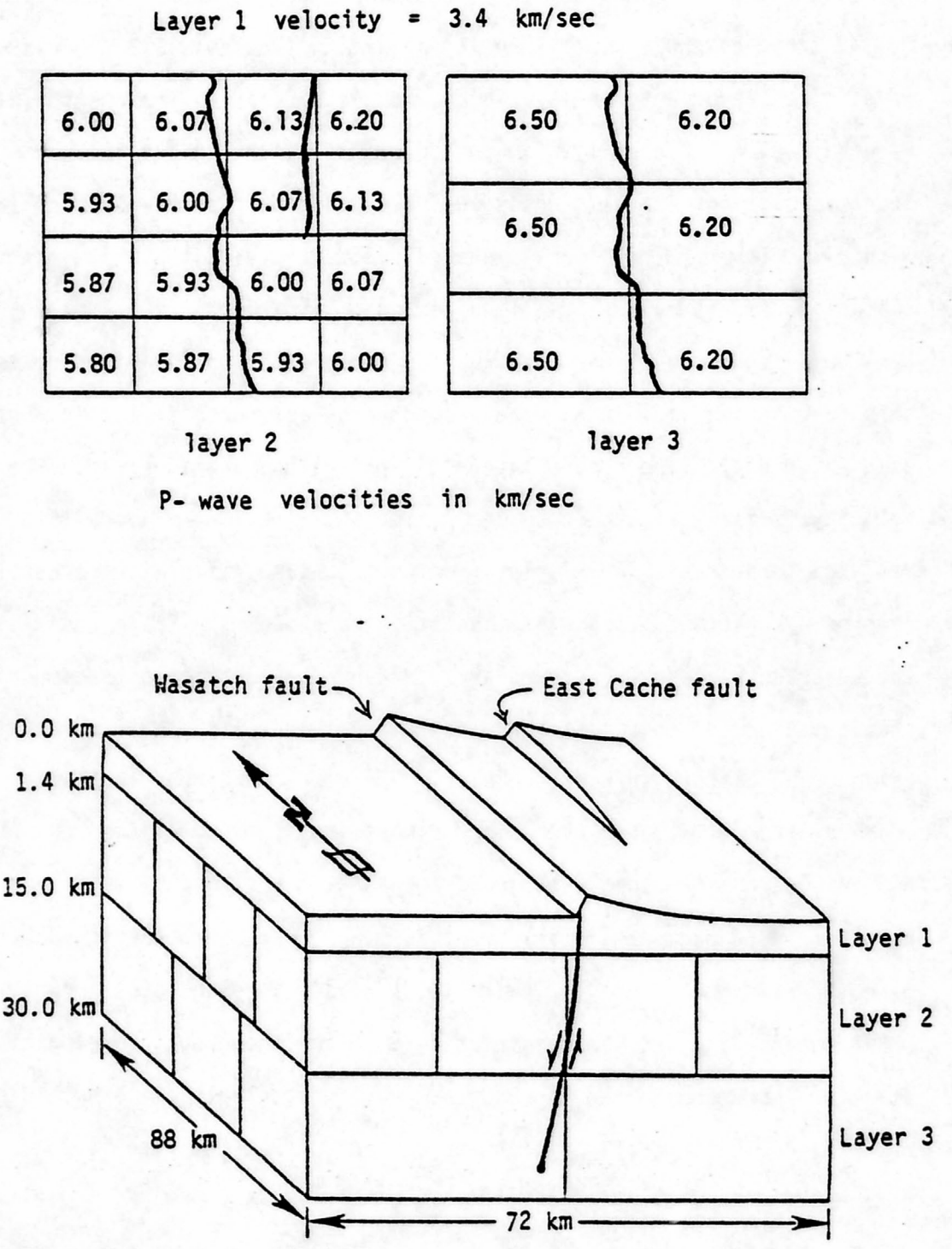

Figure 4 Idealized Wasatch Front velocity model, shown with fault locations.

Tests were performed using synthetic data sets that were generated from a three-dimensional ray-tracing algorithm (Hawley, 1979). Rays were traced through three-layer block models similar to the one shown in Figure 1. The surface layer in the model was 1.4 km thick, and had a constant velocity of 3.4 km/s which was held constant due to a lack of sources within the layer. The lower layers have lateral velocity variations representative of particular, idealized geologic situations.

The first data set was constructed to represent an idealized velocity structure in the vicinity of the Wasatch and East Cache faults in northern Utah (Figure 4). The second layer (1.4-15 km) has a gradual increase in velocity from the southwest to the northeast. The lower layer (15-30 km) has a rapid decrease in velocity from west to east, simulating crustal thickening observed across the transition zone from the Basin and Range to the Colorado Plateau (Braile et al., 1974). The location of seismograph stations used for this test correspond to those of the Wasatch Front seismograph network in northern Utah. The sixteen hypothetical epicenters were distributed evenly throughout the block model (Figure 5). An average of eight P-arrivals and three S-arrivals were calculated for each artificial event forming a data set that is overdetermined by a factor of about 2, with 163 arrival times and 86 unknowns.

A second data set was constructed to be analogous to the velocity structure surrounding the San Andreas fault in central California (Figure 6). This velocity configuration was chosen so that the results could be compared to those of Aki and Lee (1976).

In an effort to approximate real data, random noise with a Gaussian distribution and standard deviation (σ_n) of 0.05 sec was added to the

Although it appears that this estimate is the same as that which would be computed without the weighting matrix, the new estimate is different because the damping is done on the normalized parameter adjustments eliminating the problem of performing most of the damping on the large parameter adjustments.

The resolution, covariance, and correlation matrices of this solution are given respectively by the following:

$$R = V_p(\Lambda_p^2/\Lambda_p^2 + \theta^2 I)\ U_p^T \tag{15}$$

$$C = \sigma^2[V_p(\Lambda_p^2/(\Lambda_p^2 + \theta^2 I)^2)\ U_p^T \tag{16}$$

$$Corr_{ij} = \frac{C_{ij}}{(C_{ii}C_{jj})^{1/2}} \tag{17}$$

where the subscript p refers to the number of singular values used in the solution; and σ^2 is the variance of the data (Wiggins, 1972).

TESTING WITH ARTIFICIAL DATA

Testing with synthetic data calculated from a known model was used to determine the abilities and limitations of this new inversion technique. As described earlier, the non-linear travel-time equation was approximated by the linear terms of a Taylor series expansion. The testing in this section is the only way to evaluate the effects of this approximation. Furthermore, the statistical theorems used to derive the resolution and correlation matricies assume that the linearized equation is an exact representation. Therefore, these too must be tested to determine the unknown effects of the linear approximation.

adjustments, Δx, to the normalized parameter adjustments, $\Delta x'$, by

$$\Delta x' = W\Delta x. \tag{11}$$

Here $\Delta x'$ and Δx are m x 1 vectors, and W is a diagonal m x m matrix. The normalization is done by setting the diagonal elements of the weighting matrix, W_{ii}, equal to the inverse of the expected value of the corresponding parameter adjustment. In this way the normalized parameter adjustments are given by:

$$x'_i = \Delta x_i / E\{\Delta x_i\} \equiv 1 \tag{12}$$

where $E\{\}$ is the expectation operator.

Substituting the normalized parameters into the original system equation is done by defining the normalized system matrix $A' = AW^{-1}$. Then from Equation (7) we can write the normalized system equation:

$$A' \Delta x' = \Delta t. \tag{13}$$

After decomposing A' into its singular-values and eigenvectors according to Equation (5) a stable inverse operator can be formed using the damped least squares method which is then used to compute an estimate for the normalized parameter adjustments $\Delta x'$. The estimate for the desired parameter adjustments, Δx, is recovered by solving Equation (11) for Δx giving:

$$\Delta\hat{x} = W^{-1}\Delta x' \tag{14}$$

where the hat ($\hat{}$) designates that this is an estimate.

modifying the inverse operator in such a way that it minimizes a combination of the RMS and the length of the solution vector ($\Delta x^T \Delta x$). Levenberg called this approach 'damped least squares' and defined the modified inverse operator by:

$$A^* = V(\Lambda/(\Lambda^2 + \theta^2 I))\ U^T \qquad (10)$$

where θ^2 is a damping coefficient. A large θ^2 increases the stability of the solution, but decreases the parameter resolution. Hence θ^2 should be chosen as small as possible in an effort to maintain good resolution but large enough to stabilize the solution. In practice the damping factor is decreased for successive iterations as the solution approaches a minimum RMS.

The damped least squares method works very well if the inidividual parameter adjustments, Δx_i, all have approximately the same numerical value. Otherwise when θ^2 is not zero and the solution is in part controlled by minimizing the length of Δx, large parameters adjustments are damped more than small ones. In our application of the damped least squares method the adjustments to hypocenter parameters are usually five to ten times greater than the adjustments to velocity. This problem is complicated by the fact that an adjustment of 10 km in epicentral location will often have less effect on the travel-time than an adjustment of 0.2 km/s in velocity. Thus the small velocity adjustments should be damped more than the large epicentral adjustments.

One approach to solving this problem is to invert for a normalized set of parameters where, as an example, an adjustment of 10 km in epicentral location is numerically equal to an adjustment of 0.2 km/s in velocity. We obtained the normalized parameter adjustments by using a parameter weighting matrix (Jackson, 1972) that relates the original parameter

inverse operator must be used to minimize the root mean square (RMS) of the arrival time residuals. Generalized inverse operators have been thoroughly described in geophysical applications (Jackson, 1972; Wiggins, 1972; Crosson, 1976) and there are many different approaches available to compute the inverse operator. The approach used here is to first decompose the A matrix into its singular-values and eigenvectors, then form the solution in the principal-axis system.

The fundamental decomposition theorem (Lanczos, 1961) states that a matrix A can be decomposed to

$$A = U\Lambda V^T \tag{8}$$

where, if A is n x m, U is n x n and contains as columns the eigenvectors of the data space; V is m x m and contains as colums the eigenvectors of the parameter space; and Λ is n x m containing the singular-values of the system. This decomposition allows the computation of the inverse operator, A*, given by:

$$A^* = V\Lambda^{-1} U^T. \tag{9}$$

The asterisk (*) designates that, A* is a natural or generalized inverse and not a true inverse.

Difficulties often occur if the inverse operator is used to directly calculate the solution. These difficulties arise from singular-values that are either equal to or near zero, which can cause the adjustment vector Δx to become large and unstable. The cutoff point for "near zero" singular-values is dependent on both the specific application and how far the current solution is from the minimum for the RMS. Levenberg (1944), and later Marquardt (1963) showed that this instability could be controlled by

$$\left(\frac{\partial T}{\partial X}\right)_{ij} = \frac{-\Delta X_{ij}}{C^2 T_{ij}} \qquad (6)$$

where ΔX_{ij} is the distance from epicenter to station, C is the velocity at the hypocenter, and T_{ij} is the travel-time computed in the three-dimensional structure. Similar expressions are used for the Y and Z components. This approximation produces an average error of ten percent, which affects only the rate of convergence and not the final solution. Testing with synthetic data, discussed later, suggests that this error is tolerable.

FORMULATION OF THE INVERSION

Given a set of arrival time data from p earthquakes recorded at an array of q stations, a set of pq = n linear equations can be represented in matrix notation (Crosson, 1967) as:

$$A\,\Delta x = \Delta t \qquad (7)$$

The system matrix, A, contains the partial derivatives relating changes in individual parameters to changes in arrival times. The solution vector Δx contains the (4 x p) + k = m (where k is the number of medium parameters) unknown parameter adjustments. The data vector, $\Delta t = T^{obs} = T^{cal}$, contains the n arrival time residuals.

To solve for the parameter adjustments Δx, an inverse operator for the A matrix must be found. This seemingly straight forward solution is complicated on two accounts. First, because the system is a linear approximation to a non-linear problem, the solution must be computed iteratively. Second, in order to minimize random errors in timing arrivals on seismograms, the system should be overdetermined (more observed data than unknown parameters). This results in a non-square A matrix and a generalized

a second-order Runge-Kutta intergration routine is used to solve six simultaneous differential equations that can be derived from the Eikonal equation in cartesian coordinates (Eliseevnin, 1965; Julian, 1970). This poses an initial value problem, also known as the shooting method, in which the azimuth and angle of incidence of the ray are adjusted until it converges to within a given radius of the location of the recording station. In practice, we found that this technique, with a maximum error radius of 0.1 km, resulted in convergence within three or four iterations in most cases.

The travel-times were computed from the Runge-Kutta integration using:

$$T = \sum_{k=1}^{n} \frac{\Delta l_k}{C_k} \tag{4}$$

where ΔL_k is the length of the K^{th} element of the ray path and C_k is the velocity for the K^{th} ray segment. The partial derivatives with respect to the velocities are computed from:

$$\frac{\partial T}{\partial C_i} = \sum_{k=1}^{n} \frac{\Delta t_k F_i}{C_k} \tag{5}$$

where $\Delta t_k = \Delta L_k / C_k$ and F_i is the weighting factor from equation (2b).

The partial derivatives with respect to the hypocenter parameters (for direct wave travel-times) cannot be evaluated analytically without simplifying assumptions. Numerical evaluations are possible but are computationally expensive. Instead, the ray path in the three-dimensional model was approximated with the equivalent ray path in a half-space. The hypocenter partial derivatives, can then be written analytically (Aki and Lee, 1976) as:

$$C = F_1V_1 + F_2V_2 + F_3V_3 + F_4V_4 \qquad (2b)$$

where $F_1 = f(r_1)\cdot f(r_2)$, $F_2 = f(r_1)\cdot f(1-r_2)$, $F_3 = f(1-r_1)\cdot f(r_2)$, and $F_4 = f(1-r_1)\cdot f(1-r_2)$.

The block model used by Aki and Lee (1976) has no smoothing and hence allows the best possible resolution. Unfortunately, in an iterative procedure, ray-tracing in such a discontinuous medium is impractical. A simple linear interpolation solves the ray tracing problem by eliminating block boundaries but it induces such a high degree of smoothing that the resolution is unacceptably low. Experiments with a cosine interpolation function showed that it also induced too much smoothing. From these considerations the following adjustable bandwidth function was finally chosen (Figure 2):

$$f(r_i) = 0.5 + \left[\frac{(0.5 + \varepsilon^2)r_i}{\varepsilon^2 + |r_i|}\right] \qquad (3)$$

where r_i is the normalized distance from the mid-point ($r = 0$), and $2\varepsilon^2$ is approximately the bandwidth of the transition zone between two adjacent velocity blocks. We found that a bandwidth of 0.15 results in a sufficient degree of independence between adjacent velocities yet provides enough smoothing for realistic ray tracing.

Once a velocity model has been defined the next step is to compute travel-times from the sources to the receivers in the model. Ray travel times in a heterogeneous media are nonlinear functions of distance and in general have no analytic representation. In order to compute travel-times,

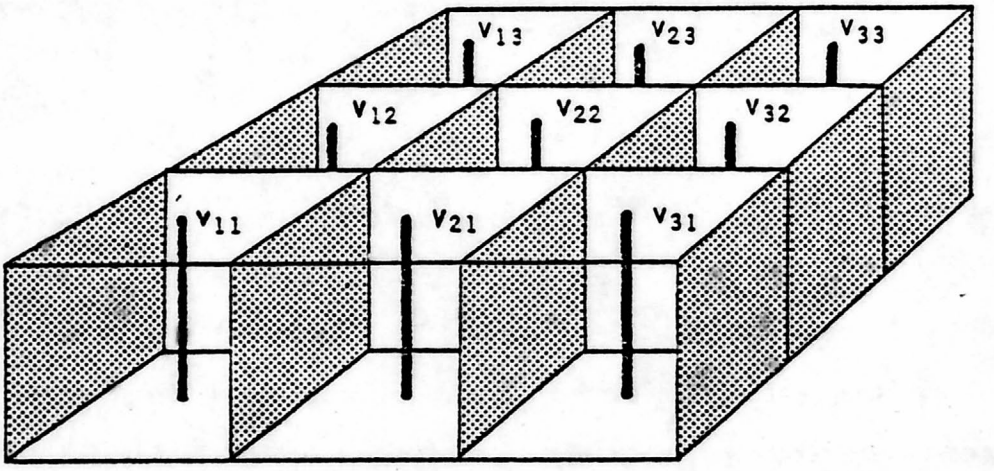

Figure 3a Location of velocity lines within blocks, used to define two-dimensional velocity function. V_{ij} subscripts refer to velocity lines within a given layer.

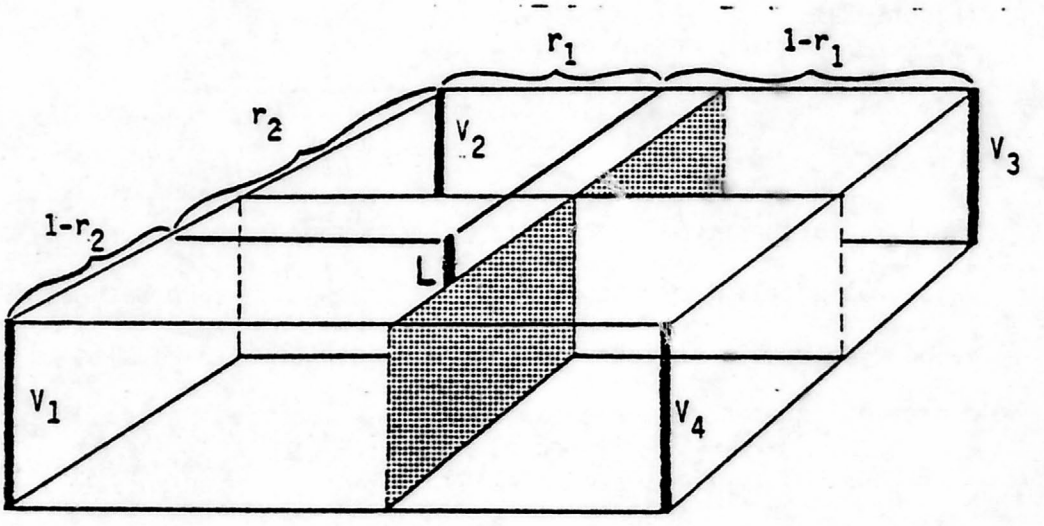

Figure 3b Geometry of two-dimensional interpolation function (equation 1). L is the line along which the interpolated velocity is desired, and the V_i subscripts refers to any four adjacent V_{ij} velocity lines (Figure 2a) that form a rectangle.

cause of the increased sensitivity to noise in the data. This effect points out the advantages of a data set with a more uniform distribution of earthquakes that provides a better sampling of the model volume.

Two important characteristics of the simultaneous inversion technique are brought out by these tests. First, solutions are both independent of the starting model and about four times more accurate than methods that assume homogeneous layers. Second, for the San Andreas test the reason for the nonuniqueness that causes the events to align away from their true locations on the fault is revealed by the correlation between longitude and velocity.

Before attempting to invert real data, two additional tests were made to determine what effect incorrect block distributions and incorrect layer thicknesses have on the solution. In seismic modeling of the real earth we can only approximate layer thicknesses, and the assumption that these layers are subdivided into rectangular blocks is at best an oversimplification. Therefore any three-dimensional modeling technique that uses rectangular blocks should be fairly independent of block size and spatial distribution. On the other hand, the earth does appear to have discrete layers as demonstrated by the discretly branched travel-time curves. Crosson (1976) showed that the correct choice of layer interfaces is important in obtaining correct layer velocities.

In the following two tests, the block sizes and numbers were changed while maintaining correct layer thicknesses; then the effect of incorrect layer thicknesses as well as redistributed blocks were made.

Test 1. In this test correct layer interfaces were used but the block configuration was changed in both layers 2 and 3 (Figure 7). Using perfect

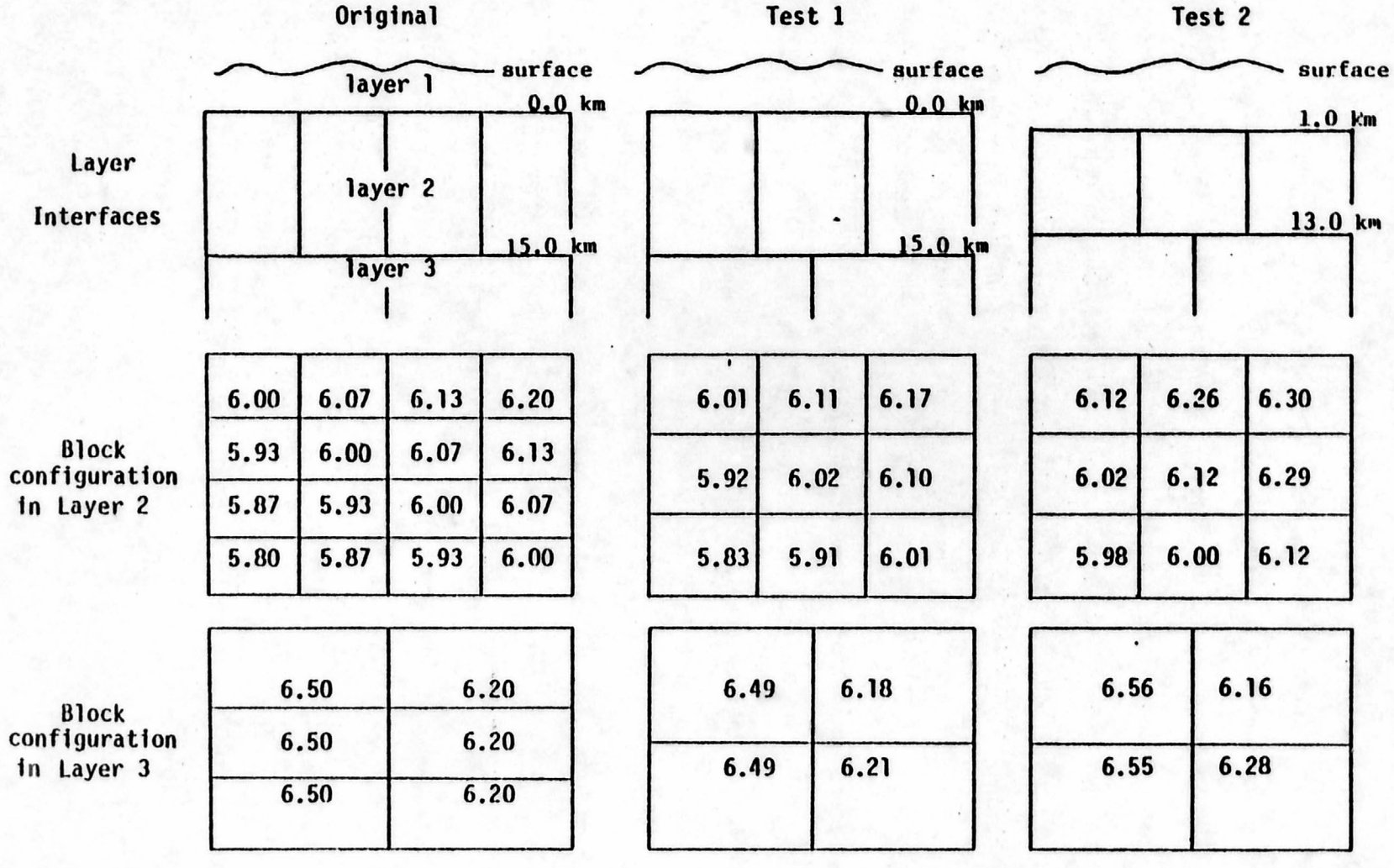

Figure 7 Geometry of redistributed blocks and interfaces used for reparameterization tests. P-wave velocities in km/sec.

data, after five iterations the RMS was reduced to 0.015 sec. The epicenter coordinates were in error by an average of only 0.08 km and depths had an average error of 0.09 km. The resultant velocity model (Figure 7) showed excellent correlation with the true velocity model.

Test 2. In this test incorrect layer thickness for all three layers were used along with the wrong block distribution of the previous test. The interface between layers 1 and 2 was moved down 1 km and the interface between layers 2 and 3 was moved up 2 km. After inversion the average errors in epicentral coordinates increased to 0.19 km and the average error in focal depth increased to 0.98 km. The errors in epicenter were still considered to be tolerable, but the errors in depth showed a definite bias toward being too shallow. This systematic decrease in focal depths was caused by the increased thickness of the lower velocity surface layer.

Increasing the thickness of the lower velocity surface layer also resulted in an average increase of 0.15 km/s in the block velocities of layer 2 (Figure 7). Raising the interface between layers 2 and 3 caused an increased thickness of higher velocity material in layer 3 which tended to compensate for the increased thickness of low velocity material in layer 1. This allowed the velocities in layer 3 to remain at approximately their correct values (Figure 7). These results showed that the technique is indeed sensitive to the choice of layer thicknesses, but less sensitive to the block size and distribution. It is important to note that changes in thickness have a very predictable effect on the average velocity of the layer. Knowing this, average velocities for headwaves and data from refraction profiles can be used to help select correct layer thicknesses. The tests also show that relative characteristics (e.g. velocity gradients

and abrupt jumps in velocity) can be recovered by relatively arbitrary block distributions, not only when correct layer thicknesses are known but even when incorrect ones are used.

APPLICATION TO THE WASATCH FRONT, UTAH

The University of Utah has operated a regional network of telemetered seismograph stations along the Wasatch Front since 1974; including a special study array of closely spaced stations along the northern Wasatch Front since 1977. The latter area was selected to apply the simultaneous inversion program because of the relatively dense station coverage allowing a more even distribution of ray paths (Figure 8). The study area is defined by an 88 km x 72 km rectangle including the northern Wasatch and the East Cache fault zones. Data were chosen by first plotting all events listed in the University of Utah earthquake catalog (see Arabasz et al., eds., 1979) that were located inside the study area, from which sixteen well-located events were selected to provide as even a distribution over the area as possible (Figure 8). Unfortunately two parts of the study area contained insufficient data to accurately define local velocities. The southwest part of the study area had no recorded events and the southeast portion had poor station coverage.

The crustal model used for the initial inversion consisted of a one km-thick surface layer with a velocity of 3.6 km/s, an average between the results of Braile et al., (1974) to the southwest and Schilly (1979) to the north. The second layer had an initial velocity of 6.0 km/s and was 15 km thick. A third layer was not used because there were few hypocenters located below 15 km. The second layer was divided into 16 blocks,

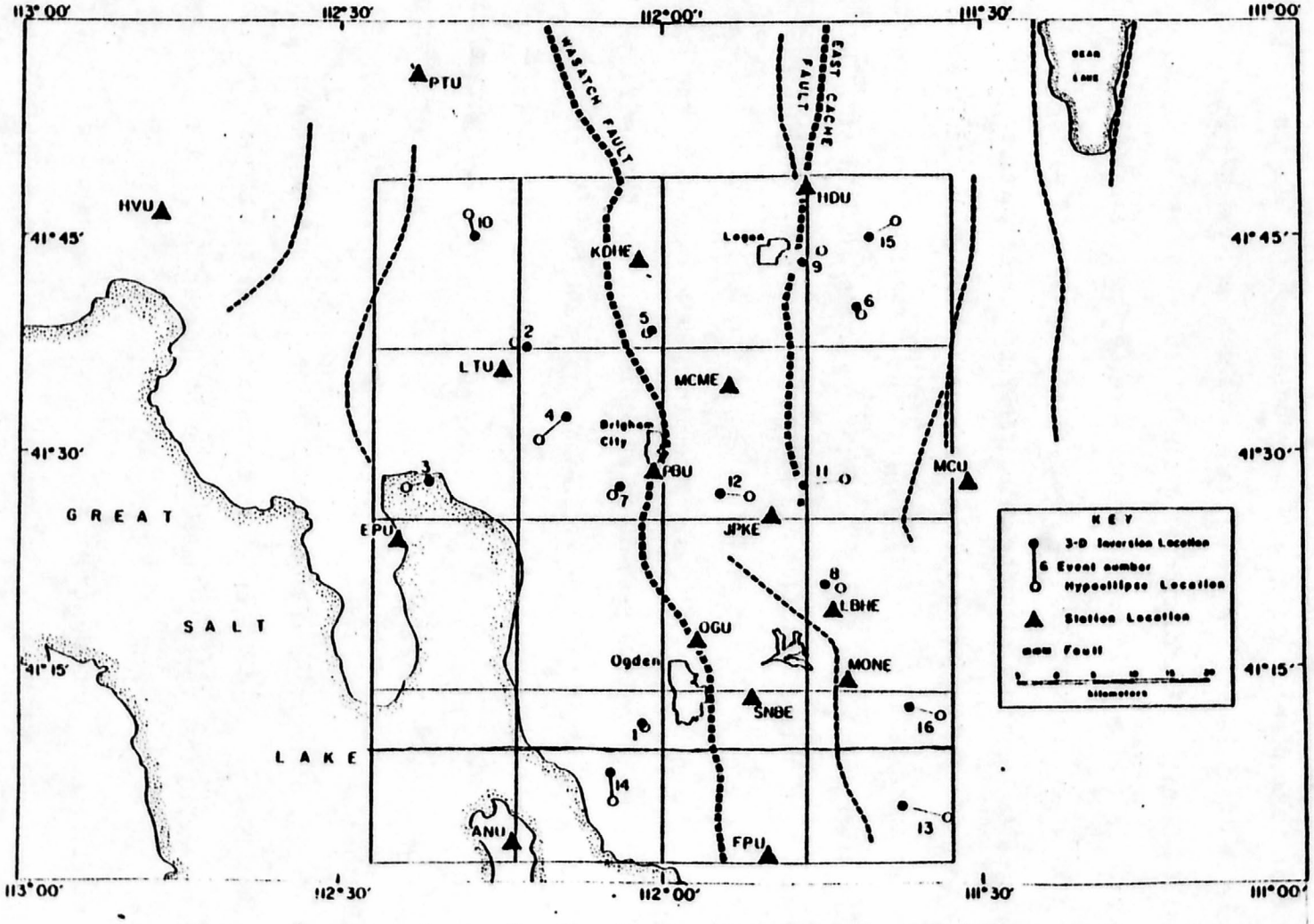

Figure 8 Comparison of epicenters computed by the 3-D Inverse and HYPOELLIPSE methods for the Wasatch Front study area events.

each measuring 22 km N-S and 18 km E-W. These dimensions were chosen so that block boundaries would roughly coincide with the Wasatch and East Cache faults. P- and S-wave arrivals were combined using a V_p/V_s ratio of 1.64 (Zandt, 1979) to produce a single laterally varying velocity model. Initial hypocenter parameters were set by placing all hypocenters at 8 km below the station with the earliest P-wave arrival time.

Simultaneous inversion for velocities and source parameters was performed using the weighting factors in Equation 18. Convergence was controlled by the damped least squares technique with θ^2 ranging from 0.20 to 0.05 over eight iterations. The final RMS of this solution was 0.21 sec. The epicenters from this calculation are plotted in Figure 8. For this run the diagonal elements of the resolution matrix for both latitude and longitude were consistently high, always greater than 0.94, except for the latitude of event #16 that had a resolution of 0.87. This single, low value was caused by a lack of stations recording that event to the south. Origin times for all events, except #16, were also well resolved as indicated by diagonal elements greater than 0.96; event #16 fell below this with a value of 0.82. Resolution of focal depths was more variable, ranging from 0.83 to 0.17.

The hypocenters were also located using the standard program HYPOELLIPSE (Lahr, 1979). The differences in epicenter locations between the two hypocenter-determination techniques was never greater than 6.0 km and averaged about 3.0 km (Figure 8). This comparison demonstrates that, similar to the synthetic tests, the three-dimensional inversion technique does not change earthquake locations by a large amount. However, the epicenters in the eastern half of the area are systematically relocated further to the west.

The principal advantage of using three-dimensional inversion lies in the additional information gained about the local velocity structure.

The velocity model computed for the study area is shown in Figure 9, along with the simple Bouguer gravity map (Cook et al., 1975), the aeromagnetic map (Zietz et al., 1976), and local topography. The block velocities for layer 2 (Figure 9) were contoured with a 0.2 km/s contour interval, with the exception of velocities in the southwest and the southeast corners which were not used because of poor data control in those two areas. Furthermore the contours on the velocity low that dips to the south is dashed at its southern extent because of the poor resolution and high standard error for the southernmost row of velocity blocks.

In the northern and central portion of the model, where sufficient data exist to resolve velocities, there is good correlation between lower seismic velocities and the north-south trending zone of low gravity anomalies (see superimposed contours in Figure 9b). These gravity lows are superimposed on a strong regional gradient that produces the predominant north-south alignment of contours on the gravity map. The regional gradient is attributed to thicknening of the lower crust; thinnest in the Basin and Range province to the west, increasing to the Rocky Mountain province to the east. Because thickening of crustal velocity layers occurs well below any of the hypocenters used to compute the velocity model, this regional gradient would not be expected to show up in the velocity model. The anomalous gravity lows that represent shallower features are located just north of Logan, north of the Great Salt Lake, and along the Wasatch fault. This trend appears as a trough in the velocity map (Figure 9a). The aeromagnetic map (Figure 9c) hints at this same trend with a ridge of magnetic highs.

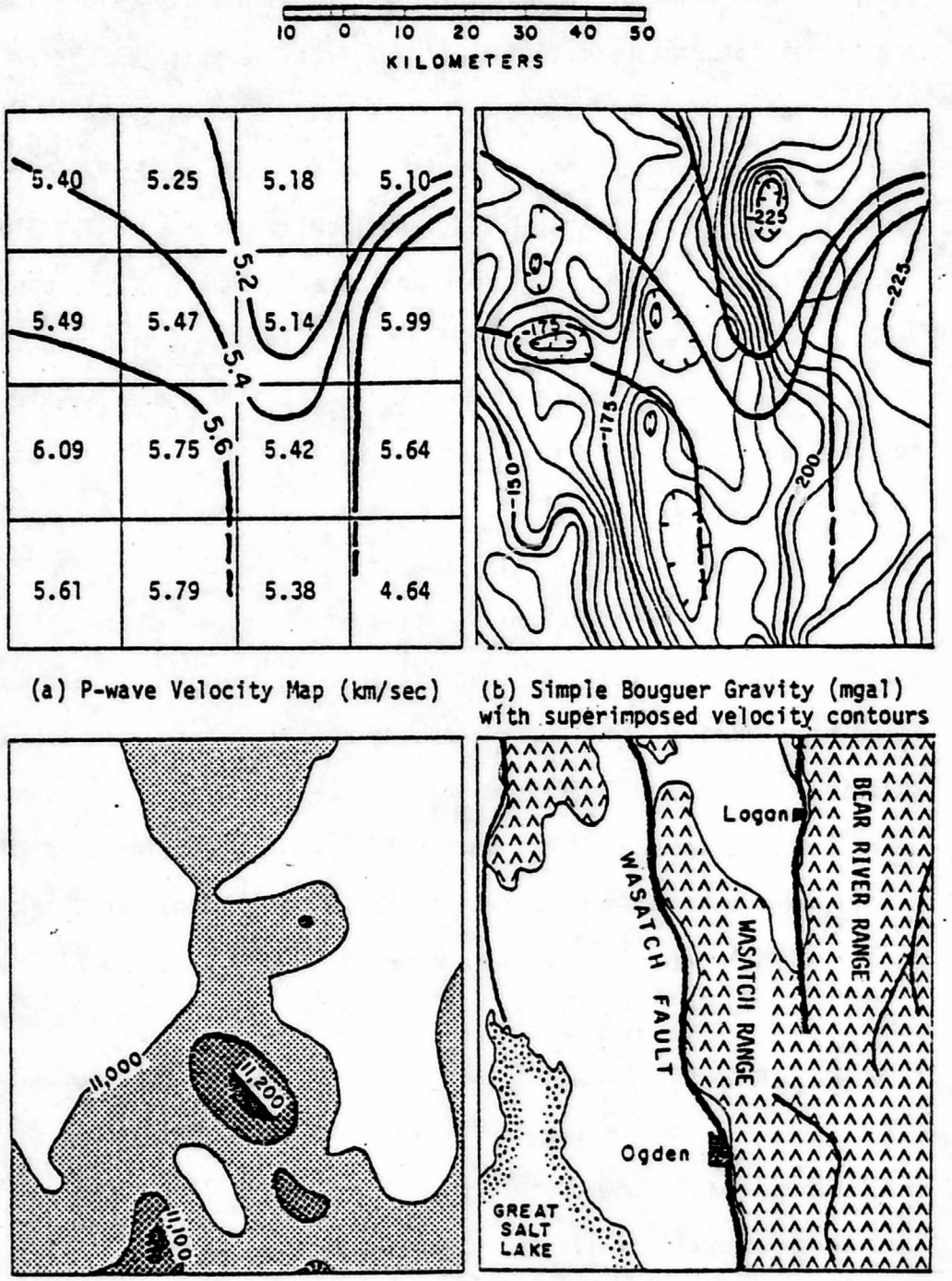

(a) P-wave Velocity Map (km/sec)

(b) Simple Bouguer Gravity (mgal) with superimposed velocity contours

(c) Total intensity Aeromagnetic Map (gammas)

(d) Topography

Figure 9 Comparison of velocity, gravity, aeromagnetics, and topography for the Wasatch Front study area.

Any explanation of this correlation would involve a detailed study of the local geology and structure that is not attempted in this paper. The purpose of presenting these results is to show that there are significant lateral velocity variations in the upper-crust along the Wasatch Front that can be determined using presently available earthquake data. The velocity variations do not directly imply deep faulting in this area, but they can be used as an additional constraint on other data to gain a better understanding of the local crustal structure.

DISCUSSION AND CONCLUSIONS

Lateral velocity variations can be calculated by three-dimensional inversion of available earthquake data from local events. The key to calculating these velocity variations is to perform a weighted simultaneous inversion. It is not necessary to have special high-quality or abundant data to calculate three-dimensional velocity models, although it will certainly produce more reliable results. This conclusion is supported by the fact that six out of the sixteen hypocenters used to compute the Wasatch Front velocity model had azimuthal gaps greater than 180 degrees, certainly far from ideal.

One problem that exists for the three-dimensional velocity modeling technique described here is the lack of deep focus earthquakes in typical intraplate fault zones such as the Wasatch Front. Without deep sources it is not possible to calculate velocity structure in lower crustal layers using this technique. In subduction zones, where deep earthquakes are common, the present technique could be used, without modification, to calculate deep velocity structures. In areas where only shallow earthquakes

exist, a combination of direct rays from local earthquakes and direct rays from teleseismic events could be used to calculate the crustal velocity structure.

Once a solution is formed it is important to be able to evaluate its quality. The resolution and correlation matrices give relative, but not absolute, evaluations of the final solution. In the Wasatch Front data it was easy to see that event #16 in the south-east corner was poorly resolved compared tc other events. For an absolute evaluation of a solution one can take these relative results and compare them to those of a similar set of artificial data where the true solutions are known.

In both cases, experimental and artificial, it was noted that the earthquake locations computed using the new inversion technique were, on the average, not changed by more than 3.0 km from the HYPOELLIPSE locations. This suggests that earthquake catalogs for areas with upper-crustal velocity variations that do not exceed 7-10% are, on the average, not in error by more than 3.0 km due to the unaccounted for effects of lateral velocity variations.

It was encouraging to see that the velocity model computed using the new three-dimensional inversion technique shows a close correlation with other geophysical data. This suggests that the new information now available from three-dimensional velocity modeling can be used to support and constrain other data sets in an effort to gain a more complete understanding of the earth's crust.

REFERENCES

Aki, K. and W. H. K. Lee. Determination of three-dimensional velocity anomalies under a seismic array using first P arrival times from local earthquakes 1. A homogeneous initial model, Jour. Geophys. Res., 80, 4381-4399, 1976.

Arabasz, W. J., R. B. Smith and W. D. Richins, editors. Earthquake Studies in Utah, 1850 to 1978, University of Utah, Salt Lake City, 1979.

Braile, L., R. B. Smith, G. T. Keller, R. Welch, and R. P. Meyer. Crustal structure across the Wasatch Front from detailed seismic refraction studies, Jour. Geophys. Res., 79, 1295-1317, 1974.

Cook, K. L., J. R. Montgomery, J. T. Smith, and E. F. Gray. Map 37: Simple Bouguer Gravity Anomaly Map of Utah, Dept. of Geology and Geophysics, University of Utah, 1975.

Crosson, R. S., Crustal structure modeling of earthquake data 1. Simultaneous least squares estimation of hypocenter and velocity parameters, Jour. Geophys. Res., 81, 3036-3046, 1976.

Eliseevnin, V. A., Analysis of waves propagating in an inhomogeneous medium, Soviet Physics-Acoustics, 10, 242, 1965.

Golub, G. and W. Kahan, Calculating the singular values and pseudo inverse of a matrix, J. SIAM Numer. Ana. Ser. B, 2, 205-224, 1965.

Hawley, B. W., Simultaneous inversion of local earthquake data for laterally varying velocity structure and hypocenters, M.S. thesis, Dept. of Geology and Geophysics, University of Utah, 1979.

Jackson, D. D., Interpretation of inaccurate, insufficient and inconsistent data, Geophys. J. R. Astr. Soc., 28, 97-109, 1972.

Julian, B. R., Ray tracing in arbitrarily heterogeneous media, Lincoln Laboratory Technical Note 1970-45, 77 pp., 1970.

Lahr, J. C., HYPOELLIPSE: A computer program for determining local earthquake hypocentral parameters, magnitude, and first motion pattern, U.S. Geol. Surv. Open-File Rept., 79-431, 53 pp., 1979.

Lanczos, C., Linear Differential Operators, D. Van Nostrand, Princeton, N.J., 1961.

Levenberg, K., A method for the solution of certain non-linear problems in least sqaures, Quart. Appl. Math., 2, 164-168, 1944.

Marquardt, D. W., An algorithm for least-squares estimation of non-linear parameters, Jour. Soc. Indust. Appl. Math., 11, 314-441, 1963.

Michaels, P., An application of the generalized linear inverse method to the location of microearthquakes and simultaneous velocity model determination, M.S. thesis, Dept. of Geology and Geophysics, University of Utah, 1973.

Schilly, M. M., Interpretation of seismic reflection and refraction data from Yellowstone and the eastern Snake River Plain, M.S. Thesis, Dept. of Geology and Geophysics, University of Utah.

Wiggins, R. A., The general linear inverse problem: implication of surface waves and free oscillations for earth structure, Rev. Geophys. Space Phys., 10, 251-285, 1972.

Zandt, G., Active seismic experiments across earthquake source zones in the Wasatch Front area, preliminary results (abstract) Earthquake Notes, E. Sec. Seismo. Soc. Amer., 49, 39 pp., 1978.

Zietz, I., R. Shuey, and J. R. Kirby Jr., Map GP-907: Aeromagnetic Map of Utah, U.S. Geol. Surv.

ATTACHMENT No. 3

EARTHQUAKE RECURRENCE RATES FROM SEISMIC MOMENT RATES IN UTAH

by

Diane Irene Doser

A thesis submitted to the faculty of The University of Utah in partial fulfillment of the requirements for the degree of

Master of Science

in

Geophysics

Department of Geology and Geophysics

The University of Utah

December 1980

ABSTRACT

Historic data on earthquake cycles in Utah are limited. Therefore, it is difficult to determine how well the historic record of seismicity reflects the seismicity of Utah over thousands of years.

An estimate of the long-term seismicity is obtained through the calculation of seismic moment rates from available geologic data on Quaternary faulting. The recurrence rates calculated from these geologic seismic moment rates agree well with recurrence rates estimated from historic data. A return period of 77 to 180 years for a magnitude 7.0 to 7.5 earthquake in the Utah region is predicted by the historic and geologic data, indicating that the area may be overdue for an earthquake in this magnitude range.

The estimation of recurrence rates from geologic data requires the use of a Utah moment-versus-magnitude relationship. This relationship is defined by spectral studies of 19 Utah events. Spectral parameters calculated for these events are within the observed range of parameters for intraplate earthquakes.

A regional strain tensor is estimated from the moment tensors of the 19 events. This tensor indicates that the amount of east-west extensional strain is nearly equal to the amount of vertical compressional strain in the Utah region.

TABLE OF CONTENTS

TABLE OF CONTENTS (continued)

LIST OF ILLUSTRATIONS

LIST OF TABLES

ACKNOWLEDGMENTS

I would like to express my gratitude to several people who helped me during the development of this thesis. My thesis committee of Dr. R. B. Smith, chairman, Dr. D. S. Chapman, and Dr. P. H. Roth provided valuable comments and assistance. Dr. Chapman kindly allowed me to use the geothermal group's digitizer and calculator for digitizing seismograms. Encouragement and suggestions from G. Zandt and T. Owens were greatly appreciated. D. Thomas assisted in the preparation of the thesis manuscript.

This work was supported by U. S. Geological Survey, Contract No. 14-08-0001-16725. American Smelting and Refining Corporation provided me with a fellowship during my first year of graduate work.

INTRODUCTION

Geologic evidence indicates that earthquakes as large as magnitude 7.0 to 7.5 have occurred in Utah during Quaternary time (Swan et al., 1978); however, no earthquake larger than magnitude 6.6 has occurred in Utah since the beginning of historic records in 1847, a period of about 130 years. Since adequate data on the earthquake cycle times are lacking, it is difficult to determine how well recurrence rates of earthquakes based on historic data reflect the long-term seismicity of Utah. "Long-term seismicity" used here refers to the seismicity of a region over thousands of years.

The main objective of this thesis was to obtain an estimate of the long-term seismicity of Utah from combined geological and seismological information, so it could be compared to the historical seismicity. The long-term seismicity was estimated by calculating seismic moment rates from geologic data in a manner similar to that used by Anderson (1979) to estimate the long-term seismicity of southern California. Since fault length, age, and displacement data were available for many of the faults throughout Utah, seismic moment rates derived from these data were calculated for several Utah regions. The moment rates were used to calculate recurrence rates that could be compared to seismically determined historical recurrence rates.

The calculation of recurrence rates from seismic moment rates requires the use of a moment-versus-magnitude relationship that is

suitable for the given region. A relationship derived for southern California proved to be inadequate for use in Utah. This necessitated the development of a moment-versus-magnitude relationship for the Utah region. Nineteen events from Utah, ranging in magnitude from 3.7 to 6.6, were used to define this relationship.

Included in this thesis is a study of the corrections that should be applied to the processing of spectral data used for seismic moment calculations. These corrections were necessary to insure the calculation of reliable spectra.

Using the new moment-versus-magnitude relationship comparisons between historic and long-term seismicity were made. In addition, source parameters of Utah earthquakes were contrasted with those of other regions to examine variations in source properties that could indicate fundamental differences in earthquake mechanisms.

REGIONAL SEISMICITY AND TECTONICS

Earthquakes in Utah occur primarily along a 50 to 100 km wide zone that marks the transition between the Basin and Range province and the Colorado Plateau and Middle Rocky Mountains provinces, that is termed the southern Intermountain seismic belt (Smith and Sbar, 1974). (See Figure 1.) A scattered pattern of earthquakes characterizes much of this zone and epicenters are generally not located along specific faults. The zone trends north-south from the Utah-Idaho border to the area around Richfield and then changes to a southwest trend that extends across the Utah-Nevada border.

The largest historic earthquakes in Utah have occurred in the Utah-Idaho border and central Utah regions. These include the 1934 Hansel Valley earthquake of magnitude 6.6 in northern Utah and several earthquakes of magnitude 6.0 to 6.5 in the Richfield and Elsinore areas. Quaternary faulting, however, is distributed throughout the zone, indicating that widespread seismicity was prevalent during prehistoric times. A lack of seismicity on some major fault segments, such as along the Wasatch fault, is also suggested by the historical record. In some places seismic activity occurs 20 km on either side of the Wasatch fault, although geologic evidence demonstrates that earthquakes as large as magnitude 7.5 have occurred on the Wasatch fault in the last 1500 years (Swan et al., 1978).

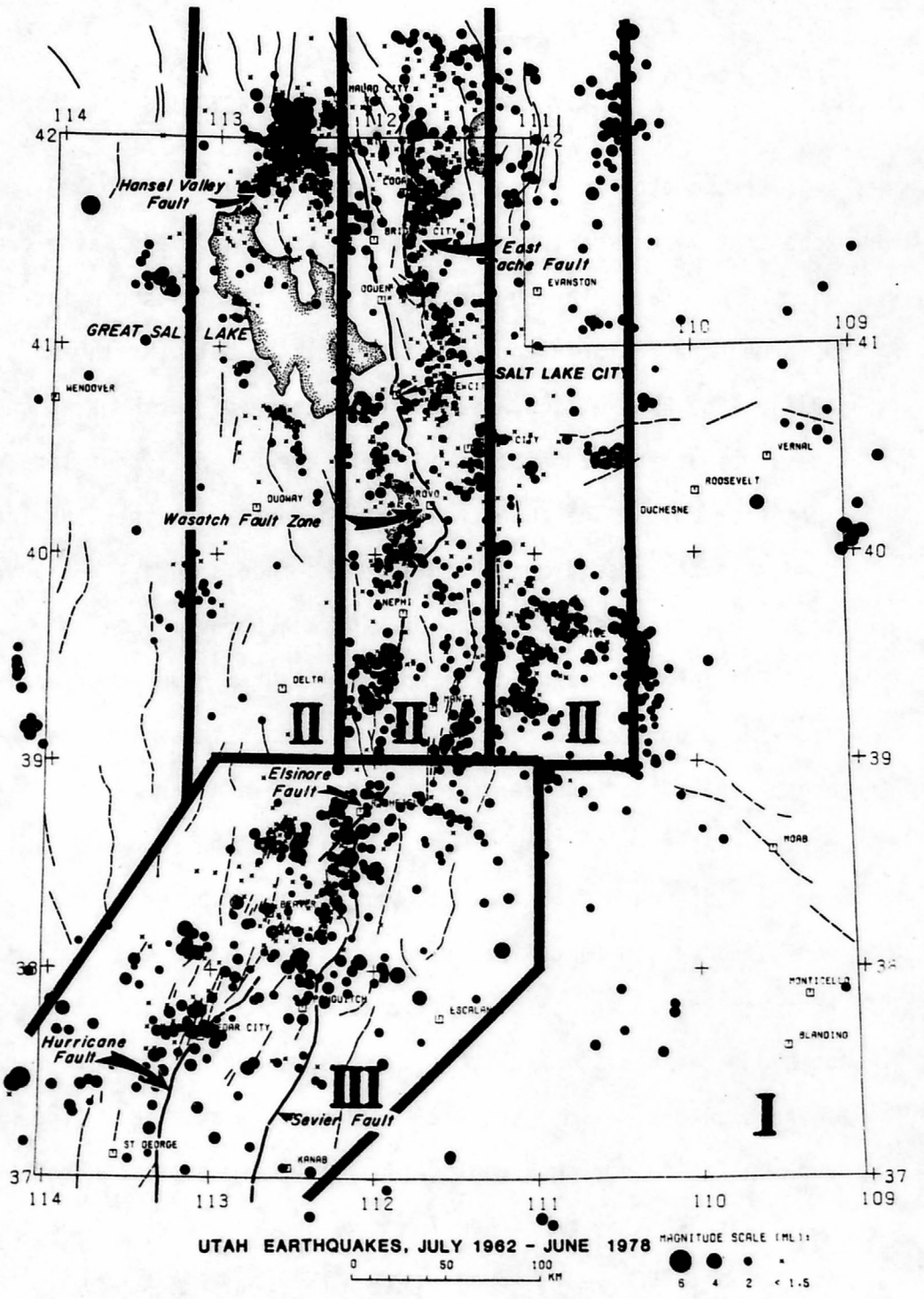

Figure 1. Utah earthquakes, July 1962-June 1978 from Smith and Arabasz (1979).

Focal depths for earthquakes in Utah rarely exceed 15 km (Smith, 1978). This maximum depth may coincide with the upper part of the low velocity layer determined by seismic refraction studies of the Utah area (Smith et al., 1975). Smith and Arabasz (1979) indicate that this low-velocity layer may be caused by a process that reduces both the shear strength and the seismic velocity, such as excess pore pressure or increased heat.

The historic earthquake activity in northern Utah-southern Idaho has been concentrated in the Hansel Valley-Pocatello Valley region and along the East Cache fault. The largest historic earthquake in Utah (M=6.6) occurred in Hansel Valley in 1934. Moderate sized earthquakes of M_L=5.7 and 6.0 have also occurred in this northern region during the last twenty years. Fault plane solutions of this region (Smith and Arabasz, 1979) (Figure 2) show general east-west extension on high angle normal faults.

Earthquakes extend south of the Wasatch Front along the Tushar and Sevier fault zones near Richfield where earthquakes of up to magnitude 6.5 have occurred. A fault plane solution in this region indicates high angle reverse faulting. This change in faulting mechanism from east-west extension on normal faults occurs near a change in the trend of the Intermountain seismic belt from north-south to southwest. Quaternary faulting south of Richfield appears to be older than that of the northern Utah region (Anderson and Miller, 1979), which may also relate to the change in the trend of the seismic belt. The southern end of the seismic zone again exhibits a change in faulting

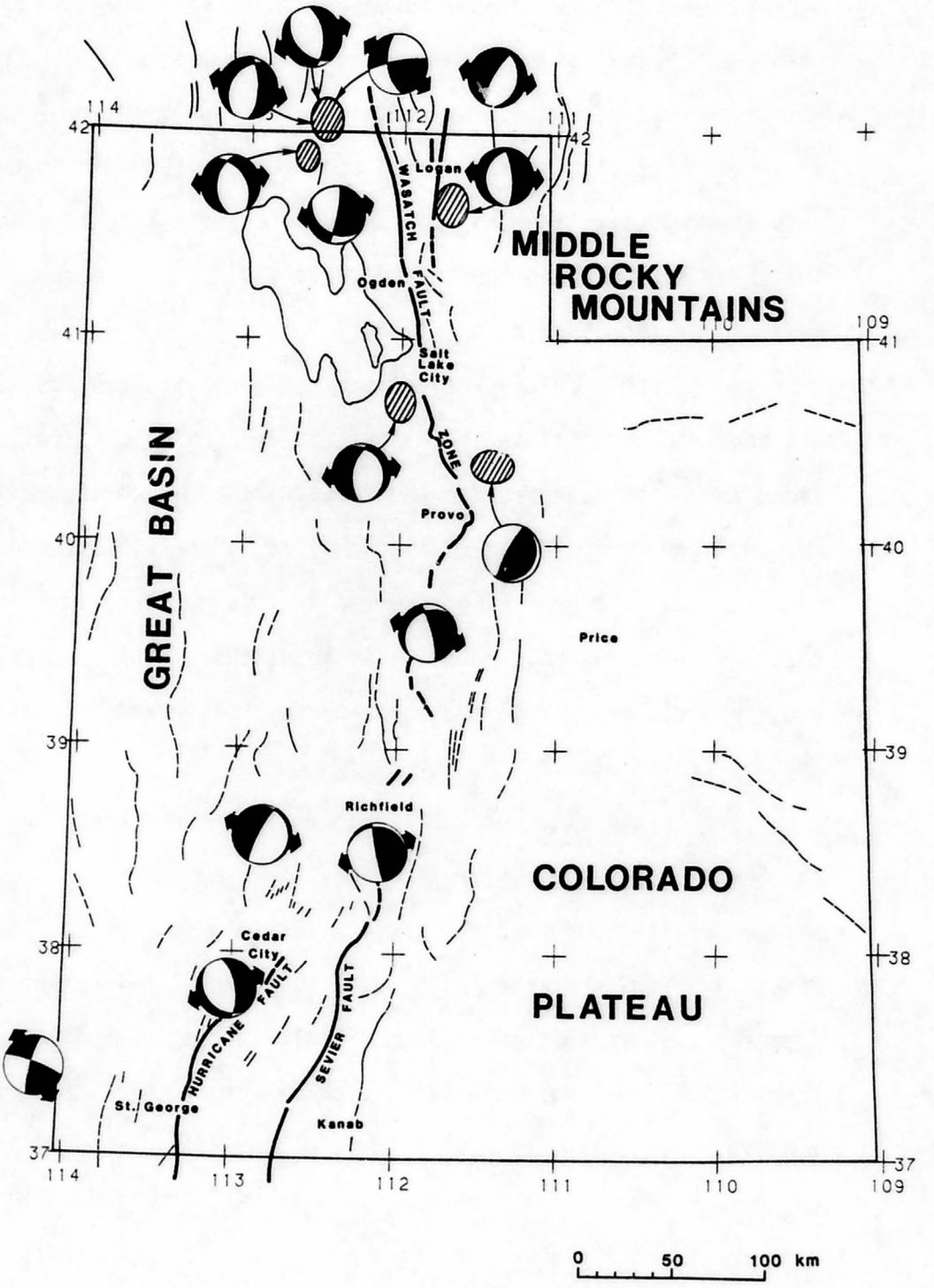

Figure 2. Fault plane solutions of earthquakes in the Utah region from Smith and Arabasz (1979). Initial compression is in black, initial extension in white.

mechanism to one of oblique strike slip motion. This pattern of strike slip faulting extends westward into southern Nevada.

As noted earlier, earthquakes occur both in the western Middle Rocky Mountain and northwestern Colorado Plateau provinces. In these regions high-angle reverse faulting mechanisms are evident, suggesting a change in the regional strain field from east-west extension to horizontal compression. An inverted U-shaped zone of earthquakes around the Price area is thought to be associated with underground mining, but it is not clear that all of these earthquakes are directly induced by the mining (Smith et al., 1974).

SEISMIC MOMENT RATES FROM GEOLOGIC DATA

Theoretical Background

Seismic moment describes the static aspect of an earthquake and is considered to be a better estimator of the "size" of an earthquake than magnitude. Seismic moment, M_o, is defined in physical terms by (Aki, 1966)

$$M_o = \mu A \bar{u} \tag{1}$$

where μ is the shear modulus, A the area of the fault plane undergoing rupture, and $\bar{u}$ is the average displacement during the earthquake. For this study $\mu = 3.3 \times 10^{11}$ dyne/cm^2 which is appropriate for crustal rock (Molnar, 1979). The long-period spectral level of body or surface waves from an earthquake is also proportional to seismic moment (Aki, 1966). This enables a calculation of seismic moment for small earthquakes that do not produce surface ruptures.

The summation of seismic moments on a fault should equal the total slip on the fault if all slip on the fault is accompanied by seismic activity (Brune, 1968). The total slip, $\bar{U}$ can thus be calculated from the sum of seismic moments

$$\bar{U} = \sum_{i=1}^{N} \frac{M_o(i)}{\mu A} \tag{2}$$

The slip rate, s, can be calculated by dividing $\bar{U}$ by the interval of time over which the seismic moments were summed. Slip rate, in turn,

can be used to calculate $\dot{M}_0$, the seismic moment rate. The moment rate is then (Brune, 1968)

$$\dot{M}_0 = \mu A s \tag{3}$$

where s is the slip rate along a fault. If geological information on fault slip rate and fault length is available and an estimate of the depth of faulting can be made, then a moment rate can be calculated for a fault using equation (3).

If faults in a region are parallel and subject to the same stress field a moment rate for the region can be estimated by summing the moment rates of the major faults throughout the region. In areas where more randomly oriented faulting occurs this method cannot be used unless slip rates on all the faults in the area are known (Anderson, 1979). It is possible to estimate a moment rate for a region with randomly distributed faulting using an equation suggested by Kostrov (1974) and Chen and Molnar (1977). This treats the area as a zone of deformation where

$$\dot{M}_0 = |2\mu l_1 l_2 r/k| \tag{4}$$

and l_1 and l_2 are the width and depth, respectively, of the zone in a plane normal to the direction of maximum horizontal deformation, r is the rate of deformation, and k is an empirically determined constant. For central Asia k = 0.75 (Chen and Molnar, 1977). This constant for central Asia will be shown to be different from the one determined from the Utah region.

Since many late Cenozoic faults in Utah exhibit parallel trends, equation (3) was used to estimate moment rates based on geologic data for several regions. Moment rates were later calculated for the same regions using equation (4) and the rates agreed well with the moment rates calculated from equation (3).

Earthquake recurrence rates can be calculated from seismic moment rates through use of Gutenberg and Richter's (1954) frequency-magnitude relationship

$$\log N(M) = a - bM \tag{5}$$

where N(M) is the number of earthquakes with magnitudes greater than or equal to M and an empirical expression relating moment to magnitude where

$$\log M_0 = cM + d. \tag{6}$$

The final expression for the recurrence rate, $N(M_0)$, for events with moments greater than or equal to M_0 (but not greater than M_0^{max}) (Molnar, 1979) is

$$N(M_0) = (1-\beta) \frac{\dot{M}_0^{\Sigma}}{(M_0^{max})^{1-\beta}} M_0^{-\beta} \tag{7}$$

where $\beta = \frac{b}{c}$ (b and c from equations (5) and (6)) $\dot{M}_0^{\Sigma}$ is the geologically determined moment rate for the region, and M_0^{max} is the moment of the largest estimated event for the region. Notice that this relationship is dependent on historically determined b-values and on a c-value from an empirically determined moment-versus-magnitude relationship. It will be shown that variations in the c-value changed recurrence rate values by as much as 80%.

Moment rates can be calculated from historic earthquake data by the use of an equation developed by Anderson (1979)

$$\dot{M}_o = \frac{10^{\alpha} 10^{(1-\beta)\gamma^{max}}}{(1-\beta)\ \ln_e 10} \qquad (8)$$

where $\beta = b/c$, $\alpha = a + \log_{10}(b \ln_e 10) + \frac{db}{c} - \log_{10}(c)$ and $\gamma^{max} = \log_{10}(M_o^{max})$. This provides a way to compare historic and prehistoric seismicity through a direct comparison of moment rates calculated from historic and geologic data. This comparison eliminates the problem of using historic b-values to compute geologic recurrence rates.

Geologic Information on Fault Dating

The dating of recent fault movements is essential in the calculation of seismic moment rates. In many areas Quaternary faults cut thick alluvial sequences that should allow for fairly straightforward dating of fault movements. However, adequate studies of stratigraphic relations and ages of alluvial deposits, for the most part, have been lacking. Even the widely accepted Lake Bonneville stratigraphic sequence developed by Morrison (1965) is currently being questioned (Scott, 1979). Lack of accurate data on the stratigraphic ages has led to the use of fault scarp morphology (Bucknam and Anderson, 1979a) to date fault movements on unconsolidated sediments in western Utah.

In southwestern Utah Quaternary volcanics are displaced by numerous faults. These faults are assigned ages that are based on the ages of the basalts they offset (Hoover, 1974; Clark, 1977; Bucknam and Anderson, 1979b).

References concerning fault displacements in Lake Bonneville and glacial sediments often discussed dates of displacements in terms of stratigraphic units displaced. In this thesis, ages for these stratigraphic units were taken from a stratigraphic correlation table compiled by Woodward-Clyde consultants (1975). Ages of fault displacements that are determined by stratigraphic relationships represent maximum ages. The amount the ages have been overestimated depends on the youth of the stratigraphic units the fault have cut. If faults cut younger stratigraphic sequences that have been finely divided into separate age units the actual ages of fault displacements are within several thousand years of the maximum ages. Ages of displacement for faults that cut sediments less than 5,000 years old are not overestimated by more than 10%. For displacements older than 15,000 years, the ages may be overestimated by as much as 40%.

Calculation of Moment Rates

An extensive search of available literature on Quaternary faulting was carried out to obtain estimates of fault lengths and slip rates in Utah. The primary source of this material was the list of references accompanying a map of Quaternary faulting in Utah by Anderson and Miller (1979). About 5% of the information was found independently from other sources. Geologic estimates of fault length and slip rate for faults used in this study are listed in Appendix A.

In order to facilitate comparisons between geologic and historical data, the regions used in this study were selected to be the same as those used by Smith and Arabasz (1979) in their study of historic

earthquake recurrence rates (Figure 3). Region I includes all of Utah and a small perimeter of surrounding state boundaries. Area II includes the Wasatch Front; area II'includes the Wasatch fault zone; and area III includes southwestern Utah.

Moment rates were calculated from geologic data for each fault or fault segment assuming that the fault dipped 60° and that the maximum depth of faulting for the fault was 10 km. The choice of a 60° dip was somewhat arbitrary, since little information on the details of fault geometry exists for this area. The depth of 10 km was chosen because 90% of the focal depths of Utah earthquakes are shallower than 10 km (Smith, 1978). The results of the moment rate estimations are also listed in Appendix A.

Discussion of Errors

One of the main sources of error involved in the moment rate calculations is the error in the age estimates based on offsets of some stratigraphic feature. Probable amounts of age overestimation were discussed in a previous section. Underestimation of ages causes overestimation of moment rates. Seventeen age estimates listed in Appendix A are underestimations. Moment rates calculated from these estimates contributed less than 5% of the total moment rate for a region.

Fault slip rates have probably varied through time and it is difficult to estimate how much they have varied. One assumption that can be made is that slip rates over the last 50,000 years are probably more representative of present day tectonics than those based on

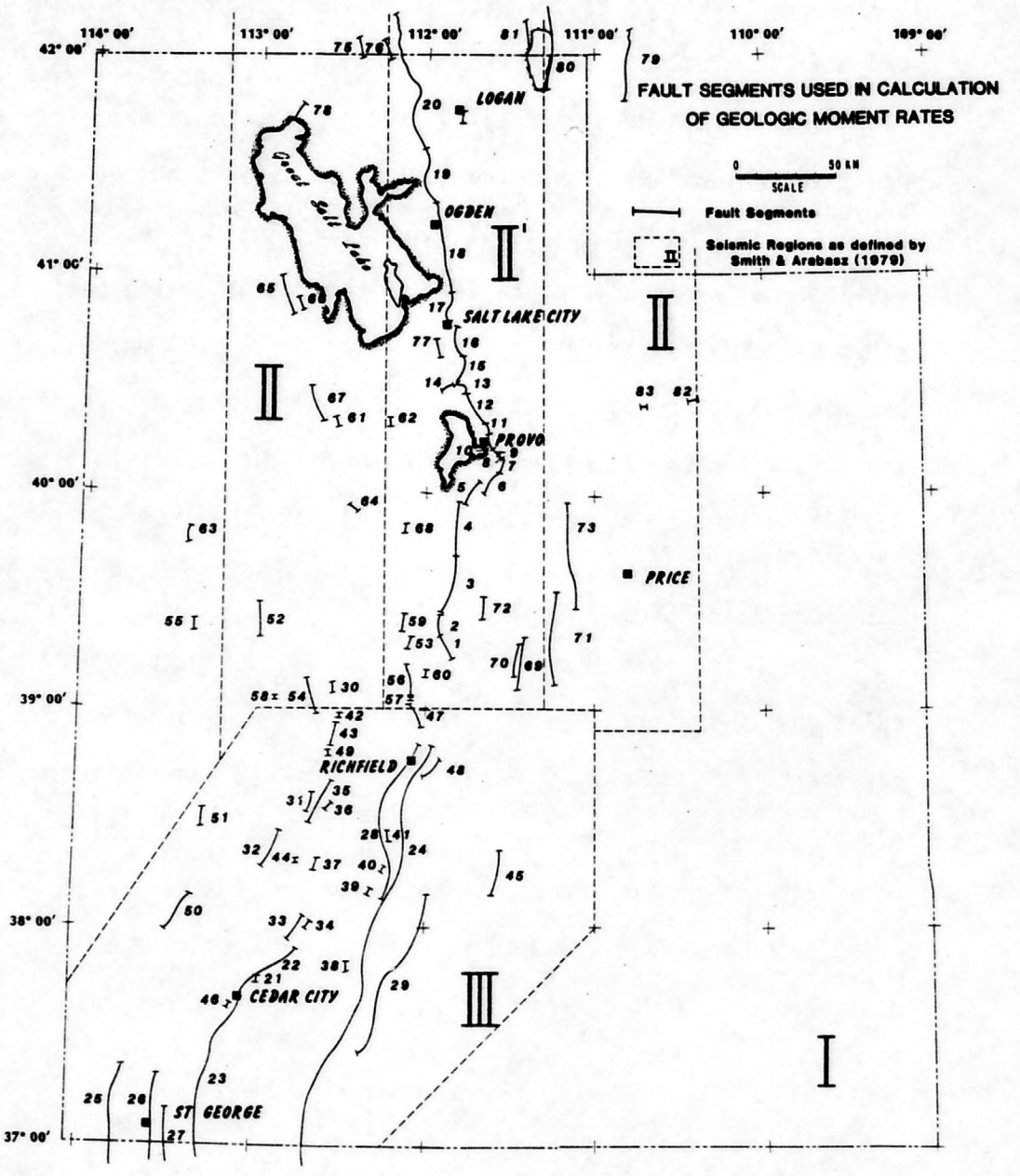

Figure 3. Map of faults and fault segments used in moment rate calculations. Numbers refer to fault listings in Appendix A.

1,000,000 years of movement. The faults that contribute the most to the total moment rate for a region have slip rates that were based on less than 50,000 years of movement. This suggests regional moment rates should reflect present day tectonics unless drastic changes in slip rate have occurred during the last 50,000 years.

Slip rates can also vary along the length of the fault itself. The fault segments that form the Wasatch fault appear to behave somewhat independently and have widely varying slip rates. Three segments of the Wasatch fault did not have offsets listed in the literature so they were assumed to have a 0.3 mm/yr slip rate, which was the minimum slip rate for fault segments with documented offsets. Detailed data on slip rates or fault segments that form other large Utah fault systems were not available, so it is not known how much error was incurred by treating the fault systems as single faults.

It is important to note that seismic moment rates are calculated by assuming all slip on a fault is caused by seismic activity. Slip on a fault is also caused by aseismic creep. This implies that the moment rate overestimates the amount of moment generated by seismic activity even if the slip rate has been calculated accurately.

The amount of fault offset can be overestimated by as much as a factor of two if back tilting of the graben is not considered (Swan et al., 1978). In most cases the documented offsets were vertical and not offsets along the fault plane itself. Slip rates calculated using vertical offsets would be 14% smaller than the true slip rate along the fault if the fault dipped 60°.

Another source of error can arise from the assumption that fault surfaces are generally planar. Seismic reflection data from central Utah (McDonald, 1976) and unpublished oil company data indicate that some faulting in the state may be along listric faults. If this is true for a majority of Utah faults, then the use of a planar fault model has resulted in an underestimation of the fault area. This means the moment rate will also be underestimated.

An additional factor which may contribute to the underestimation of moment rates for the regions is the lack of geologic data along faults that have been active during historic times. For example, little geologic data on faulting was available for the Cache Valley area, an important contributor of moderate earthquakes in historic time. Another area with little geologic data was the Pocatello Valley region along the Utah-Idaho border. Because of the lack of data in both these areas in northern Utah-southern Idaho moment rates for the Wasatch fault and the Wasatch Front regions may be underestimated by as much as 20%.

Considering all these possible sources of error, moment rate calculations for the Utah region are not thought to be underestimated by more than a factor of 2 to 3.

Calculation of Recurrence Rates

To calculate recurrence rates from geologic moment rates (using equation (7)) c, b, and M_o^{max} must be determined for the region of study. Since moment rates were calculated for the same regions as used by Smith and Arabasz (1979), b-values from their study were used.

Earthquakes as large as M_L=7.5 have been considered possible for Utah (U.S. Geological Survey, 1976), so M_0^{max} was chosen to correspond to this upper magnitude value. A c-value had not been calculated for the Utah region, and initially the relationship $\log M_0 = 1.5 M_L + 16.0$ (Thatcher and Hanks, 1973) for southern California was used.

Results of the initial recurrence rate calculations are shown in Table 1. The recurrence rates predicted by the geologic data are 50-70% smaller than those predicted by the historic data, with the exception of the Wasatch fault. Several factors could explain this disparity.

As mentioned earlier, the geologic moment rates could be underestimated by a factor of 2 to 3, which is about the difference between the historical and geological recurrence rates shown in Table 1. The difference in recurrence rates is largest in southwest Utah where some of the most reliable geologic data on faulting was available.

Another assumption made in the calculations was that a moment-versus-magnitude relationship for southern California was valid for Utah. To examine this assumption, a moment-versus-magnitude relationship was derived for the Utah region (discussed later). The resulting Utah relationship proved to be much different from the one determined for southern California.

Table 1. Recurrence rates for $7.0 \leq M_L < 7.5$ earthquakes in Utah

Area	Recurrence Rate From Historic Earthquake Data (Smith and Arabasz, 1979)	Recurrence Rate From Geologic Data Using $\log M_O = 1.5 M_L + 16.0$	Moment Rate (dyne-cm/yr x 10^{24})
Utah	0.009/yr	0.003/yr	4.4
Wasatch Front	0.0049/yr	0.002/yr	3.0
Wasatch fault	0.0008/yr	0.0012/yr	1.8
Southwest Utah	0.0036/yr	0.00093/yr	1.4

DEVELOPMENT OF A MOMENT-VERSUS-MAGNITUDE RELATIONSHIP

Data Acquisition and Processing

The calculation of moment (M_o) for events in this study was based on spectral analysis of body waves (Keilis-Borok, 1959)

$$M_o = 4\pi\rho \frac{v^3 R \Omega_o}{R_{\theta\phi}} \qquad (9)$$

where Ω_o = long-period spectral amplitude level of a P or S wave, $R_{\theta\phi}$ radiation pattern of the P or S wave, ρ = density near the source, R = hypocentral distance, and v = phase velocity of the P or S wave. For this study ρ = 2.7 grams/cm^3, v = 3.9 km/sec for an S wave and v = 6.0 km/sec for a P wave. These represent average crustal velocities and densities. Seismic moments were calculated from 82 records of body waves using this equation. Source radius and stress drop were calculated when information on corner frequencies was available.

The first step in determining the seismic moments was the development of a computer program to calculate corrected amplitude spectra from digitized seismograms of body waves. During the past decade several papers were written that described the results of spectral analysis for earthquakes. However, few describe the actual methods of spectral calculation and the corrections that must be applied to the raw spectra.

In these papers little is mentioned on the use of smoothing windows for spectral data. A program was developed to test the effects of windowing on spectral data. Windows used in this program included Bartlett, Hanning, Hamming, Parzen, Blackman, Bohman, Poisson, Cauchy, and Gaussian windows. These windows were chosen to reflect a wide variety of band width and resolution characteristics. Use of these windows produced spectra that decreased effects of negative side lobes and noise by about 40-50% as compared to a non-windowed spectra. The spectra appeared smoother and the corner frequencies were easier to determine. Application of windows did cause a decrease in the long-term sepctral amplitude level of about 10 to 20% as compared to the non-windowed spectra, however this disadvantage was slight when compared to the better resolution of corner frequencies that could be obtained through the use of windows.

Differences in the spectral shape of the various windowed spectra were slight, indicating that any of the windows would be adequate for smoothing raw spectral data. A Hamming window was chosen for the final spectral analysis program because it was easy to implement. Figure 4 shows the difference in spectral shape produced by using a Hamming window on P-wave data from Fort St. James, Canada for the August 16, 1966 Nevada-Utah border earthquake. The Hamming window considerably smooths the spectrum. The center of the window was located at the initial arrival of the phase of interest, allowing passage of most of the energy of the phase of interest and helping to filter out later phases.

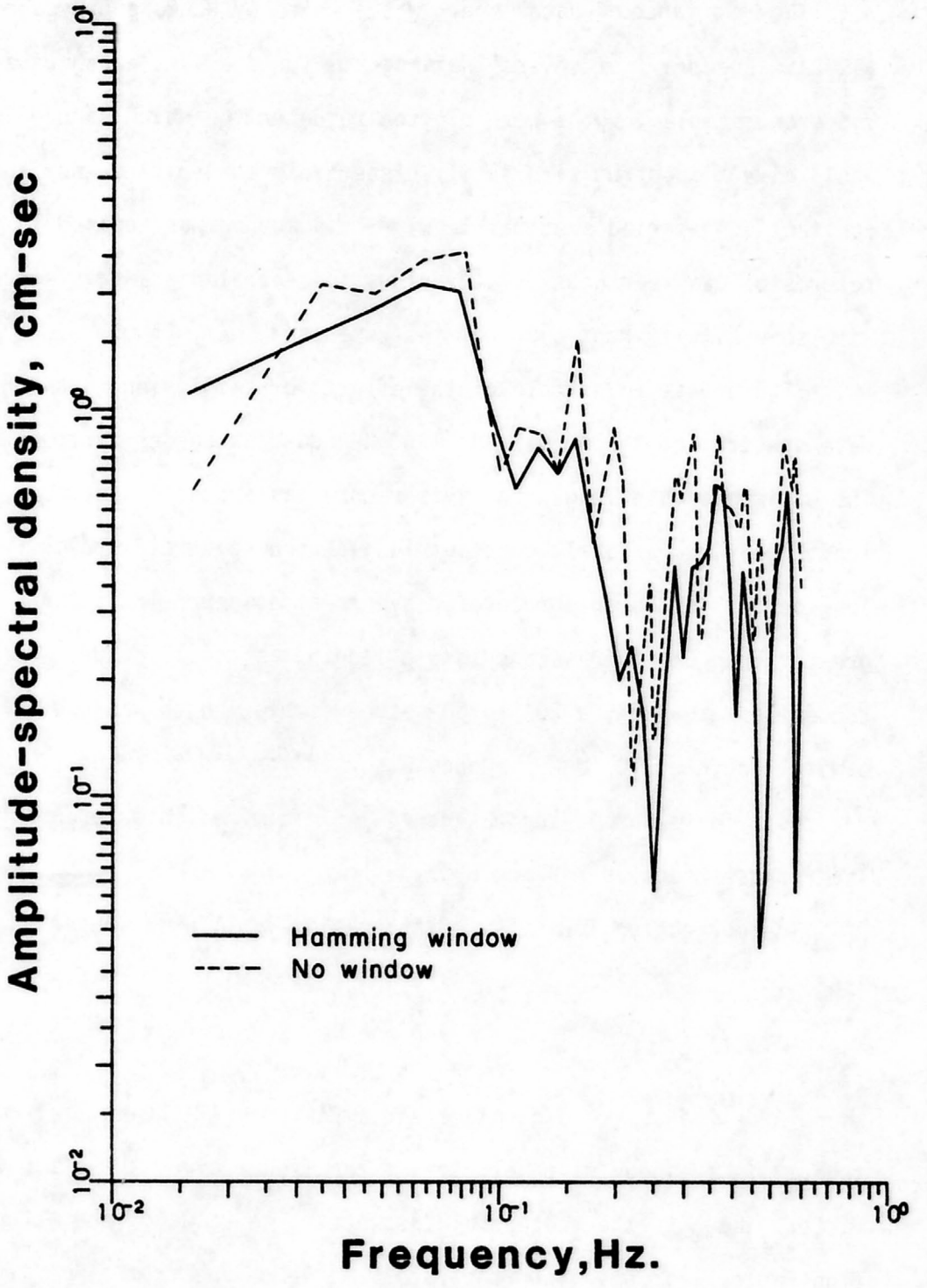

Figure 4. Windowed and non-windowed spectral data.

The importance of data length was studied by Hanks and Wyss (1972). Spectra from several seismograms for the same earthquake with different sample lengths were plotted to determine which sample length would give a spectrum with easily discernable corner frequency and constant long-period spectral level. This method was applied to the records of Utah earthquakes at various epicentral distances recorded with several different types of instruments.

Figure 5 is an example of the effects of sample length on the S-wave spectrum of the August 16, 1966 Nevada-Utah border earthquake. The optimum sample length for this record was around 60 seconds. This length provided a fairly constant long-period spectral level. For long period instruments recording events at epicentral distances greater than 5°, a 60-second sample length was usually used. At distances less than 5°, a 20- to 30-second sample length was used. A sample length of 10 to 20 seconds was used for short period ($T_o \approx 1$ sec) records. These sample lengths generally minimized interference from later phases such as P_cP and S_cS.

The correction for seismic attenuation (Julian and Anderson, 1968) is:

$$A = A_o e^{-\frac{\pi \Delta f}{Qv}} \qquad (10)$$

where A is the observed displacement amplitude, A_o the initial amplitude, v is the body wave velocity, f the frequency, Q the attenuation factor, and Δ is the epicentral distance. The value of the attenuation factor was determined separately for each spectrum. Amplitude spectra were plotted for successive values of attenuation until a

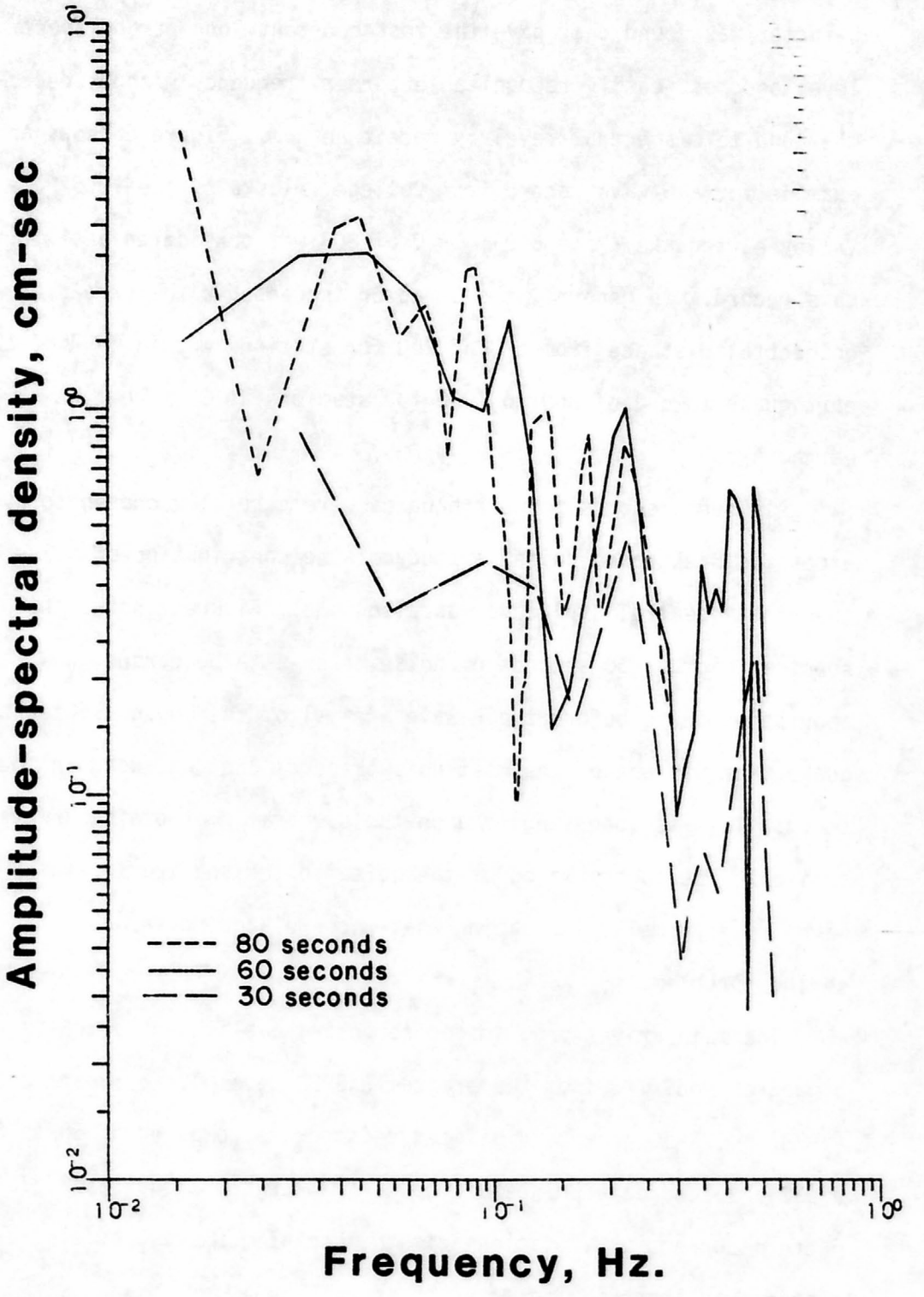

Figure 5. Variation of spectral shape with data length.

Q-factor was found that gave the most constant long-period spectral level and most easily recognizable corner frequency without decreasing the long term spectral level by more than 25%. Figure 6 shows an example for a S-wave record from College, Alaska of the 1975 Pocatello Valley earthquake (M_L = 6.0). A Q of 800 was considered best for this record. In general, the Q-factor increased with increasing epicentral distance from a Q of 200 for stations within 1-5° of the earthquake to a Q of 800 to 1000 for stations at 30° from the earthquake.

Although records for earthquakes were carefully chosen to avoid excessive background noise, a study of the contribution of noise to the final spectral amplitude was also done. Figure 7 shows the spectral plot of 50 seconds of noise taken at Albuquerque, New Mexico about one minute before the P wave arrival of the Logan 1962 earthquake that was one of the most noisy records that was used in the study. This is superimposed upon the spectral plot of the P wave arrival. The contribution of the noise to the spectrum of the P wave is very small, indicating that uncorrelated noise was not a serious problem.

The main driver program for computing amplitude spectra is EXSPEC, a program modified from the program EXSPEC developed by Herrmann (1978). EXSPEC accepts digitized seismograms composed of up to 512 equally spaced data points as input. EXSPEC also requires radiation pattern corrections, station azimuth, backazimuth, and epicentral distance as input parameters.

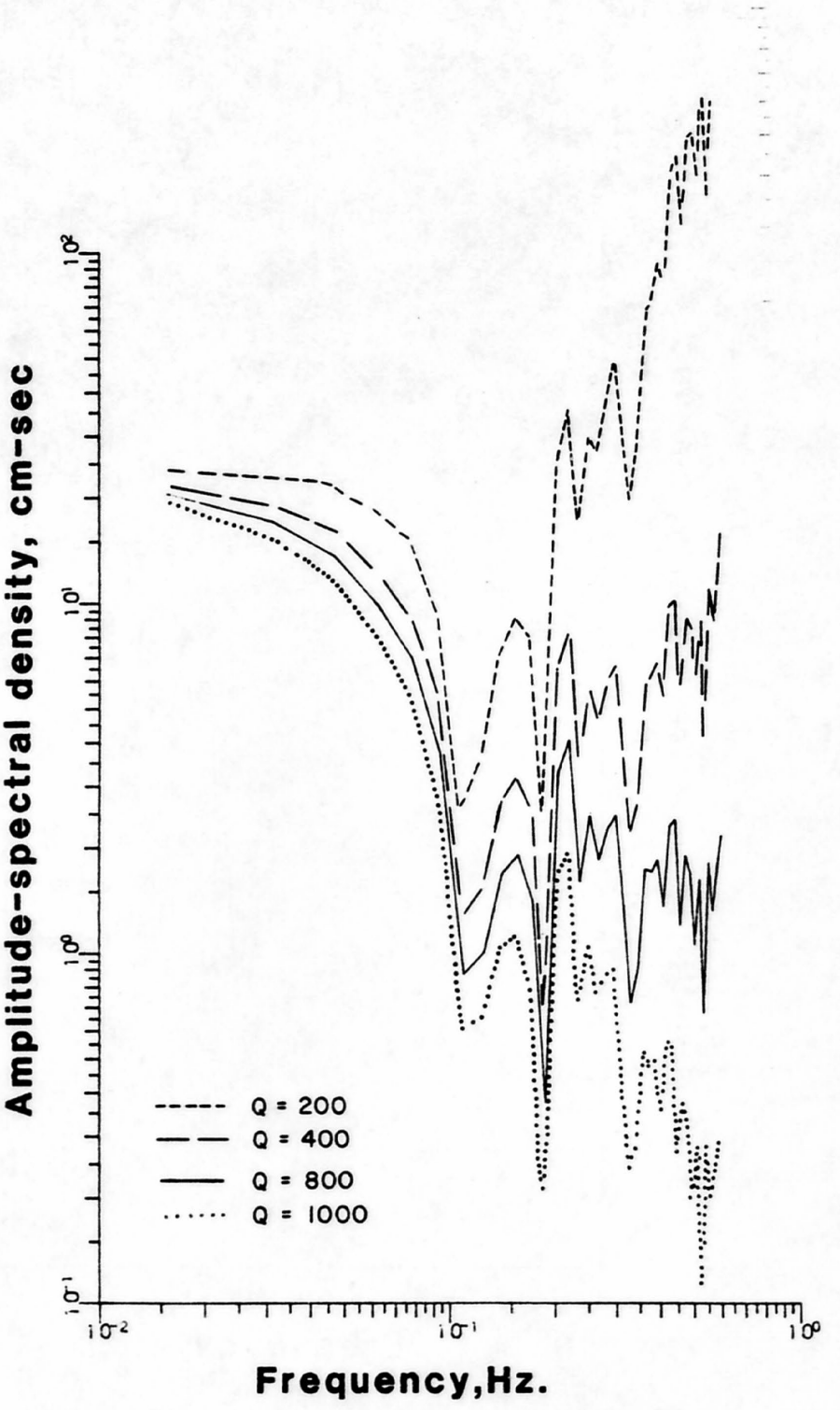

Figure 6. Variation of spectral shape with attenuation factor.

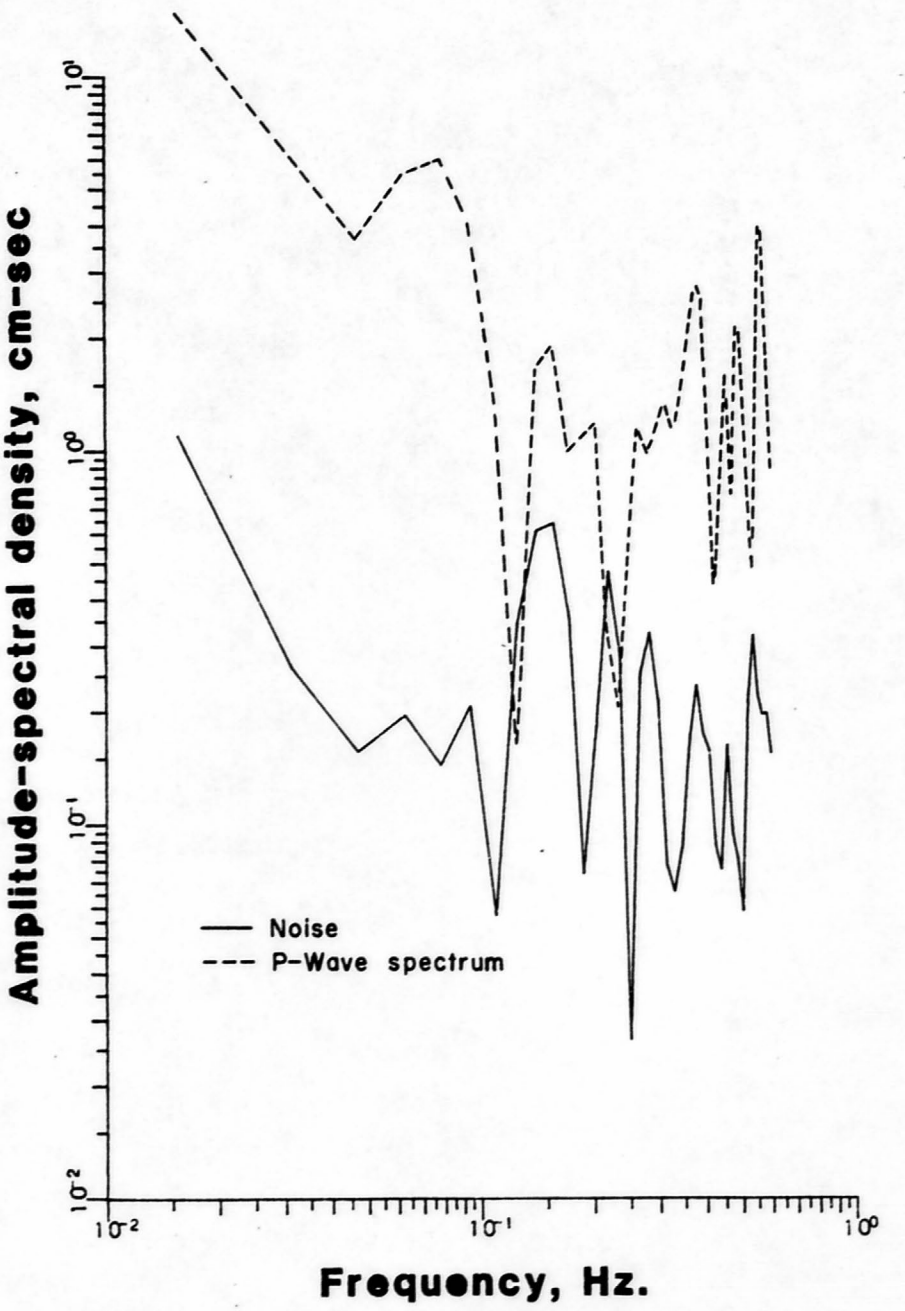

Figure 7. The effect of noise on spectral shape.

To calculate radiation pattern corrections it was first necessary to find the maximum radiation pattern values for each earthquake. Maximum radiation pattern values were used as normalization factors for each earthquake so that the radiation pattern corrections for stations recording the earthquake were between -1.0 and 1.0. The program SEARCH calculated the maximum radiation pattern values for each earthquake. Program PATT found the normalized radiation pattern corrections for each station recording a particular earthquake, using P and S-wave take off angles that were obtained from the program EDABAC. Program EDABAC also calculated station azimuth, back azimuth, and epicentral distance.

Both PATT and SEARCH used a subroutine, RADPAT, to compute radiation pattern effects. RADPAT is based on the radiation pattern equations of Ben-Menahem et al. (1965).

The original EXSPEC contained corrections for instrument response and spherical spreading that were used in the final version of EXSPEC for this thesis. Corrections for radiation pattern and attenuation were added to the original program. A subroutine for windowing, WINDOW, was also added. Modifications in input, output, and plotting routines were also made.

The final computer program sequence developed for calculation of amplitude spectra on the UNIVAC 1108 is listed in Appendix C. Appendix C includes user's guides for the program sequence.

Table 2 lists dates, magnitudes, epicenter locations, and fault plane solutions for nineteen earthquakes used to define a Utah moment-versus-magnitude relationship. The fault plane solutions listed for

Table 2. Epicenters and fault plane solutions of Utah earthquakes

Event	Date	No.	Epicenter[1]		Nodal Planes[2,3]				Magnitude (M_L)[4]
			Lat-N	Long-W	Dip	Az	Dip	Az	
Hansel Valley 1	03-13-34	1	41.8	112.9	7	80E	120	20S	6.6[5]
Hansel Valley 2	03-12-34	2	41.8	112.9	7	80E	120	20S	6.1[5]
Logan	08-30-62	3	41.8	111.8	5	32E	17	58W	5.7
Magna	98-05-62	4	40.72	112.1	330	30NE	171	60SW	5.2
Levan	07-07-63	5	39.6	111.9	170	74NE	58	40NW	4.4
Cache Valley	10-18-64	6	41.7	111.7	190	30W	5	60E	4.1
Logan 2	03-17-66	7	41.6	111.6	190	30W	5	60E	4.6
Nevada-Utah	08-16-66	8	37.4	114.2	110	80NE	14	80NW	5.6
Richfield	10-04-67	9	38.5	112.1	170	86W	95	15N	5.2
Cedar City	11-10-71	10	37.8	113.0	165	65NE	136	30SW	3.7
Elsinore	01-03-72	11	38.6	112.2	170	86W	275	15N	4.4
SW Sevier County	06-02-72	12	38.7	112.1	170	86W	275	15N	4.0
Heber	10-01-72	13	40.3	111.4	22	75W	22	15E	4.3
Pocatello Valley 1	04-14-73	14	42.0	112.6	184	55W	80	70S	4.2
Pocatello Valley 2	03-27-75	15	42.1	112.5	322	36NE	124	55SW	4.2
Pocatello Valley 3 (mainshock)	03-28-75	16	42.2	112.5	20	45NW	13	45SE	6.0
Pocatello Valley 4	03-29-75	17	42.0	112.5	353	57NE	134	40SW	4.7
Pocatello Valley 5	03-30-75	18	42.0	112.5	353	57NE	134	40SW	4.1
Hansel Valley 3	11-05-76	19	41.8	112.6	15	55W	319	49E	4.0

[1]Epicenter locations from Richins (1979).
[2]Fault Plane Solutions from Smith and Lindh (1978) and Arabasz et al. (1979).
[3]Fault plane solution used for event, not necessarily a single event solution.
[4]Magnitudes from Richins (1979).
[5]These are probably M_s magnitudes.

the earthquakes are not necessarily single event solutions. The fault plane solutions used for events 2, 11, and 12 are fault plane solutions of larger events occurring in the same general area. Fault plane solutions listed for events 4, 5, and 7 are composite fault plane solutions of microearthquakes occurring in those areas. Event 19 has a composite solution based on its aftershock sequence. The composite fault plane solutions of aftershocks in different regions of the Pocatello Valley area are used for the fault plane solutions of events 14, 15, 17, and 18. It was felt that the use of these fault plane solutions for earthquakes with no available single event solutions was better than not using a fault plane solution at all. At least the general earthquake mechanism for events in the area could be represented by this fault plane solutions.

The seismograms chosen for this study exhibited good body wave arrivals and little noise. Records were taken from a variety of instruments that ranged in period from 0.8 to 3.0 seconds (Appendix B). For the larger events, as many as 9 different stations and 16 records were used to determine an average moment value. Events below a M_L of 4.5 had fewer station records available. For several events the moment values were calculated entirely from records at Dugway, Utah. Seismograms from stations that recorded near the nodal plane rays of an event were not used for moment calculations unless the records near the nodal planes were the only records that were available.

Record sections of body waves were digitized using the program DIGIT developed by Schilly (1979) for use with a Hewlett-Packard calculator and digitizer. Sampling rates varied according to the

speed of the record. Records with paper speeds of 15 mm/min were digitized at 2 samples/second; records with paper speeds of 30 mm/min were digitized at 4 samples/second, and records with paper speeds of 60 mm/min were digitized at 10 samples/second. Digitized data were then plotted to the original seismogram scale using program SPLOT (Appendix C). The plots were overlain on the original records to insure that the records had been properly digitized.

Moment values were calculated for 82 record segments whose seismograms are shown in Appendix B. Appendix B also contains information on instrumentation, parameters used for moment calculations, moment values and spectral amplitude plots.

Spectral plots, for the most part, showed good long-term spectral levels, even for events recorded prior to 1960. Corner frequencies, however, were not as easy to determine, and on some spectral plots they were not picked. Average moment values were computed for each event (Table 3). Some of the pre-1965 events appeared to have low moment values compared to their recorded magnitudes.

Moment values from surface wave spectral analysis and AR surface wave analysis had been computed for three earthquakes of the 1975 Pocatello Valley sequence. Estimates of moment from surface wave analysis for the Pocatello Valley mainshock ranged from 6×10^{24} dyne-cm (Battis and Hill, 1977) to 2.2×10^{24} dyne-cm (Bache et al., 1980). The foreshock and aftershock 1 (M_L = 4.7) had estimated moments of 2×10^{23} dyne-cm (Battis and Hill, 1977). These published values agreed well with my moment estimates of 1.86×10^{25} dyne-cm

Table 3. M_L, m_b, and average moment for Utah earthquakes

Event	M_L[1]	m_b	Average Moment ($\times 10^{24}$ dyne-cm)
1	6.6[2]	--	77.0
2	6.1[2]	--	3.1
3	5.7	5.7	7.0
4	5.2	5.0	0.4
5	4.4	4.9	0.34
6	4.1	4.3	0.42
7	4.6	4.5	0.81
8	5.6	5.0[3]	1.1
9	5.2	5.2	2.5
10	3.7	4.5	0.057
11	4.4	4.6	0.09
12	4.0	4.6	0.045
13	4.3	4.7	0.27
14	4.2	4.4	0.33
15	4.2	4.4	0.13
16	6.0	6.1	18.6
17	4.7	4.7	0.30
18	4.1	4.0	0.13
19	4.0	--	0.058

[1]M_L magnitudes from Richins (1979).
[2]These magnitudes are probably M_S magnitudes
[3]Beck (1970), other m_b values from USCGS.

for the mainshock, 1.3 x 10^{23} dyne-cm for the foreshock, and 3 x 10^{23} dyne-cm for the aftershock.

As a separate check on moment calculations from body waves, moment values for the 1975 Pocatello Valley mainshock were computed using the AR surface wave envelope method for WWSSN stations developed by Williams (1979). The five stations used in the AR analysis were stations that had been used previously for moment determinations from body wave spectra. The results (Table 4) show good agreement between the moment calculations. Differences in moment values are well within the factor of 2 error that Hanks and Wyss (1972) suggest as reasonable based on their studies.

Moment-Versus-Magnitude Relationships

Average moment values were plotted versus local Utah magnitudes (Table 3) and are shown in Figure 8. The solid line represents a least-sqaures fit to all the data. As Table 3 indicates, the magnitudes for Hansel Valley 1(1) and Hansel Valley 2(2) are not actual M_L values but are probably M_s values. The dashed line represents a least-squares fit to the data with the exception of data points for the Hansel Valley 1(1), Hansel Valley 2(2), Magna (4) and Nevada-Utah border (8) earthquakes. These earthquakes were eliminated from the second relationship for several reasons. Events 1 and 2 do not have reliable local magnitudes. Event 4 has a very poorly determined fault plane solution. Event 8 exhibited a strike-slip mechanism, while the majority of events studied exhibited normal faulting mechanisms, suggesting a different stress field for the event. These differences may explain why events 2, 4, and 8 do not appear to fit the general

Table 4. Moment values from the AR method for the Pocatello Valley earthquake

Station	Moment from AR Method (dyne-cm)	Average Moment From Body Wave Spectra (dyne-cm)
COL	1.3×10^{25}	8.1×10^{24}
LON	8.3×10^{24}	1.3×10^{25}
WES	1.5×10^{25}	5.6×10^{24}
SHA	4.3×10^{25}	2.4×10^{25}
TUC	1.1×10^{25}	9.3×10^{24}

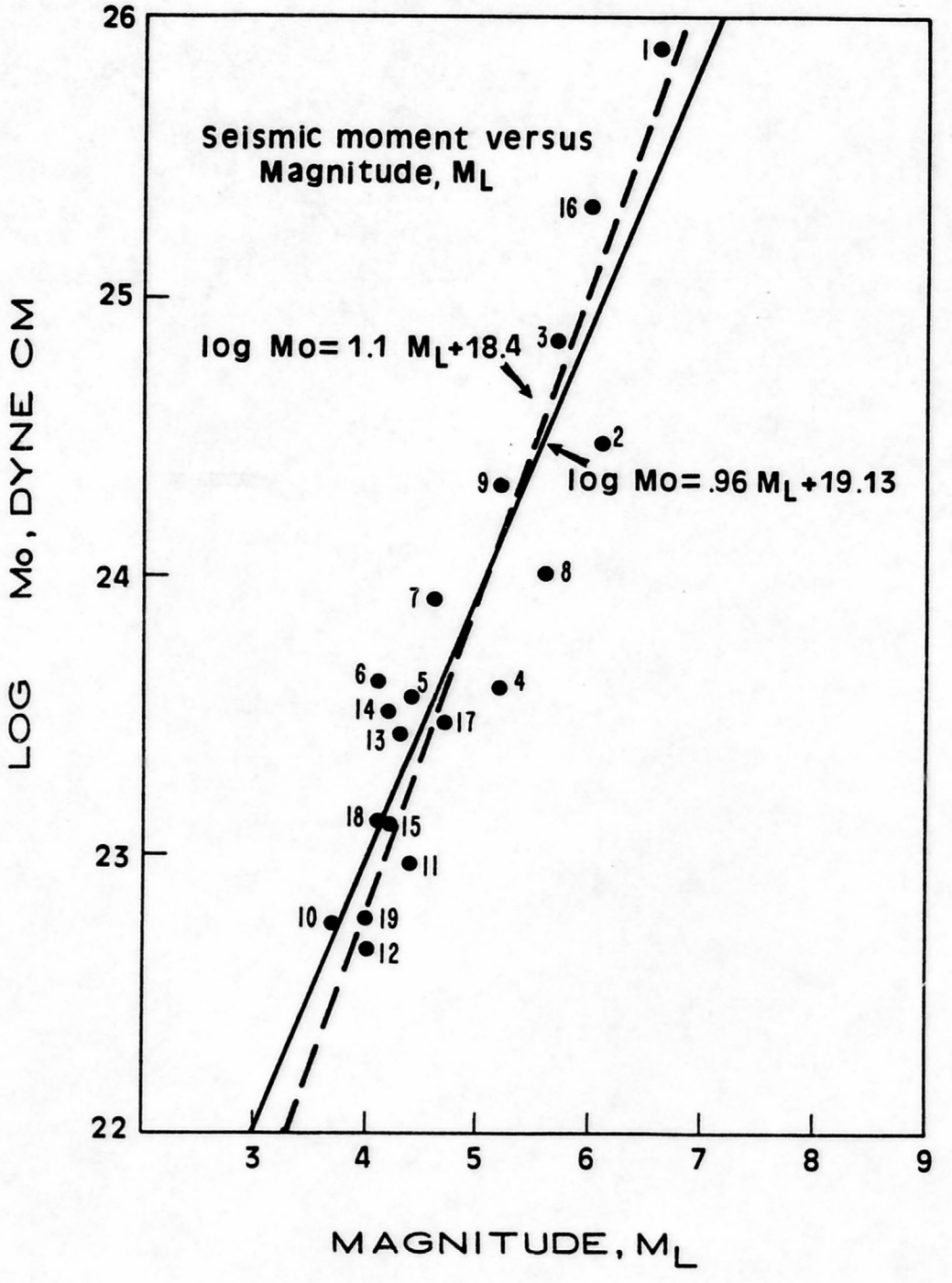

Figure 8. Moment-versus-M_L relationships for Utah. Event numbers from Table 2.

trend of the rest of the data. The two relationships developed represent "worst-case" and "best-case" relationships for moment-versus-magnitude in the Utah region. Statistical information on the fit of the data to these relationships is found in Table 5.

Neither moment-versus-M_L relationship resembles that of the southern California relationship. This observed difference may be due to differences in M_L between Utah and California. A study by Griscom (1980), however, indciates that Utah M_L should not differ from southern California M_L by more than ±0.3 units of M_L. A discussion of the implications of differences in moment-versus-magnitude relationships will follow in another section.

A relationship for moment-versus-m_b was also determined (Figure 9) using a least-squares fit to all the data. Statistical information on this relationship is also listed in Table 5. Use of m_b-versus-moment relationship has improved the fit of several of the data points including that from event 8. Since m_b reflects the energy of the body waves for an event and the moments for the events were calculated from body wave spectra, one would expect an improvement in fit when comparing m_b to moment.

Table 5. Statistical information on moment-versus-magnitude relationships

σ_a^2 = variance in y-intercept

σ_b^2 = variance in slope

R = linear-correlation coefficient

For $\log M_o = 0.96\ M_L + 19.1$

$\sigma_a^2 = 0.25$ R = 0.92

$\sigma_b^2 = 0.011$

For $\log M_o = 1.1\ M_L + 18.4$

$\sigma_a^2 = 0.44$ R = 0.94

$\sigma_b^2 = 0.021$

For $\log M_o = 1.2\ m_b + 18.0$

$\sigma_a^2 = 0.2$ R - 0.85

$\sigma_b^2 = 0.042$

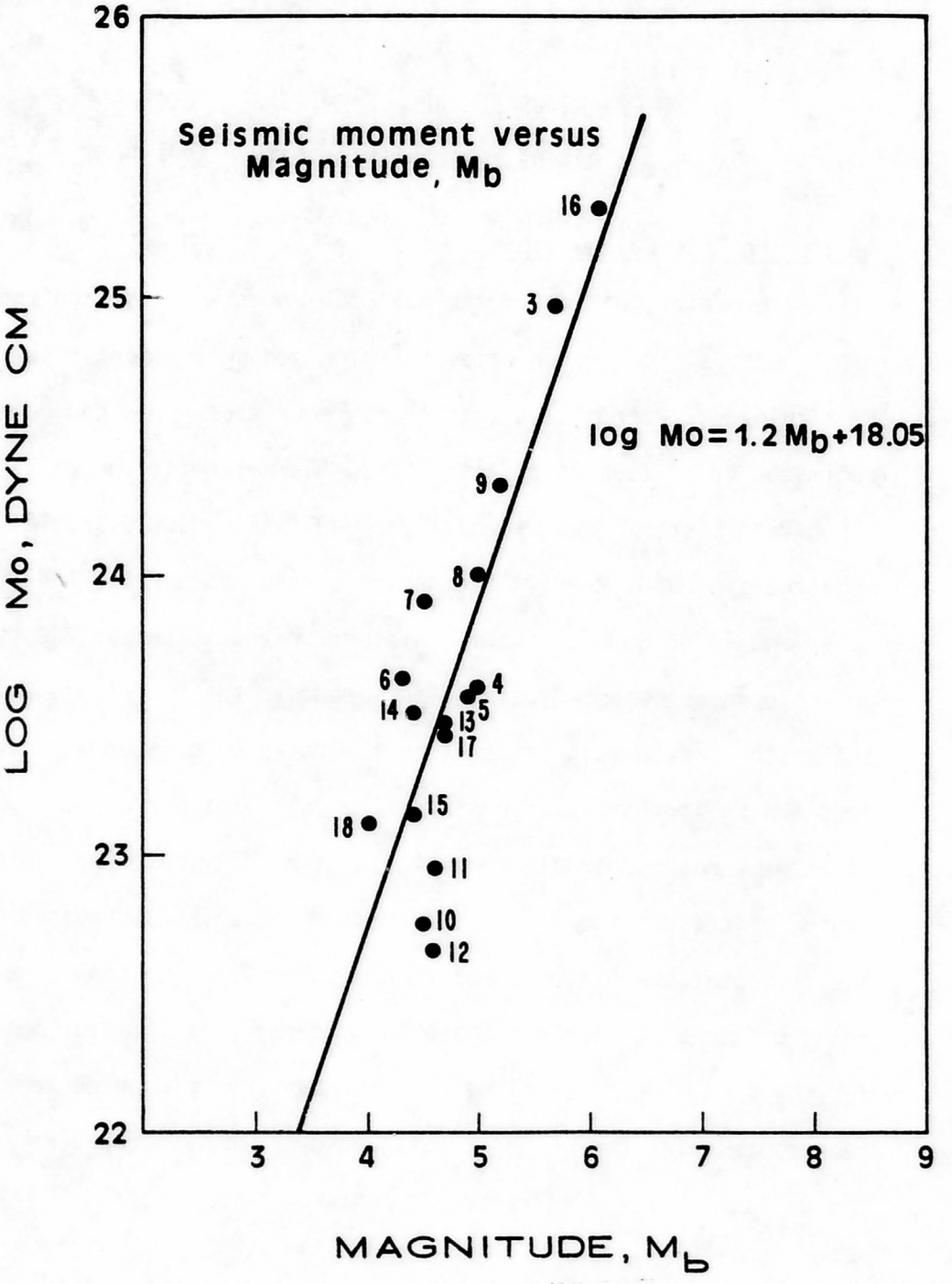

Figure 9. Moment-versus-m_b relationship for Utah. Event numbers from Table 2.

COMPARISONS OF RECURRENCE RATES FROM GEOLOGIC AND HISTORICAL SEISMICITY DATA

Recurrence Rate Calculations

After determination of the new Utah moment-versus-magnitude relationships, recurrence rates based on geologic moment rates were recalculated. Recognizing that these recurrence values could be underestimated by as much as a factor of 2, the rates fit the rates determined from historic seismic data very well (Figures 10 and 11). At magnitudes above a M_L=6.0 the geologic recurrence rates tend to put upper and lower bounds upon the historic rates. The southwestern Utah geologic rates computed using Utah moment versus M_L relationships fit the historic data much better than the rates calculated using a southern California relationship. The only area where the geologic rates were not comparable to historic seismicity rates was in the region of the Wasatch fault. One reason for this discrepancy may be the fact that the historic recurrence rates for this region were calculated from a 20 year data base as compared to a 125-year data base for the other regions. Since historic b-values were used to calculate recurrence rates for geologic data, this could also cause errors in the geologic recurrence rates.

A geologic return period of 323 to 556 years for a $7.0 \leq M_L \leq 7.5$ earthquake was predicted using the historic b-values for the region. Using the same b-values a return period of 388 to 667 years was

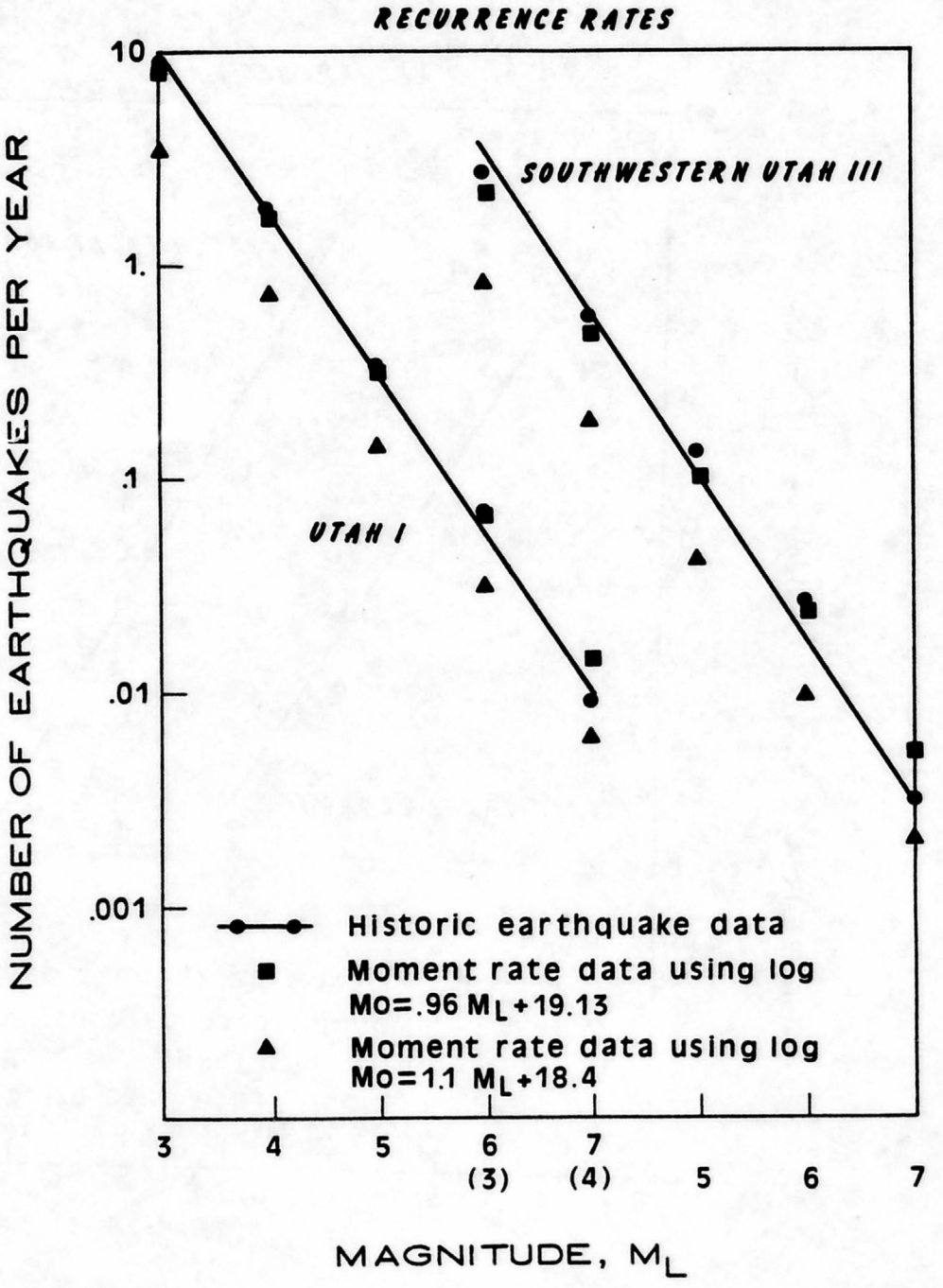

Figure 10. Earthquake recurrence data for the Utah and southwest Utah regions. Note magnitude scale is repeated.

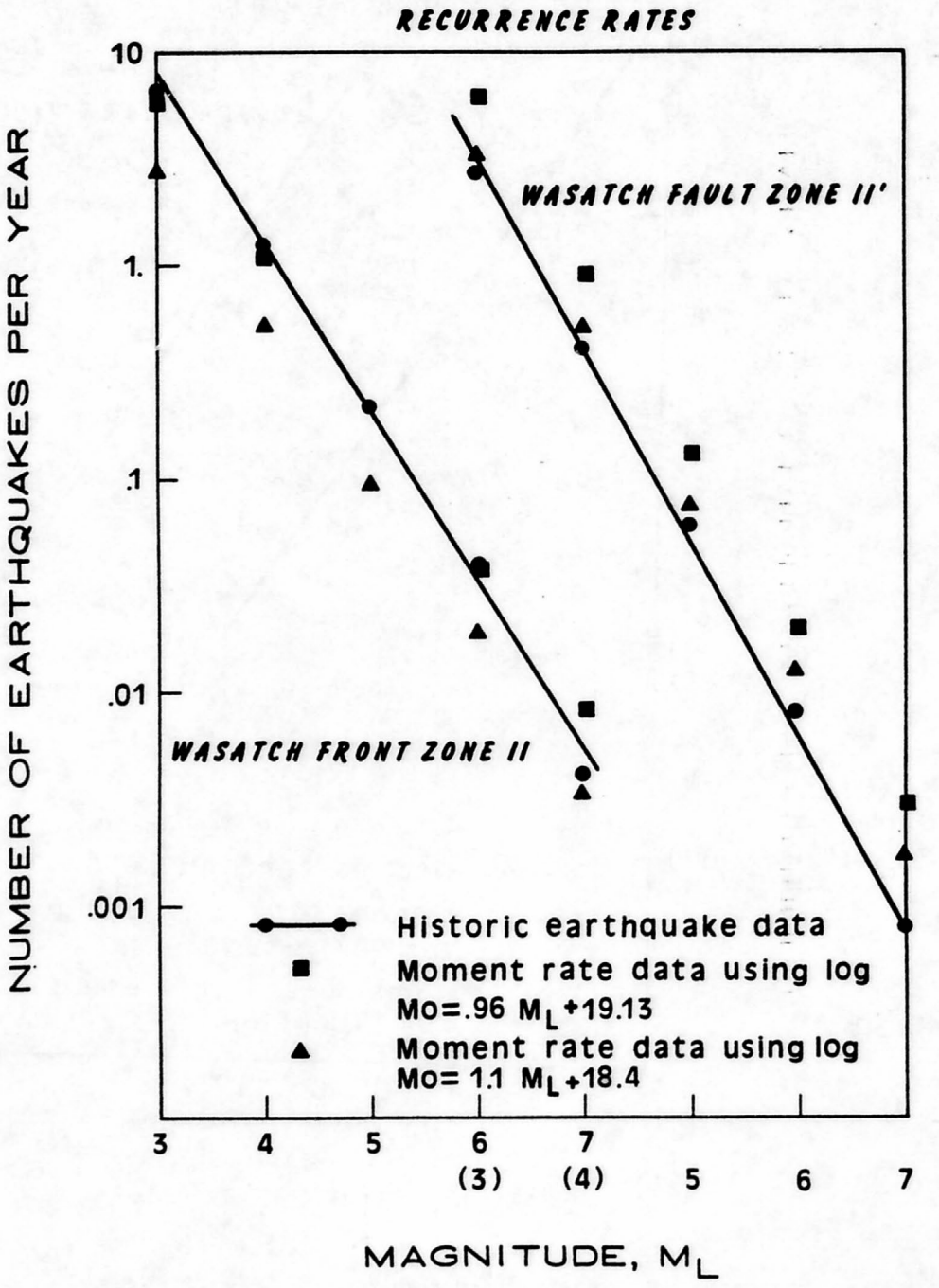

Figure 11. Earthquake recurrence data for the Wasatch Front and Wasatch fault regions. Note magnitude scale is repeated.

predicted for the Wasatch fault alone. However, if one assumes the historic b-value for the region over a longer period of time would be closer to the b-value of the Wasatch Front, then a return period of 205 to 455 years is predicted for the region and a return period of 245 to 550 years is predicted for the Wasatch fault itself. Since geologic slip rates appear to be similar in both regions, use of the Wasatch Front b-value for return period calculations gives an estimate of the minimum return period for an earthquake of $7.0 \leq M_L \leq 7.5$ in the Wasatch fault region. The return period of 250 to 550 years for a $7.0 \leq M_L \leq 7.5$ earthquake along the Wasatch fault itself agrees well with return periods calculated by Cluff et al. (1980) based on trenching data at three sites along the fault.

Table 6 lists the calculated return periods for a $7.0 \leq M_L \leq 7.5$ earthquake in Utah. The use of a southern California moment-versus-M_L relationship appears inappropriate for the Utah region. Use of this relationship yielded return periods which were much longer than those predicted from use of either Utah relationship.

The close agreement between historic and geologic recurrence rates suggests that the historical seismicity of Utah does reflect the overall long-term seismicity of Utah. However, due to the lack of historic data in the Wasatch fault region, the geologically predicted return period of 325 to 550 years is probably more representative of this region.

Moment Rates from Historical Seismicity

Moment rates were calculated from historic seismic data using equation (8), (Table 7). The historic moment rates then were directly

Table 6. Return period for a $7.0 \leq M_L \leq 7.5$ earthquake

Region	Historic (Arabasz and Smith, 1979) (years)	Utah Geologic Case I (years)	Utah Geologic Case II (years)	Southern California Case III (years)
Utah	111	77	179	333
Southwestern Utah	278	213	556	1075
Wasatch Front	204	122	278	500
Wasatch fault	1266	323	556	833

Case I: $\log M_0 = 19.1 + .96 M_L$

Case II: $\log M_0 = 18.4 + 1.1 M_L$

Case III: $\log M_0 = 16 + 1.5 M_L$

Table 7. Moment rates from historical data

Region	Historic Rate Case I (dyne-cm/yr)	Historic Rate Case II (dyne-cm/yr)	Geologic Rate (dyne-cm/yr)
Utah	3.6×10^{24}	9.5×10^{24}	4.4×10^{24}
Southwestern Utah	1.1×10^{24}	2.1×10^{24}	1.4×10^{24}
Wasatch Front	2.1×10^{24}	3.8×10^{24}	2.9×10^{24}
Wasatch fault	1.2×10^{24}	8.8×10^{23}	1.8×10^{24}

Case I: $\log M_o = .96\, M_L + 19.1$

Case II: $\log M_o = 1.1\, M_L + 18.4$

compared to geologic moment rates. This approach eliminated the problem of using historical b-values with geologic data. Table 7 lists the moment rates that were calculated using the two Utah moment-versus-M_L relationships. Use of the "worst-case" relationship (log M_0 = 19.1 + 0.96 M_L) gave historic moment rates that were 20 to 30% lower than the geologic rates. Use of the other Utah relationship gave historic moment rates that were 30 to 120% greater than the geologic rates, except in the Wasatch fault region. In both cases the historical moment rates for the Wasatch fault region were lower than the geologic rates. This again reflects the fact that the historic data base for the Wasatch fault region is very limited.

Greensfelder et al. (1980a, 1980b) computed moment rates for an area of Utah that roughly corresponded to a combination of the Wasatch Front area east of the Wasatch fault and the southwest Utah area. A moment rate derived from historical seismic data was estimated using the NOAA/USCGS files and the California moment-versus-magnitude relationship. The geologic moment rate was estimated from strain-rate data through use of equation (4). Using these moment-rate estimates, Greensfelder et al. (1980a, 1980b) found the geologic moment rate to be 50% larger than the moment rate estimated from historical seismicity. My estimates of both geologic moment rates and moment rates derived from historical seismic data were 10 times larger than those obtained by Greensfelder et al. (1980a, 1980b). In my comparisons of regional moment rates the geologic moment rate never exceeded the moment rate derived from historical seismic data by more than 35%. Use of the southern California moment-versus-magnitude relationship by

Greensfelder et al. (1980a, 1980b) to calculate their historic moment rates may have contributed to their large observed differences in moment rates.

The good agreement between historic and geologic rates indicated that the choice of M_o^{max} as the moment equivalent to a M_L = 7.5 earthwuake was appropriate for the regions. Use of M_o^{max} equivalent to a M_L = 8.0 earthquake would have increased the historic rates by 20 to 50%.

SOURCE PARAMETERS AND TECTONICS

Stress drops, average displacements, apparent stresses and source radii were calculated for the Utah earthquakes (Table 8). For some earthquakes without clear corner frequencies only apparent stress could be computed. Where corner frequencies were obvious they were chosen within ±0.2 logarithmic units. The decay of the spectra below the corner frequency generally followed an f^{-2} relationship. Comparison of corner frequencies in this study to corner frequencies predicted by Aki's (1967) ω-square scaling model showed a close agreement between the model and the observed data.

Source dimensions of the earthquakes were computed by assuming that the fault was circular. For S-waves the fault radius was determined from

$$r = \frac{2.34\,\beta}{2\pi f_c(S)} \qquad (11)$$

(Brune, 1971, corrected from Brune, 1970) where r = fault radius, β = shear wave velocity and $f_c(S)$ = the S- wave corner frequency. For P-waves the relationship used was

$$r = \frac{1.97\,\alpha}{2\pi f_c(P)} \qquad (12)$$

(Trifunac, 1972) where r = fault radius in km, α = P-wave velocity and $f_c(P)$ = the P-wave corner frequency. The assumption of a circular fault is probably valid for the smaller events. If the circular fault

Table 8. Source parameters of Utah earthquakes

r = source radius in km
$\Delta\sigma$ = stress drop in bars
$\bar{u}$ = average displacement in cm
$\eta\sigma$ = apparent stress in bars

Event	Ave r (km)	Ave $\Delta\sigma$	$\bar{u}$ (cm)	$\eta\sigma$
1	26.9	1.7	10.1	18.7
2	7.4	3.3	5.6	91.0
3	10.8	4.4	5.8	1.4
4	4.6	1.1	1.1	0.05
5	6.7	0.48	0.71	0.35
6	9.4	0.19	0.43	0.01
7	6.3	1.5	2.1	0.02
8	10.6	0.47	1.1	0.2
9	5.1	4.8	5.4	0.25
10	---	---	---	0.20
11	---	---	---	0.25
12	---	---	---	0.51
13	---	---	---	0.15
14	---	---	---	0.023
15	---	---	---	0.058
16	15.6	3.0	7.9	4.9
17	---	---	---	0.13
18	---	---	---	0.0064

model is used for events with magnitudes greater than 6 the fault area is overestimated. The circular fault model predicts a fault area of 764 km^2 for the Pocatello Valley earthquake as compared to an estimate of 23 km x 11 km (Arabasz et al., 1979) based on aftershock activity. Overestimation of fault area leads to underestimation of both stress drop and average displacement.

Stress drops were computed from

$$\Delta\sigma = \frac{7}{16}\frac{M_o}{r^3} \tag{13}$$

(Brune, 1971, corrected from Brune, 1970) where $\Delta\sigma$ is the stress drop, M_o the moment, and r the fault radius. An error of a factor of two in the corner frequency determination would lead to a factor of eight error in the stress drop determination. Stress drops appeared to be somewhat lower than results of studies of intraplate earthquakes by Richardson and Solomon (1977) that show stress drops of 2 to 70 bars.

Figure 12 compares the Utah data to an empirically determined relationship between moment, magnitude, and stress drop (Thatcher and Hanks, 1973) of

$$\log_{10}M_o = 2M_L + 14.2 - \log_{10}\Delta\sigma \tag{14}$$

for southern California earthquakes. Eight Utah earthquakes had stress drop determinations, and six of them had stress drops that fell within the range of stress drops predicted by the empirical relationship.

As mentioned earlier, stress drops for the larger events may be slightly underestimated. The circular fault model predicts a stress

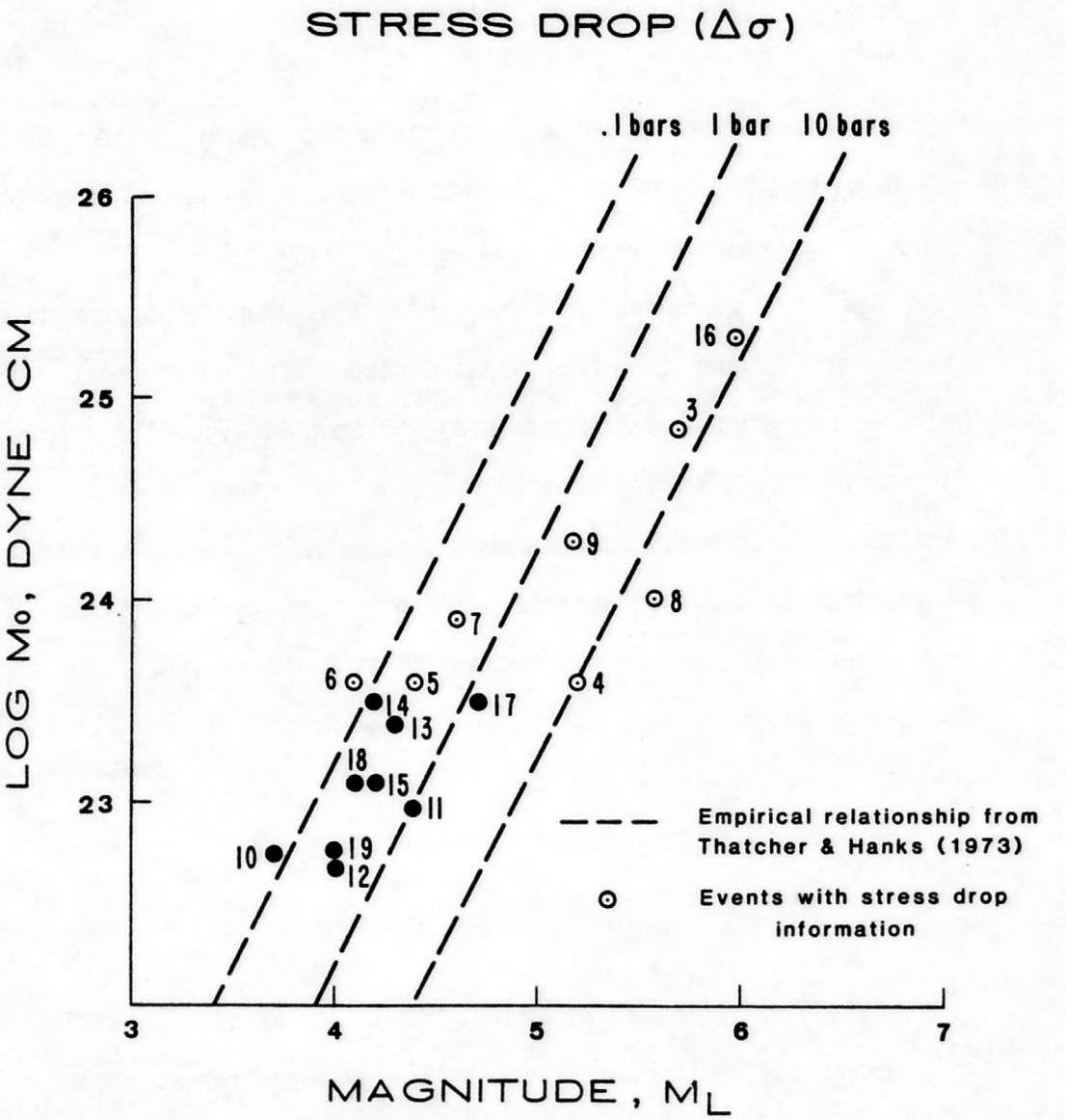

Figure 12. Stress drops of Utah earthquakes. Event numbers from Table 2.

drop of 3 bars for the 1975, M_L 6.0 Pocatello Valley earthquake. If a rectangular fault area of 23 km x 11 km (Arabasz et al., 1979) is used, a stress drop of 5.6 bars is predicted from

$$\Delta\sigma = \frac{8\mu}{3\pi} \frac{M_o}{W^2 L} \tag{15}$$

(Starr, 1928) where W is the width and L the length of the fault. Bache et al. (1980) obtained an estimated average stress drop of 20 bars using a smaller area of 144 km^2.

The stress drops of events with M_L less than 5.0 appear to be a factor of 10 lower than the stress drops determined for earthquakes of similar magnitudes by Richardson and Solomon (1977). The stress drops are probably not underestimated by assuming a circular fault model, indicating that small Utah earthquakes may have smaller stress drops than other earthquakes associated with intraplate regions.

Apparent stress calculations did not involve corner frequency measurements, so apparent stress could be calculated for all the Utah events except Hansel Valley 3(19) which did not have an m_b or M_s determination. Apparent stress, $\eta\bar{\sigma}$, is given by

$$\eta\bar{\sigma} = \mu\frac{E_s}{M_o} \tag{16}$$

(Aki, 1966) where E_s is the radiated seismic energy. The radiated seismic energy can be obtained from the energy-magnitude relation of Gutenberg and Richter (1956)

$$\log_{10} E_s = 5.8 + 2.4\, m_b \tag{17}$$

Richardson and Solomon (1977) indicated that apparent stresses

determined in this manner are only directly comparable to apparent stresses in other studies that were calculated in a similar manner.

Figure 13 shows apparent stress for the Utah events. The majority of the earthquakes studied by Richardson and Solomon (1977) have apparent stresses of 0.1 to 10 bars. Only one intraplate earthquake falls below this level. The majority of the Utah earthquakes also fall between 0.1 to 10 bars, however, there are 6 earthquakes that fall below 0.1 bars.

The majority of Utah earthquakes have stress drops and apparent stresses in the range of those found in studies of other intraplate events. However, small earthquakes in the M_L range of 3.7 to 4.5 exhibit lower stress drops and lower apparent stresses. Studies of intraplate earthquakes have little source parameter data for this magnitude range, so it is difficult to make direct comparisons of data at smaller magnitudes. In a study of southern California earthquakes, Thatcher and Hanks (1973) found variations of stress drop from tenths of a bar to a hundred bars in the M_L = 3.5 to 4.5 range. Until more data on stress drops and apparent stresses for Utah earthquakes are available, it cannot be concluded that all Utah earthquakes have significantly different stress drops and apparent stresses than other small earthquakes worldwide. Two observations that can be made for earthquakes in Utah are that earthquakes with M_L<4.5 have stress drops of less than 1 bar and apparent stresses of less than 0.5 bars and that most earthquakes with M_L>4.5 have stress drops greater than 1 bar and apparent stresses greater than 0.5 bars.

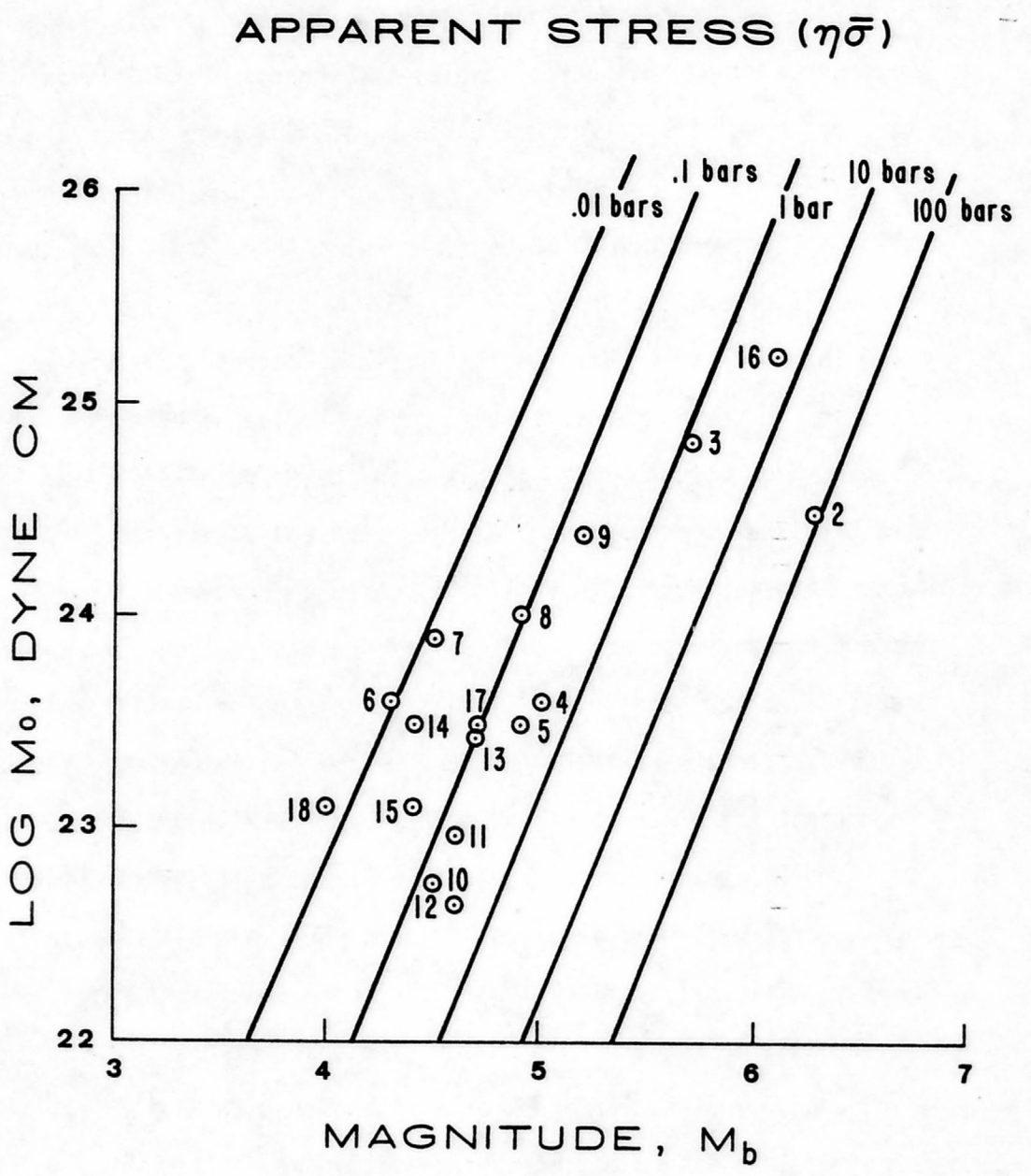

Figure 13. Apparent stresses of Utah earthquakes. Event numbers from Table 2.

Studies of microearthquakes near Price, Utah showed the events had stress drops from 0.2 to 9.6 bars (Smith et al., 1974). These microearthquakes were associated with thrust faulting in coal mines and are probably not representative of small earthquakes along normal faults.

Average displacements were calculated for those earthquakes where corner frequency information was available from

$$\bar{u} = \frac{M_o}{\mu A} \tag{18}$$

(Aki, 1966). For a circular fault $A = \pi r^2$.

Only two Utah earthquakes have any associated surface displacement that can be compared with the calculated average displacement values. The 1975, M_L 6.0 Pocatello Valley mainshock had 13 cm of observed coseismic subsidence (Bucknam, 1976). The calculated average displacement was 7.9 cm for a circular fault model. For a 23 km x 11 km model as suggested by Arabasz et al. (1979) the average displacement was calculated to be 23 cm. Using the 144 km^2 (Bache et al., 1980) for the fault area an average displacement of 39 cm was obtained. The 1934, M=6.6 Hansel Valley mainshock had an associated surface displacement of 50 cm (Shenon, 1934). The average displacement calculated for a circular fault was 10.1 cm. This indicates the use of a circular fault model is not appropriate for larger Utah earthquakes. Shenon (1934) observed a 16-km-long fault scarp associated with the earthquake. Assuming the fault extended to a depth of 10 km would yield an average displacement of 145 cm. Since no surface faulting data

are available for other Utah earthquakes, it is difficult to determine how well the calculated average displacement values reflect the actual displacements on the faults.

The fit of Utah moment data to a southern California moment-versus-M_L relationship (Thatcher and Hanks, 1973) and Wyss and Brune's (1968) moment-versus-M_L relationship for the western United States is shown in Figure 14. Larger earthquakes fit the two relationships well. Small events below M_L=5.0 fall to the left of both relationships. A major problem involved in comparing Utah data with other moment-versus-M_L relationships is the M_L may be systematically different in Utah than in other regions. This makes it difficult to determine how much of the difference between Utah data and other moment-versus-magnitude relationships is due to other effects such as differences in path effects, tectonic stress, or source mechanisms. Since the southern California and western United States relationships were based on shallow events not exceeding depths of 20 km, differences in relationships caused by depth to source should be small.

Figure 15 compares Utah moment-versus-magnitude relationships and Wyss and Brune's (1968) relationship to worldwide earthquake moment data. The approximate range of Utah moment data is indicated by the dashed line. Wyss and Brune's (1968) relationship holds between a M_L of 3.0 and 6.0. The Utah relationships have been extrapolated upward from M_L=6.6 and downward from M_L=3.7.

At local magnitudes below 3.7 the extrapolated Utah relationships do not fit any of the moment data, including data from Utah

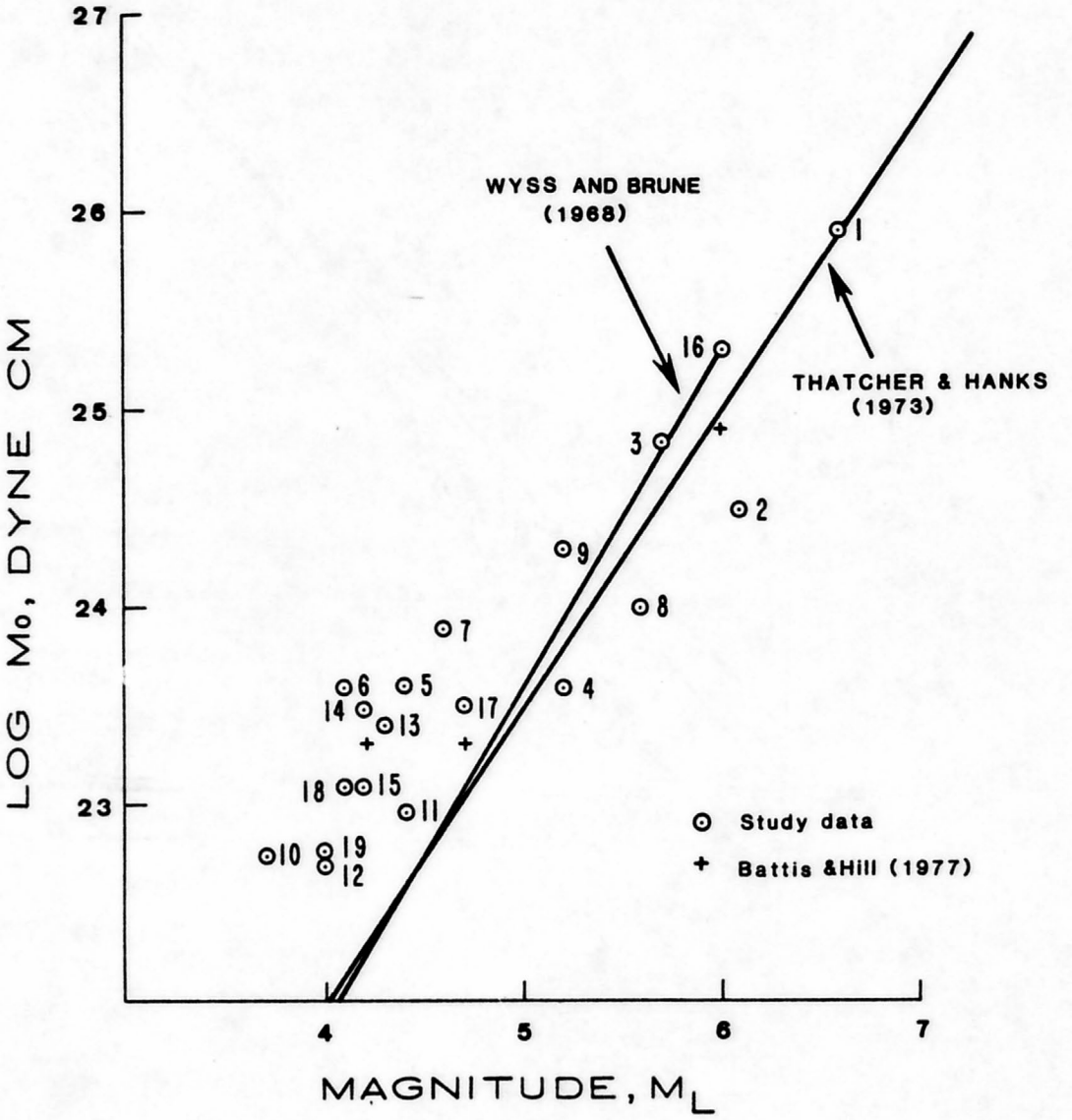

Figure 14. Comparison of Utah earthquake moment data with other moment-versus-magnitude relationships. Event numbers from Table 2.

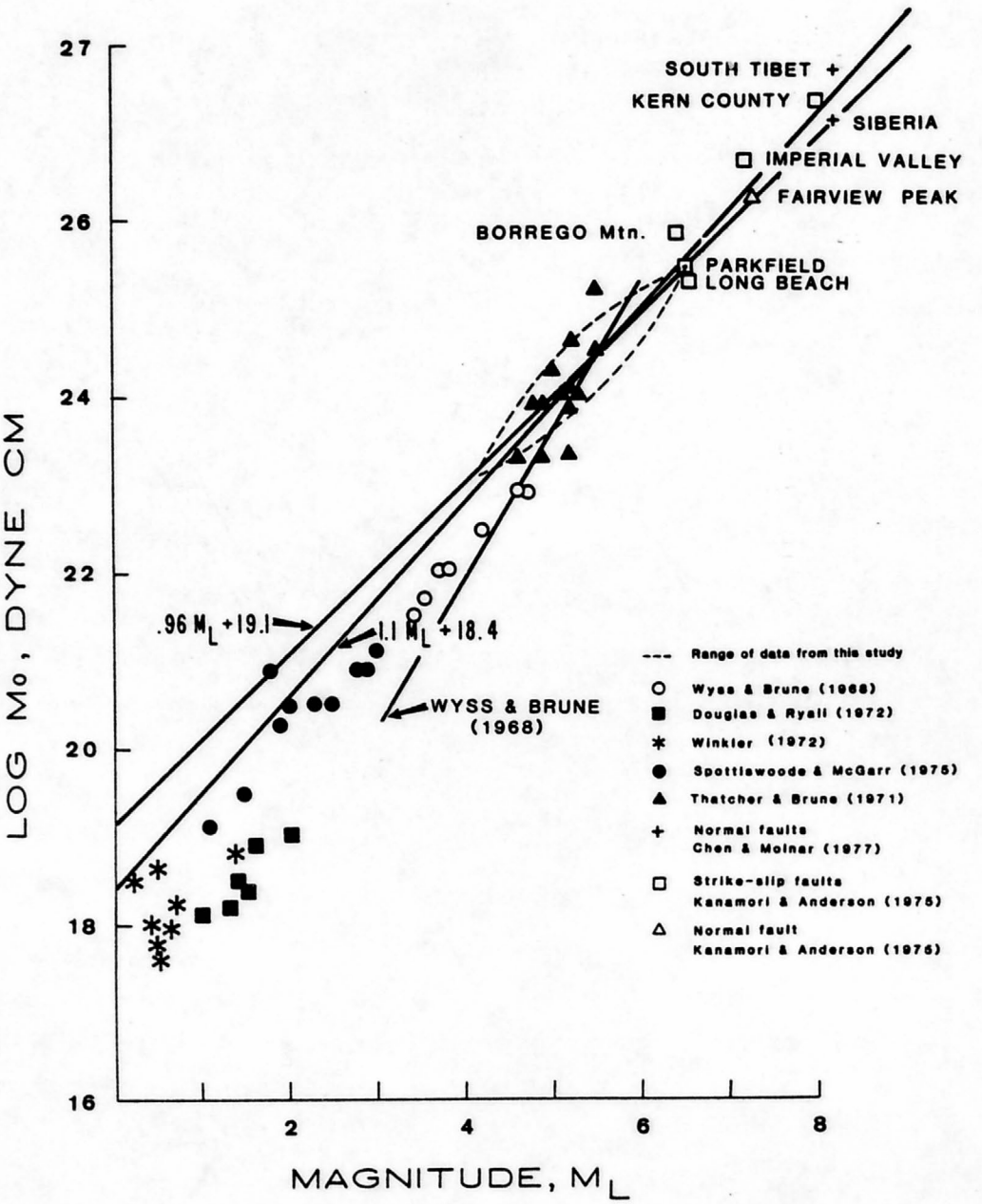

Figure 15. Comparison of Utah moment-versus-magnitude relationships with other earthquake moment data.

microearthquakes (Winkler, 1972). This indicates that the Utah relationships probably do not hold below M_L=3.7.

In the middle magnitude range moment data from earthquakes on an oceanic ridge (Thatcher and Brune, 1971) are scattered about the Utah relationships. Aftershocks of the Parkfield earthquake (Wyss and Brune, 1968) lie between the Utah and Wyss and Brune relationships. These limited data suggest that the Utah moment data are consistent with other moment data in this magnitude range.

Above M_L=6.6 the extrapolated Utah relationships follow the trend of the other moment data. It also appears that normal and strike-slip events fit the Utah relationships equally well. The good fit of the moment-versus-magnitude relationships for Utah to large earthquake moment data indicates that the relationships are probably valid above M_L=6.0. Therefore, their use in calculating the return period from geologic data for a $7.0 \leq M_L \leq 7.5$ earthquake is justified.

Figure 15 does not include enough data to determine whether differences between the moments of Utah earthquakes and earthquakes of other regions are due to differences in source mechanisms. More information must be obtained to determine whether different faulting mechanisms produce different moment-versus-magnitude relationships.

MOMENT TENSORS AND STRAIN RATES

Seismic moment tensors for the Utah region were calculated from historical earthquake moment data. The seismic moment tensor is defined as

$$M_{ij} = M_o(b_i n_j + b_j n_i) \qquad i,j = 1, 2, 3 \qquad (19)$$

(Gilbert, 1970) where M_o is the scalar moment of the earthquake, $\hat{n}$ is the unit vector normal to the fault plane, and $\hat{b}$ is a unit vector in the direction of slip. The principal axes of M_{ij} are the P, T, and B axes. The moment tensor written in the principal axes system becomes

$$\begin{matrix} M_o & 0 & 0 \\ 0 & -M_o & 0 \\ 0 & 0 & 0 \end{matrix}$$

where the 1 axis is the T axes, the 2 axis is the P axis, and the 3 axis is the B axis.

Moment tensors were calculated for each of the nineteen Utah earthquakes and were rotated from their principal axes systems to a east (1 axis), north (2 axis), and vertical (3 axis) axes system. Then the moment tensors of all the earthquakes were added together to yield a regional moment tensor of

$$\begin{matrix} 5.6 & 2.2 & -6.8 \\ 2.2 & -0.24 & 0.78 \\ -6.8 & 0.78 & -5.4 \end{matrix} \times 10^{25} \text{ dyne-cm}$$

The regional tensor was rotated into its principal axes system by diagonalizing to obtain the tensor

$$\begin{matrix} 9.1 & 0 & 0 \\ 0 & -9 & 0 \\ 0 & 0 & -0.21 \end{matrix} \times 10^{25} \text{ dyne-cm}$$

The principal values of this tensor represent eigenvalues of the original regional tensor and the principal axes of the tensor are the eigenvectors of the original tensor. This tensor indicates a maximum extensional component of 9.1×10^{25} dyne-cm along an axis striking N79°E and a maximum compressional component of -9×10^{25} dyne-cm along a near vertical axis. This formulation of the moment tensor assumed that the P and T axes of the events were at 45° to either nodal plane, or in other words, that μ_f, the internal coefficient of friction, was 0. In reality $\mu_f \sim 0.6$ for the crust (Zoback and Zoback, 1980), which implies the actual fault plane should be 30° from the P axis and 60° from the T axis.

P and T axes were recalculated for the events by assuming one of the fault planes represented the actual fault plane. This preferred fault plane is the plane listed first for each event in Table 2. The choice of the fault plane was based on either aftershock activity or geology of the area.

For μ_f = 0.6 the diagonalized moment tensor for all Utah earthquakes is

$$\begin{matrix} 9.9 & 0 & 0 \\ 0 & -10 & 0 \\ 0 & 0 & -0.19 \end{matrix} \times 10^{25} \text{ dyne-cm}$$

This tensor differed very little from the tensor for μ_f = 0. Both tensors demonstrate an east-west tensional component and a near vertical compressional component. A small compressional component in the north-south direction was also present.

The moment tensors were heavily biased by the largest earthquake in the region. In the case of Utah earthquakes the regional tensor was weighted heavily by large earthquakes in 1934 and 1975 that occurred in northern Utah. To see how much these large earthquakes affected the moment tensors for all of Utah, moment tensors were calculated separately for northern and southern Utah. The southern Utah moment tensor was calculated with data from the Levan, Richfield, Sevier County, Elsinore and Cedar City earthquakes. The northern Utah moment tensor was obtained by summing the moment tensors of the remaining Utah earthquakes.

For northern Utah the diagonalized moment tensor is

$$\begin{matrix} 9.9 & 0 & 0 \\ 0 & -9.5 & 0 \\ 0 & 0 & -0.22 \end{matrix} \times 10^{25} \text{ dyne-cm for } \mu_f=0.6$$

and for southern Utah it becomes

$$\begin{matrix} 2.8 & 0 & 0 \\ 0 & -3.7 & 0 \\ 0 & 0 & 0.92 \end{matrix} \quad \times 10^{24} \text{ dyne-cm for } \mu_f = 0.6$$

Again, the directions of the maximum tensional and compressional components (Appendix D) are the same as for the whole of Utah. The component in the north-south direction for northern Utah is compressional and in southern Utah it is tensional. The diagonal components of the southern Utah moment tensor are also over 20 times smaller in magnitude than the northern Utah components.

The average irrotational strain in a specific volume can give an idea of the deformation in the volume due to earthquakes. It is expressed as

$$\varepsilon_{ij} = \frac{1}{2\mu\Delta V} \sum_{x=1}^{N} M_{ij}(x) \qquad (20)$$

(Kostrov, 1974) where the M_{ij} are the moment tensors of earthquakes in the volume, ΔV. For Utah

$$\varepsilon_{ij} = \begin{matrix} 5 & 0 & 0 \\ 0 & -5 & 0 \\ 0 & 0 & 0.096 \end{matrix} \quad \times 10^{-8}$$

where ΔV is the area of Region I multiplied by the maximum depth of faulting (301.2 km x 1000 km x 10 km) and $\mu_f = 0.6$. The extensional strain rate over the Utah area for the last 42 years can be estimated by dividing 5×10^{-8} by 42 to obtain 1.2×10^{-9}/yr. The strain rate is underestimated because all earthquakes that occurred during this

time period have not been included in the moment tensor. The addition of these omitted earthquakes would probably only increase the calculated moment tensor and strain tensor values by less than 30%. Incorrect fault plane solutions will also effect the values of the tensors, but probably less than 10%.

Earthquakes in Utah occur along more randomly distributed planes than earthquakes along a major plate margin. For the calculation of seismic moment rates in the Utah region it was assumed that slip rates on all major faults were known so that equation (3) could be used to compute geologic moment rates. To determine whether this assumption was valid, subregions of Utah were treated as zones of deformation and equation (4) was used to compute moment rates for each region. Equation (4) assumes an empirically determined constant (k). A value of $k = 0.75$ was derived from central Asian data (Chen and Molnar, 1977). Anderson (1979) demonstrated this constant was also valid for southern California. This constant was based on the relationship between M_{22}^T and M_o^T (Anderson, 1979) where M_{22}^T is the total moment in the direction of maximum horizontal deformation and M_o^T is the total moment for all earthquakes considered. Assuming $\mu_f = 0.6$, for all of Utah, $M_{22}^T = 9.9 \times 10^{25}$ dyne-cm and $M_o^T = 1.1 \times 10^{26}$ dyne-cm, or $M_{22}^T \simeq 0.9 M_o^T$.

Moment rates were computed for each region (Table 9) using the constant of 0.9. The direction of maximum horizontal deformation is nearly east-west, so l_1 was chosen to correspond to the width of the region in the east-west direction and l_2 was chosen to be the maximum depth of faulting (10 km). Average slip rates were estimated from

geologic data used in this study or taken from Greensfelder et al. (1980a, 1980b). With the exception of the Wasatch fault region, the moment rates calculated using the zone of deformation assumption agree well with the geologic moment rates.

One problem encountered in the calculation of moment rates for zones of deformation was that the Utah subregions did not accurately define zones of deformation. For example, the whole state of Utah region should not be considered as a single zone of deformation since it is composed of three separate tectonic provinces.

Variations in slip rates, as small as 0.1 mm/yr, could change some of the moment rates substantially. It is doubtful that the slip rates even have a ±0.1 mm/yr accuracy. The fact that the moment rates agree well in spite of these difficulties indicates that the use of equation (3) to calculate moment rates for Utah was reasonable.

For the Utah region equation (4) can be rewritten as

$$\dot{M}_o = \frac{2\mu l_1 l_2 l_3 \dot{e}}{0.9} \qquad (21)$$

(Anderson, 1979) where $\dot{e}$ is the strain, l_1 is the dimension of the region in the direction of maximum deformation, l_2 is the dimension normal to l_1, and l_3 is the depth of the region. Strain rates computed using this equation are also listed in Table 9. The geologic strain rates are lower than values of 1 to 5 x 10^{-8}/yr estimated by Greensfelder et al. (1980a, 1980b) for the Wasatch region. Lawrence (1976) estimated the strain rate of the Basin and Range province to be between 3.2 x 10^{-9} and 3.2 x 10^{-8}/yr. All geologically determined

Table 9. Moment rates and strain rates for Utah

Moment Rates

Region	Moment Rate From Geologic Data (dyne-cm/yr)	Moment Rate Assuming Zones of Deformation (dyne-cm/yr)	Slip Rate (mm/yr)	l_1 (km)	l_2 (km)
Utah	4.4×10^{24}	3.3×10^{24}	1 [1]	440	10
Southwestern Utah	1.4×10^{24}	1.1×10^{24}	.8 [2]	190	10
Wasatch Front	2.9×10^{24}	1.8×10^{24}	1.2 [2]	200	10
Wasatch fault	1.8×10^{24}	7×10^{23}	1.2 [2]	80	10

Strain Rates

Region	Area x 1000 km^2	Geologically Determined Strain Rate (1 yr)
Utah	301.15	2×10^{-9}
Southwestern Utah	56.16	3.4×10^{-9}
Wasatch Front	92.81	4.3×10^{-9}
Wasatch fault	37.75	6.5×10^{-9}

[1]From Greensfelder et al. (1980a, 1980b)
[2]Average slip rate for faults in the regions based on geologic data used in this study.

strain rates fall within the range of Lawrence's values with the exception of the Utah region. The low geologically determined strain rate of the Utah area may be a result of the error in considering this area as a single zone of deformation.

CONCLUSIONS

Use of geologic data to calculate moment rates for Utah has been very successful. Return periods predicted by geologic moment rates agree surprisingly well with return periods based on historic data, suggesting that the historic seismicity is reflective of the long-term seismicity of Utah.

Results of this thesis indicate that geologic data on faults in regions with little historic earthquake data can be used to obtain an estimate of the long-term seismicity for the region. One difficulty encountered in using geologic data to calculate return periods is that some sort of moment-versus-magnitude relationship must be developed for a given study region. Use of other moment-versus-magnitude relationships may cause large errors in return-period calculations. Even if adequate data are available, and a moment-versus-magnitude relationship has been developed, it must be realized that the calculated return periods only reflect a general estimate of seismicity.

The spectral analysis of historic events in the Utah region has revealed a different moment-versus-magnitude relationship than that of southern California. The differences in the relationships may be due to differences in source mechanism, path effects, magnitude scales, or tectonic stress. The source parameters of Utah earthquakes, in general, agree with those for other intraplate earthquakes. However, it appears that Utah earthquakes less than $M_L = 4.5$ may have lower

stress drops and apparent stresses than other intraplate events. More detailed study of worldwide earthquakes versus Utah earthquakes is necessary to determine what may cause these differences.

Analysis of moment tensor data based on historic events shows that the amount of extension in the east-west direction is approximately equal to the compression in the vertical direction. A small component of compression in the north-south direction is prevalent in northern Utah, whereas the north-south component becomes tensional in southern Utah.

Moment studies of other moderate to large earthquakes in the Intermountain seismic belt should be carried out to determine whether these earthquakes resemble Utah earthquakes, since faulting mechanisms and path effects should be similar in other parts of the Intermountain seismic belt. A moment tensor for the entire region could be calculated which would reflect deformation in the entire region of the Intermountain seismic belt.

APPENDIX A

GEOLOGIC AND MOMENT RATE DATA FOR FAULTS IN THE UTAH AREA

Area II'

Fault Displacement, fault length, and age estimates for the Wasatch fault area[1,2]
(a subregion of the Utah region)

Fault or Fault Segment	Reference No.	Map Code	Last Movement (years)	Offset (meters)	Length (km)	Slip Rate (mm/yr)	Estimated Rate x 10^{22} (dyne-cm/yr)
Fayette to Sevier Reservoir	15	1	2,000	1.2	9.4	0.6	2.1
Sevier Reservoir	4	2	5,000	4	10	0.8	3.0
Sevier Reservoir to Nephi	15	3	16,000	?	30	<.3	3.4
Nephi to Santaquin	11	4	4,330-4,830	8	31	1.7	20.0
Santaquin to Salem	42	5	13,000	10.7	15.2	0.8	7.5
	42		26,000	45.7	15.2	1.8	
Salem to Spanish Fork	33	6	16,000	12.2	7.6	0.8	2.3
Spanish Fork to Hobble Creek	42	7	13,000	15	7.3	1.1	5.6
	15		26,000	76	7.3	2.9	

[1]The first twenty fault segments are segments of the Wasatch fault as defined by Cluff et al., (1970).
[2]References are listed by reference number at the end of the appendix.

Fault or Fault Segment	Reference No.	Map Code	Last Movement (years)	Offset (meters)	Length (km)	Slip Rate (mm/yr)	Estimated Rate x 10^{22} (dyne-cm/yr)
Hobble Creek to Springville	42	8	13,000	15	3.7	1.2	2.0
	42		16,000	25	3.7	1.6	
Springville to Ironton	15	9	2-3,000	3	4	1.2	1.8
Ironton to Rock Canyon	8	10	18,000	60	8	3.3	10
Rock Canyon to Provo Canyon	25	11	16,000	18	5.8	1.1	2.4
Provo Canyon to Alpine	25	12	16,000	18.3	21.6	1.1	9.1
Alpine to Corner Canyon	29	13	16,000	16.8	6.7	1.0	2.6
Jordon Narrows to Corner Canyon	30	14	16,000	15	4	0.94	1.4
Corner Canyon to Big Cottonwood	30	15	6,000	15-18	14.6	2.5-3.0	15.3
Big Cottonwood to Ft. Douglas	30	16	6,000	6.1	20.7	1.0	7.9
Ft. Douglas to Centerville	14	17	>16,000	?	18	<0.3	2.0

Fault or Fault Segment	Reference No.	Map Code	Last Movement (years)	Offset (meters)	Length (km)	Slip Rate (mm/yr)	Estimated Rate x 10^{22} (dyne-cm/yr)
Centerville to Ogden	37	18	6,000	11	48	1.8	33
Ogden to Brigham City	12	19	16,000	6.1-9.1	27	0.38-0.67	4.9
Brigham City to Malad City	14	20	>16,000	?	80	<0.3	9.1
Scipio Valley	10	53	13,000	11	6.2	0.85	2.0
Pavant Range	10	56	16,000	7	32	0.43	5.2
Maple Grove	10	57	>16,000	12	4.5	0.75	1.3
Little Valley	10	59	>16,000	8.2	13.8	0.51	2.7
Japanese Valley	4	60	50,000	4	5	0.08	0.15
West Mercur	18	62	10,000	12	8	1.2	3.7
East Tintic	31	68	16,000	8	11	0.5	2.1
Sanpete Valley	36	72	500,000	300	20	0.6	4.6
East Cache (segment)	23	74	13,000	1.2-4.8	4	0.09-0.37	0.35
Musiana	7	69	1,000,000	610	30	0.6	6.9

Fault or Fault Segment	Reference No.	Map Code	Last Movement (years)	Offset (meters)	Length (km)	Slip Rate (mm/yr)	Estimated Rate x 10^{22} (dyne-cm/yr)
Woodruff	40	76	10,000	5	11	0.5	2.1
Granger	28	77	16,000	3-6	10	0.19-0.38	1.1
Water Hollow	6	70	1,000,000	200	25	0.2	1.9
W. Bear Lake	19	81	5,000	2-3	16	0.4-0.6	3.0

Area II

Fault Displacement, fault length, and age estimates for the Wasatch Front area

(a subregion of the Utah region)

Fault or Fault Segment	Reference No.	Map Code	Last Movement (years)	Offset (meters)	Length (km)	Slip Rate (mm/yr)	Estimated Rate x 10^{22} (dyne-cm/yr)
Black Rock	24	30	--	--	15	1.4	8.0
Drum Mountain	10	52	16,000	6.7	36	0.41	5.6
Clear Lake	10	54	>16,000	2	20	0.13	0.99
Cricket Mts	10	58	16,000	15	1	0.94	0.36
Grasshopper Ridge	16	61	1,000,000	880	7	0.88	2.3
Sheeprock	10	64	>16,000	2.4	10.9	0.15	0.62
Lakeside	43	65	4,000,000	790	30	0.2	2.3
Hidden Mine	43	66	4,000,000	915	10	0.23	0.88
Stansbury	32	67	10,000	6-9	26	0.6-0.9	7.4
Joes Valley	9	71	50,000	9	12	0.18	0.82
Pleasant Valley	39	73	1,000,000	200	60	0.2	4.6
North Canyon	40	75	10,000	3-5	10	0.4	1.5

Fault or Fault Segment	Reference No.	Map Code	Last Movement (years)	Offset (meters)	Length (km)	Slip Rate (mm/yr)	Estimated Rate x 10^{22} (dyne-cm/yr)
Hansel Valley	35	78	16,000	46	18	2.9	20.0
Rock Creek	41	79	10,000	15-18	40	1.5-1.8	25.1
E. Bear Lake	26	80	50,000	43	95	0.86	31.1
Towonta Flats	22	82	26,000	12	5	0.46	0.88
Tabiona	17	83	50,000	1.6	3	0.03	0.034

Area III

Fault Displacement, fault length, and age estimates for the southwest Utah region

(a subregion of the Utah region)

Fault or Fault Segment	Reference No.	Map Code	Last Movement (years)	Offset (meters)	Length (km)	Slip Rate (mm/yr)	Estimated Rate x 10^{22} (dyne-cm/yr)
Braffits Creek	2	21	810-1,240	6	1.5	4.8-7.4	3.5
N. Hurricane	21	22	---	---	36	0.24-0.4	4.4
S. Hurricane	21	23	---	---	155	0.14-0.2	10.0
Sevier	20	24	500,000	200	200	0.4	30.1
Grand Wash	20	25	<6,000,000	200	175	0.03	2.0
Washington	20	26	<6,000,000	30	130	0.005	0.24
Main Street	20	27	<6,000,000	70	50	0.012	0.23
Tushar	34	28	4,000,000	760	130	0.19	9.4
Paunsaugunt	34	29	4,000,000	1070	100	0.27	10.3
W. Cove Fort	13	31	12,000	10-30	20	0.8-2.5	12.6
Mineral Mts.	3	32	16,000	10	37	0.63	8.9

Fault or Fault Segment	Reference No.	Map Code	Last Movement (years)	Offset (meters)	Length (km)	Slip Rate (mm/yr)	Estimated Rate x 10^{22} (dyne-cm/yr)
W. Parowan	38	33	10,000	12	18	1.2	8.2
E. Parowan	4	34	44,000	60	6	1.4	3.2
E. Cove Fort	1	35	50,000	18-20	30	0.36-0.4	4.3
Sulphurdale	4	36	>10,000	4.3	2	0.43	0.33
Beaver	4	37	>10,000	1-3	7	0.1-0.3	0.53
Panguitch	4	38	>10,000	27	6	2.7	6.2
Circleville	4	39	>10,000	3-5	5	0.3-0.5	0.76
Junction	4	40	>10,000	3.5	4	0.35	0.53
Marysvale	4	41	>10,000	12	4	1.2	1.8
Ice Springs	24	42	---	--	3	2.0	2.3
Beaver Ridge	24	43	---	--	16	0.08	0.49
Last Chance Bench	4	44	>10,000	25	2	2.5	1.9
Thousand Lake	27	45	4,000,000	600	30	0.15	1.7
Shurtz Creek	5	46	>10,000	20	3	2.0	2.3
Red Canyon	3	47	10,000	1.5-2.2	9.5	0.15-0.22	0.67
Annabella	3	48	10,000	5.2	13	0.52	2.6

Fault or Fault Segment	Reference No.	Map Code	Last Movement (years)	Offset (meters)	Length (km)	Slip Rate (mm/yr)	Estimated Rate x 10^{22} (dyne-cm/yr)
White Sage Flat	3	49	>16,000	13.2	2.5	0.83	0.79
Lund	3	50	>16,000	5.5-10	19	0.34-0.63	3.5
San Francisco Mts.	3	51	>16,000	10	13	0.63	3.1

Area I

Fault Displacement, fault length, and age estimates for the Utah area

Fault or Fault Segment	Reference No.	Map Code	Last Movement (years)	Offset (meters)	Length (km)	Slip Rate (mm/yr)	Estimated Rate x 10^{22} (dyne-cm/yr)
House Range	10	55	16,000	1	5	0.063	0.12
Fish Springs	10	63	12,000	3.3	12	0.28	1.3

References to fault displacement, fault length, and age estimates

1 Anderson (1980)

2 Anderson and Bucknam (1979a)

3 Anderson and Bucknam (1979b)

4 Anderson, Bucknam and Hamblin (1978)

5 Averitt (1962)

6 Bachman (1959)

7 Baughman (1959)

8 Bissell (1964)

9 Bucknam (1979)

10 Bucknam and Anderson (1979b)

11 Bucknam, Algermissen and Anderson (1980)

12 Buss and Peterson (1964)

13 Clark (1979)

14 Cluff, Brogan and Glass (1970)

15 Cluff, Brogan and Glass (1973)

16 Croft (1956)

17 Garvin (1969)

18 Gilluly (1932)

19 Greensfelder (1976)

20 Hamblin (1970)

21 Hamblin and Best (1979)

22 Hansen (1969)

23 Hardy (1979)

24 Hoover (1974)

25 Hunt, Varnes and Thomas (1953)

26 Kaliser (1972)

27 Luedke (1954)

28 Marine and Price (1964)

29 Marsell (1964)

30 Morrison (1965)

31 Proctor (1959)

32 Rigby (1958)

33 Rigby (1962)

34 Rowley (1968)

35 Shenon (1936)

36 Spieker (1949)

37 Swan et al., (1978)

38 Thomas and Taylor (1946)

39 Walton (1954)

40 Witkind (1975a)

41 Witkind (1975b)

42 Woodward-Clyde Consultants (1975)

43 Young (1955)

APPENDIX B

SPECTRAL AND INSTRUMENTAL DATA

Station Listings

(Tabulated responses follow station listings)

Albuquerque, New Mexico (ALQ)
Instruments: WWSSN long-period Z component
T_o=30.2 T_g= 99 Magnification=3000 15mm/min (1962)
T_o=15 T_g=100 Magnification=3000 30mm/min (1966)

Berkeley--Haviland, California (BRK)
Instruments: Wood Anderson NS, EW components
T_o=0.8 Magnification=2800 60mm/min (1934)
Galitzin Z, NS, EW components
Tabulated response 30mm/min (1962)

Berkeley-Byerly, California (BKS)
Instruments: WWSSN long period Z component
T_o=30 T_g=100 Magnification=3000
15mm/min (1962, 1963)
100 Kg short-period Benioff Z component
Tabulated response 60mm/min (1967)

College Station, Alaska (COL)
Instrument: WWSSN long-period Z, NS, EW components
T_o=15 T_g=100 Magnification=1500 15mm/min (1975)

Corvallis, Oregon (COR)
Instruments: WWSSN long-period Z component
T_o=15 T_g=100 Magnification=1500 15mm/min (1966)

Dugway, Utah (DUG)
Instruments: WWSSN long-period Z, NS EW components
T_o=30 T_g=100 Magnification=3000
30mm/min (1962-1964)
T_o=15 T_g=100 Magnification=3000
15mm/min (1966-1976)

Dallas, Texas (DAL)
Instruments: WWSSN long-period Z component
T_o=15 T_g=100 Magnification=1500 15mm/min (1975)

Flin Flon, Manitoba, Canada (FFC)
Instruments: Columbia long-period Z component
T_o=15 T_g= 88 Magnification=4600 15mm/min (1966)

Fort St. James, British Columbia, Canada (FSJ)
Instruments: Columbia long-period Z component
T_o=15 T_g= 85 Magnification=2000 15mm/min (1966)

Golden, Colorado (GOL)
Instruments: WWSSN long-period Z, NS, EW component
T_o=30 T_g=100 Magnification=1500 15mm/min (1967)

Junction City, Texas (JCT)
Instruments: WWSSN long-period Z component
T_o=15 T_g=100 Magnification=1500 15mm/min (1975)

Longmire, Washington (LON)
Instruments: WWSSN long-period Z component
T_o=15 T_g=100 Magnification=1500 30mm/min (1975)

Madison, Wisconsin (MDS)
Instruments: WWSSN long-period Z component
T_o=30 T_g=100 Magnification=750 15mm/min (1962)

Oxford, Mississippi (OXF)
Instruments: WWSSN long-period Z component
T_o=15 T_g=100 Magnification=3000 15mm/min (1975)

Palomar, California (PLM)
Instruments: WWSSN long-period Z component
T_o=30 T_g=100 Magnification=1500 30mm/min (1962)

Pasadena, California (PAS)
Instruments: Wood Anderson NS, EW components
T_o=0.8 Magnification=2800 60mm/min (1934)

Instrument VI A (short-period) Z component
Tabulated response 60mm/min (1934)

Instrument 16 (short-period) Z component
Tabulated response 30mm/min (1963,1967)

Instrument 34 A (long-period) Z component
Tabulated response 15mm/min (1975)

Instrument 34 B (long-period) EW component
Tabulated response 15mm/min (1962)

Price, Utah (PCU)
Instruments: 14 Kg short-period Benioff Z component
T_o=1.0 T_g=1.5 Magnification=96,500 60mm/min (1971)

T_o=1.0 T_g=1.5 Magnification=46,300 60mm/min (1966)

T_o=1.0 T_g=1.5 Magnification=31,350 60mm/min (1964)

Rapid City, South Dakota (RCD)
Instruments: WWSSN long-period Z component
T_o=30 T_g=100 Magnification=750 15mm/min (1962)

Salt Lake City, Utah (SLC)
Instruments: 14 Kg short-period Benioff
T_o=1.0 T_g=1.5 Magnification=42,000 60mm/min (1971)

Spring Hill, Alabama (SHA)
Instruments: WWSSN long-period Z, EW components
T_o=15 T_g=100 Magnification=1500 15mm/min(Z)(1975)

T_o=15 T_g=100 Magnification=750 15mm/min(EW)(1975)

Suffield, Alberta, Canada (SES)
Instruments: Columbia long-period Z component
T_o=15 T_g= 86 Magnification=3600 15mm/min (1966)

Tuscon, Arizona (TUC)
Instruments: WWSSN long-period Z component
T_o=15 T_g=100 Magnification=1500 15mm/min (1975)

Weston, Massachusetts (WES)
Instruments: WWSSN long-period Z, NS, EW components
T_o=15 T_g=100 Magnification=3000 15mm/min (1975)

Yellowknife, Northwest Territories, Canada (YKC)
Instruments: Columbia long-period Z component
T_o=30 T_g= 90 Magnification=2900 15mm/min (1966)

Tabulated Responses

Period	Magnification	Period	Magnification
Berkeley Galitzin			
0.5	180	6.0	1300
0.6	190	7.0	1400
0.7	200	8.0	1500
0.8	280	9.0	1400
0.9	310	10.0	1300
1.0	330	11.0	750
2.0	570	12.0	230
3.0	1000	13.0	140
4.0	1100	14.0	78
5.0	1200		
Byerely short-period Benioff			
0.2	9000	0.8	33000
0.3	27000	0.9	32000
0.4	34000	1.0	13000
0.5	40000	2.0	600
0.6	40000	3.0	200
0.7	34000	4.0	80
Pasadena VI A			
0.5	16000	2.0	1400
0.75	10000	3.0	440
1.0	5500	4.0	170
1.5	2600	5.0	92
Pasadena 16			
.5	2400	5.0	1200
.75	3000	6.0	1000
1.0	3100	7.0	840
1.5	2800	8.0	700
2.0	2400	10.0	550
3.0	700	12.0	290
4.0	1400	14.0	130

Period	Magnification	Period	Magnification
Pasadena 34A and 34B			
2.0	90	30	2000
3.0	170	40	1500
4.0	280	50	1150
6.0	550	60	800
8.0	800	70	600
10.0	1150	80	475
12.0	1350	90	300
15.0	1650	100	300
20.0	2050		

Spectral Data for Utah Events

Event	Station (phase)	Distance (deg)	Azimuth (deg)	Q	Moment x 10^{24} (dyne-cm)	$R_{\theta\phi}$
1	BRK(EW)	8.2	244.5	400	70	0.93
	BRK(NS)	8.2	244.5	400	80	0.93
	PAS(EW)	8.7	210.3	200	90	0.93
	PAS(NS)	8.7	210.3	200	66	0.93
2	PAS(EW)	8.7	210.3	200	2.6	0.93
	PAS(P)	8.7	210.3	200	2.6	0.93
	PAS(SV)	8.7	210.3	400	2.6	0.93
3	ALQ(P)	8.0	146.8	200	5.6	0.14
	PLM(P)	10.2	207.1	400	14.0	0.095
	PLM(SV)	10.2	207.1	400	1.2	0.55
	BRK(SV)	9.0	247.5	400	4.0	0.54
	BKS(P)	8.9	247.4	400	2.9	0.39
	BKS(SV)	8.9	247.4	400	2.0	0.54
	RCD(P)	6.7	67.3	600	12.0	0.289
	MDS(SV)	17.2	77.1	600	3.0	0.70
	BRK(NS)	9.0	247.5	400	4.2	0.66
	BRK(EW)	9.0	247.5	400	4.0	0.66
	WES(P)	29.9	75.1	400	22.0	0.32
4	PAS(EW)	8.1	218.3	600	0.92	0.47
	DUG(SV)	0.8	226.7	200	0.2	0.6
	DUG(NS)	0.8	226.7	200	0.28	0.54
	DUG(EW)	0.8	226.7	200	0.2	0.54
5	BKS(P)	8.3	261.2	400	0.42	0.43
	BKS(SV)	8.3	261.2	600	0.36	0.78
	PAS(SV)	7.4	224.7	400	0.24	0.77
6	DUG(SV)	1.7	208.5	200	0.11	0.99
	DUG(NS)	1.7	208.5	200	0.58	0.15
	DUG(EW)	1.7	208.5	200	0.85	0.15
7	DUG(SV)	1.7	213.4	200	0.12	0.99
	DUG(NS)	1.7	213.4	200	0.6	0.16
	DUG(EW)	1.7	213.4	200	0.9	0.16
	PCU(P)	2.1	164.1	200	1.6	0.75
8	FFC(SV)	19.4	22.5	1000	0.7	0.74
	FSJ(SV)	19.4	341.1	800	0.7	0.68
	YKC(SV)	25.1	359.7	800	1.2	0.97
	FSJ(P)	19.4	341.1	400	2.0	1.0
	SES(SV)	13.2	8.9	800	0.7	0.56

Event	Station (phase)	Distance (deg)	Azimuth (deg)	Q	Moment x 10^{24} (dyne-cm)	$R_{\theta\phi}$
	COR(SV)	9.9	319.1	400	0.9	0.49
	COR(PZ)	9.9	319.1	800	1.6	0.99
	ALQ(SV)	6.7	109.1	400	0.46	0.44
	SES(P)	13.2	8.9	400	1.3	0.64
9	GOL(P)	5.4	75.0	400	8.3	0.096
	GOL(SV)	5.4	75.0	800	1.0	0.33
	GOL(NS)	5.4	75.0	400	1.0	0.90
	GOL(EW)	5.4	75.0	400	0.4	0.90
	PAS(SV)	6.5	230.3	200	1.6	0.33
	BKS(SV)	8.0	268.7	200	2.4	0.33
10	PCU(P)	2.5	42.9	200	0.047	0.55
	SLC(P)	3.1	16.4	200	0.087	0.63
11	DUG(SV)	1.5	342.3	200	0.12	0.33
	DUG(EW)	1.5	342.3	200	0.06	0.95
12	DUG(SV)	1.4	339.5	200	0.06	0.33
	DUG(EW)	1.4	339.5	200	0.03	0.95
13	DUG(NS)	1.1	264.9	400	0.14	0.38
	DUG(EW)	1.1	264.9	400	0.17	0.38
	DUG(SV)	1.1	264.9	400	0.5	0.10
14	DUG(SV)	3.9	184.4	200	0.5	0.26
	DUG(NS)	3.9	184.4	200	0.2	0.48
	DUG(EW)	3.9	184.4	200	0.3	0.48
15	DUG(SV)	1.9	186.6	200	0.14	0.77
	DUG(NS)	1.9	186.6	200	0.12	0.97
16	TUC(P)	10.0	171.6	400	9.3	0.29
	LON(P)	8.1	307.5	200	13.0	0.28
	SHA(P)	22.6	112.6	800	36.0	0.54
	SHA(SV)	22.6	112.6	1000	12.0	0.99
	SHA(EW)	22.6	112.6	400	24.0	0.76
	JCT(P)	15.5	134.8	600	52.0	0.18
	OXF(P)	19.6	105.4	800	57.0	0.41
	PAS(P)	9.2	210.9	800	12.5	0.36
	WES(P)	30.3	75.5	800	6.7	0.55
	WES(NS)	30.3	75.5	800	2.2	0.82
	WES(EW)	30.3	75.5	800	8.0	0.82
	DAL(P)	15.6	121.8	600	40.0	0.26
	COL(SV)	30.2	330.7	800	5.0	0.92
	COL(NS)	30.2	330.7	800	8.4	0.77
	COL(EW)	30.2	330.7	800	4.0	0.77
	COL(P)	30.2	330.7	800	15.0	0.62

Event	Station (phase)	Distance (deg)	Azimuth (deg)	Q	Moment x 10^{24} (dyne-cm)	$R_{\theta\phi}$
17	DUG(NS)	1.8	205.3	200	0.2	0.98
	DUG(EW)	1.8	205.3	200	0.4	0.98
18	DUG(SV)	1.8	185.6	200	0.1	1.0
	DUG(EW)	1.8	185.6	200	0.16	0.99
19	DUG(NS)	1.7	183.1	200	0.058	0.7

The following pages of plots are computer generated plots of body wave spectra used for seismic moment calculations in this thesis. The spectra shown have been corrected for attenuation, instrument response, spherical spreading and radiation pattern. The original seismograms used for spectral calculations are shown below the spectral plots. Numbers below the seismogram indicate the sample length in seconds. Where no number is listed the seismogram is 60 seconds long. (Amplitudes of the seismograms are not true amplitudes.) Event names are abbreviations of the names found in Table 3. Stations abbreviations are found in the Station Listings of Appendix B.

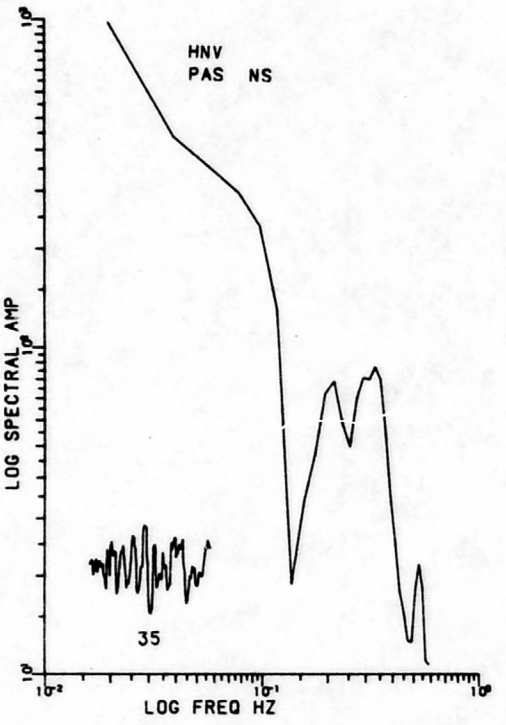
HNV
PAS NS
LOG SPECTRAL AMP
35
LOG FREQ HZ

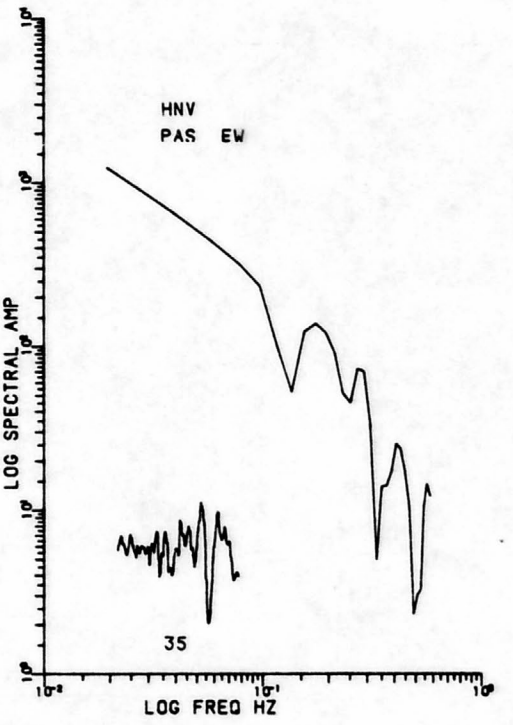
HNV
PAS EW
LOG SPECTRAL AMP
35
LOG FREQ HZ

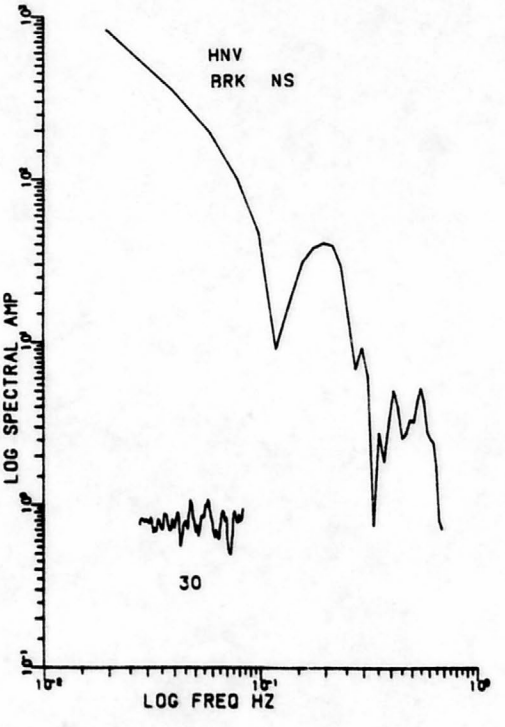
HNV
BRK NS
LOG SPECTRAL AMP
30
LOG FREQ HZ

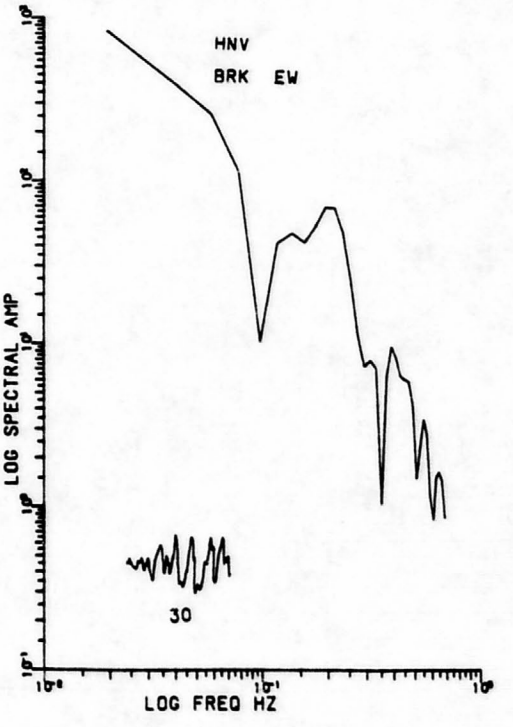
HNV
BRK EW
LOG SPECTRAL AMP
30
LOG FREQ HZ

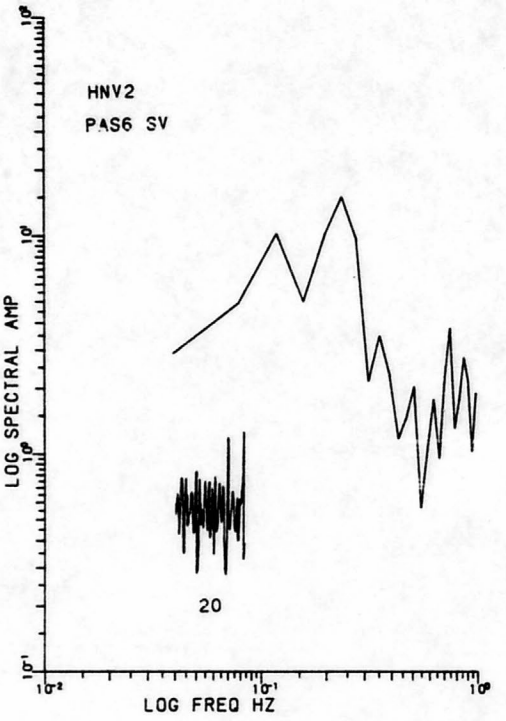
HNV2
PAS6 SV
LOG SPECTRAL AMP
LOG FREQ HZ
20

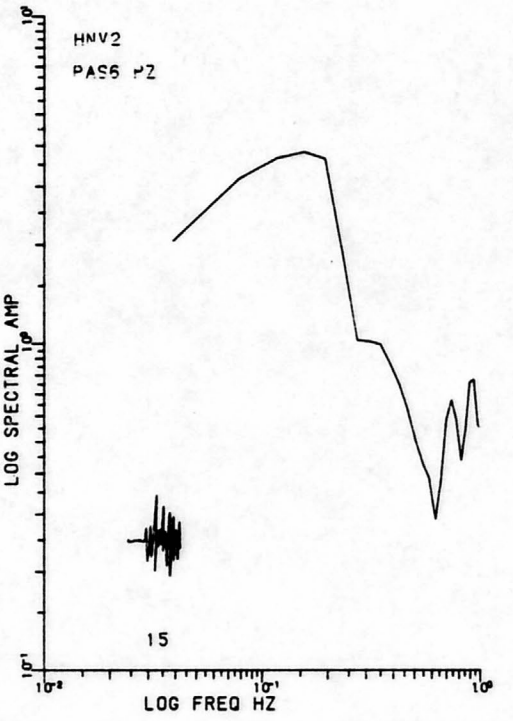
HNV2
PAS6 PZ
LOG SPECTRAL AMP
LOG FREQ HZ
15

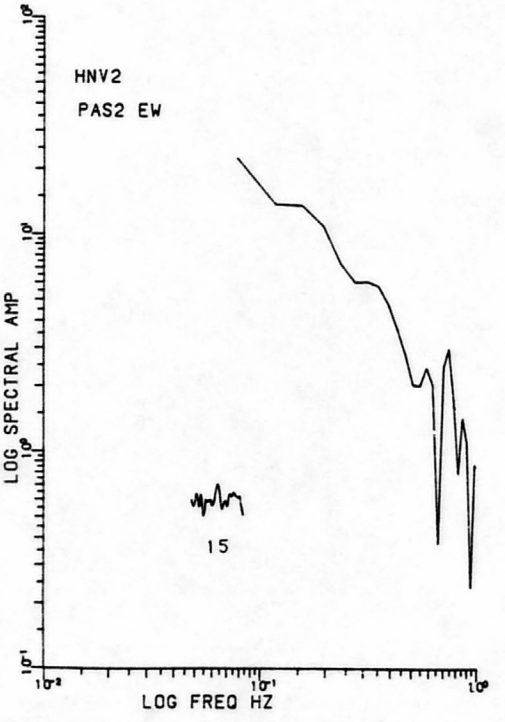
HNV2
PAS2 EW
LOG SPECTRAL AMP
LOG FREQ HZ
15

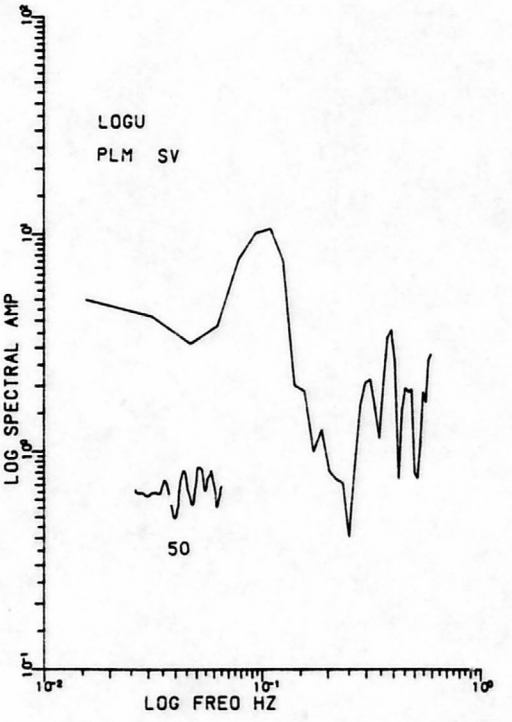
LOGU
PLM SV
LOG SPECTRAL AMP
LOG FREQ HZ
50

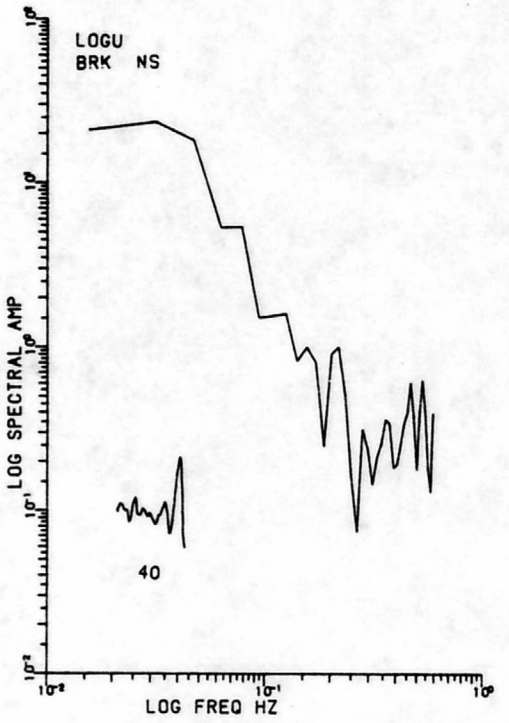
LOGU
BRK NS
LOG SPECTRAL AMP
40
LOG FREQ HZ

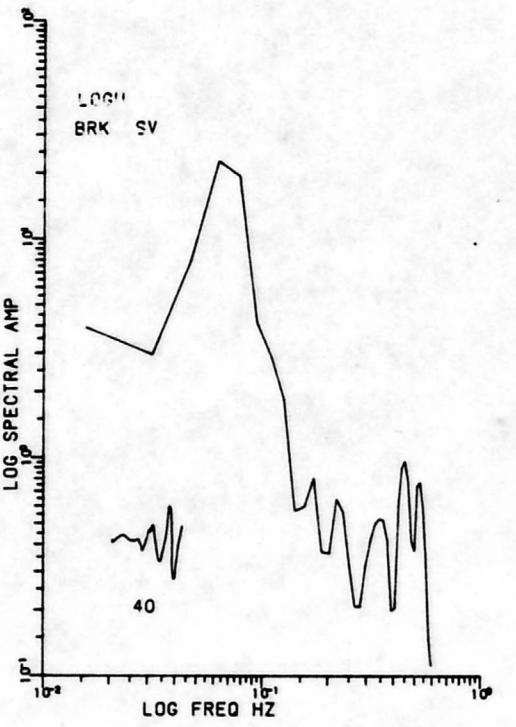
LOGU
BRK SV
LOG SPECTRAL AMP
40
LOG FREQ HZ

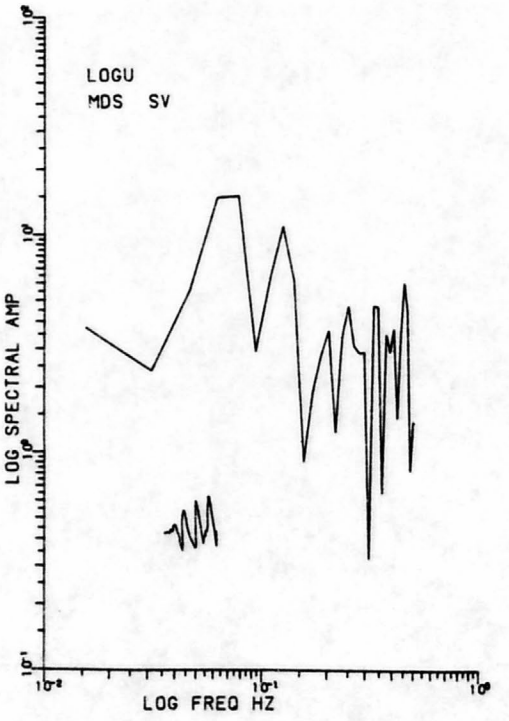
LOGU
MDS SV
LOG SPECTRAL AMP
LOG FREQ HZ

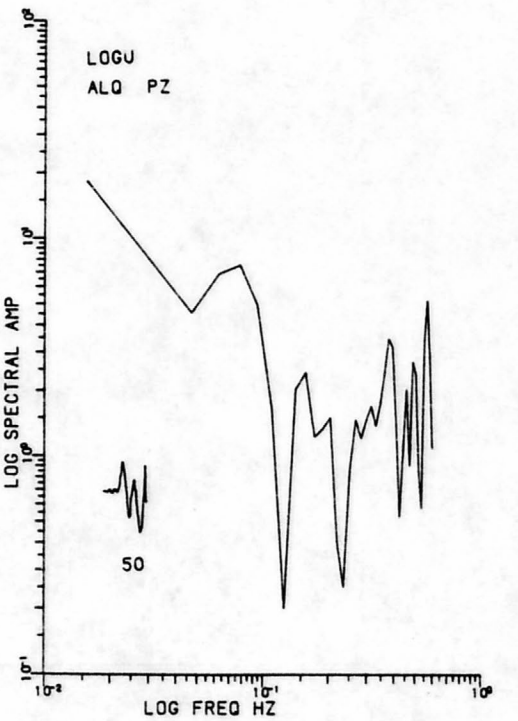
LOGU
ALQ PZ
LOG SPECTRAL AMP
50
LOG FREQ HZ

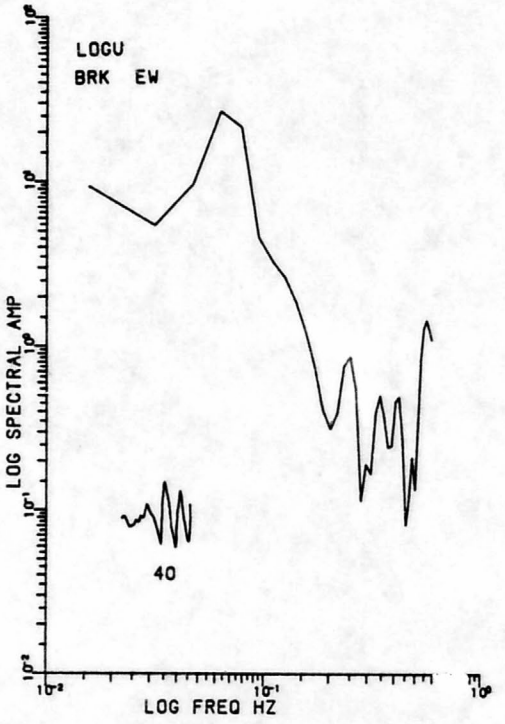
LOGU
BRK EW
LOG SPECTRAL AMP
40
LOG FREQ HZ

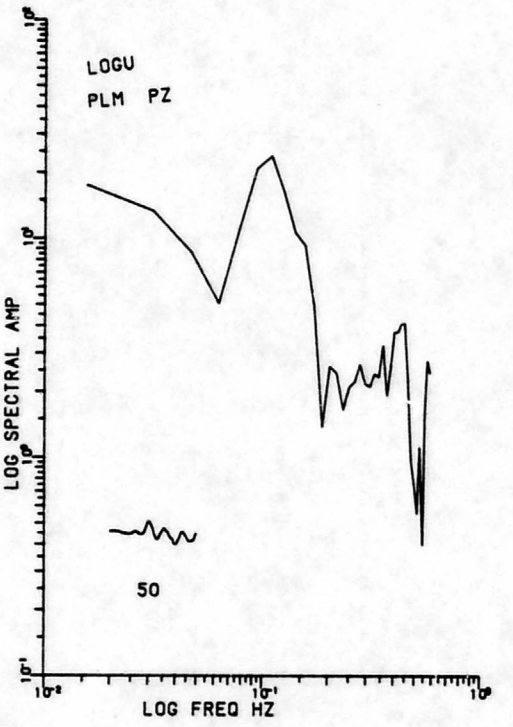
LOGU
PLM PZ
LOG SPECTRAL AMP
50
LOG FREQ HZ

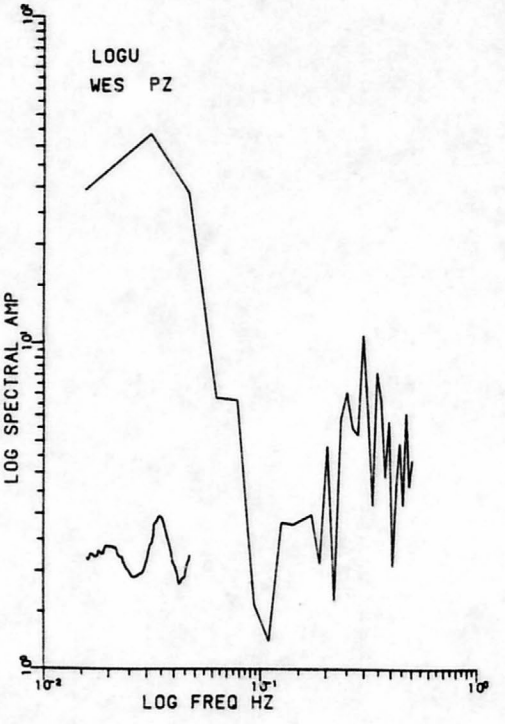
LOGU
WES PZ
LOG SPECTRAL AMP
LOG FREQ HZ

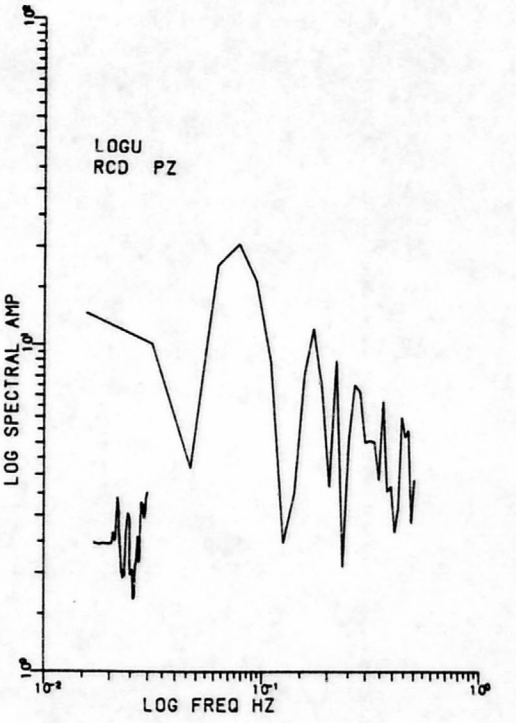
LOGU
RCD PZ
LOG SPECTRAL AMP
LOG FREQ HZ

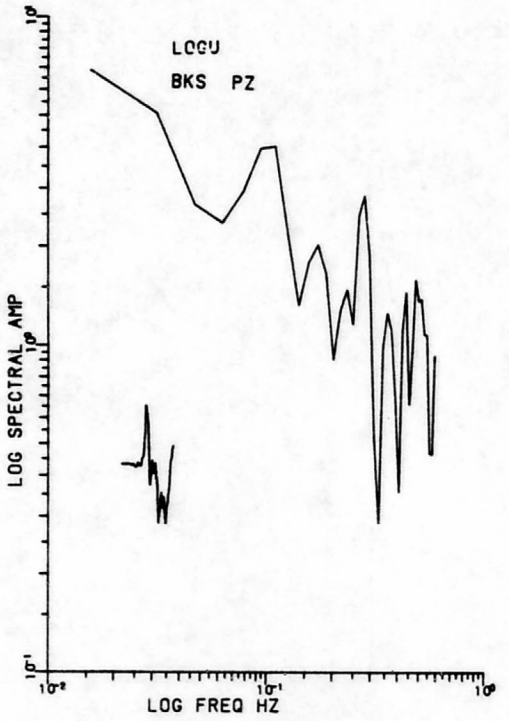
LOGU
BKS PZ
LOG SPECTRAL AMP
LOG FREQ HZ

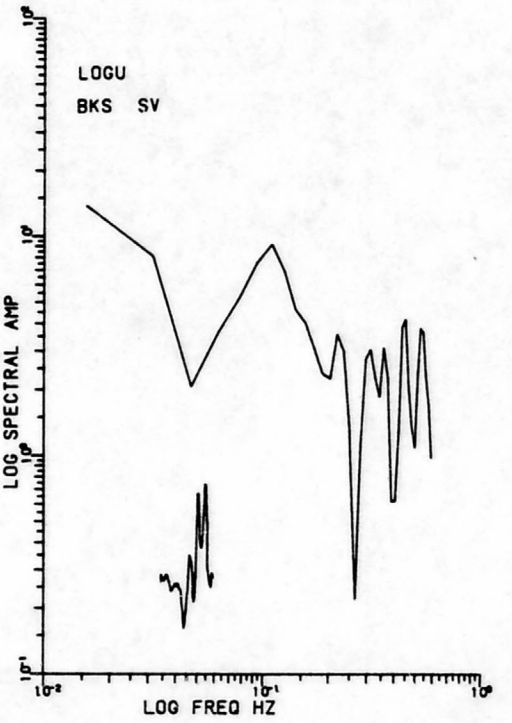
LOGU
BKS SV
LOG SPECTRAL AMP
LOG FREQ HZ

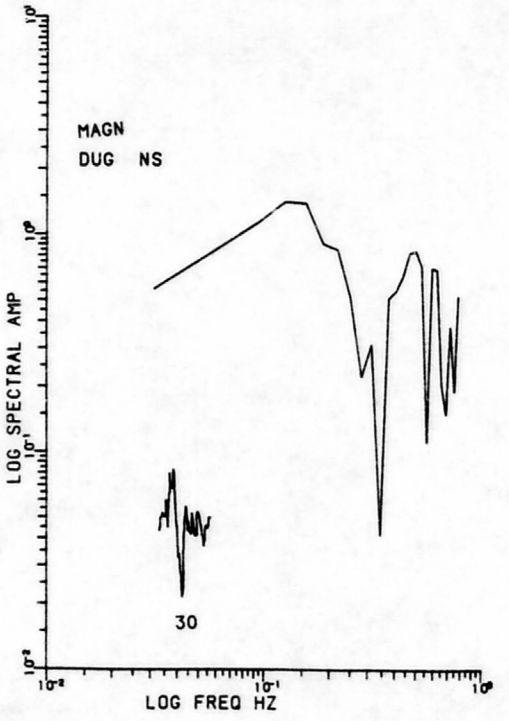
MAGN
DUG NS
30
LOG SPECTRAL AMP
LOG FREQ HZ

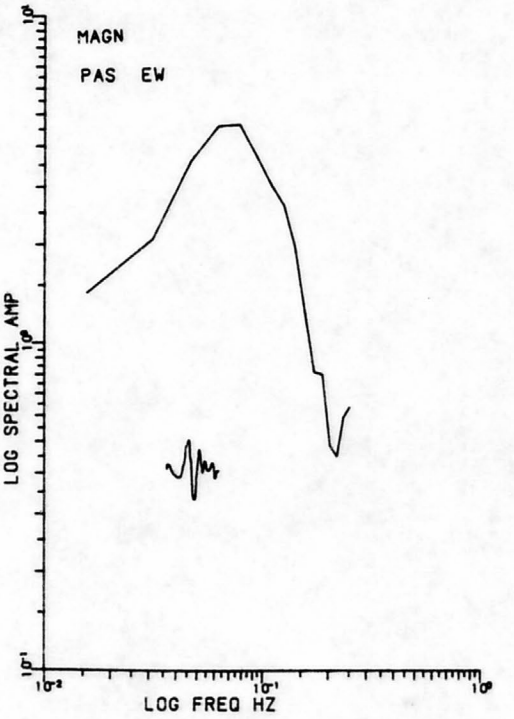
MAGN
PAS EW
LOG SPECTRAL AMP
LOG FREQ HZ

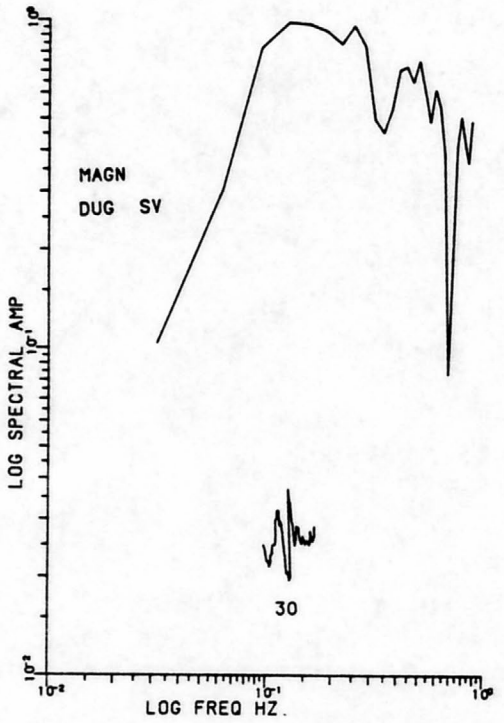
MAGN
DUG SV
LOG SPECTRAL AMP
30
LOG FREQ HZ.

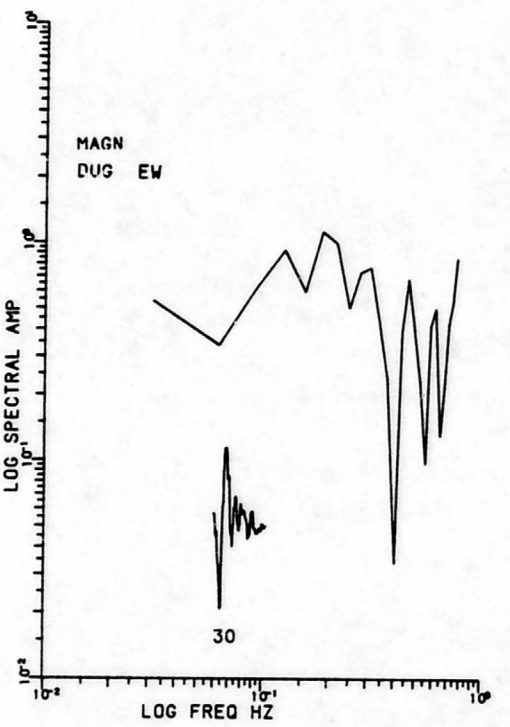
MAGN
DUG EW
LOG SPECTRAL AMP
30
LOG FREQ HZ

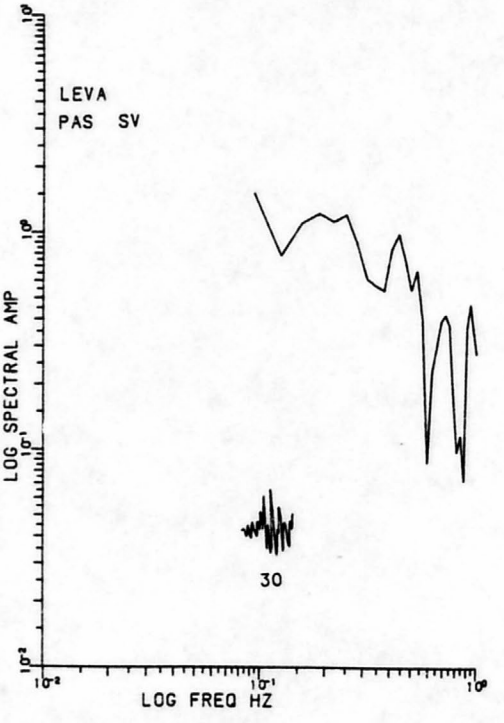
LEVA
PAS SV
LOG SPECTRAL AMP
30
LOG FREQ HZ

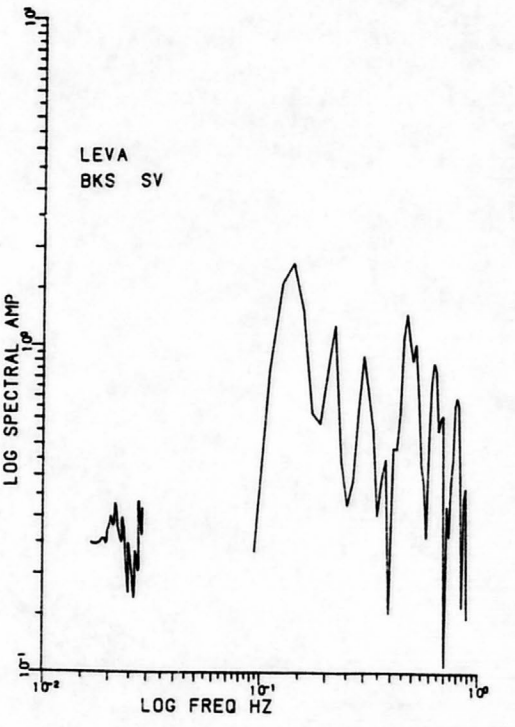
LEVA
BKS SV
LOG SPECTRAL AMP
LOG FREQ HZ

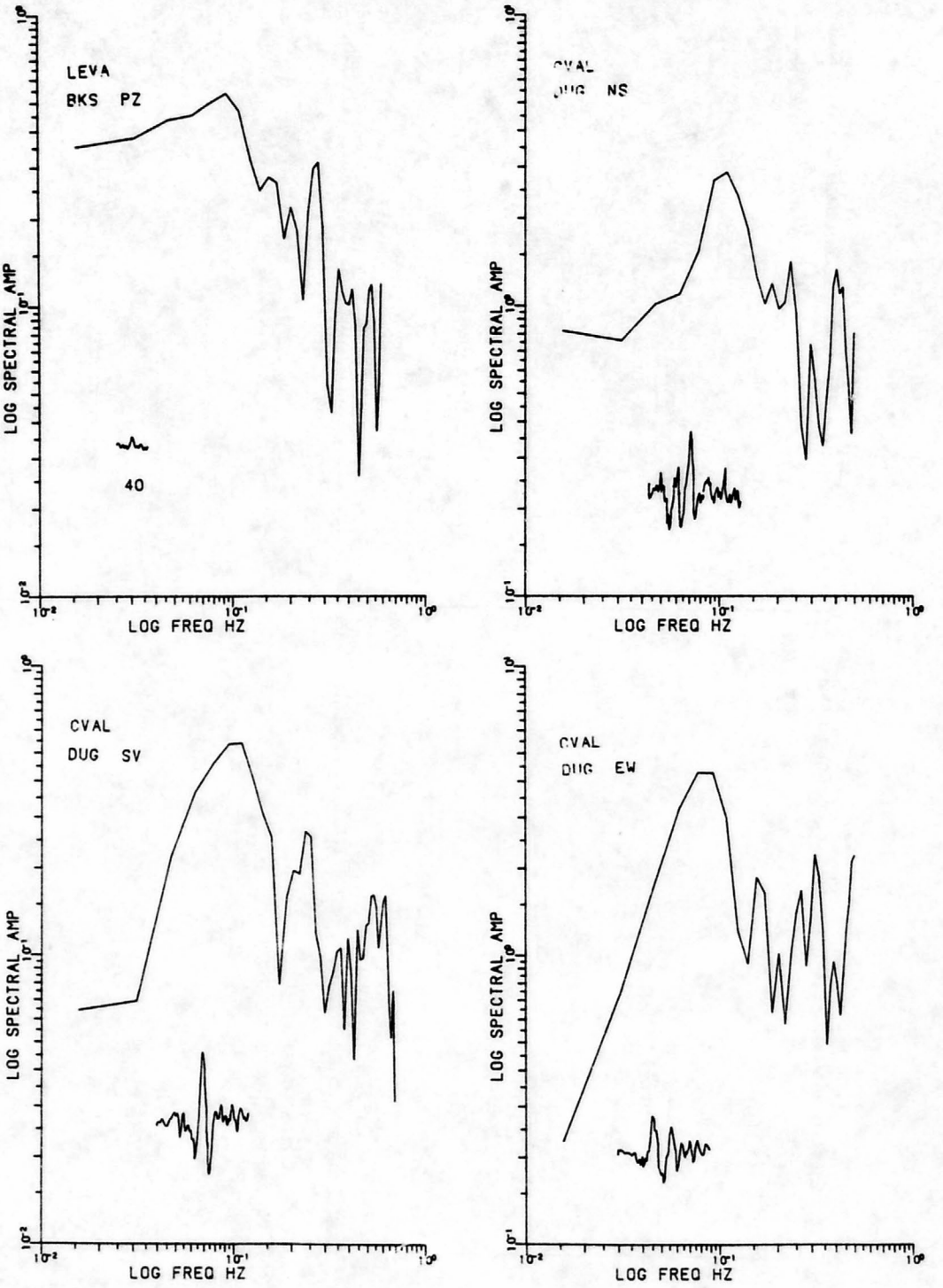
LEVA
BKS PZ
40
LOG SPECTRAL AMP
LOG FREQ HZ
CVAL
DUG NS
LOG SPECTRAL AMP
LOG FREQ HZ
CVAL
DUG SV
LOG SPECTRAL AMP
LOG FREQ HZ
CVAL
DUG EW
LOG SPECTRAL AMP
LOG FREQ HZ

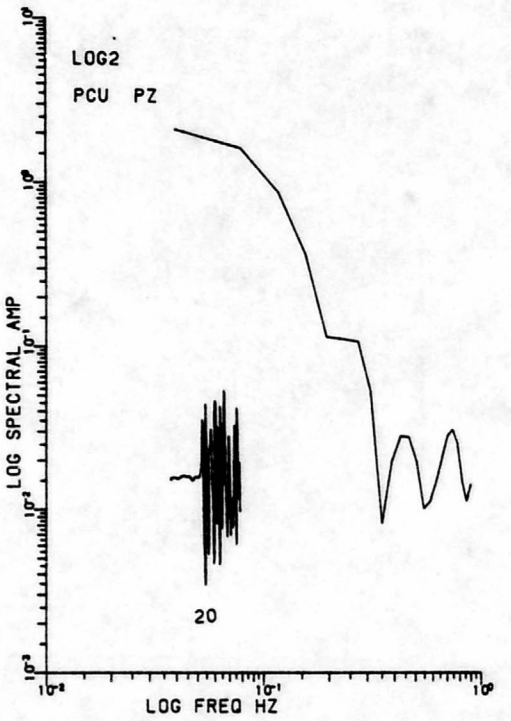
LOG2
PCU PZ
20
LOG SPECTRAL AMP
LOG FREQ HZ

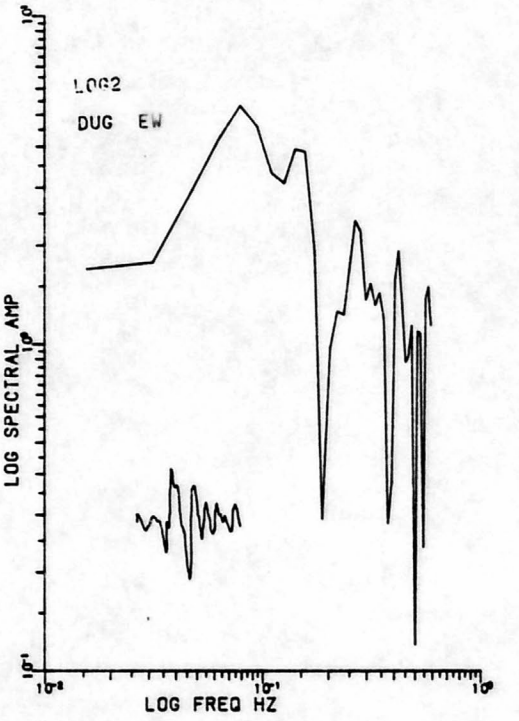
LOG2
DUG EW
LOG SPECTRAL AMP
LOG FREQ HZ

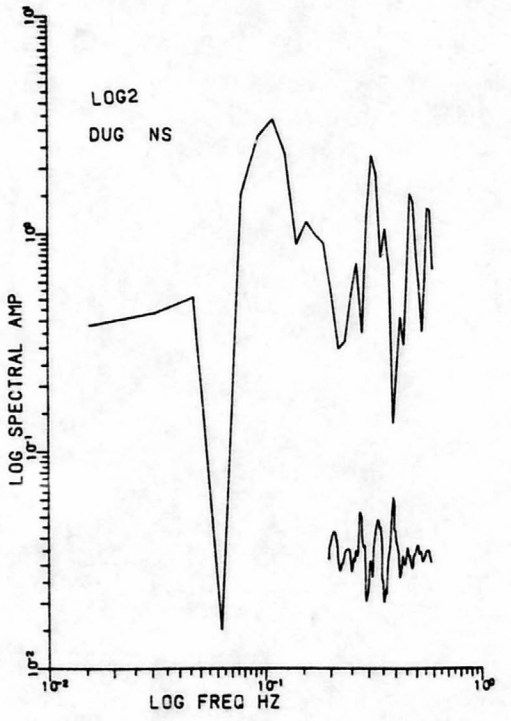
LOG2
DUG NS
LOG SPECTRAL AMP
LOG FREQ HZ

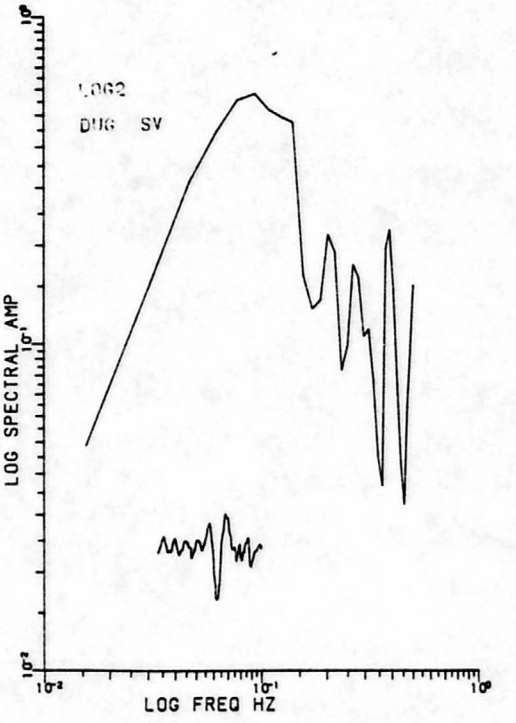
LOG2
DUG SV
LOG SPECTRAL AMP
LOG FREQ HZ

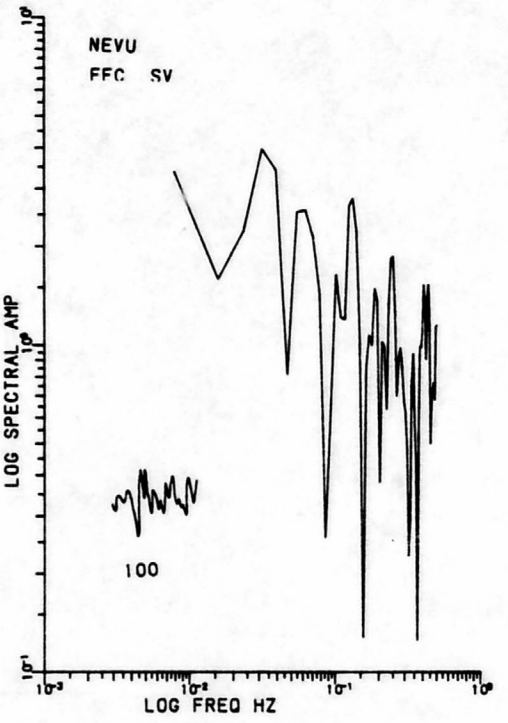
NEVU
FFC SV
LOG SPECTRAL AMP
100
LOG FREQ HZ

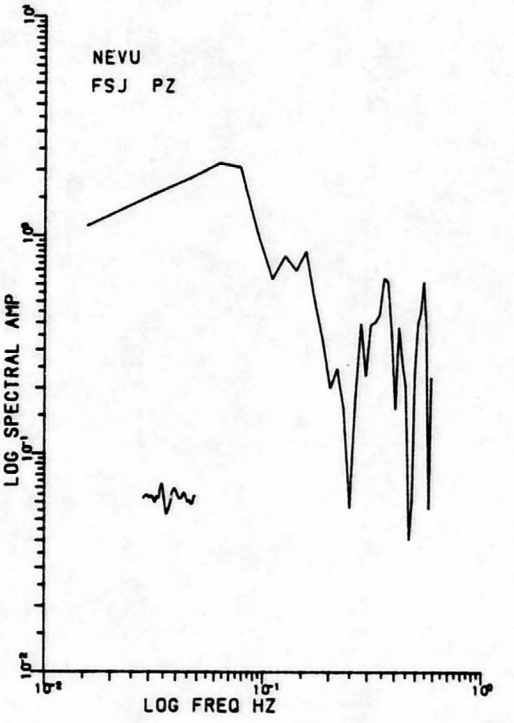
NEVU
FSJ PZ
LOG SPECTRAL AMP
LOG FREQ HZ

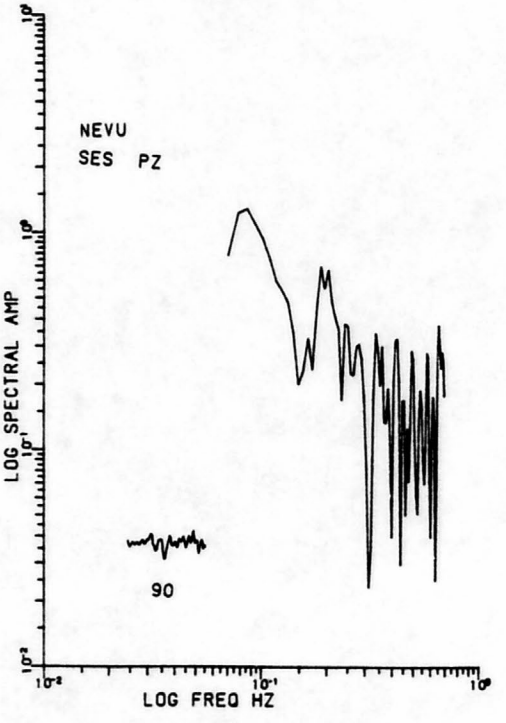
NEVU
SES PZ
LOG SPECTRAL AMP
90
LOG FREQ HZ

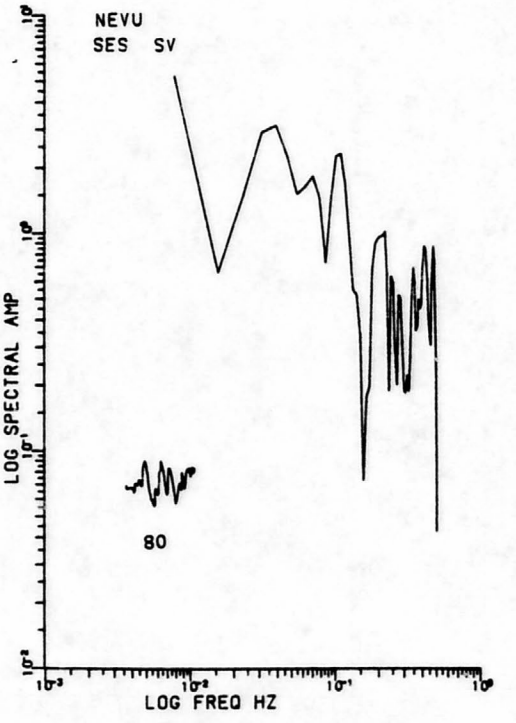
NEVU
SES SV
LOG SPECTRAL AMP
80
LOG FREQ HZ

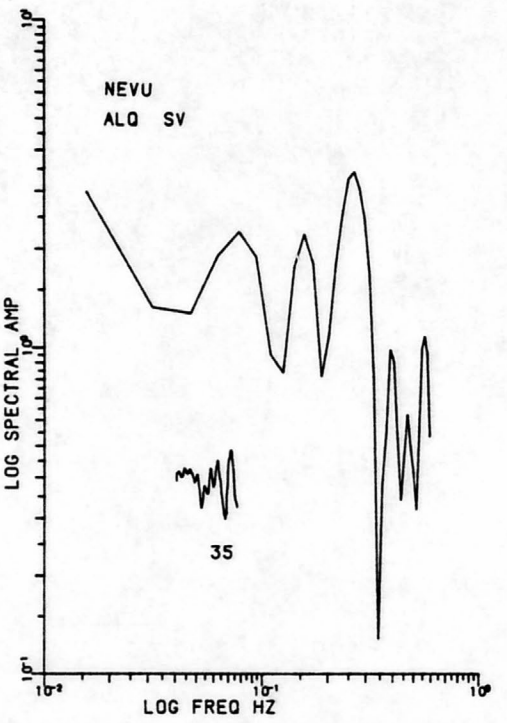
NEVU
ALQ SV
LOG SPECTRAL AMP
LOG FREQ HZ
35

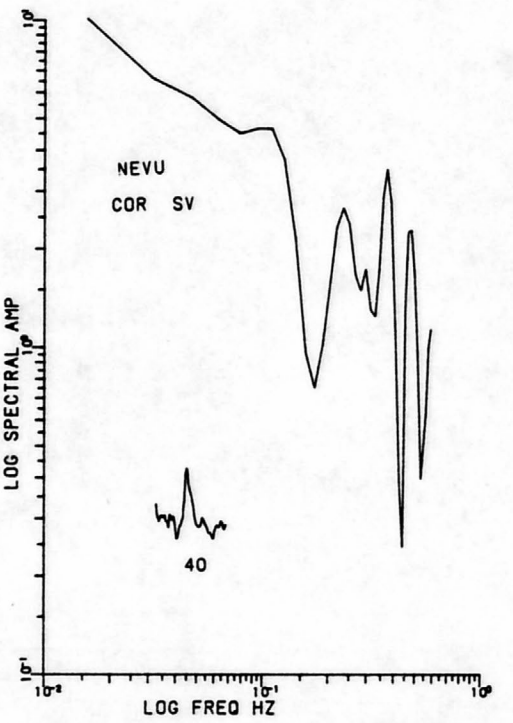
NEVU
COR SV
LOG SPECTRAL AMP
LOG FREQ HZ
40

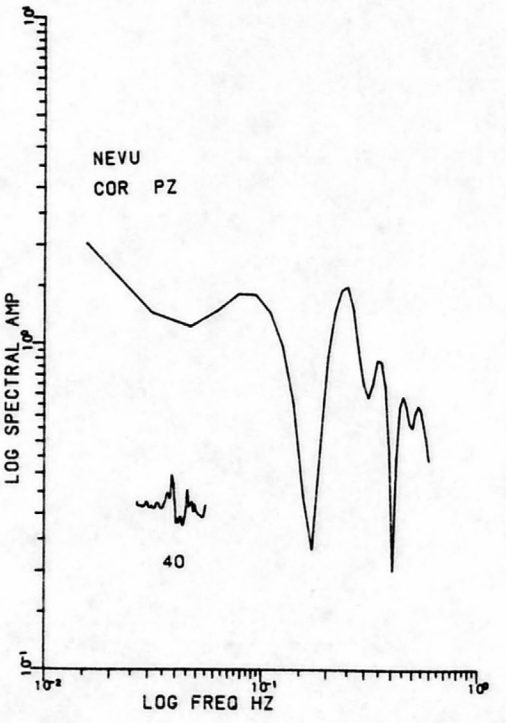
NEVU
COR PZ
LOG SPECTRAL AMP
LOG FREQ HZ
40

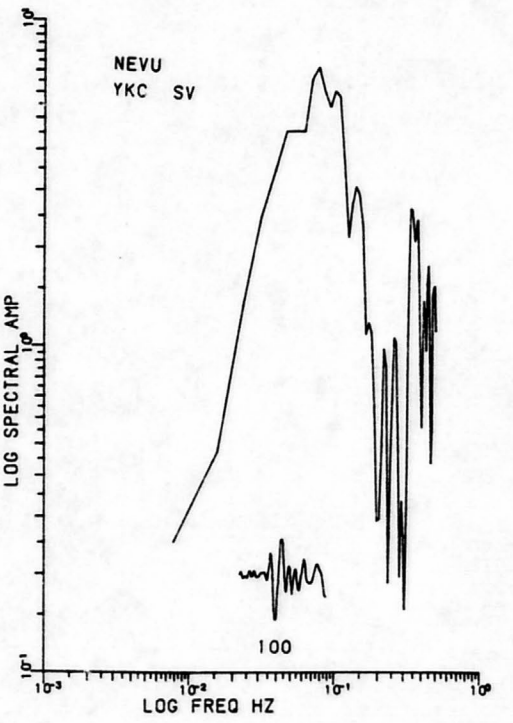
NEVU
YKC SV
LOG SPECTRAL AMP
LOG FREQ HZ
100

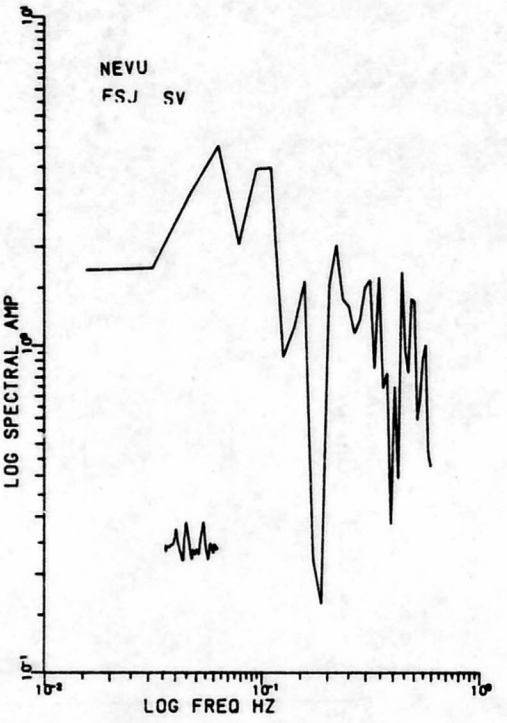
NEVU
FSJ SV
LOG SPECTRAL AMP
LOG FREQ HZ

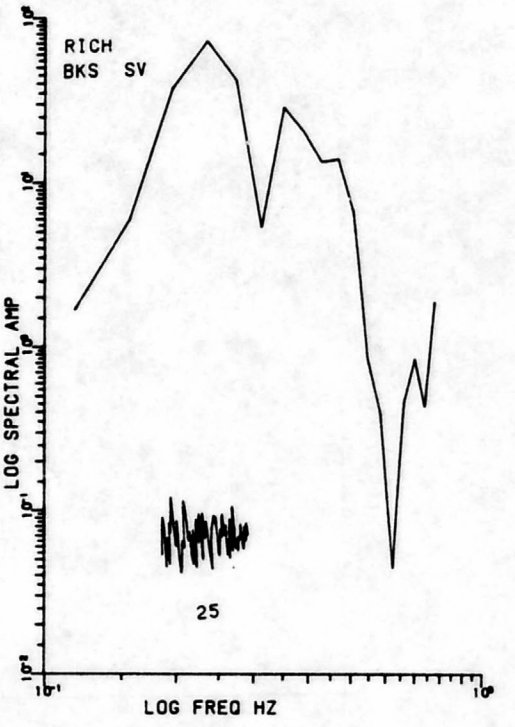
RICH
BKS SV
25
LOG SPECTRAL AMP
LOG FREQ HZ

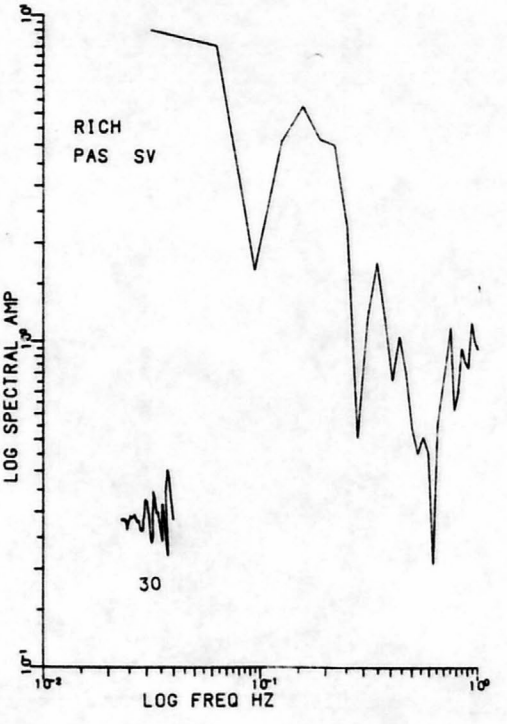
RICH
PAS SV
30
LOG SPECTRAL AMP
LOG FREQ HZ

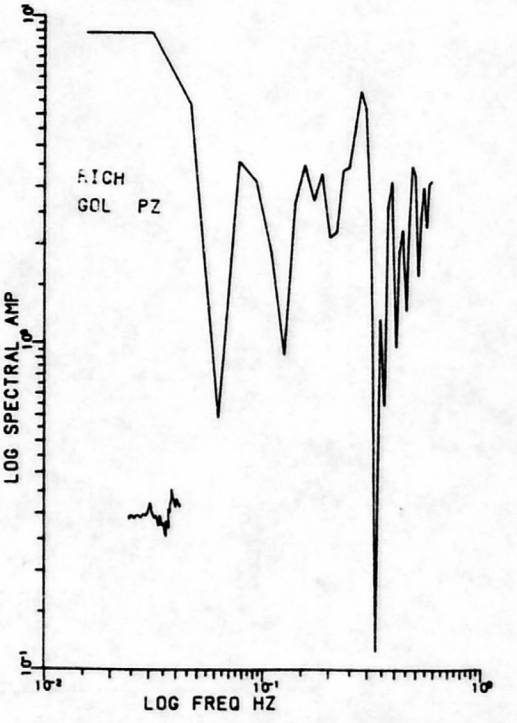
RICH
GOL PZ
LOG SPECTRAL AMP
LOG FREQ HZ

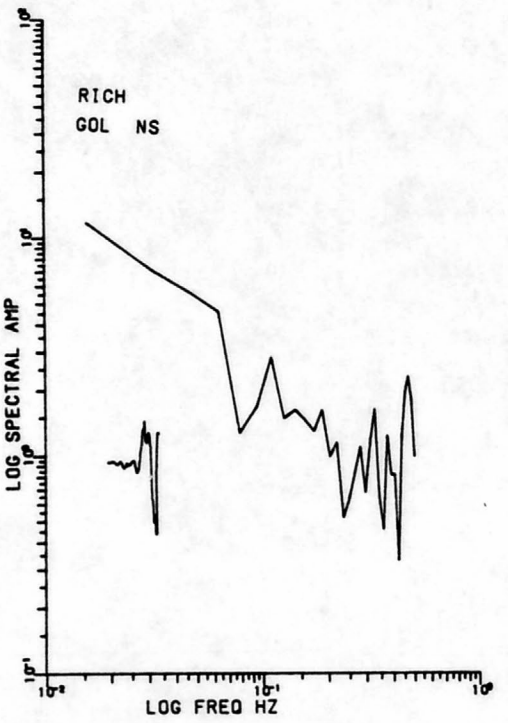
RICH
GOL NS
LOG SPECTRAL AMP
LOG FREQ HZ

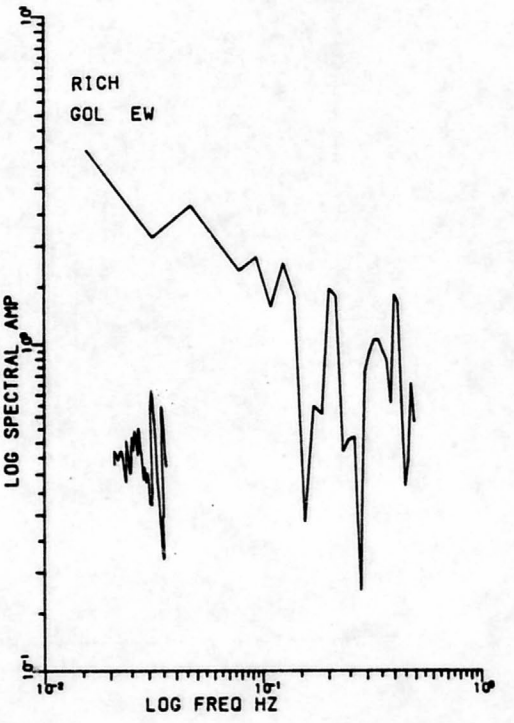
RICH
GOL EW
LOG SPECTRAL AMP
LOG FREQ HZ

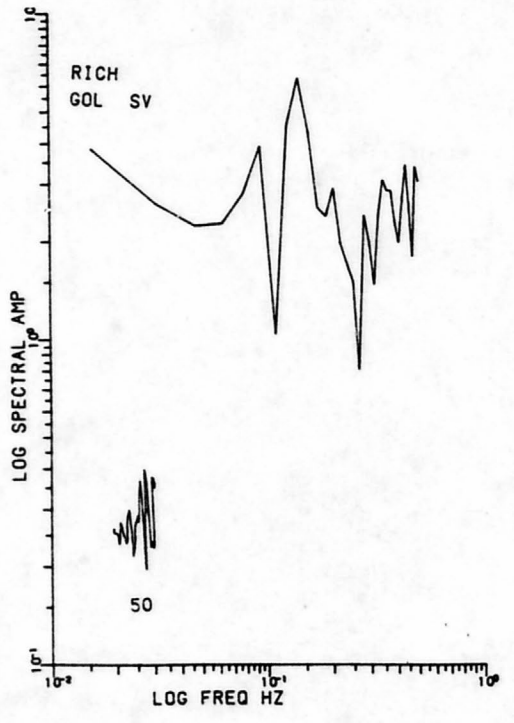
RICH
GOL SV
50
LOG SPECTRAL AMP
LOG FREQ HZ

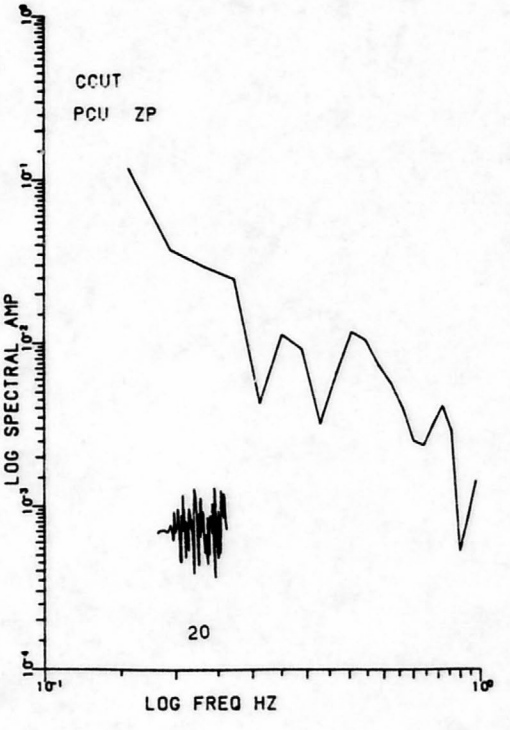
CCUT
PCU ZP
20
LOG SPECTRAL AMP
LOG FREQ HZ

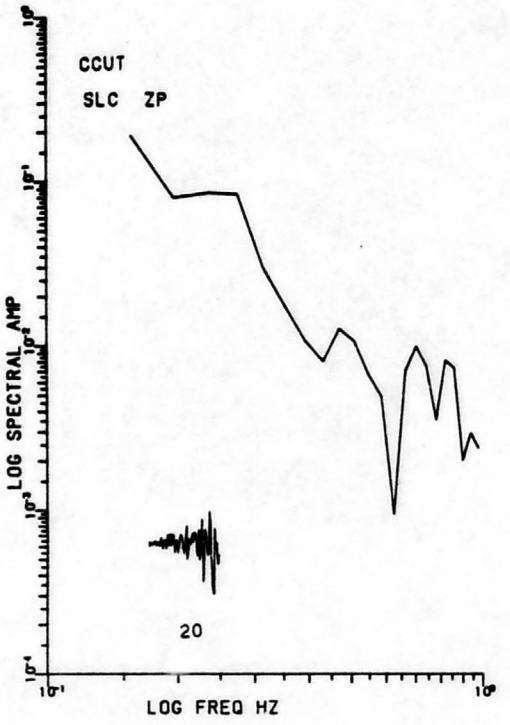
CCUT
SLC ZP
LOG SPECTRAL AMP
LOG FREQ HZ
20

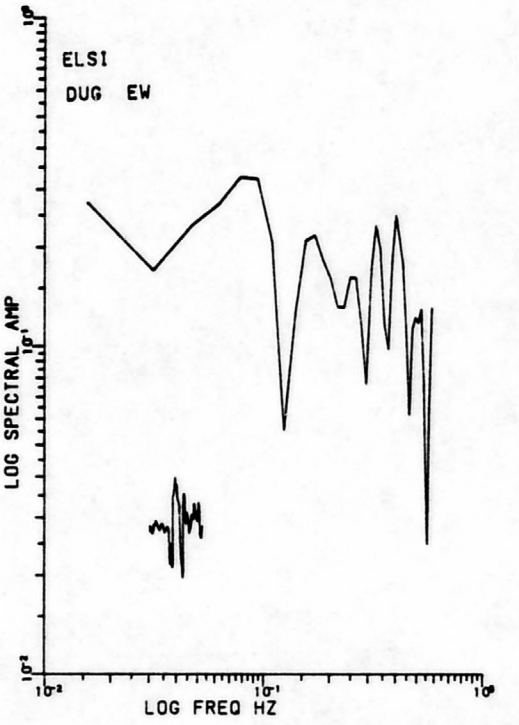
ELSI
DUG EW
LOG SPECTRAL AMP
LOG FREQ HZ

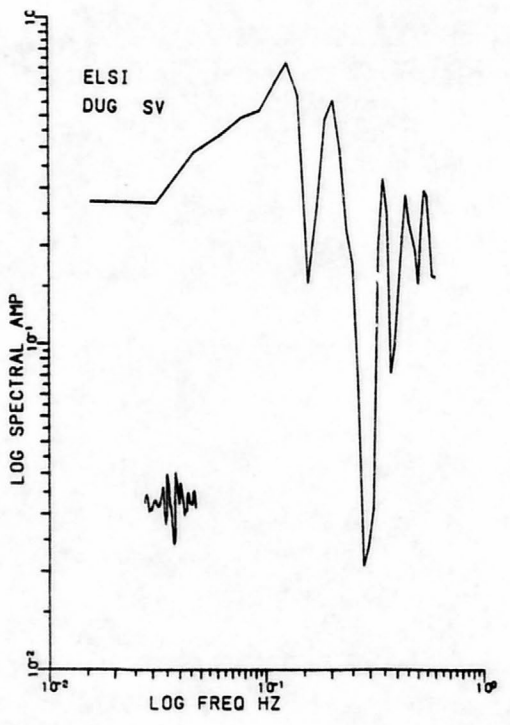
ELSI
DUG SV
LOG SPECTRAL AMP
LOG FREQ HZ

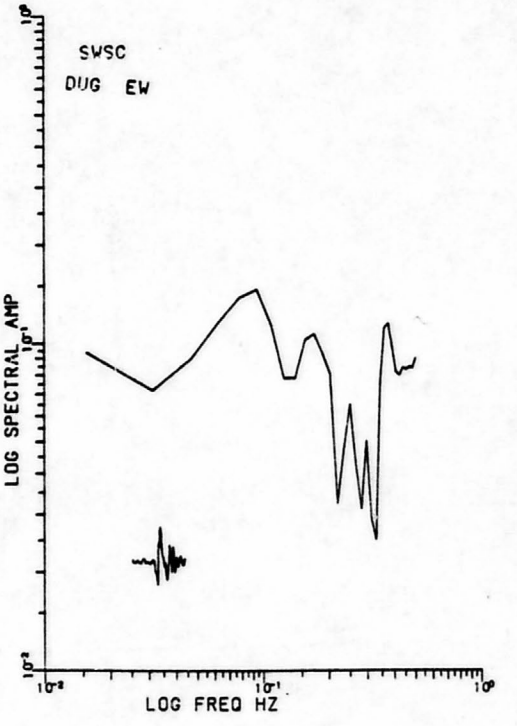
SWSC
DUG EW
LOG SPECTRAL AMP
LOG FREQ HZ

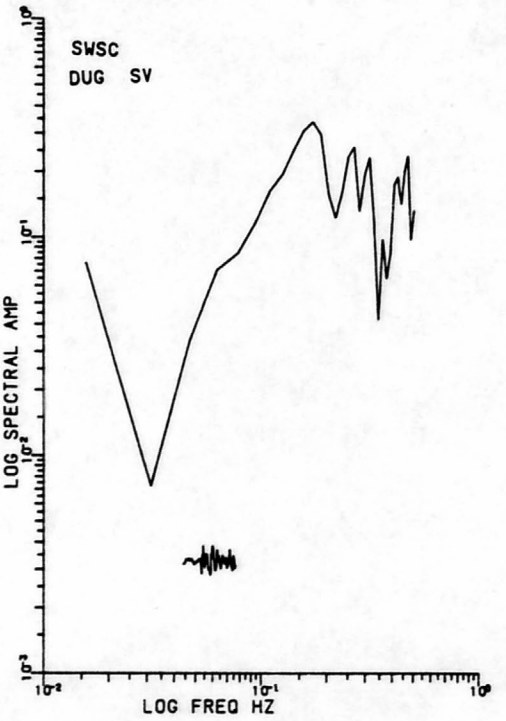
SWSC
DUG SV
LOG SPECTRAL AMP
LOG FREQ HZ

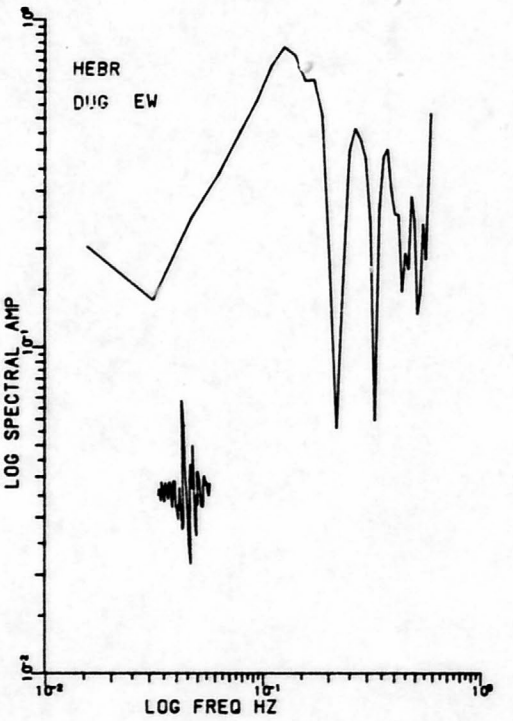
HEBR
DUG EW
LOG SPECTRAL AMP
LOG FREQ HZ

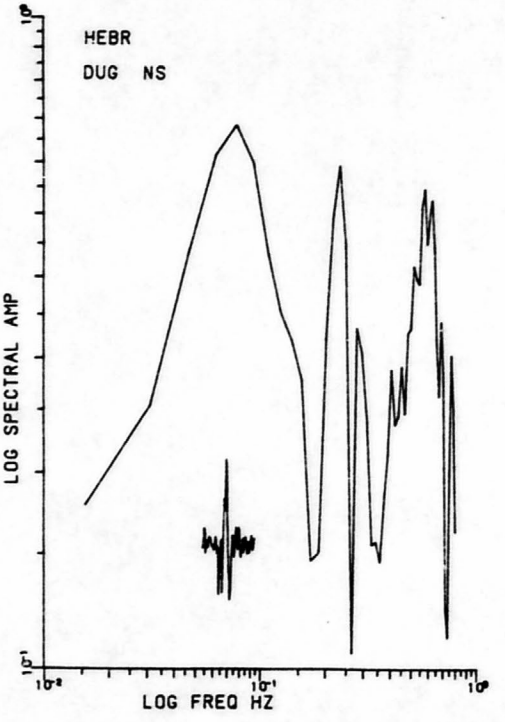
HEBR
DUG NS
LOG SPECTRAL AMP
LOG FREQ HZ

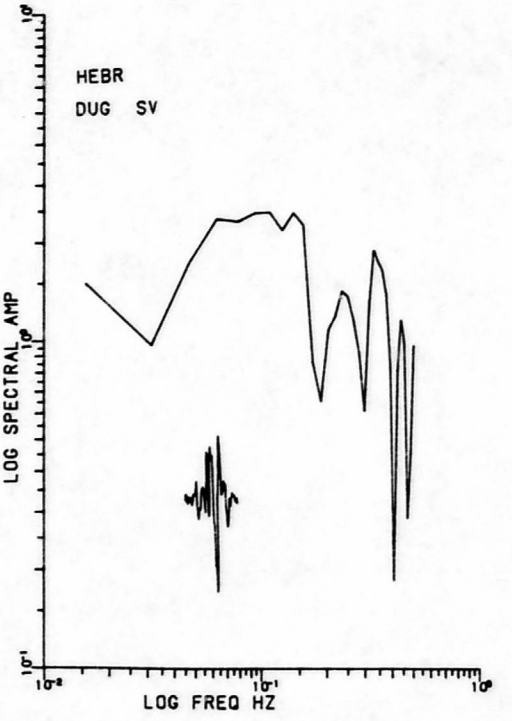
HEBR
DUG SV
LOG SPECTRAL AMP
LOG FREQ HZ

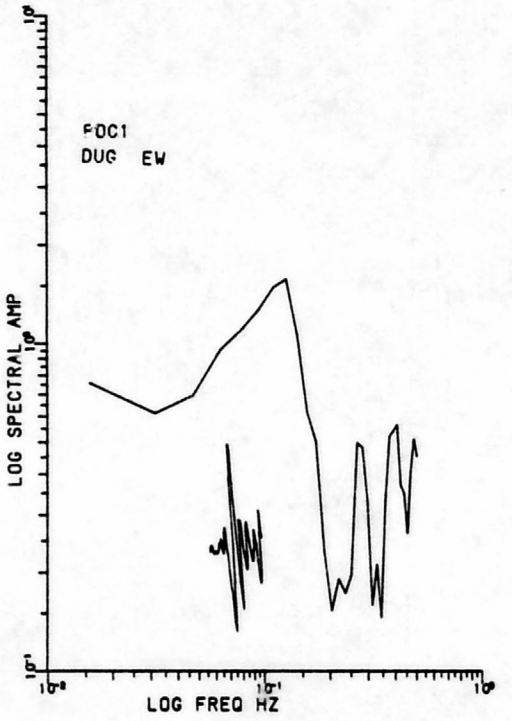
POC1
DUG EW
LOG SPECTRAL AMP
LOG FREQ HZ

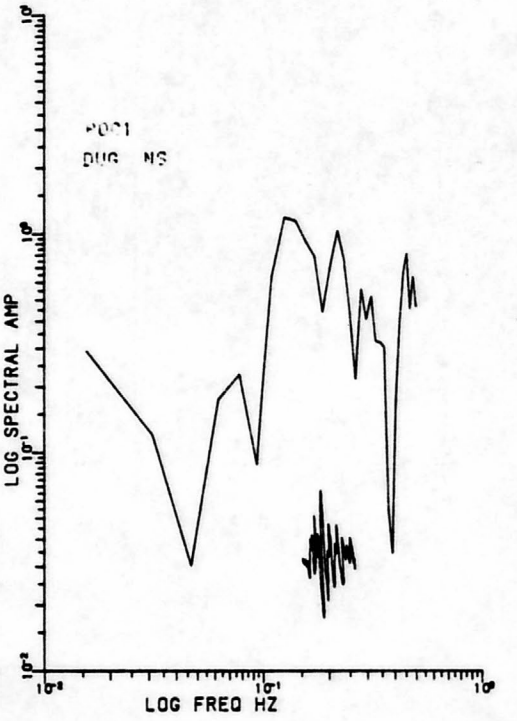
POC1
DUG NS
LOG SPECTRAL AMP
LOG FREQ HZ

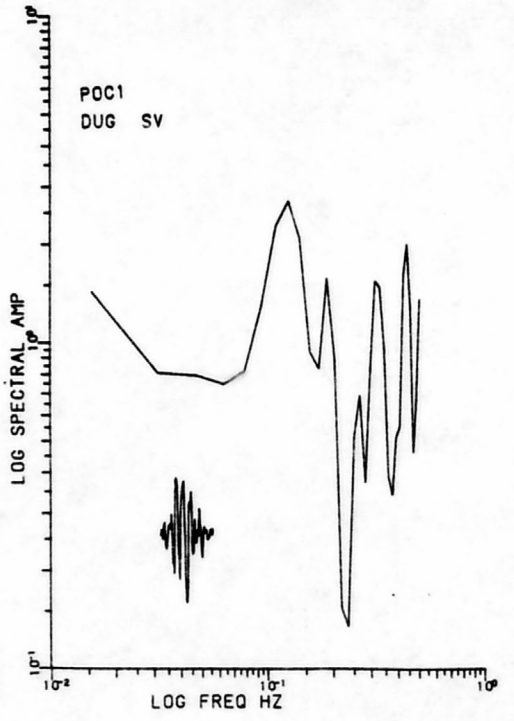
POC1
DUG SV
LOG SPECTRAL AMP
LOG FREQ HZ

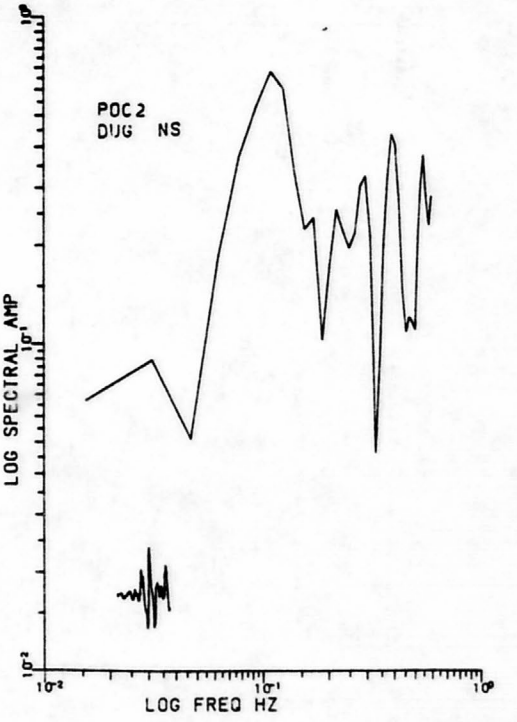
POC2
DUG NS
LOG SPECTRAL AMP
LOG FREQ HZ

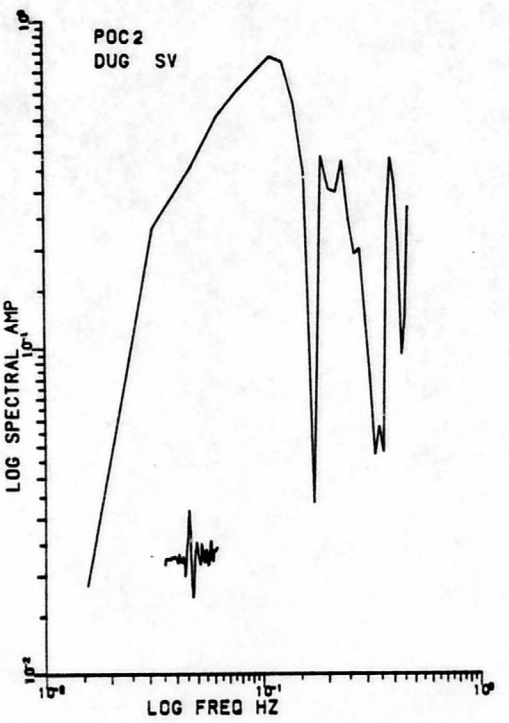
POC2
DUG SV
LOG SPECTRAL AMP
LOG FREQ HZ

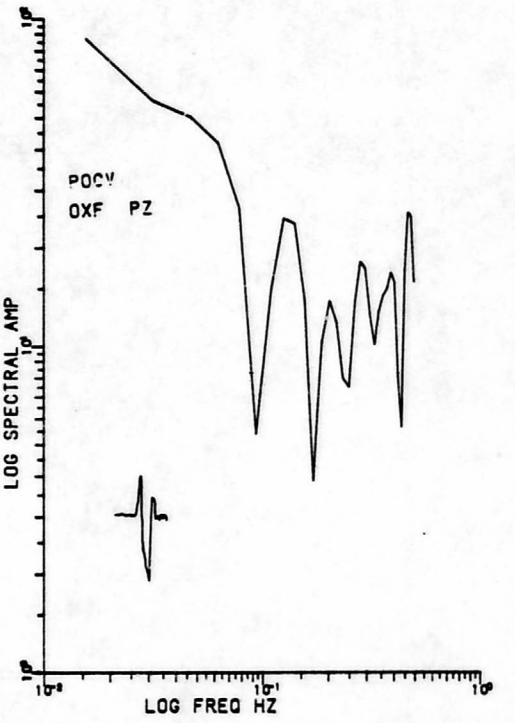
POCV
OXF PZ
LOG SPECTRAL AMP
LOG FREQ HZ

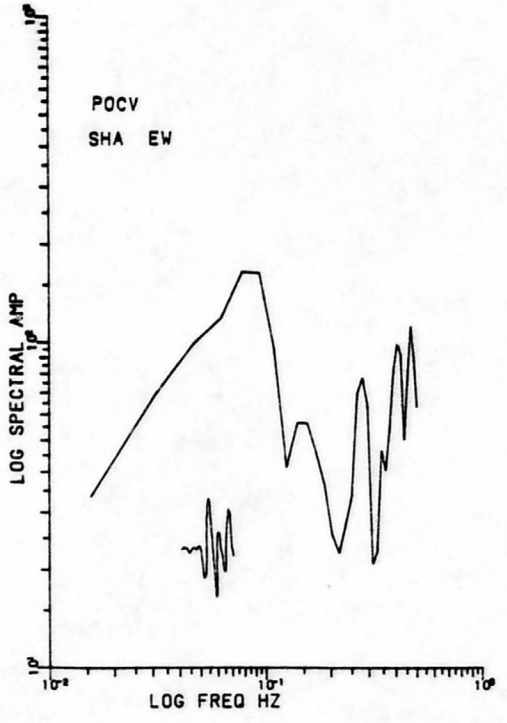
POCV
SHA EW
LOG SPECTRAL AMP
LOG FREQ HZ

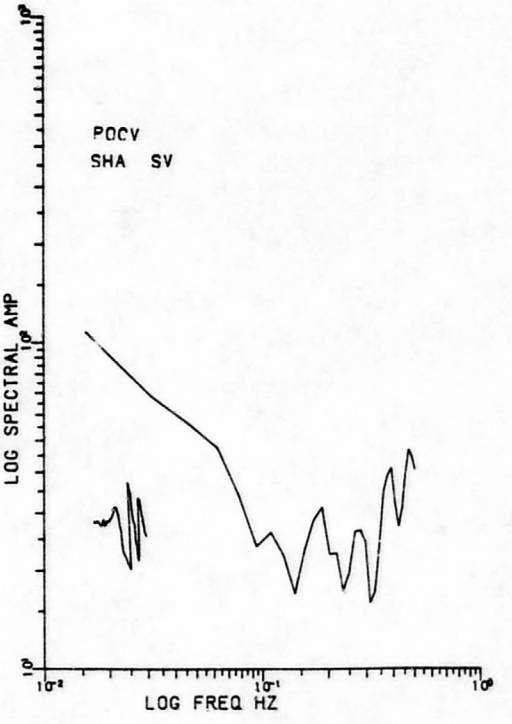
POCV
SHA SV
LOG SPECTRAL AMP
LOG FREQ HZ

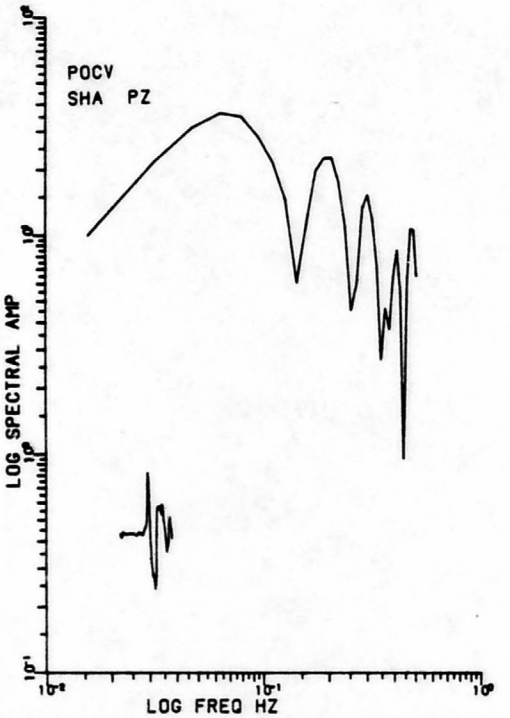
POCV
SHA PZ
LOG SPECTRAL AMP
LOG FREQ HZ

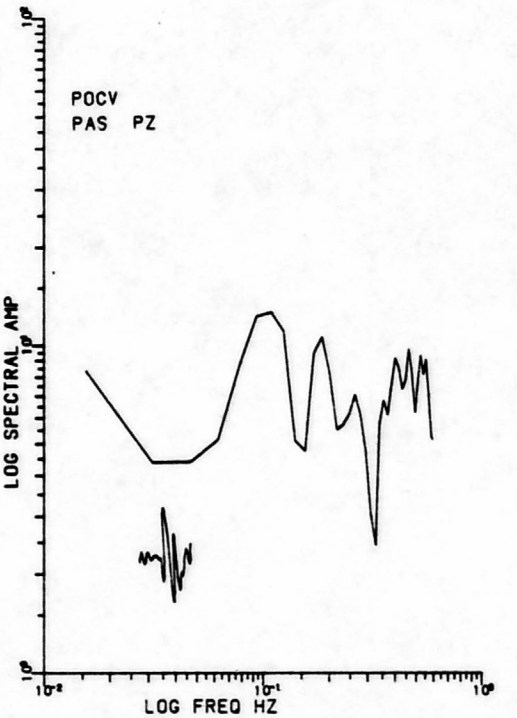
POCV
PAS PZ
LOG SPECTRAL AMP
LOG FREQ HZ

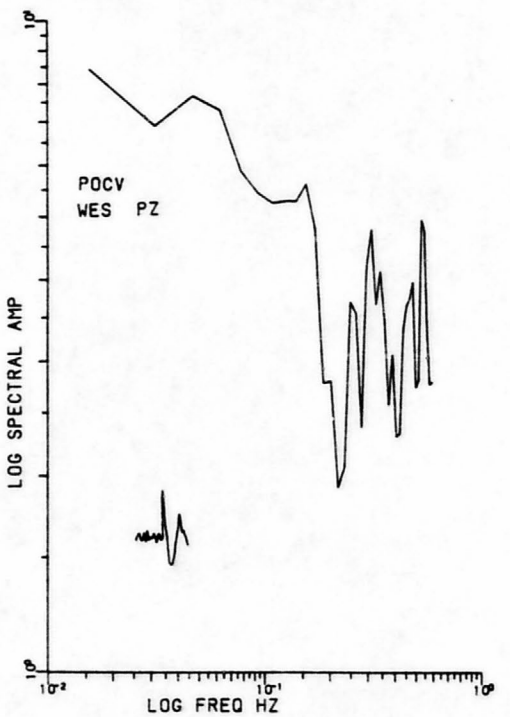
POCV
WES PZ
LOG SPECTRAL AMP
LOG FREQ HZ

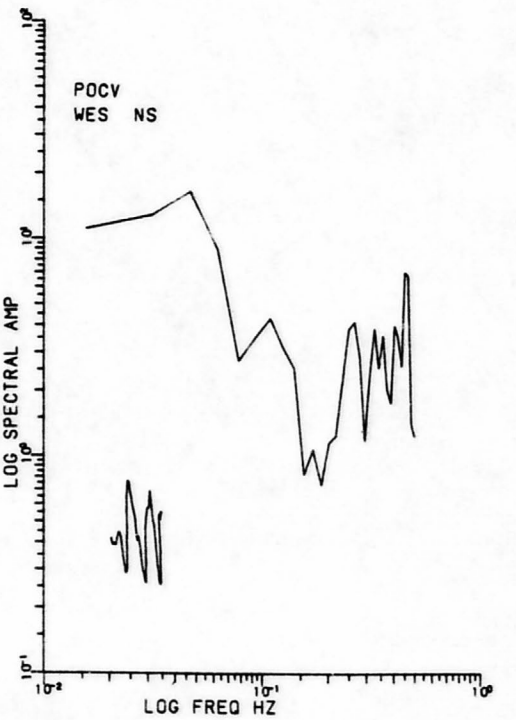
POCV
WES NS
LOG SPECTRAL AMP
LOG FREQ HZ

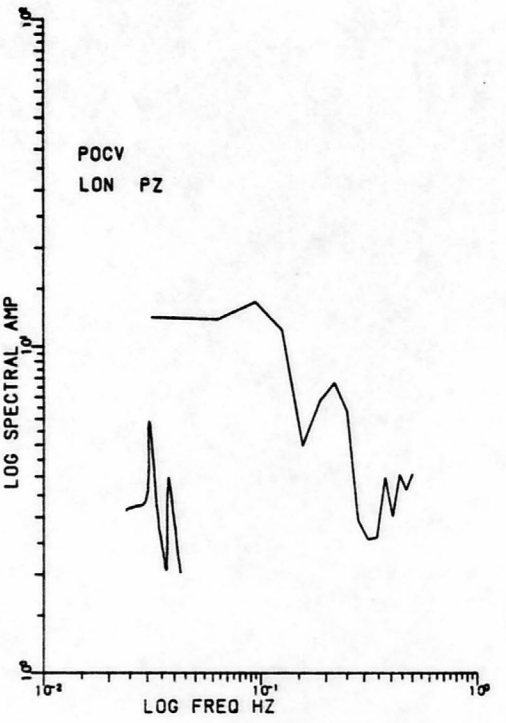
POCV
LON PZ
LOG SPECTRAL AMP
LOG FREQ HZ

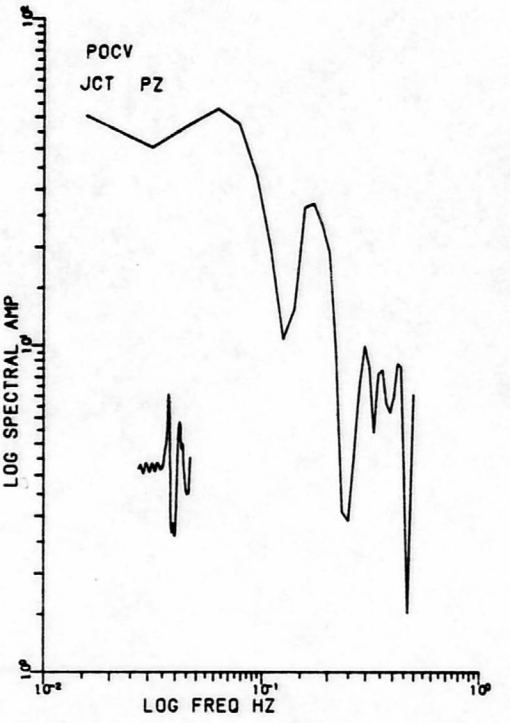
POCV
JCT PZ
LOG SPECTRAL AMP
LOG FREQ HZ

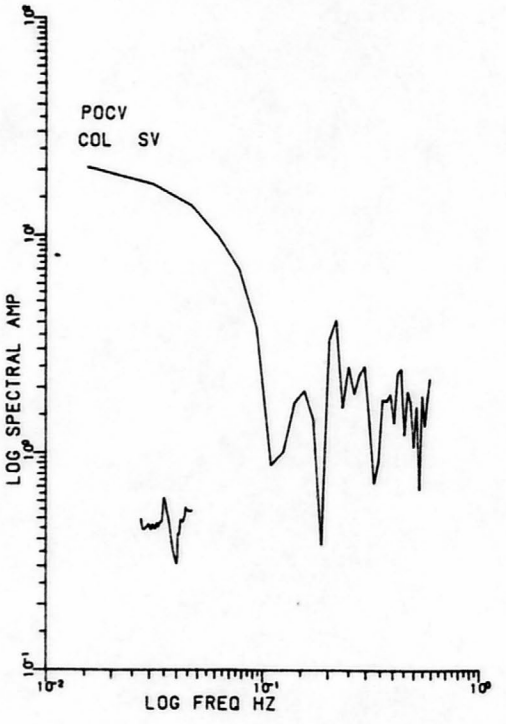
POCV
COL SV
LOG SPECTRAL AMP
LOG FREQ HZ

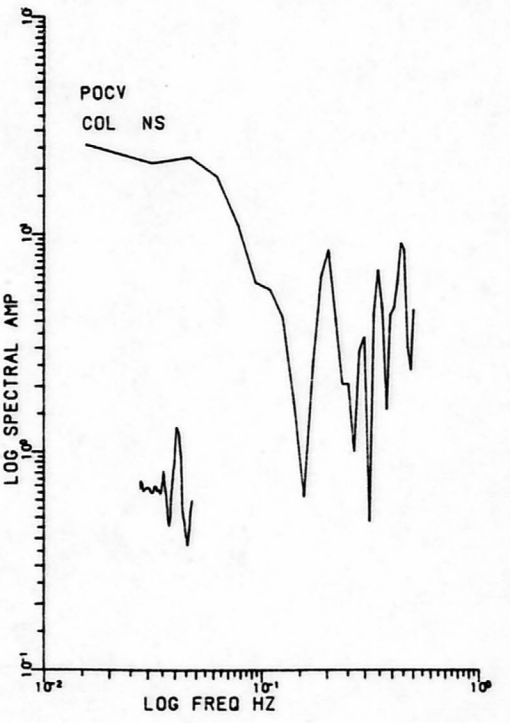
POCV
COL NS
LOG SPECTRAL AMP
LOG FREQ HZ

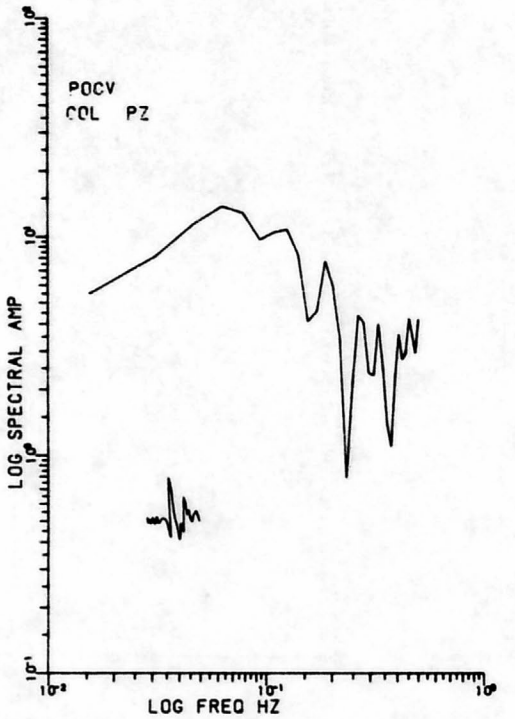
POCV
COL PZ
LOG SPECTRAL AMP
LOG FREQ HZ

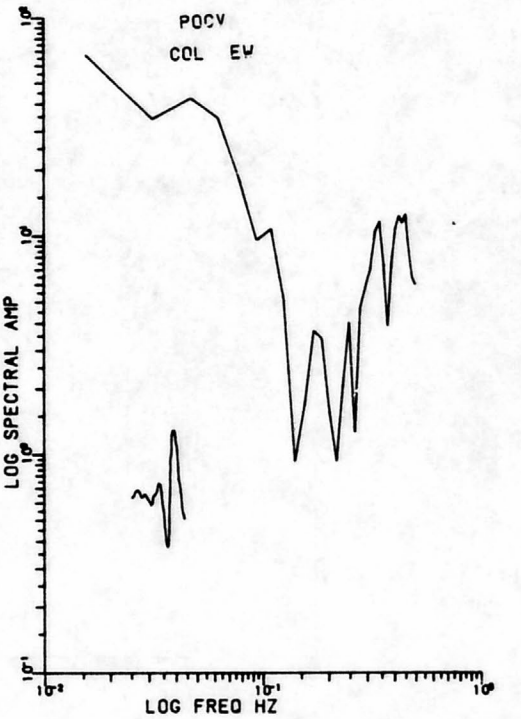
POCV
COL EW
LOG SPECTRAL AMP
LOG FREQ HZ

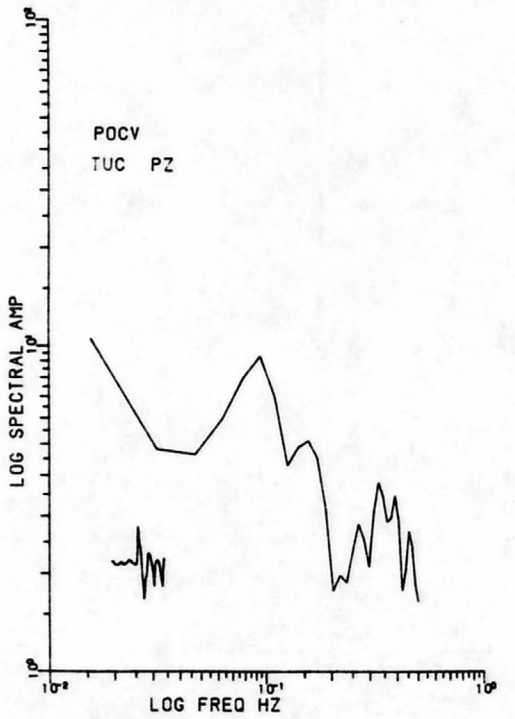
POCV
TUC PZ
LOG SPECTRAL AMP
LOG FREQ HZ

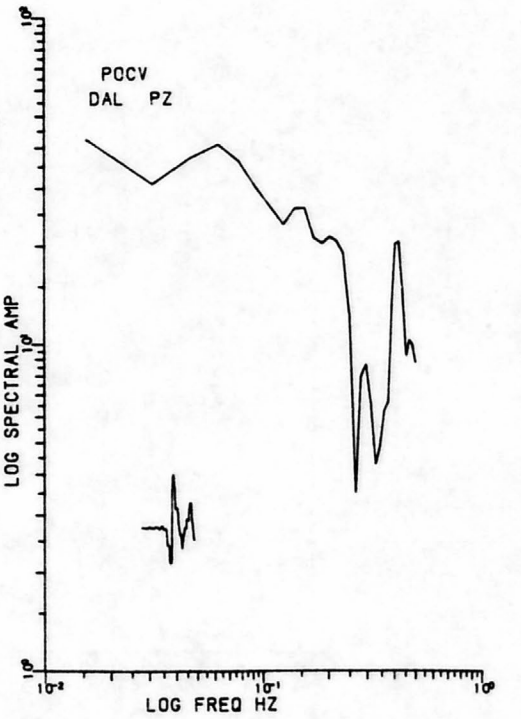
POCV
DAL PZ
LOG SPECTRAL AMP
LOG FREQ HZ

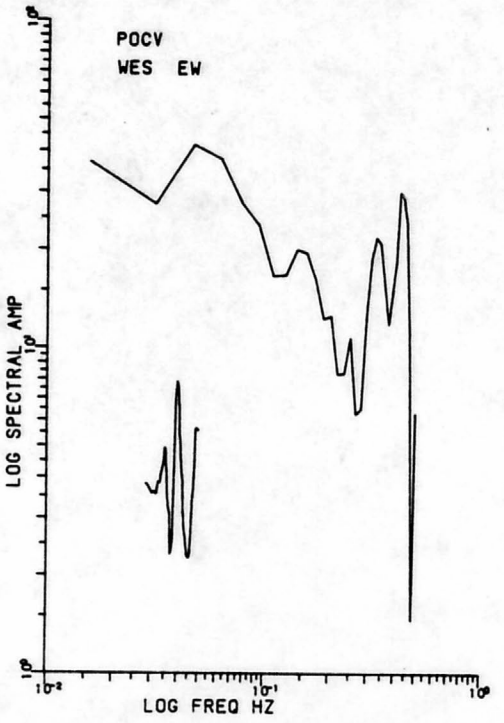
POCV
WES EW
LOG SPECTRAL AMP
LOG FREQ HZ

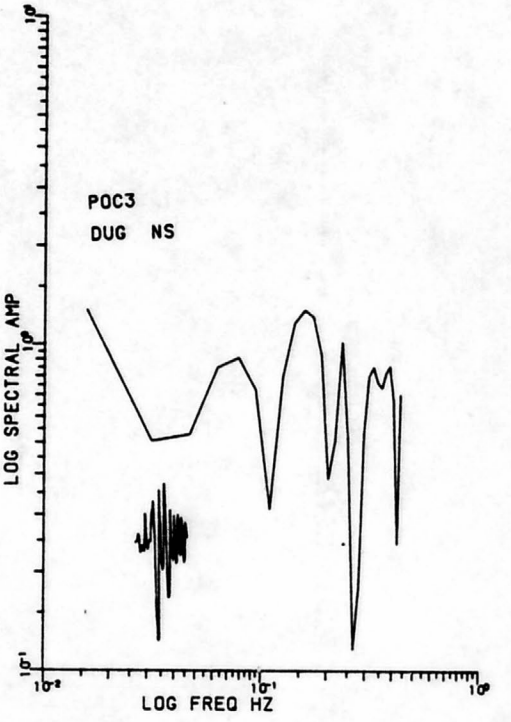
POC3
DUG NS
LOG SPECTRAL AMP
LOG FREQ HZ

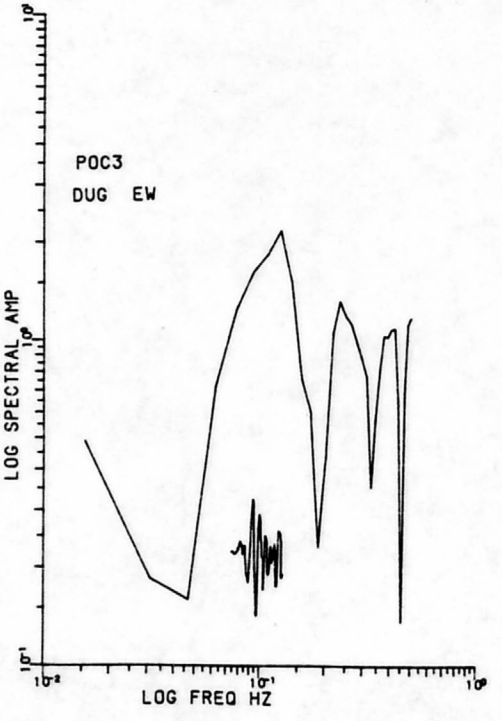
POC3
DUG EW
LOG SPECTRAL AMP
LOG FREQ HZ

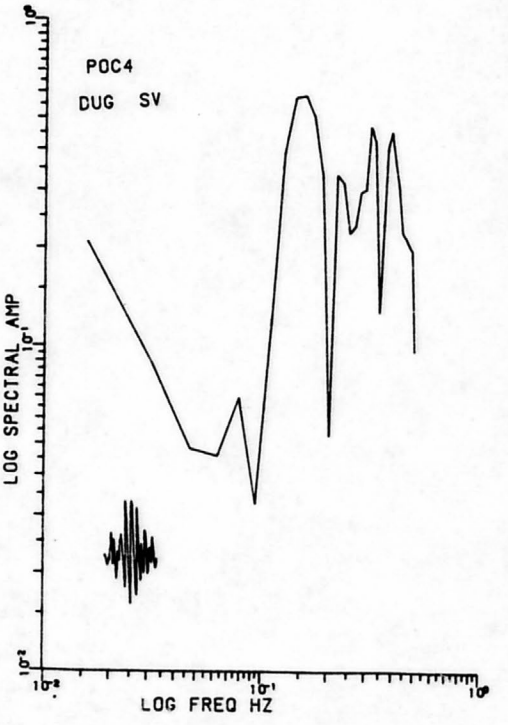
POC4
DUG SV
LOG SPECTRAL AMP
LOG FREQ HZ

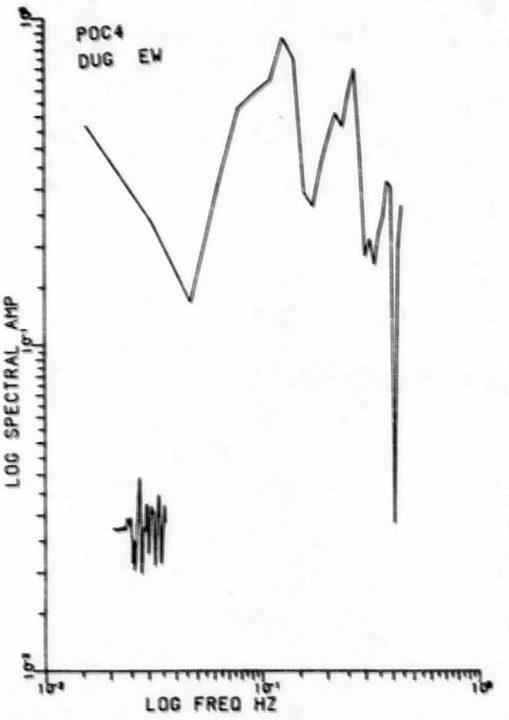
POC4
DUG EW
LOG SPECTRAL AMP
LOG FREQ HZ

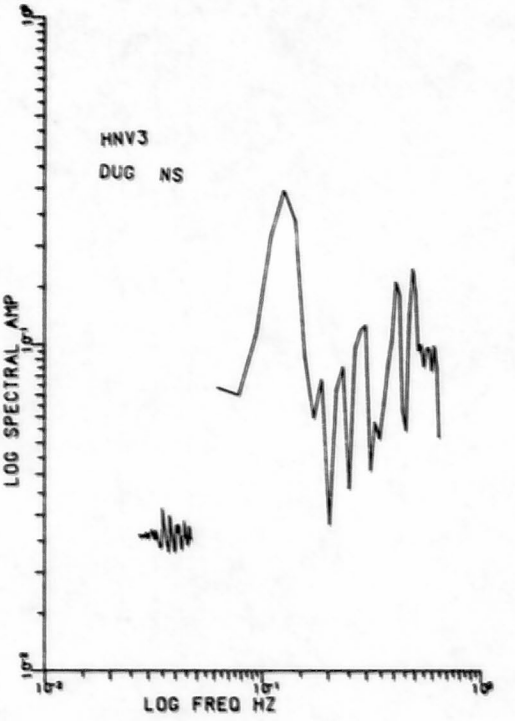
HNV3
DUG NS
LOG SPECTRAL AMP
LOG FREQ HZ

Source Parameters for Utah Events

Event	Station	f_c (hz)	r (km)	$\Delta\sigma$ (bars)
1	BRK(NS)	0.037	39.2	5.8
	BRK(EW)	0.06	24.2	2.2
	PAS(EW)	0.06	24.2	2.8
	PAS(NS)	0.073	19.9	3.7
2	PAS(P)	0.22	9.7	1.9
	PAS(SV)	0.30	4.8	10.3
	PAS(EW)	0.19	7.6	2.6
3	PLM(P)	0.16	12.7	3.0
	PLM(SV)	0.19	7.6	1.2
	BRK(SV)	0.1	14.5	0.57
	BKS(P)	0.26	7.8	2.7
	RCD(P)	0.18	11.3	3.6
4	DUG(SV)	0.27	4.8	0.79
	DUG(NS)	0.3	4.3	1.5
5	BKS(P)	0.2	10.2	0.17
	PAS(SV)	0.45	3.2	0.32
6	DUG(SV)	0.14	10.4	0.043
	DUG(NS)	0.2	7.3	0.65
	DUG(EW)	0.14	10.4	0.23
7	PCU(P)	0.2	5.5	4.2
	DUG(SV)	0.21	6.9	0.16
	DUG(EW)	0.22	6.6	1.4
8	FSJ(SV)	0.11	13.2	0.13
	YKC(SV)	0.16	9.1	0.70
	FSJ(P)	0.14	14.6	0.28
	COR(SV)	0.18	8.1	0.74
	COR(P)	0.25	8.2	1.3
9	PAS(SV)	0.26	5.6	4.0
	BKS(SV)	0.43	3.4	16.7
	GOL(EW)	0.23	6.3	0.70
16	DAL(P)	0.18	11.3	12.1
	COL(P)	0.14	14.6	2.1
	COL(NS)	0.085	17.1	0.73
	COL(EW)	0.08	18.2	0.29
	COL(SV)	0.09	16.1	0.14

Event	Station	f_c (hz)	r (km)	$\Delta\sigma$ (bars)
	LON(P)	0.13	15.7	1.5
	SHA(P)	0.14	14.6	5.0
	JCT(P)	0.14	14.6	3.4
	OXF(P)	0.1	20.4	2.9
	SHA(SV)	0.09	16.1	1.3
	WES(P)	0.15	13.6	1.2
	WES(NS)	0.085	17.1	0.19
	WES(EW)	0.11	13.2	1.5

APPENDIX C

PROGRAM LISTINGS

User's guide to EXSPEC

Purpose: EXSPEC performs a Fourier spectral analysis of a time series of up to 512 points. EXSPEC corrects for radiation pattern, spherical spreading, attenuation, and instrument response. EXSPEC is modifed from a program by R. B. Herrmann (1978)

Program Units

PROGRAM EXSPEC: This is the main program. The program can rotate horizontal components to form the radial and transverse components of ground motion.

SUBROUTINE FOUR2: This subroutine preforms a Cooley-Tukey fourier transform.

SUBROUTINE TREND: This subroutine removes the DC offset from the seismogram.

SUBROUTINE WINDOW: Smooths the seismogram with a Hamming window.

SUBROUTINE CARDIN: This reads in the digitized seismogram. The seismogram must be a series of amplitudes in mm taken at equally spaced data points.

SUBROUTINE INSTRM: This is the main control link for removing instrument response from the spectra. Only the positive frequency components of the spectra have the instrument response removed.

SUBROUTINE SEISM1: This is the response of a 15-100 WWSSN system with magnifications of 275, 750, 1500, 3000, and 6000. The response is removed in the period range between 1 and 200 seconds.

SUBROUTINE SEISM2: This is the response of a 30-100 WWSSN system with magnifications of 375, 750, 1500, 3000, and 6000. Again, the instrument response is removed only in the range of 1 to 200 seconds.

SUBROUTINE SEISM4: Reads in tabulated displacement or velocity sensitivity curves. If velocity sensitivity is read in it is converted to displacement sensitivity. No correction for phase response can be made.

SUBROUTINE SEISM5: This is the instrument response of a standard Wood-Anderson torsion seismometer with $T_0 = 0.8$.

SUBROUTINE SEISM8: Accepts the constants for a seismometer-galvonometer system which are used to correct the data for instrument response.

SUBROUTINE PRIN: Lists the frequency, period and amplitude data for a spectrum and plots the spectrum on a log-log plot. The spectrum is plotted on the CALCOMP plotter.

Input data

Card	Column	Name	Format	Explanation
1	1-3	NUMPL	I3	Number of plot desired
For each event the following cards are needed:				
A	1-4	M	I4	Number of points in fast fourier transform (power of 2) maximum is M=512
	5-8	ICONT	I4	Instrument response option
				1 WWSSN 15-100 system
				2 WWSSN 30-100 system
				3 tabulated displacement or velocity sensitivity
				4 Wood-Anderson seismometer
				5 Accepts constant for Hagiwara's equation

Card	Column	Name	Format	Explanation
	9-12	IDATA	I4	1 one component read in 2 EW read first followed by NS E and N are positive. Both seismograms must have the same starting time and DT. Transverse component is positive clockwise about source. Radial component is positive away from source
B	1-4	STA	A4	Station name
	5-8	COMP	A4	Component
	9-18	DIST	F10.5	Station distance from epicenter in km
	19-28	DEG	F10.5	Station distance from epicenter in degrees
	29-38	DT	F10.5	Sampling interval
	39-48	PEAK	F10.5	Peak response of instrument
C	1-4	EVENT	A4	Event name
	5-14	RP	F10.5	Radiation pattern value
	15-24	V	F10.5	Velocity of body wave
	25-34	BAZ	F10.5	Backazimuth measured clockwise from north
	35-44	RQ	F10.5	Attenuation factor
	45-54	F1	F10.5	Desired beginning frequency for plot
	55-64	F2	F10.5	Desired end frequency for plot
Format for digitized data				
		DUMMY(I)	F(F6.2)	Digitized equispaced data (end of trace signified by 99.00). Data must be in mm.

Card	Column	Name	Format	Explanation
Instrument response options:				
If ICONT =3				
First card	1-5	N	I5	Number of responses to be read in If N<0 velocity sensitivity read in If N>0 displacement sensitivity read in
N/4 cards		(PER(I), RESP(I))	8F10.5	PER=period listed in order of increasing period RESP=velocity or displacement sensitivity
If ICONT=5 instrument card is:				
	1-10	TS	F10.5	Seismometer natural period
	11-20	HS	F10.5	Seismometer damping factor
	21-30	TG	F10.5	Galvonometer natural period
	31-40	HG	F10.5	Galvonometer damping factor
	41-50	SIGMA	F10.5	Coupling factor σ^2

```
C          EXSPEC IS A MODIFIED VERSION OF A PROGRAM BY R. HERRMANN
C         IN COMPUTER PROGRAMS IN EARTHQUAKE SEISMOLOGY
C         EXSPEC PERFORMS A FOURIER SPECTRAL ANALYSIS ON
C         DIGITIZED DATA AND CORRECTS FOR RADIATION PATTERN,
C         SPHERICAL SPREADING,ATTENUATION AND INSTRUMENT RESPONSE
C         EXSPEC WINDOWS THE DATA AND REMOVES THE MEAN BEFORE
C         TRANSFORMING IT
C         THE SPECTRUM IS PLOTTED ON A LOG-LOG PLOT
C          THE SPECTRAL AMPLITUDE PLOTTED BY EXSPEC IS ACTUALLY
C          THE AMPLITUDE*DISTANCE/RADIATION PATTERN
C
C         NUMPL=NUMBER OF PLOTS TO BE GENERATED
C         M=NUMBER OF POINTS IN FAST FOURIER TRANSFORM, MUST BE
C         A POWER OF TWO
C         ICONT IS USED TO CHOOSE INSTRUMENT RESPONSE OPTION
C              1=15-100 WWSSN SYSTEM
C              2=30-100 WWSSN SYSTEM
C              3=ACCEPTS TABULATED VELOCITY OR DISPLACEMENT RESPONSES
C              4=WOOD-ANDERSON TORSION SEISMOMETER
C              5=ACCEPTS CONSTANTS FOR HAGIWARA'S EQUATION
C         IDATA IS THE OPTION FOR PROCESSING DATA
C              1=ONE COMPONENT READ IN
C              2=EW READ FIRST FOLLOWED BY NS, COMPUTES RADIAL AND
C              TRANSVERSE COMPONENTS
C         STA=STATION NAME
C         COMP=COMPONENT OF STATION
C         DIST=STATION DISTANCE TO EPICENTER IN KM
C         DEG=STATION DISTANCE TO EPICENTER IN DEGREES
C         DT=DIGITIZING INTERVAL USED
C         PEAK=PEAK RESPONSE OF INSTRUMENT
C         EVENT=EVENT NAME
C         RP=RADIATION PATTERN VALUE
C         V=VELOCITY OF BODY WAVE
C         RQ=DESIRED ATTENUATION FACTOR
```

```
C          BAZ=BACKAZIMUTH FROM STATION TO EPICENTER MEASURED CLOCKWISE
C          FROM NORTH
C          F1=DESIRED BEGINNING FREQUENCY FOR PLOT
C          F2=DESIRED END FREQUENCY FOR PLOT
C
C
      DIMENSION DATA (1024),DUMMY(512),DATUM(512)
      READ (5,15) NUMPL
15    FORMAT(I3)
      DIM=FLOAT(NUMPL)*8.
      CALL IDPLOT (DIM,9.0)
      CALL CALOPR('#4 PEN, BLACK INK FOR THIS PLOT, PLEASE',39,.TRUE.)
      IF (IDATA.EQ.2) NUMPL=NUMPL/2
      DO 300 LLL=1,NUMPL
      READ (5,10) M,ICONT,IDATA
10    FORMAT(3I4)
      N=M
      N2=N*2
      ND2=N/2
      DO 100 ITYPE=1,IDATA
      READ (5,25) STA,COMP,DIST,DEG,DT,PEAK
25    FORMAT(2A4,4F10.5)
      READ (5,30) EVENT,RP,V,BAZ,RQ,F1,F2
30    FORMAT(A4,6F10.5)
      WRITE (6,21) EVENT
21    FORMAT (1X,A4)
C           READ IN THE DATA CARDS
      CALL CARDIN(DUMMY,NPTS)
C         REMOVE THE MEAN FROM THE DATA
      CALL TREND (DUMMY,NPTS)
      DO 40 I=1,NPTS
C         CORRECT FOR SPHERICAL SPREADING
      DUMMY(I)=DUMMY(I)*DIST*.1
40    CONTINUE
```

```
C          WINDOW THE DATA
      CALL WINDOW (DUMMY,NPTS)
      DO 45 I=1,N2
      DATA(I)=0.0
45    CONTINUE
      DO 50 I=1,NPTS
      J=2*I-1
      DATA(J)=DUMMY(I)
50    CONTINUE
C          TRANSFORM THE DATA
      CALL FOUR2 (DATA,N,1,-1)
      DF=1./(N*DT)
      DO 55 I=1,N
      DATA(I)=DATA(I)*DT
55    CONTINUE
C          CORRECT FOR INSTRUMENT RESPONSE
      CALL INSTRM(DATA,N,DF,PEAK,ICONT)
      IF (ITYPE.EQ.IDATA) GO TO 100
      DO 124 I=1,N
124   DATUM(I)=DATA(I)
100   CONTINUE
      IF (IDATA.NE.2) GO TO 200
C          IF ICONT=2 COMPUTES RADIAL AND TRANSVERSE COMPONENTS
      BAZ=BAZ*.0174533
      A=SIN(BAZ)
      B=COS(BAZ)
      DO 160 I=1,N
      RADIAL=-DATA(I)*B-DATUM(I)*A
      TRANS=DATA(I)*A-DATUM(I)*B
      DATA(I)=TRANS
160   DATUM(I)=RADIAL
200   RN=N
      IF (IDATA.NE.2) GO TO 65
C          PLOT THE SPECTRUM AND PRINT OUT SPECTRAL INFORMATION
```

```
      CALL PRIN(DATUM,ND2,STA,COMP,DIST,DEG,BAZ,DT,RQ,V,RP,F1,F2)
65    CALL PRIN(DATA,ND2,STA,COMP,DIST,DEG,BAZ,DT,RQ,V,RP,F1,F2)
300   CONTINUE
      CALL FINI
      STOP
      END



C           CARDIN READS IN THE DIGITIZED DATA IN A 5F6.2 FORMAT
C           DATA SET MUST BE TERMINATED BY A 99.00
C           THE DATA MUST BE EQUALLY SPACED AND IN UNITS OF MM
C           UP TO 512 POINTS CAN BE READ IN THROUGH THIS SUBROUTINE
C
      SUBROUTINE CARDIN (DUMMY,NPTS)
      DIMENSION DUMMY(1)
      DO 910 I=1,512,5
      J=I+4
      READ (5,911) (DUMMY(K),K=I,J)
      WRITE (6,919) (DUMMY(K),K=I,J)
919   FORMAT(1X,5(F6.2,1X))
911   FORMAT(5F6.2)
      DO 910 K=I,J
      IF (DUMMY(K)-99.) 910,912,912
910   CONTINUE
912   NPTS=K-1
      WRITE (6,909) NPTS
909   FORMAT(1X,'NPTS= ',I5)
      RETURN
      END



C           TREND FINDS THE MEAN OF THE DIGITIZED DATA AND SUBTRACTS
```

```
C           IT FROM THE DATA
C
      SUBROUTINE TREND (X,NPTS)
      DIMENSION X(1)
      SUM=0.0
      DO 1 I=1,NPTS
      SUM=SUM+X(I)
1     CONTINUE
      DC=SUM/FLOAT(NPTS)
      DO 2 I=1,NPTS
2     X(I)=X(I)-DC
      WRITE(6,5) DC
5     FORMAT(1X,'DC= ',E11.4)
      RETURN
      END



C           WINDOW USES A HAMMING WINDOW TO WINDOW THE DIGITIZED DATA
C           BEFORE TRANSFORMING IT
C
      SUBROUTINE WINDOW(DUMMY,NPTS)
      DIMENSION DUMMY(1)
      LX1=NPTS-1
      PI=3.141592654
      PI2=2.*PI
      CON=PI2/FLOAT(LX1)
      DO 200 I=1,NPTS
      II=I-1
      IF (I.GT.LX1) GO TO 200
      DUMMY(I)=DUMMY(I)*(.54-.46*COS(CON*II))
200   IF (I.GT.LX1) DUMMY(I)=0.0
      RETURN
      END
```

```
C           COOLEY TOOKEY FAST FOURIER TRANSFORM
C           DATA IS A ONE DIMENSIONAL COMPLEX ARRAY (THE REAL AND
C           IMAGINARY PARTS OF THE DATA ARE LOCATED IMMEDIATELY
C           ADJACENT IN STORAGE)
C           ISIGN=1, FORWARD TRANSFORM
C
      SUBROUTINE FOUR2(DATA,NN,IDUM,ISIGN)
      DIMENSION DATA(1)
      N=2*NN
      IF (ISIGN.EQ.-1) GO TO 1002
       DO 1001 IIII=1,N
1001  DATA(IIII)=DATA(IIII)/FLOAT(NN)
1002  CONTINUE
      J=1
      DO 5 I=1,N,2
      IF (I-J) 1,2,2
1     TEMPR=DATA(J)
      TEMPI=DATA(J+1)
      DATA(J)=DATA(I)
      DATA(J+1)=DATA(I+1)
      DATA(I)=TEMPR
      DATA(I+1)=TEMPI
2     M=N/2
3     IF (J-M)5,5,4
4     J=J-M
      M=M/2
      IF (M-2)5,3,3
5     J=J+M
      MMAX=2
6     IF(MMAX-N)7,10,10
7     ISTEP=2*MMAX
      THETA=6.28185307/FLOAT(ISIGN*MMAX)
```

```
      SINTH=SIN(THETA/2.)
      WSTPR=-2.*SINTH*SINTH
      WSTPI=SIN(THETA)
      WR=1.0
      WI=0.0
      DO 9 M=1,MMAX,2
      DO 8 I=M,N,ISTEP
      J=I+MMAX
      TEMPR=WR*DATA(J)-WI*DATA(J+1)
      TEMPI=WR*DATA(J+1)+WI*DATA(J)
      DATA(J)=DATA(I)-TEMPR
      DATA(J+1)=DATA(I+1)-TEMPI
      DATA(I)=DATA(I)+TEMPR
8     DATA(I+1)=DATA(I+1)+TEMPI
      TEMPR=WR
      WR=WR*WSTPR-WI*WSTPI+WR
9     WI=WI*WSTPR+TEMPR*WSTPI+WI
      MMAX=ISTEP
      GO TO 6
10    RETURN
      END



C           INSTRM CORRECTS FOR THE INSTRUMENT RESPONSE DESIGNATED
C           BY ICONT
C           BOTH AMPLITUDE AND PHASE CHARACTERISTICS OF THE INSTRUMENT
C           RESPONSE ARE CONSIDERED EXCEPT WHEN ICONT=3
C
      SUBROUTINE INSTRM(X,NN,DF,PEAK,ICONT)
      COMMON/INSI/MAGIN,NP,PER(100),RESP(100)
      COMMON/HAGI/TS,TG,HS,HG,SIGMA,PK,FPK
      DIMENSION X(1)
      MAGIN=0
```

```
      X(1)=0.0
      X(2)=0.0
      NN2=NN/2
      DO 10 I=2,NN2
      XI=I-1
      FREQ=XI*DF
      J=2*I-1
      K=2*I
      GO TO (1,2,3,4,5),ICONT
1     CALL SEISM1(FREQ,PEAK,XR,XI)
      GO TO 7
2     CALL SEISM2(FREQ,PEAK,XR,XI)
      GO TO 7
3     CALL SEISM4(FREQ,PEAK,XR,XI)
      GO TO 7
4     CALL SEISM5(FREQ,PEAK,XR,XI)
      GO TO 7
5     CALL SEISM8(FREQ,XR,XI)
7     CONTINUE
      TEMPR=XR*X(J)-XI*X(K)
      TEMPI=XR*X(K)+XI*X(J)
      X(J)=TEMPR
10    X(K)=TEMPI
      IF (ICONT.LT.5) RETURN
C           NORMALIZATION FOR HAGIWARA'S EQUATION
      PK=SQRT(PK)
      FAC=PK/PEAK
      DO 20 I=2,NN2
      J=2*I-1
      K=2*I
      X(J)=FAC*X(J)
      X(K)=FAC*X(K)
20    CONTINUE
      WRITE (6,30) TS,TG,HS,HG,SIGMA,PK,FPK
```

```
30    FORMAT(1X,'HAGIWARAS EQUATION',' TS=',F10.2,' TG=',F10.2,' HS=',
     1F10.2,' HG=',F10.2,' SIGMA=',F6.3,' PK=',E10.3,' AT',E10.3,' HZ')
      RETURN
      END



C          15-100 WWSSN SYSTEM, INSTRUMENT CONSTANTS FROM U. CHANDRA
C          BSSA 1970 VOL 60  PP 539-563
C
      SUBROUTINE SEISM1 (FREQ,PEAK,XR,XI)
      IF (FREQ.GT.1.0) FREQ=1.0
      IF (FREQ.LT.0.005) FREQ=0.005
      WE=6.2831853*FREQ
      INDEX=(PEAK+1.)/375.
      GO TO (1,2,2,3,3,3,3,4,4,4,4,4,4,4,4,5),INDEX
1     FMAG=278.
      SIGMA=.003
      GO TO 6
2     FMAG=556.
      SIGMA=0.013
      GO TO 6
3     FMAG=1110.
      SIGMA=0.047
      GO TO 6
4     FMAG=2190.
      SIGMA=0.204
      GO TO 6
5     FMAG=3950.
      SIGMA=.805
6     ZETA=.93
      ZETA1=1.
      WN=.418879
      WN1=.062831853
```

```
      AR=(WE*WE-WN*WN)*(WE*WE-WN1*WN1)-4.*ZETA*ZETA1*WN*WN1*(1.-SIGMA)
     1*WE*WE
      AI=2.*WE*(ZETA1*WN1*(WN*WN-WE*WE)+ZETA*WN*(WN1*WN1-WE*WE))
      FACTOR=1./(FMAG*WE*WE*WE)
      XR=-AI*FACTOR
      XI=AR*FACTOR
      RETURN
      END


C           30-100 WWSSN SYSTEM, INSTRUMENT CONSTANTS FROM U. CHANDRA
C           BSSA 1970 VOL 60, PP 539-563
C
      SUBROUTINE SEISM2(FREQ,PEAK,XR,XI)
      IF (FREQ.GT.1.) FREQ=1.0
      IF (FREQ.LT.0.005) FREQ=0.005
      WE=6.2831853*FREQ
      INDEX=(PEAK+1.)/375.
       GO TO (1,2,2,3,3,3,3,4,4,4,4,4,4,4,4,5),INDEX
1     FMAG=251.9
      SIGMA=0.003
      GO TO 6
2     FMAG=503.1
      SIGMA=0.012
      GO TO 6
3     FMAG=1001.5
      SIGMA=0.044
      GO TO 6
4     FMAG=1941.9
      SIGMA=.195
      GO TO 6
5     FMAG=2241.8
      SIGMA=0.767
```

```
6       ZETA=1.5
        ZETA1=1.
        WN=0.2094395
        WN1=0.062831853
        AR=(WE*WE-WN*WN)*(WE*WE-WN1*WN1)-4.*ZETA*ZETA1*WN*WN1*(1.-SIGMA)
       1*WE*WE
        AI=2.*WE*(ZETA1*WN1*(WN*WN-WE*WE)+ZETA*WN*(WN1*WN1-WE*WE))
        FACTOR=1./(FMAG*WE*WE*WE)
        XR=-AI*FACTOR
        XI=AR*FACTOR
        RETURN
        END



C            SEISM4 CALCULATES THE AMPLTITUDE RESPONSE FOR
C            TABULATED VALUES, IT DOES NOT CALCULATE THE PHASE
C            RESPONSE   TABULATED PERIODS MUST BE LISTED IN ORDER
C            OF INCREASING PERIOD
C            N=NUMBER OF RESPONSE PAIRS
C            N=NEGATIVE  VELOCITY SENSITIVITY READ IN AND CONVERTED TO
C            DISPLACEMENT SENSITIVITY
C            N=POSITIVE  DISPLACEMENT SENSITIVITY READ IN
C            RESPONSE PAIRS ARE READ IN IN AN 8F10.4 FORMAT
C
        SUBROUTINE SEISM4 (FREQ,PEAK,XR,XI)
        COMMON/INST/MAGIN,M,PER(100),RESP(100)
        IF (MAGIN.NE.0) GO TO 100
        READ(5,1) N
        M=IABS(N)
        READ (5,2) (PER(I),RESP(I),I=1,M)
1       FORMAT(I5)
2       FORMAT(8F10.4)
        IF(N.LT.0) WRITE (6,300)
```

```
      IF (N.GT.0) WRITE (6,301)
      WRITE (6,302)
      WRITE (6,303) (PER(I),RESP(I),I=1,M)
300   FORMAT(1X,'VELOCITY SENSITIVITY')
301   FORMAT(1X,'DISPLACEMENT SENSITIVITY')
302   FORMAT(8X,'PER',8X,'RESP',4(9X,'PER',8X,'RESP')/)
303   FORMAT(1X,10F12.2)
      IF (N) 3,4,4
3     DO 5 I=1,M
5     RESP(I)=RESP(I)*6.2831853/PER(I)
4     CONTINUE
      MAGIN=1
100   CONTINUE
      IF (FREQ.LT.0.005) FREQ=0.005
      T=1./FREQ
      IF(T.LE.PER(1))T=PER(1)
      IF (T.GE.PER(M)) T=PER(M)
      DO 200 I=1,M
      IF (T.GE.PER(I).AND.T.LE.PER(I+1)) GO TO 160
200   CONTINUE
160   XR=RESP(I)+(RESP(I+1)-RESP(I))/(PER(I+1)-PER(I))*(T-PER(I))
      XR=1./XR
      XI=0.0
      RETURN
      END



C          RESPONSE OF A STANDARD WOOD-ANDERSON INSTRUMENT TO=.8
C
      SUBROUTINE SEISMS(FREQ,PEAK,XR,XI)
      WN=1.25
      ZETA=0.8
      WNWE=WN/FREQ
```

```
      XR=-(WNWE*WNWE-1.)/PEAK
      XI=-2.*ZETA*WNWE/PEAK
      RETURN
      END



C           SEISM8  READS IN A SET OF SEISMOGRAPH CONSTANTS IN
C           5F10.2 FORMAT
C
C           TS=SEISMOMETER NATURAL PERIOD
C           HS=SEISMOMETER DAMPING FACTOR
C           TG=GALVANOMETER NATURAL PERIOD
C           HG=GALVANOMETER DAMPING FACTOR
C           SIGMA=COUPLING FACTOR(SIGMA**2)
C
C           THE PROGRAM USES HAGIWARA'S EQUATION TO FIND THE
C           INSTRUMENT RESPONSE
C
      SUBROUTINE SEISM8 (FREQ,XR,XI)
      COMMON/INST/MAGIN,M,PER(100),RESP(100)
      COMMON/HAGI/TS,TG,HS,HG,SIGMA,PK,FPK
      IF (MAGIN.NE.0) GO TO 100
      READ(5,1) TS,HS,TG,HG,SIGMA
1     FORMAT(5F10.2)
      MAGIN=1
      PK=0.0
      FPK=0.0
100   CONTINUE
      IF(FREQ.GT.1.0) FREQ=1.0
      IF (FREQ.LT.0.005) FREQ=0.005
      WE=6.2831853*FREQ
      WN=6.2831853/TS
      WN1=6.2831853/TG
```

```
      ZETA=HS
      ZETA1=HG
      AR=(WE*WE-WN*WN)*(WE*WE-WN1*WN1)-4.*ZETA*ZETA1*WN*WN1*(1.-SIGMA)
     1*WE*WE
      AI=2.*WE*(ZETA1*WN1*(WN*WN-WE*WE)+ZETA*WN*(WN1*WN1-WE*WE))
      FACTOR=1./(WE*WE*WE)
      XR=-AI*FACTOR
      XI=AR*FACTOR
      XPK=1./(XR*XR+XI*XI)
      IF (XPK.GT.PK) FPK=FREQ
      IF(XPK.GT.PK) PK=XPK
      RETURN
      END



C           PRIN LISTS THE PERIOD, FREQUENCY, AND AMPLITUDE DATA
C           FOR THE SPECTRUM AS WELL AS DISTANCE, DEGREES, STATION,
C           COMPONENT, BACKAZIMUTH, AND DT
C           THEN A PLOT ROUTINE IS CALLED TO PLOT A LOG-LOG PLOT WITH
C           DIMENSIONS OF 5 BY 7.5 INCHES
C           IF MULTIPLE PLOTS ARE MADE THEY ARE SEPARATED BY 3 INCHES
C           THE STATION AND COMPONENT ARE INCLUDED IN THE PLOT TITLE
C           THE PLOT IS IN BLACK INK SUITABLE FOR COPYING
C           IF THIS IS NOT DESIRED THE CALL CALOPR STATEMENT IN THE
C           MAIN PROGRAM CAN BE REMOVED AND THE PLOTS WILL BE IN
C           BALLPOINT PEN
C
      SUBROUTINE PRIN(X,M,STA,COMP,DIST,DEG,BAZ,DT,RQ,V,RP,F1,F2)
      DIMENSION X(1),FR(600),AM(600),TITLE(2),XAX(3),YAX(4)
      DATA XAX /'LOG ','FREQ',' HZ '/
      DATA YAX /'LOG ','SPEC','TRAL',' AMP'/
      PI=3.1415926
      WRITE (6,99) STA,COMP
```

```
99    FORMAT (1X,A4,2X,A4)
      TITLE(1)=STA
      TITLE(2)=COMP
      CALL SYMBOL (0.,0.,.14,TITLE,0.,8)
      WRITE (6,97) DIST,DEG,BAZ,DT,RQ
97    FORMAT(1X,'DIST=',F10.4,' DEG=',F10.5,' BAZ=',F10.5,' DT=',F10.5,
     1' Q=',F10.5)
      WRITE (6,98)
98    FORMAT (12X,'PERIOD',13X,'FREQUENCY',11X,'AMPLITUDE')
       N=0
      DO 10 I=2,M
      PER=2.*FLOAT(M)*DT/FLOAT(I-1)
      FREQ=1./PER
      IF (FREQ.GT.F1) GO TO 20
      N=0
20    IF (FREQ.GT.F2) GO TO 30
      II=2*I
      III=II-1
      AMP=SQRT(X(II)*X(II)+X(III)*X(III))
C           CORRECT FOR ATTENUATION AND RADIATION PATTERN
      AMP1=AMP*EXP((FREQ*PI*DIST)/(RQ*V))/RP
      WRITE (6,100) PER,FREQ,AMP1
100   FORMAT(1X,3(9X,E11.4))
      N=N+1
      AM(N)=AMP1
      FR(N)=FREQ
10    CONTINUE
30    CONTINUE
      CALL PLOT(1.,1.,-3)
      CALL LGSCAL(FR,N,5.,XSC,XCYC,1)
      CALL LGSCAL(AM,N,7.5,YSC,YCYC,1)
      CALL LGAXIS(0.,0.,XAX,-12,5.0,0.0,XSC,XCYC)
      CALL LGAXIS (0.,0.,YAX,16,7.5,90.0,YSC,YCYC)
      CALL LINE (FR,AM,N,1)
```

```
      CALL PLOT (7.0,-1.,-3)
      RETURN
      END
```

User's guide to SEARCH

Purpose: SEARCH finds the maximum radiation pattern value for SV, SH, and P.

Program units

PROGRAM SEARCH: Searches the area around an earthquake for maximum radiation pattern values by calculating radiation patterns for azimuzths from 0^{o} to 360^{o} and takeoff angles from 0^{o} to 180^{o} in increments of 5^{o}.

SUBROUTINE RADPAT: Calculates the SH, SV, and P radiation patterns at a station for an event given the fault plane solution of the event, take-off angle and station azimuth. RADPAT is based on the radiation patterns of Ben-Menahem et al. (1965).

Input data

Card	Column	Name	Format	Explanation
1	1-3	N	I3	Number of events
2 to N+1	1-5	ID	A5	Event name
	6-10	PL1	F5.0	Hade of preferred fault plane
	11-15	DIR1	F5.0	Strike of preferred fault plane
	16-20	PL2	F5.0	Hade of auxiliary fault plane
	21-25	DIR2	F5.0	Strike of auxiliary fault plane

The output for each event is listed as:

Event name, maximum P wave radiation, maximum SH wave radiation, and maximum SV radiation pattern.

```
C          PROGRAM SEARCH
C
C          SEARCH FINDS THE MAXIMUM VALUES OF THE SH,SV AND P
C          RADIATION PATTERNS FOR AN EVENT
C          RADIATION PATTERNS ARE CALCULATED FOR DIFFERENT VALUES OF
C          TAKEOFF ANGLE AND AZIMUTH (IN INCREMENTS OF FIVE DEGREES)
C
C          N=NUMBER OF EVENTS
C          ID=EVENT NAME
C          PL1,DIR1=PLUNGE AND AZIMUTH OF PREFERRED FAULT PLANE
C          PL2,DIR2=PLUNGE AND AZIMUTH OF THE AUXILIARY PLANE
C           PLUNGE IS THE HADE OF THE FAULT (90-PLUNGE=DIP)
C          BP,BSH,BSV=MAXIMUM RADIATION PATTERN VALUES FOR THE EVENT
C
      RP=0.
      RSH=0.
      RSV=0.
      FN=1.
      READ (5,44) N
44    FORMAT(I3)
      DO 10 I=1,N
      BP=0.
      BSH=0.
      BSV=0.
      READ (5,20) ID,PL1,DIR1,PL2,DIR2
 20   FORMAT (A5,4F5.0)
      DO 30 J=1,72
      THETA=(J-1)*5
      DO 30 K=1,72
      ANG=(K-1)*5
      CALL RADPAT (PL1,DIR1,PL2,DIR2,THETA,ANG,FN,RP,RSH,RSV)
      AP=ABS(RP)
      ASH=ABS(RSH)
      ASV=ABS(RSV)
```

```
      IF (AP.GT.BP) BP=AP
      IF (ASH.GT.BSH) BSH=ASH
      IF (ASV.GT.BSV) BSV=ASV
 30   CONTINUE
      WRITE (6,50) ID,BP,BSH,BSV
 50   FORMAT (A5,3F8.5)
 10   CONTINUE
       STOP
       END



C          RADPAT DETERMINES THE RADIATION PATTERN FOR A SHEAR FAULT
C         (SEE BEN-MENACHEM,SMITH AND TENG, BSSA,VOL 55, PG 219)
C
C         PL1,DIR1,PL2,DIR2 ARE THE PLUNGES AND AZIMUTHS OF THE
C         FAULT PLANES
C         THETA IS THE STATION AZIMUTH
C         ANG IS THE TAKEOFF ANGLE OF THE RAY AT THE SOURCE
C         FN IS THE NORMALIZATION FACTOR
C         RP,RSH,RSV ARE THE COMPUTED RADIATION PATTERN VALUES
C
      SUBROUTINE RADPAT(PL1,DIR1,PL2,DIR2,THETA,ANG,FN,RP,RSH,RSV)
      OPI=57.295778
      AZI=DIR1-90.
      DELTA=(90.-PL1)/OPI
      PL2=PL2/OPI
      X=COS((DIR2-AZI)/OPI)*COS(PL2)
      Y=(1.-X*X)**.5
      ARG=Y/X
      ALAND=ATAN(ARG)
      THETA=(DIR1+90.-THETA)/OPI
      ANGI=(-1.*ANG)/OPI
      A=COS(THETA)*COS(ALAND)
```

```
      B=SIN(THETA)*SIN(ALAND)
      E=SIN(ALAND)*SIN(2.*DELTA)/4.
      EGA1=A+B*COS(DELTA)
      EGA2=A*COS(DELTA)+B*COS(2.*DELTA)
      EGA3=SIN(2.*THETA)*SIN(ALAND)*COS(DELTA)+COS(2.*THETA)*
     1COS(ALAND)
      EGA4=COS(THETA)*COS(2.*DELTA)*SIN(ALAND)-SIN(THETA)*
     2COS(ALAND)*COS(DELTA)
      F=SIN(THETA)*SIN(DELTA)*EGA1/2.
      C0=E-F
      C1=-SIN(DELTA)*EGA3
      D1=EGA4
      C2P=EGA2/2.
      D2P=E+F
      C2SV=-2.*D2P
      D2SV=EGA2
      RP=(C0+C2P*SIN(2.*ANGI)+D2P*COS(2.*ANGI))*2./FN
      RSH=(C1*SIN(ANGI)+D1*COS(ANGI))/FN
      RSV=(C2SV*SIN(2.*ANGI)+D2SV*COS(2.*ANGI))/FN
      RETURN
      END
```

User's Guide to SPLOT

Purpose: SPLOT plots digitized seismograms at their original scale.

The data cards follow the same format as for EXSPEC with the exception that the first card for each seismogram has an extra value (CPMM) added to it.

Card	Column	Name	Format	Explanation
1	1-3	N	I3	Number of plots
	4-5	NP	I2	Selects pen for plot
				NP=1 a standard pen is used
				NP=2 a #4 black ink pen is used

Data cards for each seismogram follow this format:

A	13-22	CPMM	F10.5	Number of samples/mm taken when record was digitized
B	1-4	TITLE(1)	A4	Station name
	5-8	TITLE(2)	A4	Component
C	1-4	TITLE(3)	A4	Event name

These cards are followed by digitized data points in a 5F6.2 format with the end of each seismogram denoted by a 99.00.

```
C           SPLOT TAKES A DIGITIZED SEISMOGRAM AND PLOTS IT AT THE SAME
C           SCALE AS THE ORIGINAL SEISMOGRAM
C
C           THE DATA TO BE READ IN IS IN THE SAME FORMAT THAT IT IS
C           IN FOR EXSPEC EXCEPT THAT THE VALUE OF CPMM IS ADDED TO
C           THE FIRST DATA CARD FOR A STATION (FOLLOWING VALUES
C           FOR M,ICONT AND IDATA)
C           TITLE(1)=STATION
C           TITLE (2)=COMPONENT
C           TITLE (3)= EVENT
C
C           CPMM IS THE NUMBER OF SAMPLES/MM TAKEN WHEN THE RECORD
C           WAS DIGITIZED
C           M IS THE NUMBER OF SEPARATE SEISMOGRAMS TO BE PLOTTED IN
C           ONE PLOT
C           TITLE IS THE PLOT TITLE
C           NP IS USED TO SELECT A PEN FOR THE PLOT
C           IF NP=1 THE STANDARD BALLPOINT PEN IS USED
C           IF NP=2 A #4 BLACK INK PEN IS USED
C           (WITH THE #4 PEN THE PLOT IS DARKER AND WILL COPY BETTER)
C
C           THE SECTION OF SEISMOGRAM TO BE PLOTTED CAN BE UP TO THREE
C            INCHES LONG AND EIGHT INCHES HIGH
C           THERE WILL BE .5 INCHES BETWEEN EACH SEISMOGRAM PLOTTED
C
C
      DIMENSION DAT(800),TITLE(3),TIME(800)
      READ(5,9) M,NP
9     FORMAT (I3,I2)
      RM=3.75*M
      CALL IDPLOT (RM,8.0)
       IF (NP.EQ.1) GO TO 40
       CALL CALOPR('#4 PEN, BLACK INK FOR THIS PLOT, PLEASE',39,.TRUE.)
40     CONTINUE
```

```
      DO 14 L=1,M
      READ (5,12) CPMM,TITLE(1),TITLE(2),TITLE(3)
12    FORMAT(12X,F10.5/2A4/A4)
      DO 90 I=1,512,5
      J=I+4
      READ(5,911) (DAT(MM),MM=I,J)
911   FORMAT (5F6.2)
      DO 90 KK=I,J
      IF (DAT(KK)-99.) 90,91,91
90    CONTINUE
91    N=KK-1
      CALL SYMBOL (0.,0.,.14,TITLE,0.,16)
      CALL PLOT(.5,4.,-3)
      DO 13 K=1,N
      RK=K-1
      DAT(K)=DAT(K)/25.4
      TIME(K)=RK/(25.4*CPMM)
      CALL PLOT (TIME(K),DAT(K),2)
13    CONTINUE
      CALL PLOT (3.,-4.,-3)
14    CONTINUE
      CALL FINI
      STOP
      END
```

User's guide to RAD

Purpose: RAD calculates normalized radiation patterns for stations.

Program units

RAD: is the main program which handles input and output

SUBROUTINE RADPAT: Calculates radiation pattern for each station.

(Based on the radiation patterns of Ben-Menahem et al. (1965)).

Input

First Card	Column	Name	Format	Explanation
	1-2	NQ	I2	Number of events
For each event have an event card:				
	1-5	ID	A5	Event name
	6-10	PL1	F5.0	Hade of preferred fault
	11-15	DIR1	F5.0	Strike of preferred fault
	16-20	PL2	F5.0	Hade of auxiliary fault
	21-25	DIR2	F5.0	Strike of auxiliary fault
	26-32	FP	F7.5	Maximum P radiation pattern (obtained from SEARCH)
	33-39	FSH	F7.5	Maximum SH radiation pattern
	40-46	FSV	F7.5	Maximum SV radiation pattern
	47-48	NSTA	I2	Number of stations for event
Each event card followed by NSTA station cards with this format:				
	1-3	STA	A3	Station Name
	4-10	AZ	F7.1	Station azimuth
	11-17	ANGS	F7.1	S-wave take-off angle
	18-24	ANGP	F7.1	P-wave take-off angle

```
C          RAD IS THE DRIVER PROGRAM FOR A ROUTINE TO CALCULATE
C          RADIATION PATTERNS
C
C          NQ=NUMBER OF EVENTS
C          ID=EVENT NAME
C          PL1,DIR1=PLUNGE AND AZIMUTH OF PREFERRED FAULT IN FAULT
C          PLANE SOLUTION
C          PL2,DIR2=PLUNGE AND AZIMUTH OF AUXILIARY FAULT PLANE
C         FP=MAXIMUM P RADIATION VALUE FOR EVENT
C          FSH=MAXIMUM SH RADIATION VALUE
C         FSV=MAXIMUM SV RADIATION VALUE
C          FP,FSH AND FSV SERVE AS NORMALIZATION FACTORS FOR EACH EVENT
C          AND ARE OBTAINED FROM THE PROGRAM SEARCH
C          NSTA=NUMBER OF STATIONS FOR AN EVENT
C          STA=STATION NAME
C          AZ=STATION AZIMUTH
C          ANGS,ANGP=P AND  S TAKEOFF ANGLES
C          (COMPUTED BY THE PROGRAM EDABAC)
C          RP,RSH,RSV=FINAL NORMALIZED RADIATION PATTERN VALUES
C          FOR A STATION
C
      READ (5,9) NQ
9     FORMAT (I2)
      DO 10 I=1,NQ
      READ (5,11) ID,PL1,DIR1,PL2,DIR2,FP,FSH,FSV,NSTA
11    FORMAT (A5,4F5.0,3F7.5,I2)
      WRITE (6,12) ID
12    FORMAT (/1X,'EVENT  ',A5)
      DO 20 J=1,NSTA
      READ (5,13) STA,AZ,ANGS,ANGP
13    FORMAT (A3,3F7.1)
      WRITE (6,14) STA
14    FORMAT (1X,'STATION  ',A3)
      CALL RADPAT (PL1,DIR1,PL2,DIR2,AZ,ANGP,FP,RP,RSH,RSV)
```

```
      WRITE (6,15) RP
15    FORMAT (1X,'P RADIATION IS ',F8.5)
      CALL RADPAT (PL1,DIR1,PL2,DIR2,AZ,ANGS,FSH,RP,RSH,RSV)
      WRITE (6,16) RSH
16    FORMAT (1X,'SH RADIATION IS ',F8.5)
      CALL RADPAT (PL1,DIR1,PL2,DIR2,AZ,ANGS,FSV,RP,RSH,RSV)
      WRITE (6,17) RSV
17    FORMAT (1X,'SV RADIATION IS ',F8.5)
20    CONTINUE
10    CONTINUE
      STOP
      END
```

User's guide to EDABAC

Purpose: EDABAC calculates station azimuth, backazimuth, epicentral distance and P and S-wave takeoff angles. It is modifed from Herrmann (1978).

Program units

EDABAC: Main program that controls output

SUBROUTINE AZEP: Computes azimuth, backazimuth and epicentral distance in degrees and kilometers

SUBROUTINE PANG: Calculates P-wave takeoff angles

SUTROUTINE SANG: Calculates S-wave takeoff angles

Input format

Card 1

Column	Name	Format	Explanation
1-5	VP	F5.2	Velocity of P-wave
6-10	VS	F5.2	Velocity of S-wave
11-12	NQ	I2	Number of events

The next thirty cards that are read in contain data from a Jeffreys-Bullen travel time table in the following format:

First 20 cards

1-60	(JP(I), JS(I))	6(2I5)	JP=P arrival time JS=S arrival time

Next 10 cards:

1-60	DEL(J)	12F5.1	Epicentral distance in degrees

Column	Name	Format	Explanation
NQ event cards have this format:			
2-6	ENAME	A5	Event name
7-15	EP	F9.3	Event latitude north=positive
16-24	EL	F9.3	Event longitude east=positive
25-26	NSTA	I2	Number of station for the event
Each event card is followed by NSTA station cards			
2-4	STN	A3	Station name
5-13	STNP	F9.3	Station latitude north=positive
14-22	STNL	F9.3	Station longitude east=positive

```
C          EDABAC IS A MODIFIED VERSION OF R. HERRMANN'S PROGRAM
C         OF THE SAME NAME (FROM COMPUTER PROGRAMS IN EARTHQUAKE
C         SEISMOLOGY VOLUME ONE)
C
C         EDABAC CALCULATES STATION AZIMUTH,BACKAZIMUTH, DISTANCE
C          FROM EVENT (IN KM AND DEGREES) AND P AND S TAKEOFF
C         ANGLES FOR A SHALLOW (LESS THAN 10 KM) EVENT
C
C         JS,JP AND DEL  ARE TAKEN FROM THE J-B TRAVEL TIME TABLES
C         JS,JP=S AND P ARRIVAL TIMES
C         DEL=DISTANCE TO THE EVENT
C         VP,VS=VELOCITIES OF P AND S WAVES
C         NQ=NUMBER OF EVENTS
C         ENAME=EVENT NAME
C         EP=EVENT LATITUDE
C         NORTH=POSITIVE
C         EL=EVENT LONGITUDE
C         EAST=POSITIVE
C         NSTA=NUMBER OF STATIONS RECORDING EVENT
C         STN=STATION NAME
C         STNP=STATION LATITUDE
C         NORTH=POSITIVE
C         STNL=STATION LONGITUDE
C         EAST=POSITIVE
C
      DIMENSION JS(120),JP(120),DEL(120)
      READ (5,10) VP,VS,NQ
10    FORMAT (2F5.2,I2)
      READ (5,11) (JP(I),JS(I),I=1,120)
11    FORMAT (6(2I5))
      READ (5,12) (DEL(J),J=1,120)
12    FORMAT (12F5.1)
      DO 200 I=1,NQ
      READ (5,13) ENAME,EP,EL,NSTA
```

```
13      FORMAT (1X,A5,2F9.3,I2)
        WRITE (6,22) ENAME
22      FORMAT (1X,'EVENT',A5)
        DO 100 M=1,NSTA
        READ (5,14) STN,STNP,STNL
14      FORMAT (1X,A3,2F9.3)
        ESQ1=.9932315
        RAD1=.01745329
        EPIPR=EP*RAD1
        EPIPR=90.*RAD1-ATAN(ESQ1*(SIN(EPIPR)/COS(EPIPR)))
        EPIPC=EPIPR/RAD1
        IF (EL) 20,30,30
20      EPILC=360.+EL
        GO TO 35
30      EPILC=EL
35      CALL AZEP(RANGE,AZ,STNP,STNL,EPILC,EPIPC,ANGI,EPIPR,BAZ)
        IF (ANGI-10.) 320,335,335
320     DO 325 NN=1,20
        AN=NN
        AN=AN*.5
        IF(ANGI-AN) 330,330,325
325     CONTINUE
330     K=NN+2
        GO TO 385
335     IF (ANGI.GT.102.) GO TO 300
        DO 345 NM=10,107
        AN=NM
        IF (ANGI-AN) 350,350,345
345     CONTINUE
350     K=NM+12
385     CALL SANG (SAN,K,DEL,JS,VS)
        CALL PANG (PAN,K,DEL,JP,VP)
        WRITE (6,40) STN,RANGE,AZ
40      FORMAT (1X,' STATION  ',A3,' RANGE= ',F10.1,' AZ= ',F7.1)
```

```
      WRITE (6,45) BAZ
45    FORMAT(1X,'BACKAZ=',F7.1)
      WRITE (6,50) SAN,PAN
50    FORMAT(1X,' SS= ',F6.1,' PS= ',F6.1)
100   CONTINUE
200   CONTINUE
      GO TO 390
300   WRITE (6,310)
310   FORMAT (1X,'ANGI IS GREATER THAN 94 DEGREES')
390   STOP
      END



C          AZEP CALCULATES THE RANGE OF THE EVENT AND THE AZIMUTH AND
C          THE BACKAZIMUTH FOR A STATION
C
      SUBROUTINE AZEP(RANGE,AZ,STNP,STNL,EPILC,EPIPC,ANGI,EPIPR,BAZ)
      RAD=.01745329
      ESQ=.9932315
      STPC=STNP*RAD
      BAZ=0.
      STNPR=90.*RAD-ATAN(ESQ*(SIN(STPC)/COS(STPC)))
      STPC=STNPR/RAD
      IF (STNL) 211,212,212
211   STLC=360.+STNL
      GO TO 213
212   STLC=STNL
213   IF (STPC-180.) 69,68,68
68    ANGI=180.-EPIPC
      AZ=180.
      BAZ=0.0
      GO TO 998
69    PANG=ABS(STLC-EPILC)
```

```
      IF (PANG-180.) 71,71,70
70    PANG=360.-PANG
71    PANG=PANG*RAD
      PI=3.1415927
      OPI=57.295780
      ANGI=(COS(EPIPR)*COS(STNPR))+(SIN(EPIPR)*SIN(STNPR)*COS(PANG))
      SNANG=SQRT(ABS(1.-ANGI*ANGI))
      ANGI=ATAN(SNANG/ANGI)
      IF (ANGI) 220,221,221
220   ANGI=ANGI+PI
221   AZ=(COS(STNPR)-COS(EPIPR)*COS(ANGI))/(SIN(EPIPR)*SIN(ANGI))
      SNAZ=SQRT(ABS(1.-AZ*AZ))
      AZ=ATAN(SNAZ/AZ)
      IF (AZ) 230,231,231
230   AZ=AZ+PI
231   AZ=OPI*AZ
      BAZ=(COS(EPIPR)-COS(STNPR)*COS(ANGI))/(SIN(STNPR)*SIN(ANGI))
      SNBAZ=SQRT(ABS(1.-BAZ*BAZ))
      BAZ=ATAN(SNBAZ/BAZ)
      IF (BAZ) 240,241,241
240   BAZ=BAZ+PI
241   BAZ=BAZ*OPI
      ANGI=ANGI*OPI
      IF (STLC-EPILC)72,74,73
72    IF (STLC-EPILC+180.)80,77,81
73    IF (STLC-EPILC-180.)80,77,81
74    IF (STPC-EPIPC)75,78,76
75    AZ=0.
      BAZ=180.
      GO TO 998
76    AZ=180.
      BAZ=0.0
      GO TO 998
77    IF (STPC+EPIPC-180.)78,78,79
```

```
78      AZ=0.
        BAZ=0.0
        GO TO 998
79      AZ=180.
        BAZ=180.
        GO TO 998
80      BAZ=360.-BAZ
        GO TO 998
81      AZ=360.-AZ
998     RANGE=ANGI*111.195
        RETURN
        END


C           SANG CALCULATES THE S WAVE TAKEOFF ANGLE AT THE SOURCE
C
        SUBROUTINE SANG(SAN,K,DEL,JS,VS)
        DIMENSION DEL(120),JS(120)
        SJ5=JS(K-2)
        SJ6=JS(K+2)
        BH=(SJ6-SJ5)/10.
        U=BH*VS/((DEL(K+2)-DEL(K-2))*111.195)
        U=ABS(U)
        IF (U-1.) 511,516,516
511     SAN=ATAN(U/SQRT(1.-U*U))
        GO TO 517
516     SAN=1.5708
517     SAN=SAN*57.2958
        RETURN
        END
```

```
C          PANG CALCULATES THE P-WAVE TAKEOFF ANGLE AT THE SOURCE
C
      SUBROUTINE PANG (PAN,K,DEL,JP,VP)
      DIMENSION DEL(120),JP(120)
      PJ5=JP(K-2)
      PJ6=JP(K+2)
      G=(PJ6-PJ5)/10.
      C=G*VP/((DEL(K+2)-DEL(K-2))*111.195)
      Y=ABS(C)
      IF (Y-1.)510,515,515
510   PAN=ATAN(Y/SQRT(1.-Y*Y))
      GO TO 518
515   PAN=1.5708
518   PAN=PAN*57.2958
      RETURN
      END
```

APPENDIX D

MOMENT TENSOR INFORMATION

Moment tensors for the Utah region

(east and north are the 1 and 2 axes, the 3 axis is vertically upward)

for $\mu_f = 0$

$$M_{ij} = \begin{matrix} 5.6 & 2.2 & -6.8 \\ 2.2 & -0.24 & 0.78 \\ -6.8 & 0.78 & -5.4 \end{matrix} \quad \times 10^{25} \text{ dyne-cm}$$

with principal values:

9.1×10^{25} dyne-cm at (0.86, 0.17, -0.49)

-9×10^{25} dyne-cm at (-0.44, 0.21, -0.88)

-2.4×10^{24} dyne-cm at (-0.07, 0.97, 0.25)

for $\mu_f = 0.6$

$$M_{ij} = \begin{matrix} 8.1 & 1.7 & -5.5 \\ 1.7 & -0.95 & 2.3 \\ -5.5 & 2.3 & -7.1 \end{matrix} \quad \times 10^{25} \text{ dyne-cm}$$

with principal values:

9.9×10^{25} dyne-cm at (0.95, 0.086, -0.28)

-1×10^{26} dyne-cm at (-0.3, 0.15, -0.95)

-1.9×10^{24} dyne-cm at (-0.042, 0.97, 0.23)

For Northern Utah

with $\mu_f = 0$

$$M_{ij} = \begin{matrix} 5.6 & 2.4 & -6.5 \\ 2.4 & -0.042 & 0.81 \\ -6.5 & 0.81 & -5.4 \end{matrix} \quad \times 10^{25} \text{ dyne-cm}$$

with principal values:

9×10^{25} dyne-cm at (0.88, 0.2, -0.39)

-8.7×10^{25} dyne-cm at (-0.42, 0.2, -0.86)

-7×10^{23} dyne-cm at (-0.1, 0.96, 0.26)

with $\mu_f = 0.6$

$$M_{ij} = \begin{matrix} 8.0 & 1.8 & -5.3 \\ 1.8 & -1.0 & 2.3 \\ -5.3 & 2.3 & -7.0 \end{matrix} \times 10^{25} \text{ dyne-cm}$$

with principal values:

9.8×10^{25} dyne-cm at (0.95, 0.097, -0.29)

-9.5×10^{25} dyne-cm at (-0.3, 0.12, -0.95)

-2.2×10^{24} dyne-cm at (-0.11, 0.98, 0.17)

For southern Utah

with $\mu_f = 0$

$$M_{ij} = \begin{matrix} 1.3 & -7.9 & -27.5 \\ -7.9 & -2.9 & -5.3 \\ -27.5 & -5.3 & 1.6 \end{matrix} \times 10^{23} \text{ dyne-cm}$$

with principal values:

2.9×10^{24} dyne-cm at (-0.71, 0.06, 0.71)

-2.94×10^{24} dyne-cm at (0.68, 0.34, 0.67)

3×10^{22} dyne-cm at (-0.2, 0.94, -0.27)

with $\mu_f = 0.6$

$$M_{ij} = \begin{matrix} 1.7 & -0.54 & -2.3 \\ -0.54 & -0.38 & -2.1 \\ -2.3 & -2.1 & -1.3 \end{matrix} \times 10^{24} \text{ dyne-cm}$$

with principal values:

2.8×10^{24} dyne-cm at (0.86, 0.26, -0.47)

-3.7×10^{24} dyne-cm at (0.37, 0.63, 0.69)

9.2×10^{23} dyne-cm at (-0.38, 0.84, -0.4)

REFERENCES

Aki, K. (1966). Generation and propagation of G-waves from the Niigata earthquake of June 16, 1964, 2, Estimation of earthquake moment, release energy, and stress strain drop from the G-wave spectrum, Bull. Earthquake Res. Inst., Tokyo Univ. 44, 73-88.

Aki, K. (1967). Scaling law of seismic spectrum, J. Geophys. Res. 72, 1217-1231.

Anderson, L. W., and D. G. Miller (1979). Quaternary fault map of Utah, Fugro Inc., Long Beach, Calif.

Anderson, J. G. (1979). Estimating the seismicity from geological structure for seismic-risk studies, Bull. Seis. Soc. Am. 69, 135-158.

Anderson, R. E. (1980). The status of seismotectonic studies of southwestern Utah, Proceedings Conference X - Earthquake Hazards Along the Wasatch and Sierra-Nevada Frontal Fault Zones, U.S. Geol. Surv. Open File Report 80-801, 519-547.

Anderson, R. E., and R. C. Bucknam (1979a). Two areas of probable Holocene deformation in southwestern Utah, Tectonophysics, 52, 417-430.

Anderson, R. E., and R. C. Bucknam (1979b). Map of fault scarps on unconsolidated sediments, Richfield 1° x 2° quadrangle, Utah, U.S. Geol. Survey Open File Report OF79-1236.

Anderson, R. E., R. C. Bucknam, and W. K. Hamblin (1978). Road log to the Quaternary tectonics of the intermountain seismic belt between Provo and Cedar City, Utah, Geol. Soc. Amer., Rocky Mtn. Sec. Annual Meeting, Provo, Utah.

Arabasz, W. J., W. D. Richins, and C. J. Langer (1979). The Idaho-Utah border (Pocatello Valley) earthquake sequence of March-April 1975, in Earthquake studies in Utah 1850 to 1978, W. J. Arabasz, R. B. Smith, and W. D. Richins, editors, Univ. of Utah Seismograph Stations, Salt Lake City, Utah, 339-373.

Arabasz, W. J., R. B. Smith, and W. D. Richins (1979). Earthquake Studies along the Wasatch Front, Utah: Network monitoring, seismicity, and seismic hazards in Earthquake Studies in Utah 1850 to 1978, W. J. Arabasz, R. B. Smith, and W. D. Richins, editors, Salt Lake City, Utah, 253-286.

Averitt, P. (1962). Geology and coal resources of the Cedar City quadrangle, Iron County, Utah, U.S. Geol. Survey Prof. Paper 389, 72 pp.

Bache, T. C., D. G. Lambert and T. G. Barker (1980). A source model for the March 28, 1975 Pocatello Valley earthquake from time-domain modelling of teleseismic P waves, Bull. Seis. Soc. Amer. 70, 405-418.

Bachman, M. E. (1959). Geology of the Water Hollow fault zone, Sevier and Sanpete Counties, Utah, M.S. thesis, Ohio State University.

Battis, J. C. and K. J. Hill (1977). Analysis of seismicity and tectonics of the central and western United States, Interim Scientific Report No. 1, Texas Instruments, Inc.

Baughman, R. L. (1959). The geology of the Musiana graben area, Sevier and Sanpete Counties, Utah, M. S. thesis, Ohio State University

Beck, P. J. (1970). The southern Nevada-Utah border earthquakes August to December, 1966, M.S. thesis, Univ. of Utah, Salt Lake City, Utah.

Ben-Menahem, A., S. W. Smith, and T. L. Teng (1965). A procedure for source studies from spectrums of long-period seismic waves, Bull. Seism. Soc. Am. 55, 203-235.

Bissell, H. J. (1964). The Wasatch fault of the south-central Wasatch Mountains, in The Wasatch Fault Zone in North Central Utah, Utah Geological Society Guidebook No. 18, R. E. Marsell, editor, Geol. Soc. of Utah, 15-28.

Brune, J. N. (1968). Seismic moment, seismicity, and rate of slip along major fault zones, J. Geophys. Res. 73, 777-780.

Brune, J. N. (1970). Tectonic stress and the spectra of seismic shear waves from earthquakes, J. Geophys. Res. 75, 4997-5009

Brune, J. H. (1971). Correction (to Brune (1970)), J. Geophys. Res. 76, 5002.

Bucknam, R. C. (1976). Leveling data from the epicentral area of the March 27, 1975, earthquake in Pocatello Valley, Idaho, U.S. Geol. Surv. Open-file Report. 76-52.

Bucknam, R. C. (1979). Written communication.

Bucknam, R. C., and R. E. Anderson (1979a). Estimation of fault-scarp ages from a scarp-height-slope angle relationship, Geology 7, 11-14.

Bucknam, R. C. and Anderson, R. E. (1979b). Map of fault scarps on unconsolidated sediments, Delta 1° x 2° quadrangle, Utah, U.S. Geol. Survey Open-File Report OF-79-366.

Bucknam, R. C., S. T. Algermissen, and R. E. Anderson (1980). Patterns of late Quaternary faulting in western Utah and an application in earthquake hazard evaluation, in Proceedings of Conference X - Earthquake Hazards Along the Wasatch and Sierra-Nevada Frontal Fault Zones, U.S. Geol. Surv. Open-File Report 80-801, 299-314.

Buss, W. R., and D. Peterson (1964). The Wasatch fault zone in Weber and Davis Counties, Utah, in The Wasatch Fault Zone in North Central Utah, Utah Geol. Soc. Guidebook No. 18, R. E. Marsell, editor, Utah Geol. Soc., 52-65.

Chen, W. P. and P. Molnar (1977). Seismic moments of major earthquakes and the average rate of slip in central Asia, J. Geophys. Res. 82, 2945-2969.

Clark, E. E. (1979). Late Cenozoic volcanic and tectonic activity along the eastern margin of the Great Basin in the proximity of Cove Fort, Utah, Brigham Young Univ. Geol. Studies, 24, no. 1, 87-113.

Cluff, L. S., G. E. Brogan, and C. E. Glass (1970). Wasatch fault, northern portion: Earthquake fault investigation and evaluation, Report to Utah Geol. and Min. Survey, Woodward-Clyde and Associates, 109 pp.

Cluff, L. S., G. E. Brogan, and C. E. Glass (1973). Wasatch fault, southern portion: Earthquake fault investigation and evaluation, Report to U.S. Geol. Surv., Woodward-Lundgren and Associates, 131 p.

Cluff, L. S., A. S. Patwardhan, and K. J. Coppersmith (1980). Estimating the probability of occurrence of surface faulting earthquakes on the Wasatch fault zone, Utah, in Proceedings of Conference X - Earthquake Hazards Along the Wasatch and Sierra-Nevada Frontal Fault Zones, U. S. Geol. Surv. Open-File Report 80-801, 276-298.

Croft, M. G. (1956). Geology of the northern Onaqui Mountains, Tooele County, Utah, Brigham Young Univ. Geol. Studies, 3, no. 1, 1-45.

Douglas, B. M. and A. Ryall (1972). Spectral characteristics and stress drops for microearthquakes near Fairview Peak, Nevada, J. Geophys. Res. 77, 351-359.

Garvin, R. G. (1969). Stratigraphy and economic significance, Currant Creek Formation, northwest Uinta Basin, Utah, Utah Geol. and Mineral. Survey Spec. Studies 27, 62 pp.

Gilbert, F. (1970). Excitation of the normal modes of the earth by earthquake sources, J. Roy. Astron. Soc. 22, 223-226.

Gilluly, J., (1932). Geology and ore deposits of the Stockton and Fairfield quadrangles, Utah, U.S. Geol. Survey Prof. Paper 173, 171 p.

Greensfelder, R. W. (1976). Maximum probable earthquake acceleration on bedrock in the state of Idaho, Idaho Department of Transportation Division of Highways, Research Project 79.

Greensfelder, R. W., F. C. Kintzer and M. R. Somerville (1980a). Seismotectonic regionalization of the Great Basin, and comparison of moment rates computed from Holocene strain and historic seismicity, Proceedings of Conference X - Earthquake Hazards Along the Wasatch and Sierra-Nevada Frontal Fault Zones, U. S. Geol. Surv. Open File Report 80-801, 433-493.

Greensfelder, R. W., F. C. Kintzer, and M. R. Somerville (1980b). seismotectonic regionalization of the Great Basin, and comparison of moment rates computed from Holocene strain and historic seismicity: Summary, Bull. Geol. Soc. Am. 97, 518-523.

Griscom, M. (1980). Space-time seismicity patterns in the Utah region and an evaluation of local magnitude as the basis of a uniform earthquake catalog, M.S. thesis, Univ. of Utah, Salt Lake City, Utah.

Gutenberg, B. and C. F. Richter (1954). Seismicity of the Earth and Associated Phenomena, Princeton Univ. Press.

Hamblin, W. K. (1970). Structure of the western Grand Canyon region, in Guidebook to the Geology of Utah, no. 23, W. K. Hamblin and M. G. Best, Editors, Utah Geol. Soc., 3-20.

Hamblin, W. K., and M. G. Best (1979). Patterns and rates of recurrent movement along the Wasatch-Hurricane-Sevier fault zone during late Cenozoic time, Summaries of Technical Reports for National Earthquake Hazards Reduction Program, vol. VIII, 126-127.

Hanks, T. C. and M. Wyss (1972). The use of body wave spectra in the determination of seismic source parameters. Bull. Seis. Soc. Am., 62, 561-589.

Hansen, W. R. (1969). The geologic story of the Uinta Mountains, U.S. Geol. Surv, Bull., 1291, 144 pp.

Hardy, C. T. (1979). Oral communication.

Herrmann, R. B. (1978). Computer Programs in Earthquake Seismology, Vol. 1, R. B. Herrmann, editor, Department of Earth and Atmospheric Sciences, Saint Louis University, Saint Louis, Missouri.

Hoover, J. D. (1974). Periodic Quaternary volcanism in the Black Rock Desert, Utah, Brigham Young Univ. Geol. Studies 21, part 1, 3-72.

Hunt, G. B., H. D. Varnes, and H. E. Thomas (1953). Lake Bonneville-geology of northern Utah Valley, U.S. Geol. Surv. Prof. Paper 257-A.

Julian, B. R. and D. L. Anderson (1968). Travel times, apparent velocities and amplitudes of body waves, Bull. Seis. Soc. Am. 58, 339-366.

Kaliser, B. N. (1972). Environmental geology of the Bear Lake area, Rich County, Utah, Utah Geol. and Mineral. Survey Bull. 96, 1-32.

Kanamori, H., and D. L. Anderson(1975). Theoretical basis of some empirical relations in seismology, Bull. Seis. Soc. Amer., 1073-1095.

Keilis-Borok, V. I. (1959). An estimation of the displacement in an earthquake source and of source dimensions, Ann. Geofis., 12, 205-214.

Kostrov, V. V. (1974). Seismic moment and energy of earthquakes, and seismic flow of rocks, IZV. Acad. Sci. SSR, Phys. Solid Earth, 1, 23-40.

Lawerence, R. D. (1976). Strike slip faulting terminates the Basin and Range Province in Oregon, Bull. Geol. Soc. Am., 87, 846-580.

Luedke, R. G. (1954). Geology of the Capitol Reef area, Wayne and Garfield Counties, Utah, in Geology of Portions of High Plateaus and Adjacent Canyonlands of Central and South Central Utah, Intermtn. Assoc. of Petroleum Geologists Fifth Annual Field Conf., 39-62.

McDonald, R. E. (1976). Tertiary tectonics and sedimentary rocks along the transition, Basin and Range Province to plateau and thrust belt province, Utah, in Rocky Mtn. Assoc. of Geologists, 1976 Symposium on Geology of the Cordilleran Hinge-line, J. G. Hill, editor, 281-318.

Marine, I. W., and D. Price (1964). Geology and groundwater resources of the Jordon Valley, Utah, Utah Geol. and Mineral Survey Water-Res. Bull., 7.

Marsell, R. E. (1964). The Wasatch fault zone in Salt Lake County; Utah in The Wasatch Fault Zone in North Central Utah, Utah Geological Society Guidebook No. 18, R. E. Marsell, editor, Utah Geol. Soc., 31-50.

Molnar, P. (1979). Earthquake recurrence intervals and plate tectonics, Bull. Seis. Soc. Am., 69, 115-133.

Morrison, R. B. (1965). Lake Bonneville Quaternary stratigraphy of eastern Jordan Valley, south of Salt Lake City, Utah, U.S. Geol. Survey Prof. Paper 477, 80 pp.

Proctor, P. D., (1959). Structural geology-Broad Canyon-Fivemile Pass areas, in Geology of the Southern Oquirrh Mountains and Fivemile Pass-North Boulter Mountains Area, Tooele and Utah Counties, Utah, Guidebook to the Geology of Utah No. 14, H. J. Bissel, editor, Utah Geol. Soc., 198-210.

Richardson, R. M., and S. C. Solomon (1977). Apparent stress and stress drop for intraplate earthquakes and tectonic stress in the plates, Pageoph. 115, 317-331.

Richins, W. D. (1979). Earthquake data for the Utah region, 1850 to 1978, in Earthquake Studies in Utah 1850 to 1978, W. J. Arabasz, R. B. Smith, and W. D. Richins, editors, Univ. of Utah Seismograph Stations, Salt Lake City, Utah, 57-252.

Rigby, J. K. (1958). Geology of the Stansbury Mountains, in Geology of the Stansbury Mountains, Tooele County Utah, Guidebook to the Geology of Utah No. 13, J. K. Rigby, editor, Utah Geol. Soc., 1-134.

Rigby, J. K. (1962). Some geomorphic features of the southern Wasatch Mountains and adjacent areas, Brigham Young Univ. Geol. Studies 9, part 1, 80-84.

Rowley, P. D. (1968). Geology of the southern Sevier Plateau, Utah, Ph.D. thesis, Univ. of Texas at Austin, 340 pp.

Schilly, M. M. (1979). Lithospheric structure of an intraplate hot spot, the Yellowstone-Snake River Plain region, M.S. thesis, Univ. of Utah, Salt Lake City, Utah.

Scott, W. E. (1979). Stratigraphic problems in the usage of Alpine and Bonneville Formations in the Bonneville Basin, Utah, Geol. Soc. America Abs. with Programs, 11, 302.

Shenon, P. J. (1936). The Utah earthquake of March 12, 1934 (extracts from unpublished report), pp. 43-48 in Neumann, F., United States Earthquakes, 1934, U.S. Coast and Geodetic Survey, serial 4593.

Smith, R. B. (1978). Seismicity, crustal structure, and intraplate tectonics of the interior of the western Cordillera, in Cenozoic Tectonics and Regional Geophysics of the Western Cordillera, R. B. Smith and G. P. Eaton, editors, Memoir 152, Geol. Soc. of Am., 85, 111-144.

Smith, R. B., and W. J. Arabasz (1979). Seismicity, tectonics, and crustal structure in Utah: Important aspects from new data in Earthquake Studies in Utah 1850 to 1978, W. J. Arabasz, R. B. Smith, and W. D. Richins, editors, University of Utah Seismograph Stations, Salt Lake City, Utah 395-408.

Smith, R. B. and A. G. Lindh (1978). Fault-plane solutions of the Western United States: A compilation, in Cenozoic Tectonics and Regional Geophysics of the Western Cordillera, R. B. Smith and G. P. Eaton, editors, Memoir 152, Geol. Soc. Am., 85, 107-110.

Smith, R. B. and M. L. Sbar (1974). Contemporary tectonics and seismicity of the western United States with emphasis on the Intermountain seismic belt, Bull. Geol. Soc. Am. 85, 1205-1218.

Smith, R. B., L. W. Braile, and G. P. Keller (1975). Upper crustal low velocity layers: possible effects of high temperatures over a mantle upwarp at the Basin Range-Colorado Plateau transition, Earth and Planetary Science Letters 28, 197-204.

Smith, R. B., P. L. Winkler, J. G. Anderson, and C. H. Scholz (1974). Source mechanisms of microearthquakes associated with underground mines in eastern Utah, Bull. Seism. Soc. Amer., 64, 1295-1317.

Spieker, E. M. (1949). The transition between the Colorado Plateau and the Great Basin, in Central Utah, in The Transition Between the Colorado Plateau and the Great Basin in Central Utah, Guidebook to the Geology of Utah No. 4, Utah Geol. Soc., 1-106.

Spottiswoode, S. M. and A. McGarr (1975) Source parameters of tremors in a deep-level gold mine, Bull. Seis. Soc. Amer., 65, 93-112.

Starr, A. T. (1928). Slip in a crystal and rupture in a solid due to shear, Proc. Cambridge Phil. Soc. 24, 489-500.

Swan, F. H., III, D. P. Schwartz, K. L. Hanson, P. L. Kneupfer, and L. S. Cluff (1978). Study of earthquake recurrence intervals on the Wasatch Fault, Utah, semi-annual technical report for the U.S. Geol. Survey, contract No. 14-08-0001-16827, 31 p.

Thatcher, W. and J. N. Brune (1971). Seismic study of an ocean ridge earthquake swarm in the Gulf of Californis, Geophys. J.R. Astr. Soc. 22, 473-489.

Thatcher, W. and T. C. Hanks (1973). Source parameters of southern California earthquakes, J. Geophys. Res. 78, 8547-8576.

Thomas, E. H. and G. H. Taylor (1946). Geology and groundwater resources of Cedar City and Parowan Valleys, Iron County, Utah, U.S. Geol. Survey Water Supply Paper 993.

Trifunac, M. D. (1972). Stress estimates for the San Fernando, California, earthquake of February 9, 1971: Main event and thirteen aftershocks, Bull. Seis. Soc. Am. 62, 721-750.

United States Geological Survey (1976). A study of Earthquake losses in the Salt Lake City, Utah area, Open File Report 76-89, 357 pp.

Walton, P. T. (1954). Wasatch Plateau gas fields, Utah, in Geology of portions of High Plateaus and Adjacent Canyonlands of Central and South Central Utah, Intermtn. Assoc. of Petroleum, Geologists Fifth Annual Field Conf., 79-85.

Williams, B. R. (1979). M_S calculations from a generalized AR parameter method for WWSSN instruments, Bull. Seis. Soc. Am., 69, 309-351.

Winkler, P. L. (1972). Source mechanisms of earthquakes associated with coal mines in eastern Utah, M.S. thesis, Univ. of Utah, Salt Lake City, Utah.

Witkind, I. J. (1975a). Preliminary map shown known and suspected active faults in Idaho, U.S. Geol. Survey Open File Report OF-75-278.

Witkind, I. J. (1975b). Preliminary map showing known and suspected active faults in Wyoming, U.S. Geol. Survey Open File Report OF-75-279.

Woodward-Clyde Consultants (1975). Study of earthquake recurrence intervals on the Wasatch fault, Utah, Final technical report for U.S. Geol. Survey. Contract No. 14-08-0001-16827, 37 p.

Wyss, M. and J. N. Brune (1968). Seismic moment, stress, and source dimensions for earthquakes in the California-Nevada region, J. Geophys. Res. 73, 4651-4694.

Young, J. C. (1955). Geology of the southern Lakeside Mountains, Utah, Utah Geol. and Mineral. Survey Bull. 56, 1-108.

Zoback, M. L. and M. D. Zoback (1980). Faulting patterns in north-central Nevada and strength of the crust, J. Geophys. Res., 85, 275-284.

VITA

Name	Diane Irene Doser
Birthdate	December 22, 1956
Birthplace	Syracuse, New York
High School	Montabella High School Edmore, Michigan
University 1974-1978	Michigan Technological University Houghton, Michigan
Degree 1978	B.S. in Applied Geophysics Michigan Technological University Houghton, Michigan
Professional Organizations	Society of Exploration Geophysicists, Seismological Society of America
Publications	D. I. Doser and R. B. Smith, Earthquake recurrence intervals from seismic moment rates in Utah (abstract), Earthquake Notes 50, 70, 1979.

ATTACHMENT No. 4

FLEXURE AND NORMAL FAULTING IN LITHOSPHERIC PLATES WITH APPLICATION TO THE WASATCH FRONT, UTAH

by

Thomas Joseph Owens

A thesis submitted to the faculty of The University of Utah in partial fulfillment of the requirements for the degree of

Master of Science

in

Geophysics

Department of Geology and Geophysics

The University of Utah

December 1980

ABSTRACT

A mathematical model of normal faulting in the lithosphere has been developed that consists of a thin plate supported by a fluid substratum. A normal fault is introduced as a cut through the entire plate. The thin plate is assumed to have an elastic-perfectly plastic rheology and the flexure and stress distribution are calculated as displacement on the fault increases. The elastic-perfectly plastic rheologic model has the characteristic that stress in the plate cannot increase beyond a specified yield value. Solutions of this problem were applied to the Wasatch Front region of Utah. When constrained by the observed fault displacement, microseismicity, and tilting of fault blocks the model indicates that the lithospheric layer in the eastern Basin and Range has an effective mechanical thickness of about 20 km, a low elastic modulus, 0.8 to 1.5×10^{10} n/m^2, a low yield strength, 1 to 2 kb, and must be unconstrained at the fault. A comparison of results from similar studies in oceanic regions indicates similar temperatures at the base of the lithospheric layer in both regimes. This comparison also suggests several topics where further study would be beneficial in the Wasatch Front region. These topics include research involving the rheology of the lithosphere in this region, the incorporation of these modeling results into earthquake cycle studies, and an evaluation of possible vertical loading mechanisms for normal faults.

TABLE OF CONTENTS

LIST OF ILLUSTRATIONS

LIST OF SYMBOLS

w	-	vertical displacement of the plate (flexure)
w_o	-	flexure at x = 0 at onset of plasticity
w_{max}	-	flexure at x = 0 at maximum extent of plasticity zone
w_o^*	-	normalization factor for nondimensional flexure $w_o^* = w_o$ at $x = 0$, $\phi = 0$
$\bar{w}$	-	nondimensional flexure
X	-	distance
$\bar{X}$	-	nondimensional distance ($X = \frac{X}{\alpha}$)
Z	-	vertical direction, z positive upwards
M	-	bending moment
$\bar{M}$	-	nondimensional bending moment
M_o	-	bending moment at onset of plasticity
M_c	-	critical bending moment
σ_x	-	bending stress
$\bar{\sigma}_x$	-	nondimensional bending stress
σ_{max}	-	maximum bending stress
$\bar{\sigma}_{max}$	-	nondimensional bending stress (maximum)
ϵ_x	-	bending strain
σ_o	-	yield stress
h	-	thickness of plate
α	-	flexural parameter of plate
N	-	flexural rigidity of plate

LIST OF SYMBOLS (continued)

ρ_c - plate density

ρ_s - substratum density

E - Young's modulus

ν - Poisson's ratio

ACKNOWLEDGMENTS

This thesis benefited from the input of many people during the course of my research. My committee of Dr. Robert B. Smith; chairman, Dr. David S. Chapman, and Dr. Ronald L. Bruhn provided useful comments concerning the presentation of this material. Dr. Geroge Zandt deserves special credit and thanks for first applying this modeling idea to the Wasatch Front and for the many, many hours he spent discussing both the technical and philosophical aspects of this project with me. Two lengthy discussions with Dr. William G. Pariseau helped me clarify this problem in my own mind. Diane Doser and Kevin Furlong often listened to the problems associated with this project. Donna M. Thomas assisted in preparing this manuscript.

Financial support was provided by several sources. Dr. Robert B. Smith acquired funds for the computing this project required. Shell Oil Company provided me with a fellowship during my first year of graduate work. During my second year, I was supported by a University of Utah Graduate Research Fellowship. The University of Utah Seismograph Stations, through U.S. Geological Survey contract no. 14-08-0001-16725, supported the preparation of this manuscript.

INTRODUCTION

Determining the relationship between the observed geophysical and geological characteristics and the tectonic processes of a region involves the development of mechanical models to simulate various factors that may influence deformation in the area. The complexities involved in modeling earth processes require that the model development be an evolutionary procedure which begins with a simple earth model that can be evaluated with relative ease by comparison of the model predictions with available data. This model can then be modified and improved so that at each stage in the analysis the influence of a new parameter on the model predictions can be adequately determined. The ultimate goal in an analysis such as this is an effective evaluation of which parameters dominate the tectonism of the region within the constraints of observed geophysical and geological data.

Considered in this framework, this thesis is a variation and improvement of a mechanical model of the Wasatch Front, Utah which was originally proposed by Zandt (1979) and modified by Zandt and Owens (1980) to help interpret some complexities in the seismicity patterns of the area. Simply stated, the model consists of a homogeneous layer overlying a substratum that responds only with bouyancy forces. A fault that penetrates the entire plate is introduced and the model responds to maintain isostatic equilibrium. The variable in this study is the mechanical behavior, or rheology, of the plate. In this

study, an ideal elastic-perfectly plastic rheology is assumed for the plate. This rheology is thought to be a more realistic approximation to the long-term mechanical behavior of the lithosphere than those used in previous studies cited above (Forsyth, 1980). The theoretical characteristics of the deformation predicted in this analysis will be shown to be consistent with much of the observed data in the region. The limitations the observed data place on the model result in the encouraging prediction of a thin lithospheric layer of low strength in the eastern Basin and Range.

Following a brief section reviewing the geologic setting and pertinent data constraints of the Wasatch Front, the model will be presented in detail and the consequences of assuming an elastic-perfectly plastic rheology for the plate will be evaluated. These results will then be compared to the predictions of elastic and viscoelastic models as presented by Zandt and Owens (1980). Finally, a discussion of the implications and limitations of the model will lead to recommendations of what the next cycle of model improvements for the Wasatch Front should involve.

The Wasatch Front

The Wasatch Front, Utah marks the physiographic boundary between the Basin and Range province to the west and the Middle Rocky Mountains and Northern Colorado Plateau on the east (Figure 1). It forms part of the Intermountain Seismic belt as defined by Sbar *et al.* (1972) and Smith and Sbar (1974). The Wasatch fault, a major north-south trending west-dipping normal fault zone along which the young

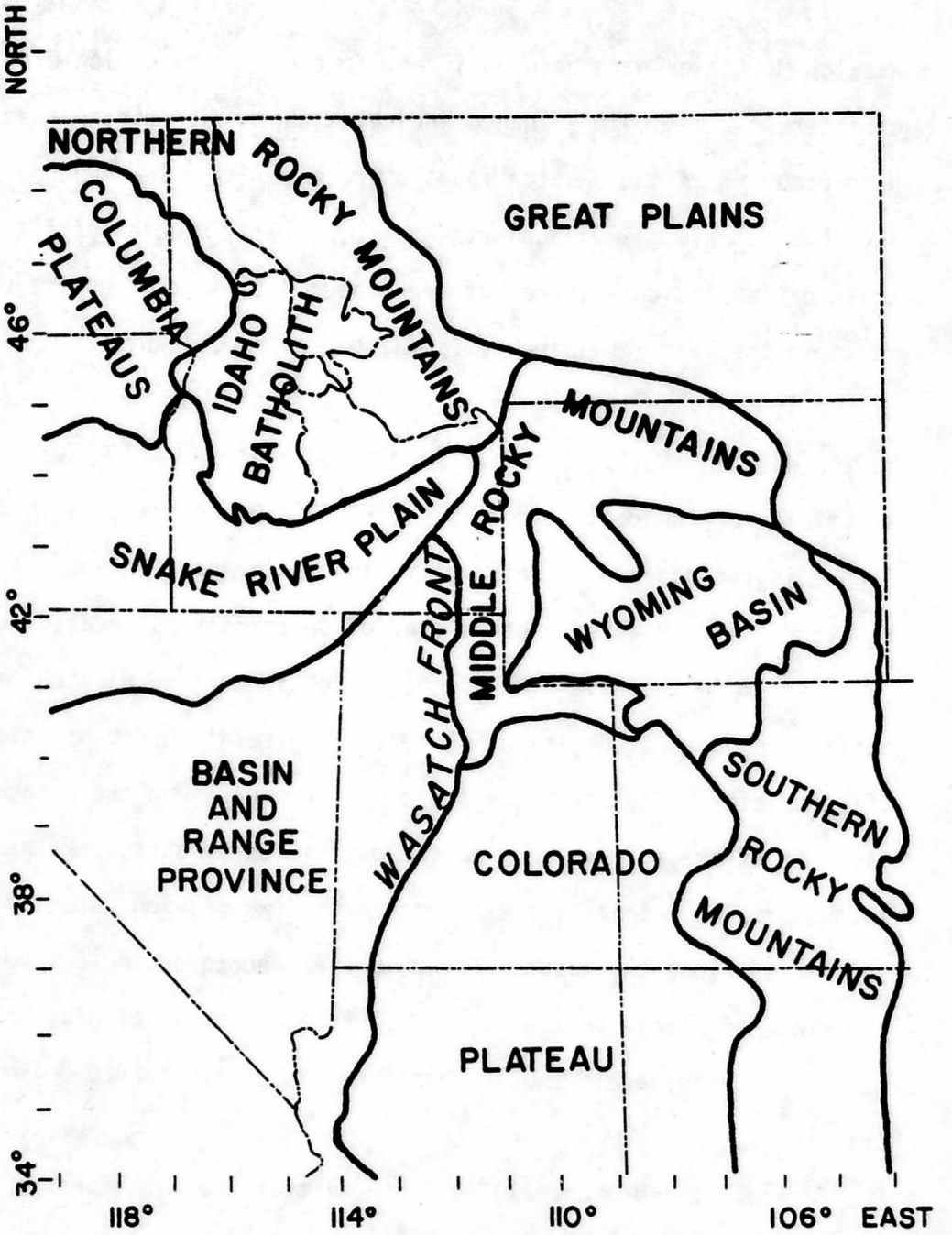

Figure 1. Physiographic map of the central western United States showing the Wasatch Front region.

Wasatch Mountains have been uplifted, is the primary geologic feature of interest. Geologic evidence indicates that major earthquakes (M~7) have occurred on the Wasatch fault as recently as a few hundred years ago (Swan et al., 1979; Schwartz et al., 1979). Studies of fission track dating indicate there has been about 3 to 4 km of uplift on the fault in the last 7 million years (Naeser et al., 1980).

Seismicity in the region is rather diffuse, but roughly centered on the Wasatch fault. Figure 2 from Arabasz et al. (1979) shows the seismicity of the region from 1974 to 1978. Of interest in this figure is the absence of seismicity along major portions of the Wasatch fault. However a broad zone of seismicity is located roughly 15 to 45 km to the east of the central section of the Wasatch fault outlined by the rectangle in Figure 1. The relationship of this zone of seismicity offset from the fault to earthquakes on the main Wasatch fault is of great importance to the evaluation of earthquake hazards in this region. In this thesis, as in the two previous studies, the seismicity along the Wasatch Front is presumed to be indicative of the state of stress in the region. Therefore, areas of high predicted stress in these models should correlate with the observed seismicity patterns.

Priestley and Brune (1978) indicate that the lithospheric thickness in the eastern Basin and Range is about 60 km using surface wave analysis. Walcott (1970b), in his work on Lake Bonneville rebound, found that the thickness of the lithosphere in long-term mechanical studies is about 20 km with the hot lower lithosphere acting as the asthenosphere normally would. This value correlates with a prediction

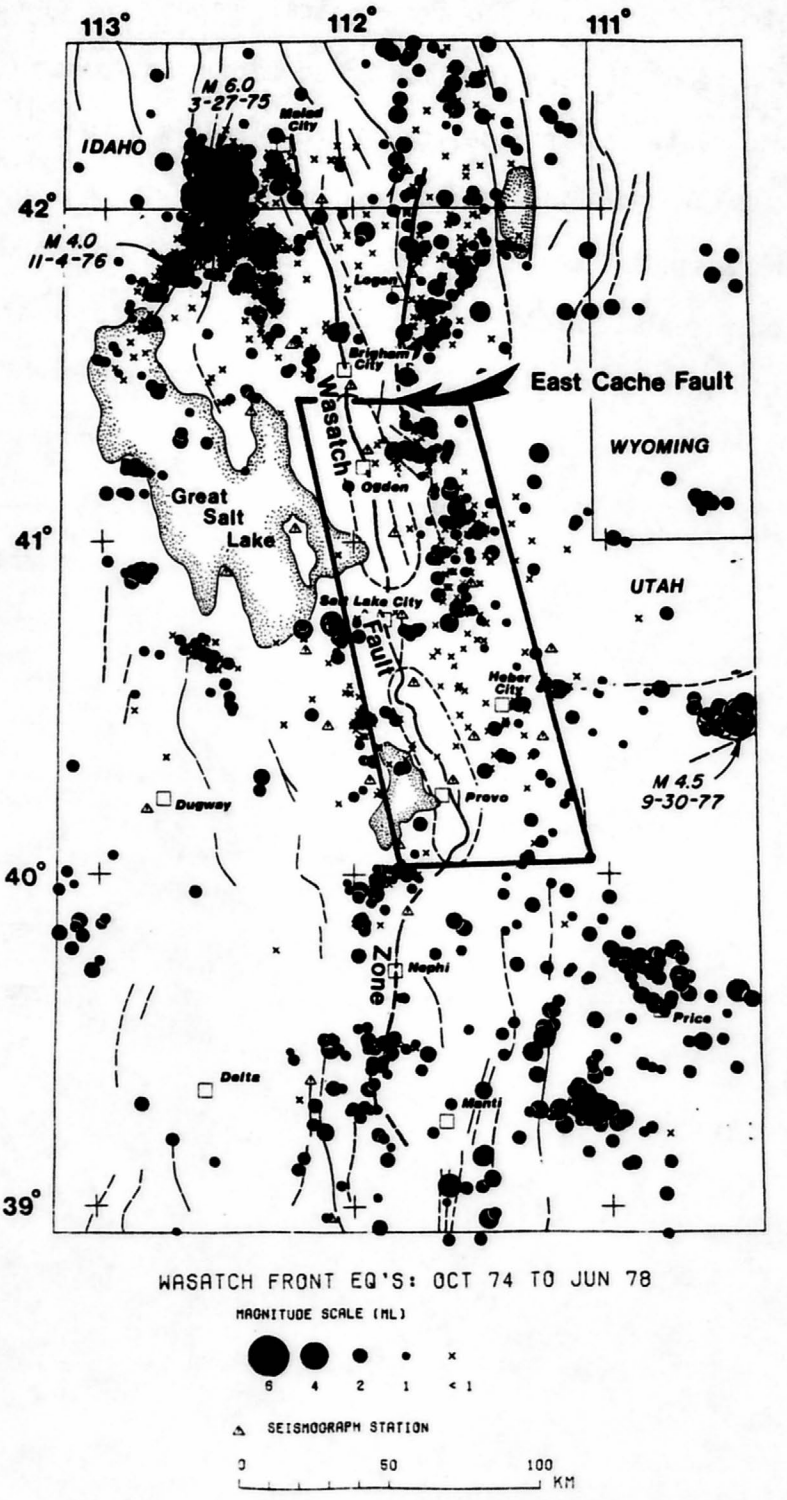

Figure 2. Seismicity map of the Wasatch Front from 1974 to 1978 (from Arabasz et al., 1979). Rectangle outlines the region of major interest for this study.

of 19 km for Basin and Range mechanical lithosphere by Murrell (1976) based on temperature effects on creep mechanisms. The thickness of the thin plate in the model to be presented is assumed to represent the long-term effective mechanical thickness of the lithosphere in the eastern Basin and Range. A value of 20 km will be used for the thickness of the plate in this study, although a discussion of possible variations in this value will be presented later.

DESCRIPTION OF THE MODEL

Representing the earth as a thin plate overlying a fluid-like substratum in modeling tectonic problems is not a new concept. Heiskanen and Vening Meinesz (1958) and Bott (1976) applied the model with an elastic layer to problems in graben formation. Walcott (1970a), Watts and Cochran (1974) and McNutt and Menard (1978) are among many researchers to apply the elastic plate model to a variety of long-term surface loading problems, while Walcott (1970b) proposed that the lithosphere behaved as if it had a viscoelastic rheology under these loads. In addition, the model has been applied extensively to approximate the bending of the lithosphere at subduction zones assuming an elastic rheology (see, for example, Caldwell et al., 1978; Parsons and Molnar, 1976) and also an elastic-perfectly plastic rheology (Turcotte et al., 1978). A useful overview of the various rheologies that have been assumed in oceanic studies and their respective merits when compared to a variety of observations can be found in Forsyth (1980). This study found that an elastic-perfectly plastic plate rheology with a depth-dependent yield strength such as that presented by Chapple and Forsyth (1979) and Bodine and Watts (1979) appeared to be the most appropriate rheologic model. It was also the best approximation to the yield envelope presented by Goetze and Evans (1979) based on experimental rock mechanics data. The rheology that is assumed in this study, elastic-perfectly plastic with constant

yield stress, is a simplification of Forsyth's preferred model, but is one that Forsyth (1980) found to be quite adequate in many respects in oceanic regions. A discussion of some of the factors that appear to influence the mechanical behavior of the lithosphere will be discussed in a later section. In this chapter the model as applied to the Wasatch Front will be described in detail, the work of Zandt and Owens (1980) will be reviewed, and the predictions obtained by assuming an elastic-perfectly plastic plate rheology will be presented.

Fundamentals of the Model

The basic model shown in Figure 3a (modified from Zandt and Owens, 1980) consists of a thin homogeneous layer overlying a fluid half-space which only contributes bouyancy forces during loading. It is a two-dimensional plane strain problem since there is assumed to be no variation in the deformation, stress, or material properties in the y-direction. This thin layer is then completely cut by a normal fault (Figure 3b), presumed to be caused by horizontal extension. It is now assumed that the hanging wall and footwall sides of the fault are completely decoupled so that their responses can be analyzed separately. This is equivalent to assuming that the fault is frictionless. This assumption, although probably invalid at any given moment, is considered adequate for analyzing the long term effects of motion on the Wasatch fault. Discussion of this assumption can be found in Zandt and Owens (1980) and will be continued in a later section.

The decoupling of the layer across the fault essentially removes the material above the fault from creating a downward force on the

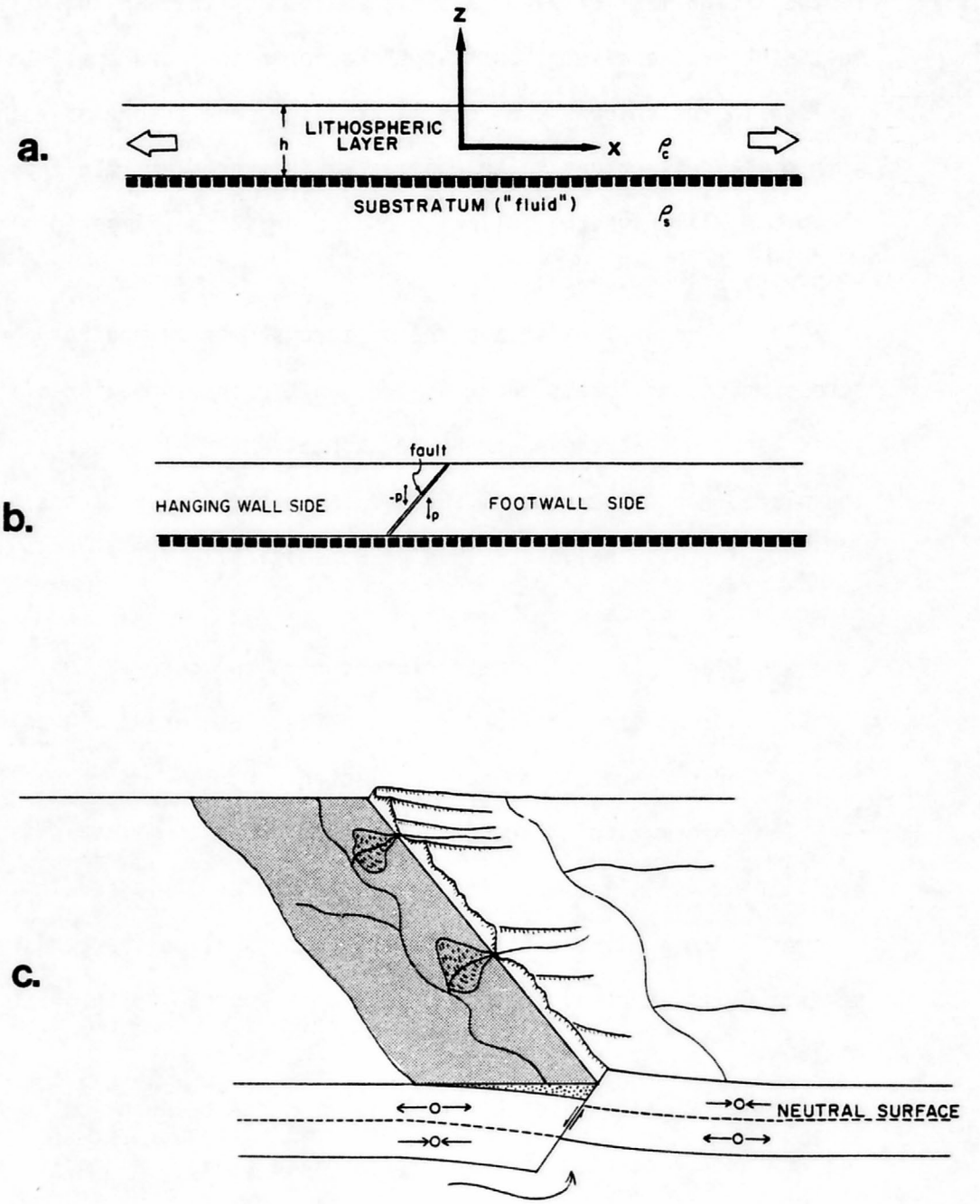

Figure 3. Schematic illustration of fundamental mechanical model. The sequence of events is described in the text. Figure modified from Zandt and Owens (1980).

footwall block. In order to maintain isostatic equilibrium, the footwall side must rise (by a similar argument the hanging wall side must sink). The assumption that the deformations are small in comparison to the thickness of the layer allows the theory of thin plates with small deflections to be applied to this problem. In this case, the plate will have the following characteristics (Timoshenko and Woinowsky-Krieger, 1959):

1) There will exist a plane of zero stress (a neutral surface) across which the stress changes sign. After the formation of the fault it is assumed that there are no horizontal external forces acting on the plate, hence the neutral surface is in the middle of the plate (at z=0) in this analysis. This is schematically illustrated in Figure 3c.

2) Plane sections remain plane during the deformation.

3) Normal stresses transverse to the plate are small compared to the bending stresses and are neglected.

The deformation of the thin plate in order to maintain isostatic equilibrium is called the flexure of the plate. This bending induces a moment across plane sections of the plate, called the bending moment, which is considered to be the only source of stress in the plate.

The assumptions stated here allow for the calculation of the flexure and associated stress for the plate under the conditions outlined above. In order to do this several relationships associated with the model are required. First,

$$\frac{d^2M}{dx^2} + \rho_s g w = 0. \qquad (1)$$

Equation (1) is a statement of equilibrium of forces, where M = the bending moment, w = the vertical displacement, or flexure, and ρ_s = the density of the substratum, and g = the acceleration due to gravity. A list of all the symbols and notations used in this study is included in the front of this thesis. A bending moment versus bending stress, σ_x, relationship is also required (from Nadai, 1963, pg 250):

$$M = \int_{\frac{-h}{2}}^{\frac{h}{2}} \sigma_x z dz \qquad (2)$$

A third relationship which will be useful relates the bending strain, ε_x, to the curvature of the plate (Nadai, 1963, pg 250):

$$\varepsilon_x = z \frac{d^2w}{dx^2}. \qquad (3)$$

Equations (1), (2), and (3) do not require the assumption of any material properties whatsoever and are therefore valid for thin plates of any rheology. The general procedure to derive w in the elastic and elastic-plastic cases is to use knowledge of σ_x versus z and ε_x versus σ_x relationships for that rheology to combine equations (2) and (3) into a moment versus curvature relationship valid for that particular rheology then solve for w using (1) and the new moment-curvature relationship.

Previous Wasatch Front Models

Zandt and Owens (1980) used the model described above to model the Wasatch Front assuming elastic and viscoelastic rheologies. Several characteristics of the theoretical solutions were chosen by them to compare with observed data to determine the fit of the solution. These characteristics are listed below.

1) Flexure shape. The shape of the theoretical flexure represents the predicted basement topography of the Wasatch Front region. This comparison can only be qualitative because the observed topography is complicated by erosional effects as well as any pre-existing topography. The observed eastward tilting of the Wasatch Mountains of about 10° (Eardley, 1933) should be kept in mind when considering the flexure shape.

2) Maximum Amplitude of the Flexure. The predicted displacement along the Wasatch fault is another important parameter in the model. None of the models presented by Zandt and Owens (1980) adequately accounted for the 3 to 4 km of uplift postulated for the Wasatch fault. The major complicating factor surrounding this parameter is the effect of sediment loading and erosion on the maximum uplift.

3) Theoretical Graben Width. Bott (1976) used a similar model to predict the width of grabens in an elastic crust. The theoretical graben width was considered to be the distance from the fault to the point of maximum bending moment. This corresponds to the point of maximum stress in the elastic case. Zandt and Owens (1980) compared this parameter to estimates of graben widths of 8 to 26 km for

valleys just west of the Wasatch fault. These estimates were obtained from gravity data by Cook and Berg (1961). The significance of these estimates to the model is not obvious since the valleys are bounded on the west by at best only small displacement normal faults. In the elastic-perfectly plastic model which is considered here this parameter cannot be used since there will only be a zone of maximum stress rather than a specific point.

4) Theoretical Stress Distribution. Under the assumption that the observed seismicity in the Wasatch Front region is directly related to the magnitude and distribution of stress in the crust, the predicted areas of high stress in the models should correlate with the observed regions of seismicity. This correlation should ideally include the bimodal depth distribution of earthquake focal mechanisms predicted by the existence of the neutral surface. In the Wasatch Front region there does not exist sufficient data to construct such a relationship. However, compressional focal mechanisms do exist east of the Wasatch fault near Heber City, Utah (Arabasz et al., 1979). This indicates the existence of compressional stress in this region although a depth-stress relationship cannot be constructed. Along with the maximum amplitude of the flexure, the theoretical stress distribution was most important in the analysis by Zandt and Owens (1980).

In this analysis the observed uplift on the Wasatch fault, the eastward tilting of the Wasatch Mountains, and the observed microseismicity pattern associated with the central portion of the Wasatch fault (Figure 2) will be used to evaluate the fit of the model in

this region. Other data available in the Wasatch Front region that cannot be used as constraints in this analysis include earthquake focal depth information (Arabasz et al., 1979) and geodetic leveling and strain data (Prescott et al., 1979). The geodetic data are not useful because without a theoretical earthquake cycle model for the region and knowledge of what stage in that cycle the geodetic data reflect, there is no way of separating long-term trends in the data from short-term effects. Earthquake focal depth data are not very useful because of the problem of determining the transition between stick-slip and stable-slide failure zones. This will be discussed in more detail in a later section.

A brief summary of the work of Zandt and Owens (1980) is included in the Appendix. The mathematics of their models is presented within the framework used in this study and the results are summarized. The major problem with the elastic models is an underestimation of the amplitude at the fault, while less critically over estimating the graben width. The viscoelastic model was an attempt at a more realistic model. Table 1 illustrates that although the introduction of viscoelasticity helped in some respects, there are still problems with some of the model parameters. The analysis of an elastic-perfectly plastic plate model described in the next section is a further modification of the basic model that also permits some interesting conclusions regarding the Wasatch Front.

Table 1. Theoretical Results of Plate Models from Zandt and Owens (1980)

Rheology	Theoretical Graben width (km)	Amplitude at fault (meters) isostatic	Amplitude at fault (meters) with sediment factor	Maximum Stress (bars) isostatic	Maximum Stress (bars) with sediment factor
Elastic (unconstrained)	24 - 48	296 - 493	890 - 1500	305 - 508	916 - 1500
Elastic (constrained)	48 - 80	209 - 349	628 - 1000	-447 - -447	-1400 - -1700
Viscoelastic (unconstrained) $\frac{t}{\tau} = 10$	14 - 24		1500 - 2600		
Viscoelastic (constrained) $\frac{t}{\tau} = 10$	29 - 48		1100 - 1700		

An Elastic-Plastic Plate Model

Zandt and Owens (1980) postulated that some inelastic behavior of the lithosphere would probably have to occur if there is 3 to 4 km of uplift of the Wasatch Mountains along the Wasatch fault. This conclusion was based on the predicted stresses in the 5-10 kilobar range in an elastic model satisfying the observed uplift. In this section, this inelastic behavior is modeled by an elastic-perfectly plastic rheology (Prager and Hodge, 1951). The solid line in Figure 4 illustrates the one-dimensional stress-strain curve for this rheology. The material is plastic below the yield stress, σ_o, while above σ_o the deformation is plastic without strain hardening. This idealized behavior is supported by experimental rock mechanics studies by Griggs et al. (1960). Their stress-strain curve for the Dun Mountain dunite is plotted on Figure 4 for comparison in a manner similar to Turcotte et al. (1978). Griggs et al. (1960) ran this test at a confining pressure of 5 kilobars (kb) and a temperature of 300°C and obtained a σ_o value slightly less than 10 kb. While the pressure and temperature conditions of their test may not correspond to the conditions in the model presented below, the experimental support for the basic rheological assumption is encouraging.

Before describing the mathematics of the elastic-perfectly plastic plate model, an important point must be made concerning the motivation and assumptions implicit in the model. In the elastic models of Zandt and Owens (1980) once the isostatic equilibrium position is reached no further vertical displacement will occur without some vertical loading mechanism acting on the model. A rough

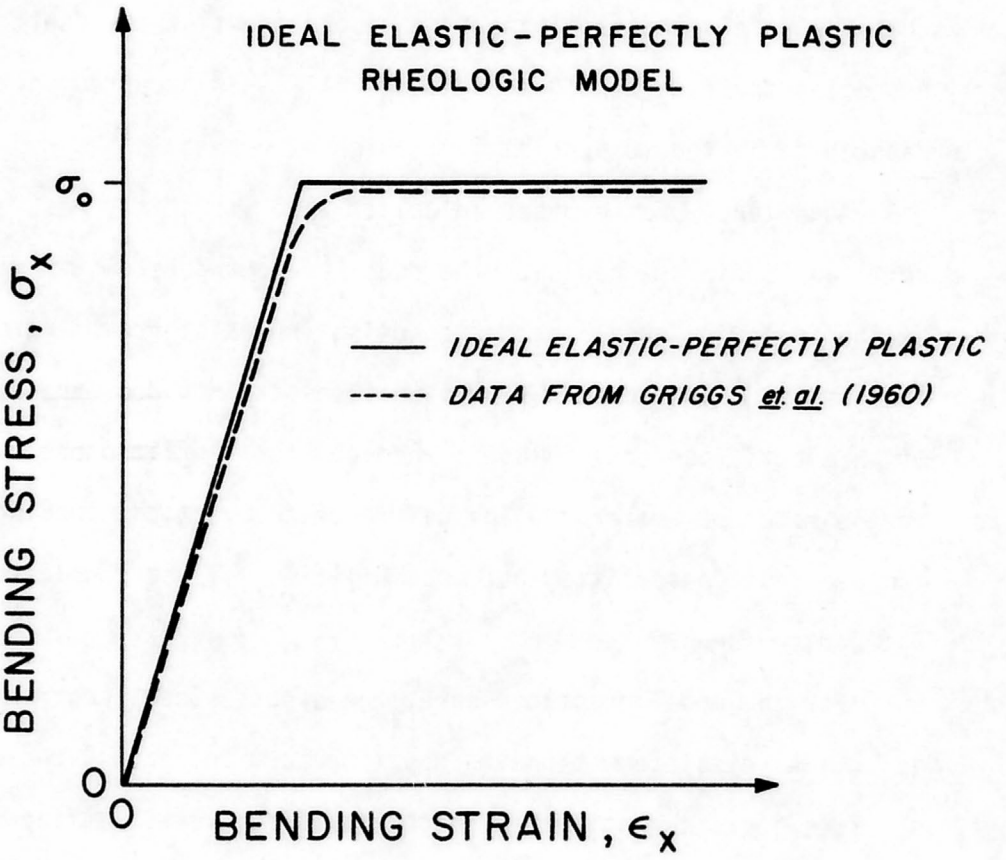

Figure 4. Ideal one-dimensional stress-strain relationship for the elastic-perfectly plastic rheology.

estimate of the effect of sediment loading by Zandt and Owens (1980) increased the amplitude somewhat (see Table 1), but the fact remained that the models underestimated the displacement at the fault. However, accepting the fact that 3 to 4 km of uplift has occurred on the Wasatch fault led to prohibitively high stresses.

Acceptance of the observed uplift also implicitly assumes some vertical loading mechanism. The model presented below was motivated by the following questions: "Accepting the existence of large displacements on the Wasatch fault, what constraints does the assumption of an elastic-perfectly plastic rheology for the lithosphere impose on the model parameters?" The nature of the vertical loading mechanism need not be specified but possibilities will be considered in a later discussion.

For the model presented here, the hypothesized scenario of events is: (1) As displacement on the Wasatch fault increases, the bending stresses increase until they reach a critical level, defined by σ_o, and a plastic zone (initially only one point wide) is formed. (2) Further displacement causes a widening of this plastic zone until a limit (defined by the mathematics of the problem) is reached. Figure 5 schematically illustrates the geometrical aspects of the problem and will be referenced regularly in the following sections. In the following analysis compression is positive and bending moments are assumed to be positive clockwise.

Model mathematics. Calculation of the deformation of a plate of elastic-perfectly plastic rheology supported by a fluid substratum can be performed within the framework of equations (1), (2), and (3).

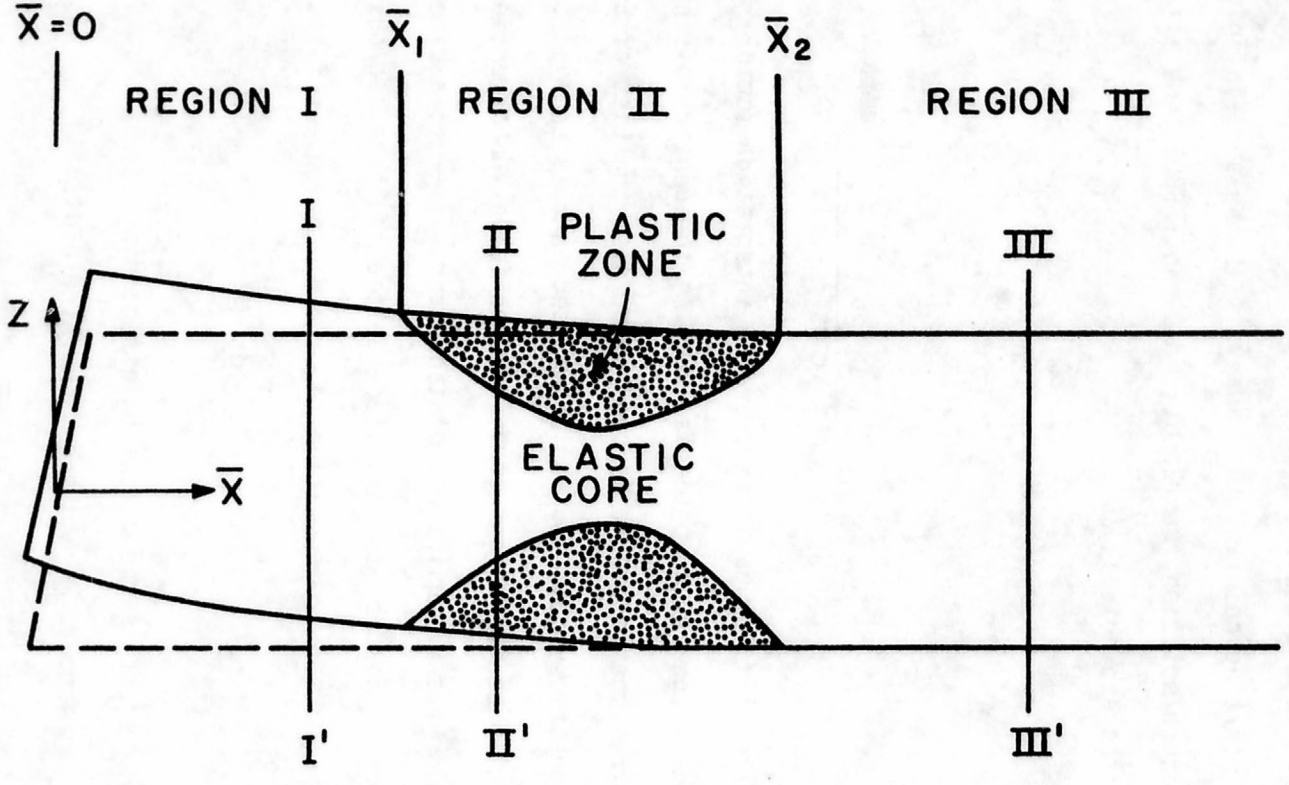

Figure 5. Schematic drawing of the elastic-perfectly plastic plate model. Bending stress-depth cross-sections for profiles I-I', II-II', and III-III' are shown in Figure 6.

This analysis follows closely that of Turcotte et al. (1978) who applied a similar model to the problem of bending of the oceanic lithosphere at trenches.

The starting point of this analysis is the semi-infinite elastic plate flexure solution from Zandt and Owens (1980) (see also equation (A-7) in the Appendix):

$$w = w_o e^{-\frac{x}{\alpha}} \cos\left(\frac{x}{\alpha} + \phi\right) \tag{4}$$

where

$$w_o = \frac{2P}{\rho_s g\, \alpha(\cos\phi - \sin\phi)} \tag{5}$$

and α = the flexural parameter, ϕ = an integration factor related to the boundary condition at the fault, ρ_s = the density of the substratum, and P = the isostatic force. Refer also the List of Symbols for definitions of symbols and variables used in this analysis.

It will be convenient to define the following dimensionless variables: $\bar{x} = \frac{x}{\alpha}$; a dimensionless distance and $\bar{w} = \frac{w}{w_o^*}$; a dimensionless flexure normalized by the amplitude at the fault at the onset of failure, w_o^*. So from equation (4) the dimensionless flexure is:

$$\bar{w} = \frac{e^{-\bar{x}} \cos(\bar{x} + \phi)}{\cos\phi - \sin\phi}. \tag{6}$$

Also of interest is the dimensionless bending moment, $\bar{M}$. In terms of the bending moment, M, and the flexural rigidity, N, we have

$$\bar{M} = \frac{d^2\bar{w}}{d\bar{x}^2} = \frac{\alpha^2}{N w_o^*} M \tag{7}$$

or

$$\bar{M} = \frac{2e^{-\bar{x}}\sin(\bar{x}+\phi)}{\cos\phi - \sin\phi}. \tag{8}$$

In the elastic case, the maximum bending stress can be expressed in terms of the bending moment, (for derivation see the Appendix)

$$\sigma_{max} = \pm\frac{6M}{h^2} \tag{9}$$

and in terms of $\bar{M}$,

$$\sigma_{max} = \frac{\pm Ehw_o^*}{2(1-\nu^2)\alpha^2}\bar{M}. \tag{10}$$

If we now recall that in the elastic case the stress distribution is linear with depth (illustrated in Figure 6a), we have

$$\sigma_x = \sigma_{max}\left[\frac{2z}{h}\right] \tag{11}$$

or

$$\sigma_x = \frac{Ehw_o^*}{2(1-\nu^2)\alpha^2}\left[\frac{2z}{h}\right]\bar{M} \tag{12}$$

We can now write a nondimensional bending stress:

$$\bar{\sigma}_x = \frac{2(1-\nu^2)\alpha^2}{Ehw_o^*}\sigma_x \tag{13}$$

or

$$\bar{\sigma}_x = \bar{M}\left[\frac{2z}{h}\right] \tag{14}$$

so that $\bar{\sigma}_{max} = \bar{M}$ in any plane vertical cross section of the slab.

In order to determine the onset of plasticity during the bending process a yield criteria must be established. It is assumed that

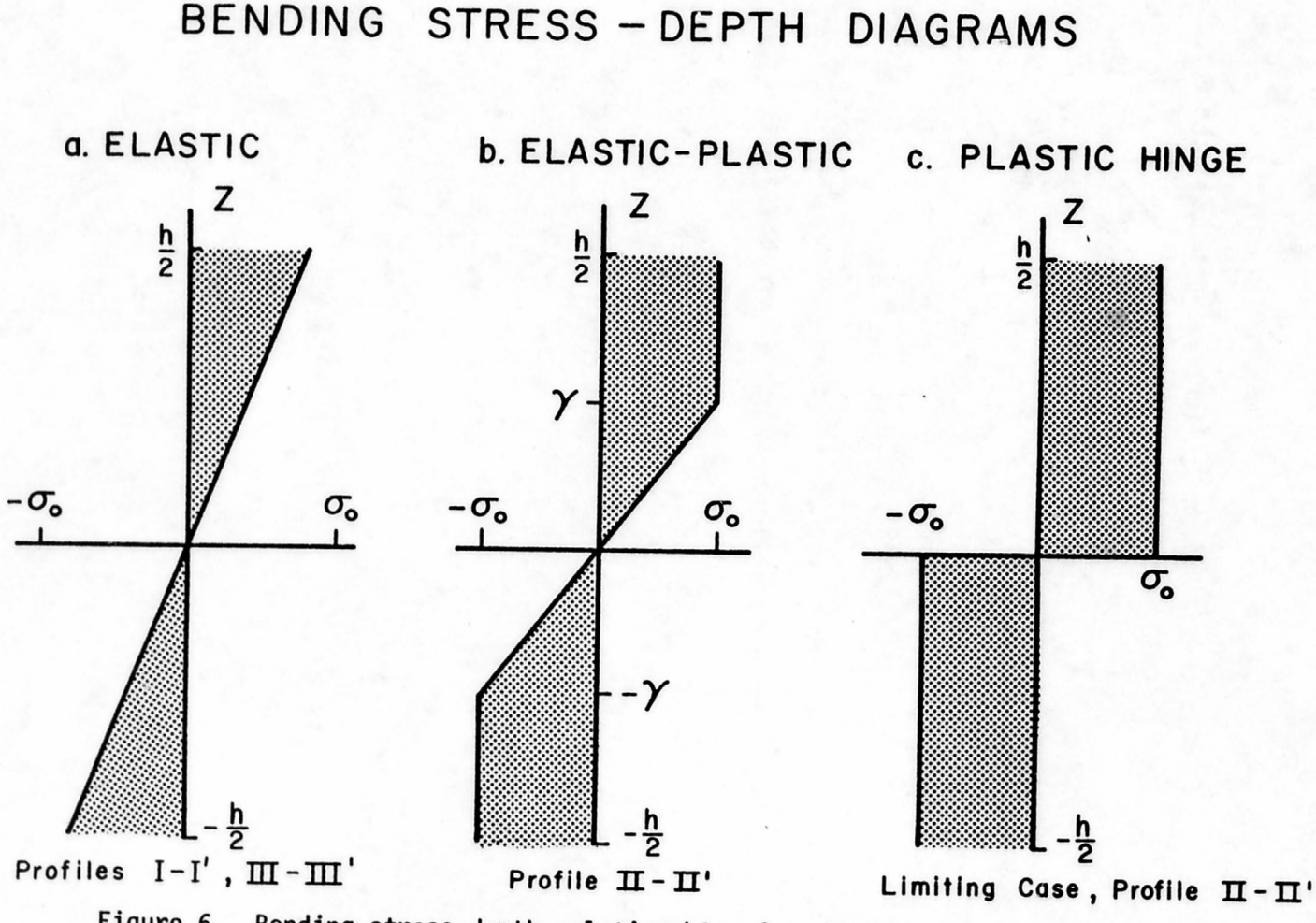

Figure 6. Bending stress-depth relationships for elastic and elastic-perfectly plastic rheologies.

plastic behavior commences when the bending stress exceeds σ_o:

$$|\sigma_x| = \sigma_o \tag{15}$$

This yield condition neglects the mean stress and assumes, as thin plate theory predicts, that the shearing stress is small compared to the bending stress. Chapple and Forsyth (1979) found that the error in neglecting the mean stress is negligible, while for yield stresses of one kilobar or less ignoring the shear stresses in determining plasticity could cause an underestimation of the strength of the lithosphere. Turcotte et al. (1978) related σ_o to the more familiar yield theories in plasticity analysis. They state that σ_o is equivalent to the uniaxial yield stress predicted by the Tresca yield criteria (Hill, 1950).

Using equations (10)and (15) we find that the magnitude of $\overline{M}$ in terms of the yield stress at the onset of plasticity is

$$\overline{M}_o = \frac{2(1-\nu^2)\alpha^2}{Ehw_o^*}\sigma_o \tag{16}$$

This indicates that in this elastic-plastic analysis the general solution (Equation (4)) for a bending elastic plate is no longer valid if $\overline{M} > \overline{M}_o$. After the onset of plasticity, equation (4) is valid only in Region III of Figure 5 since that is the only region where a semi-infinite elastic plate still exists.

In region II, the partially plastic zone, the bending stress versus depth distribution is (Prager and Hodge, 1951):

$$\sigma_x = \sigma_o \text{ for } \gamma \leq z \leq \frac{h}{2}$$

$$\sigma_x = \sigma_o \frac{z}{\gamma} \text{ for } -\gamma \leq z \leq \gamma \qquad (17)$$

$$\sigma_x = -\sigma_o \text{ for } -\frac{h}{2} \leq z \leq -\gamma$$

where γ is the distance from the center of the plate to the elastic-plastic interface, as illustrated in Figure 6b. Equation (17) can be combined with equation (2) to determine the bending moment due to this stress distribution:

$$M = \int_{\frac{-h}{2}}^{-\gamma} -\sigma_o z dz + \int_{-\gamma}^{\gamma} \sigma_o (\frac{z}{\gamma}) z dz + \int_{\gamma}^{\frac{h}{2}} \sigma_o z dz \qquad (18)$$

or

$$M = \frac{\sigma_o h^2}{4} (1 - \frac{4}{3}(\frac{\gamma}{h})^2). \qquad (19)$$

We can now define, as in Turcotte et al. (1978).

$$M_c = \frac{\sigma_o h^2}{4} \qquad (20)$$

as the critical bending moment. This corresponds to the bending moment when $\gamma = 0$, i.e. when the entire plate is plastic at some point. At this point, a "plastic hinge" develops and the curvature of the plate becomes infinite -- a physically unstable configuration. Notice that $M_c = \frac{3}{2} M_o$ is only slightly larger than the bending moment at the onset of plasticity.

In the elastic core ($-\gamma \leq z \leq \gamma$) of Region II, we know from Hooke's law and equation (3) that the relationship between σ_x and the curvature is:

$$\sigma_x = \frac{Ez}{1-\nu^2}\left[\frac{d^2w}{dx^2}\right] \tag{21}$$

So that at $z = \gamma$

$$\sigma_o = \frac{E\gamma}{1-\nu^2}\left[\frac{d^2w}{dx^2}\right] \tag{22}$$

Equations (19), (20) and the relationship $M_c = \frac{3}{2} M_o$ can be combined to obtain an expression for γ;

$$\gamma = \frac{h\sqrt{3}}{2}\left(1-\frac{2}{3}\left(\frac{M}{M_o}\right)\right)^{\frac{1}{2}}. \tag{23}$$

This expression can be substituted into (22) to give a moment versus curvature relationship valid in Region II:

$$\frac{d^2w}{dx^2} = \frac{2\sigma_o(1-\nu^2)}{Eh\sqrt{3}\left(1-\frac{2}{3}\left(\frac{M}{M_o}\right)\right)^{\frac{1}{2}}} \tag{24}$$

From this expression we see that when $M = M_o$, the curvature is infinite. The stress-depth distribution of this unstable case is given in Figure 6c (from Kachanov, 1971, pg 106).

Equation (24) represents the required moment-curvature relationship for the elastic-perfectly plastic region. Along with equation (1), it forms the necessary system for evaluating the flexure in this region. When equations (1) and (24) are written in terms of the

dimensionless variables defined earlier, we have the following system:

$$\frac{d^2\bar{w}}{d\bar{x}^2} = \frac{\bar{M}_o}{\sqrt{3}\left(1-\frac{2}{3}\left(\frac{\bar{M}}{\bar{M}_o}\right)\right)^{\frac{1}{2}}} \tag{25}$$

$$\frac{d^2\bar{M}}{d\bar{x}^2} = -4\bar{w} \tag{26}$$

These equations can be written as a system of first order differential equations,

$$\begin{aligned} q &= \bar{M}' \\ q' &= -4\bar{w} \\ u &= \bar{w}' \\ u' &= \frac{\bar{M}_o}{\sqrt{3}\left(1-\frac{2}{3}\left(\frac{\bar{M}}{\bar{M}_o}\right)\right)^{\frac{1}{2}}} \end{aligned} \tag{27}$$

This system was solved numerically given initial conditions at the Region II-Region III boundary using a standard 5th order Runge-Kutta differential equation solver from the IMSL library as part of the solution scheme described later in this chapter.

We must now find a solution valid in Region I of Figure 5. The plate is elastic in this region, therefore the governing differential equation is equation (A-5) in the Appendix:

$$N \frac{d^4w}{dx^4} + \rho_s g w = 0. \qquad (28)$$

The general solution is (after the introduction of our dimenionless variables)

$$\bar{w} = e^{\bar{x}}(A \cos \bar{x} + B \sin \bar{x}) + e^{-\bar{x}}(C \cos \bar{x} + D \sin \bar{x}) \qquad (29)$$

However in this case the elastic zone is bounded and there is no criteria for eliminating the exponentially growing solution. Continuity requirements at the Region II-Region I boundary provide the four necessary conditions for solving equation (28). These continuity conditions are that w, M, and their first derivatives be continuous at $\bar{x}_1$. Expressing the constants A, B, C, and D to satisfy these conditions is the final step to constructing a solution valid in Region I. This is a straightforward, yet cumbersome process which will not be presented here. It is essentially the same as given in Hetenyi (1946, p. 4-9).

Method of Solution

A valid solution for the flexure of the entire slab must satisfy several criteria:

1) The boundary condition at $\bar{x} = 0$ (at the fault) must be maintained throughout the process. This means the flexure must remain constrainted or unconstrained (as defined by Zandt and Owens (1980)) throughout the solution process.

2) Continuity of $\bar{w}$, $\bar{M}$, and their first derivatives must be maintained at both $\bar{x}_1$ and $\bar{x}_2$.

3) Equation (29) must be used in Region I. Note that in the case where $\bar{x}_1 = 0$, no Region I exists.

4) Equation 4 must be satisfied in Region III.

5) The system described in equation (27) must be applied in Region II.

6) $\bar{M} = \bar{M}_0$ at both $\bar{x}_1$ and $\bar{x}_2$.

The solution method developed to satisfy these conditions was a shooting method in which a solution was generated in Region III and then the solutions in Regions II and I were constructed. At $\bar{x} = 0$, the bending moment was compared with the desired value as determined by the fault constraint condition and, if these values were not equal within a tolerance, a new solution in Region III was generated and the procedure repeated. The only parameters that were specified were the moment condition at $\bar{x} = 0$ and the location of $\bar{x}_2$, the right-hand extent of Region II. Once a solution is found for one value of $\bar{x}_2$, it is incremented and the process is continued until the critical moment is reached. The solution calculated at the final increment is considered to be the maximum effect the introduction of elastic-perfectly plastic rheology can have on the model. In the following section some theoretical characteristics of the model will be discussed and the application of the model to the Wasatch Front will be considered.

Elastic-Perfectly Plastic Model Predictions

Using the method described in the previous section, the flexure of an elastic-perfectly plastic plate was calculated using both the constrained and unconstrained end conditions considered by Zandt and Owens (1980). The unconstrained case requires that the bending

moment at the fault be zero. This condition is thought to be representative of the long term behavior of the fault. The constrained case requires considerable bending moment acting at the fault. It is considered an end member representing the extreme case of constraint on the fault and will be shown to have some interesting implications concerning seismicity in the Wasatch Front region (see also Zandt and Owens, 1980).

The theoretical data will be presented in terms of the dimensionless variables in graphical form. In order to convert these theoretical curves to predicted parameters of the model it is necessary to assume some values for the constants in the normalization factors. The values assumed are tabulated in Table 2 and are similar to the values used by Zandt and Owens (1980). The only factor not included in this table is w_o^*. This can be calculated by combining equations (16), (8), and the knowledge that the onset of plasticity occurs at the point where the absolute magnitude of the stresses is largest in the elastic solution. For the unconstrained case ($\phi = -\frac{\pi}{4}$ in equation (4)) $\bar{x} = 0$. If we refer to the location of this point of maximum stress as $\bar{x}_m$, we have the following relationship:

$$w_o^* = \frac{\alpha^2 h^2 e^{\bar{x}_m}(\cos\phi - \sin\phi)\sigma_o}{12N \sin(\frac{\pi}{4})} \qquad (30)$$

This shows that w_o^* is proportional to the yield stress, so the larger the yield stress the greater the deflection must be before a plastic zone develops. If all of the theoretical solutions are normalized

Table 2. Summary of Material Properties

Parameter	Range	Value Assumed
Young's Modulus (E)	8×10^9 - 6×10^{10} n/m^2	
Poisson's ratio (ν)	.25 - .50	.25
Plate thickness (h)	10 - 20 km	20 km
Plate density (ρ_c)	2600 - 2700 kg/m^3	2700 kg/m^3
Substratum density (ρ_s)	2800 - 3000 kg/m^3	2900 kg/m^3
Fault hade (θ)	20° - 40°	30°
Flexural rigidity (N)	6×10^{21} - 4×10^{22} n-m	
Flexural Parameter (α)	30 - 50 km	

g = 9.8 n/kg

1 bar = 10^5 n/m^2

using this definition of w_0^*, it is simple to calculate predicted parameters for various values of σ_o.

For each end condition, the predicted maximum amplitude of the flexure at the onset of plasticity, w_0 and at the maximum extent of plasticity, w_{max} will be calculated for a variety of values of the flexural parameter, α, within the range defined in Table 2. If the thickness of the plate is fixed, then smaller values of α correspond to weaker plates. This implies that a plate with a smaller α will deflect more and produce lower stresses than one with a larger α under the same load.

The calculations will be presented for σ_o values of 1, 2, and 3 kilobars. This range of yield stress is thought to be appropriate based on the results of Turcotte et al., (1978) who found σ_o to be in the 2 to 4 kilobar range for their models of the oceanic lithosphere. It is felt that the temperature regime of the Wasatch Front region would reduce the yield stress somewhat (Goetze and Evans, 1979). It is useful to note that σ_o should represent an average yield strength for the entire plate since there is probably some variation in the actual σ_o as a function of depth due to both temperature and pressure increases. Models incorporating this depth-dependent σ_o feature might prove useful and will be discussed in a later section.

In addition to the predicted amplitude of the flexure, the maximum extent of the plastic zone will be calculated for comparison with the observed seismicity pattern. Here it is assumed that when the yield strength is reached failure will occur either seismically or through some stable flow mechanism, depending on the pressure and

temperature. As a result the predicted plastic zone should correlate with the observed seismicity patterns at least in plan view while the depth distribution would be hard to correlate since the transition between seismic and plastic failure is not well defined.

Unconstrained case. Figure 7 shows the flexure curve for the unconstrained case just before a plastic hinge developed as compared to the elastic solution at the onset of plasticity. The introduction of an elastic-perfectly plastic rheology can nearly double the amplitude of the flexure without increasing the maximum stress in the model. This is illustrated in Figure 8, a plot of $\bar{\sigma}_{max}$ versus $\bar{x}$ for the same two cases as Figure 7.

The plastic zone in this analysis can be characterized by both its maximum depth (γ_{max}) and width extent ($\bar{x}_2 - \bar{x}_1$). Figure 9 is a plot of the development of the plastic zone with increasing w_o. Figures 10a and 10b isolate the dependence of the width and depth, respectively, of the plastic zone on changes in w_o. From Figure 10a we see that the width of the zone changes very rapidly just after the onset of plasticity and then more slowly as the uplift continues. On the other hand, the change in γ_{max} is much more linear with increasing w_o. These two relationships indicate that a unit increase in w_o has a greater effect on the width of the plastic zone just after the onset of plasticity while causing γ_{max} to change more as the uplift continues.

The predictions of the unconstrained case are summarized in Table 3. It can be seen that all values of α predict a zone of failure larger than the observed zone of seismicity (about 30 km

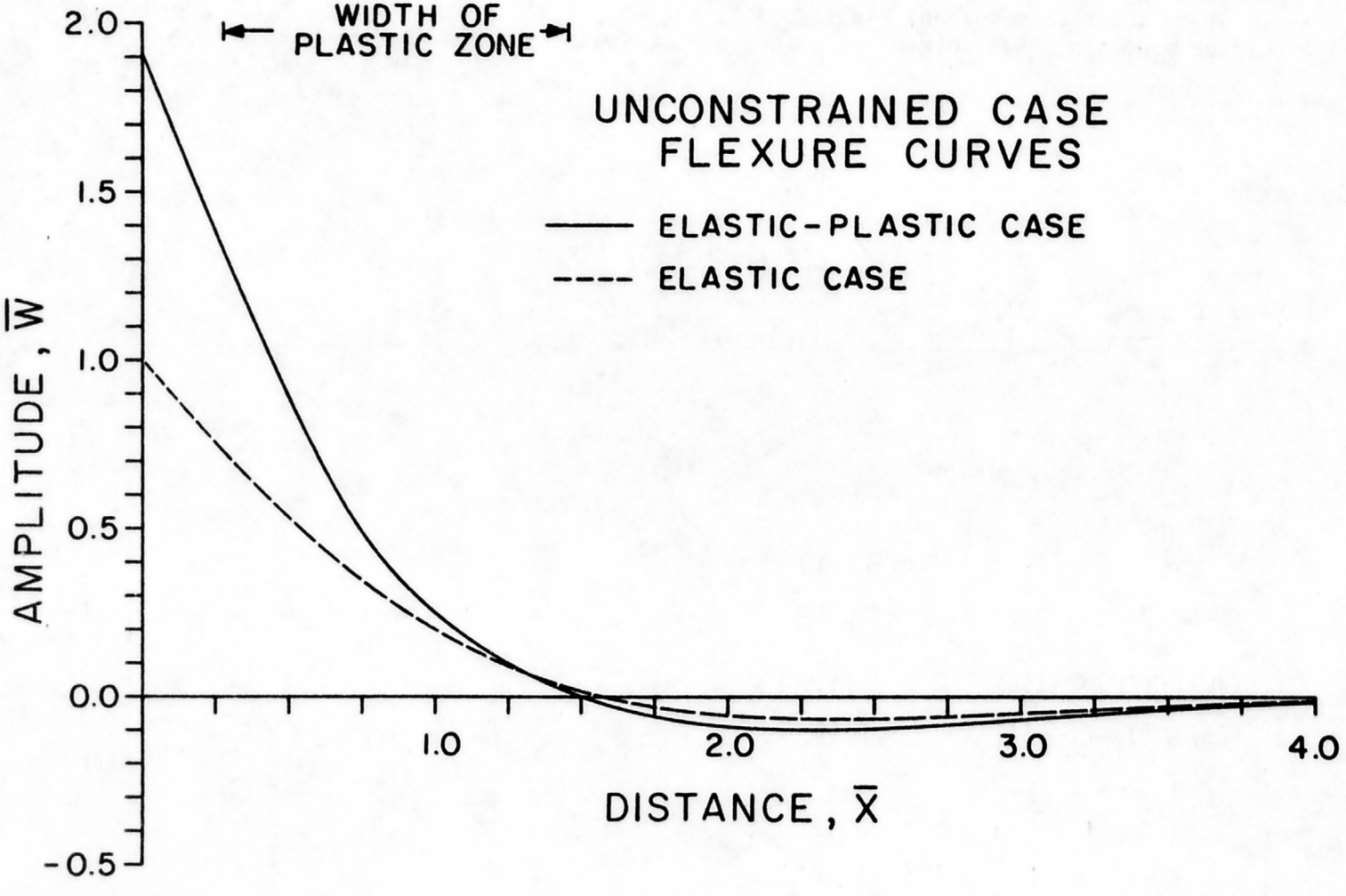

Figure 7. Dimensionless flexure versus distance for the unconstrained case. The elastic case at the onset of plasticity (dashed line) and the elastic-plastic case just before the critical point (solid line) are shown.

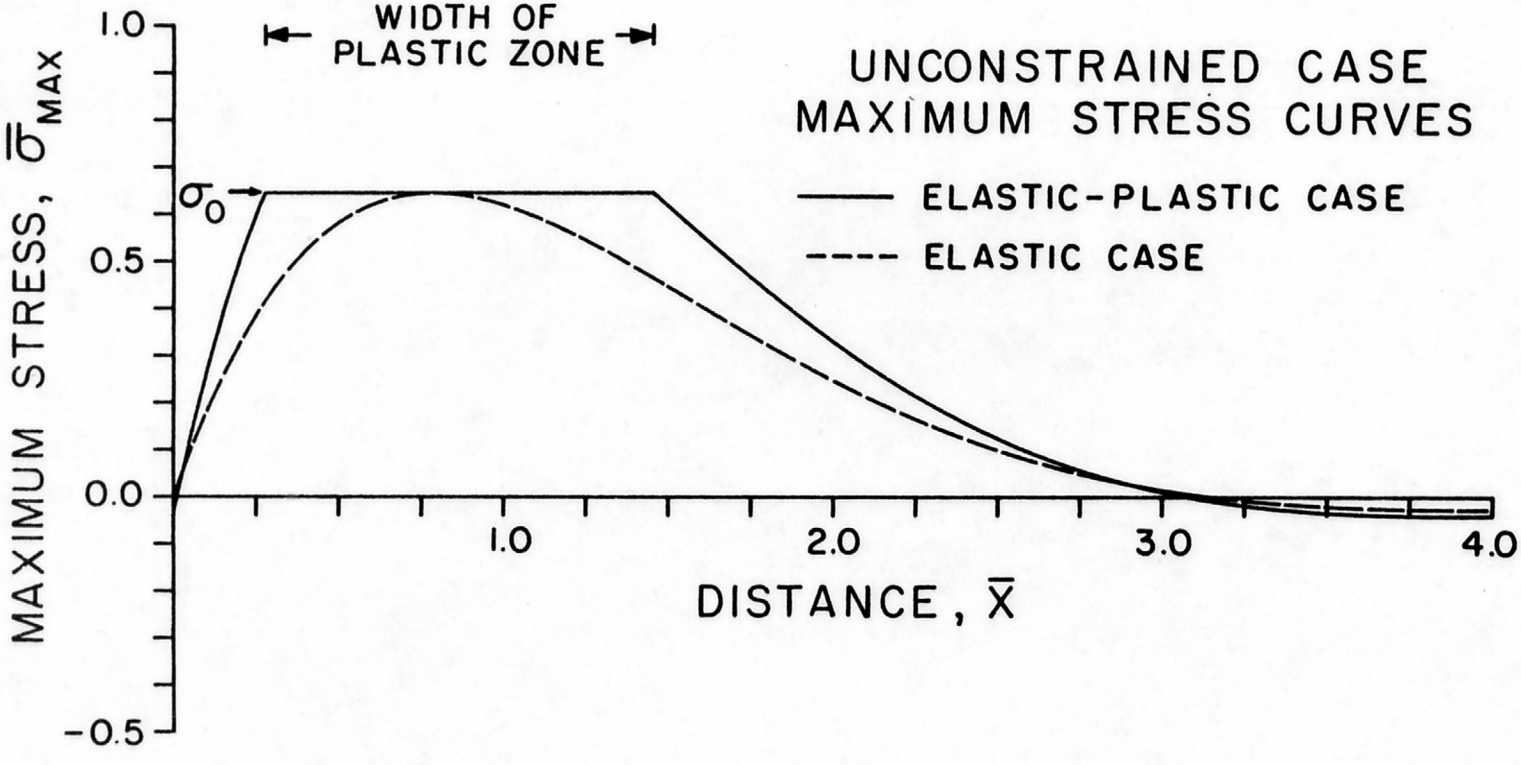

Figure 8. Dimensionless maximum stress at the top of the plate versus distance for the unconstrained case. The elastic and elastic-plastic curves are for the same cases as in Figure 7.

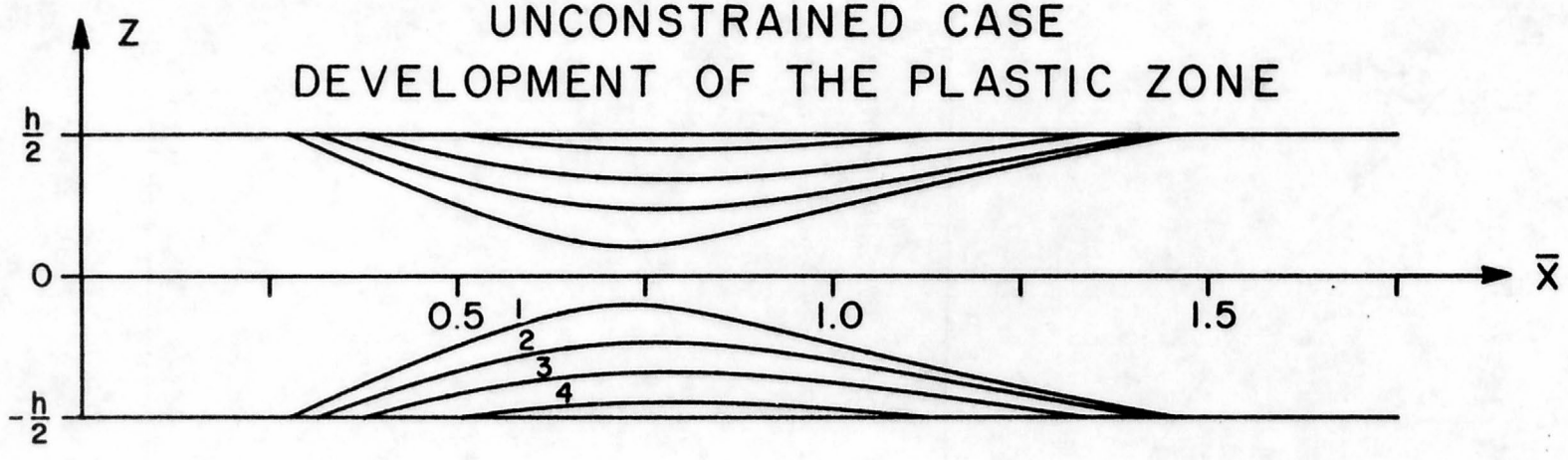

Figure 9. Cross-sectional view of the development of the plastic zone for the unconstrained case. Curves labeled 1, 2, 3, and 4 correspond to $\bar{w}_o$ values of 1.91, 1.52, 1.30, 1.10 respectively. The plastic zone is symmetric about the $\bar{x}^o$ axis.

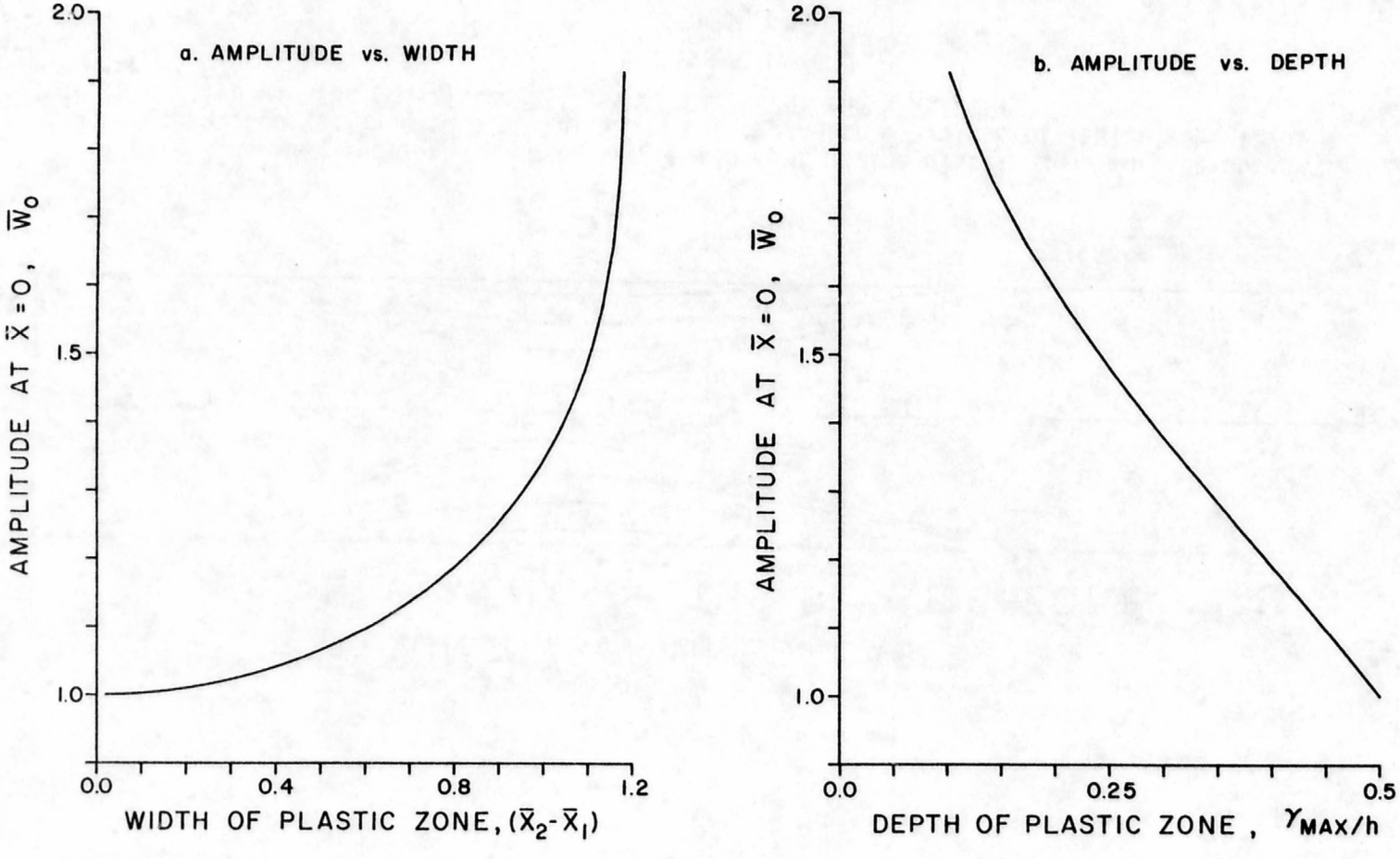

Figure 10. Relationships of the flexural amplitude at the fault to the depth and width extent of the plastic zone in the unconstrained case.

Table 3. Model Parameters for the Unconstrained Case

α (km)	σ_o =	1	2	3 kb	Maximum Extent of Failure Zone (km)
30	w_o	1.6 km	2.1 km	4.7 km	8.4 - 44
	w_{max}	3.0	5.9	8.9	
35	w_o	1.2	2.3	3.5	9.7 - 51
	w_{max}	2.2	4.4	6.6	
40	w_o	0.92	1.8	2.8	11 - 58
	w_{max}	1.8	3.5	5.3	
45	w_o	0.72	1.4	2.2	13 - 65
	w_{max}	1.4	2.8	4.1	
50	w_o	0.59	1.2	1.8	14 - 73
	w_{max}	1.1	2.3	3.4	

wide, roughly centered 30 km east of the Wasatch fault). However, two observations can be made concerning this correlation. First, the center of the seismic zone is predicted well for the lower values of α. Second, the width of the zone of seismicity listed in Table 3 is a maximum width -- the width just before the critical point is reached -- so that a smaller zone is possible. The predicted amplitude of the uplift is also in the correct range when compared to the observed 3 to 4 km of uplift. This parameter also requires that α be in the lower range of the possible values unless the yield stress is quite high. Arguing in favor of a strong lithosphere with a large yield strength in a province such as the eastern Basin and Range would be difficult, so that the observation that this elastic-perfectly plastic plate model suggests a weak lithosphere is encouraging. The tilting of the upthrown side of the fault is calculated to be 10 to 12 degrees for the values of α that fit the uplift and seismicity data (α = 30 to 35 km). This correlates very well with the observed tilting of 10 degrees.

Constrained case. The theoretical results for the constrained case are presented in Figure 11, $\bar{w}$ versus $\bar{x}$, and Figure 12, $\bar{\sigma}_{max}$ versus $\bar{x}$. It is obvious that the relative increase in flexure is much less for the constrained case as compared to the unconstrained case. The reason for this is that the slope of the stress curve is much larger in the constrained case so that the plastic zone develops to its limit much more rapidly. This seems to indicate that the model cannot support any significant moment at the fault without becoming unstable, supporting the assumption that the long term

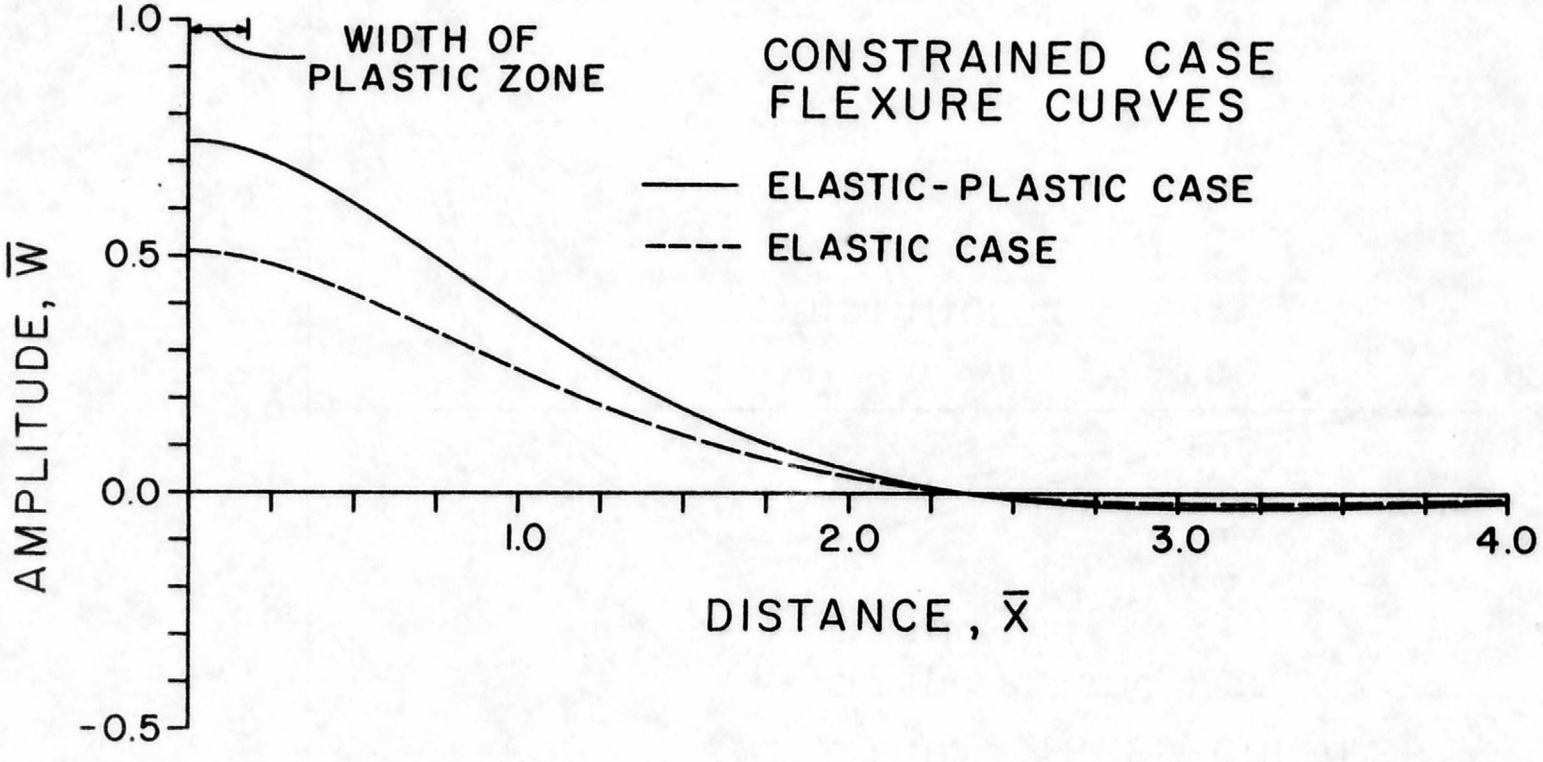

Figure 11. Dimensionless flexure versus distance for the constrained case. The elastic case at the onset of plasticity (dashed line) and the elastic-plastic case just before the critical point (solid line) are shown.

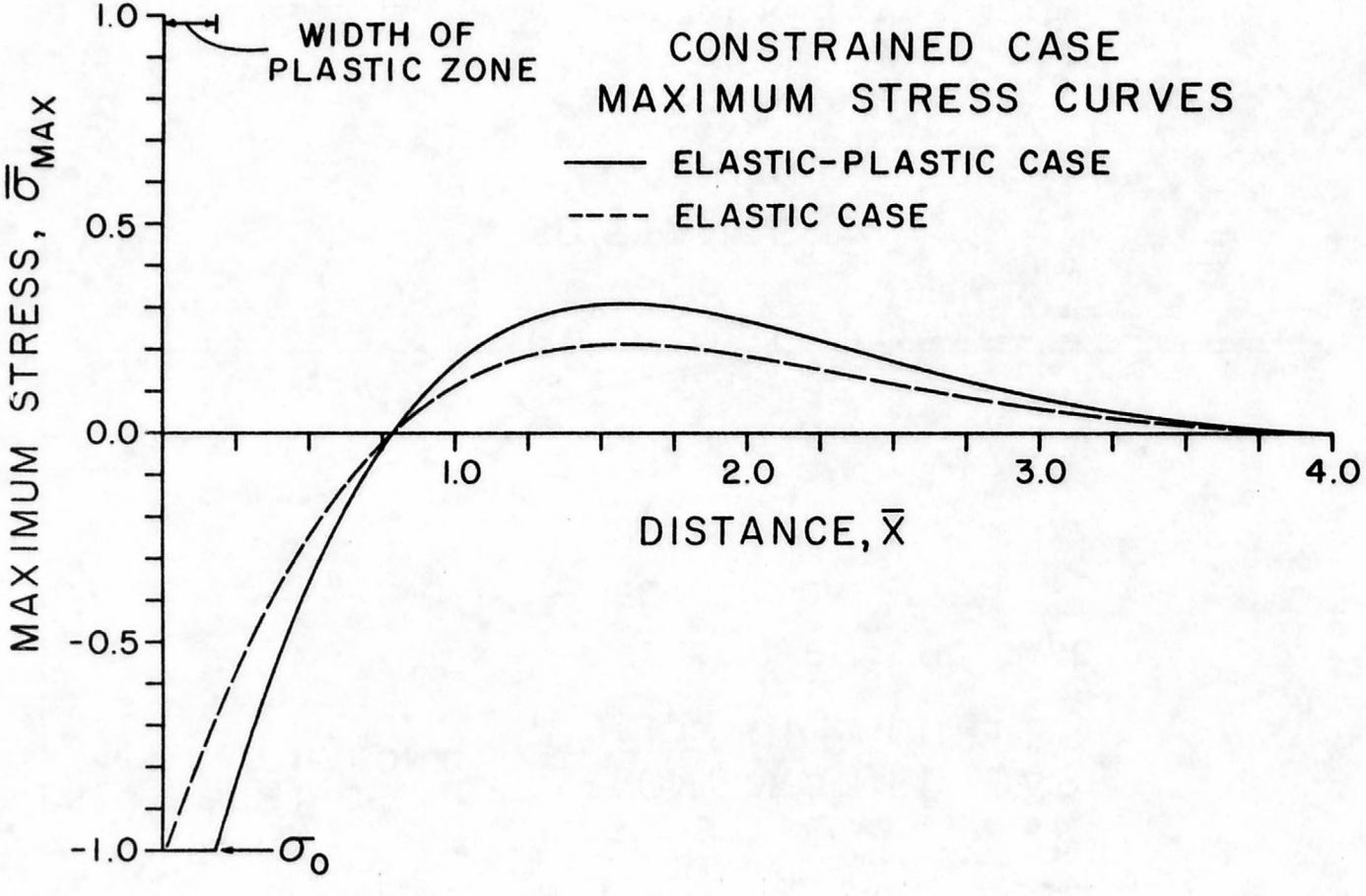

Figure 12. Dimensionless maximum stress at the top of the plate versus distance for the constrained case. The elastic and elastic-plastic curves are for the same cases as in Figure 11.

behavior of the fault is best represented by the unconstrained case. Figure 13 shows a cross section of the development of the plastic zone with increasing w_o, demonstrating how rapidly the plastic zone approaches a plastic hinge. This is further illustrated in Figure 14b, a plot of w_o versus γ_{max}. The slope of this curve is much greater than in the unconstrained case so that the critical point is reached more rapidly. This relationship dominates the development of the plastic zone so that the width of the plastic zone does not change much as the uplift changes (Figure 14a).

The actual model predictions for the constrained case are presented in Table 4. It is obvious that the constrained case is inadequate in all respects when compared to the observed seismicity and uplift data along the main Wasatch fault. This was also observed for the constrained case in the models considered by Zandt and Owens (1980). However, as they pointed out, the constrained model does have some interesting implications. For instance, the prediction of failure immediately next to the fault is similar to the observed seismicity in the vicinity of the East Cache fault (see Figure 2) in northeastern Utah. Zandt and Owens (1980) speculated that perhaps the East Cache fault is currently constrained while large portions of the Wasatch fault are currently unconstrained. With the observation that the model does not seem to be able to support significant constraint at the fault, this would indicate that areas with seismicity located off the main fault are safer than those areas where the seismicity pattern correlates with a constrained flexure case. This hypothesis was one interesting idea that resulted from the work of

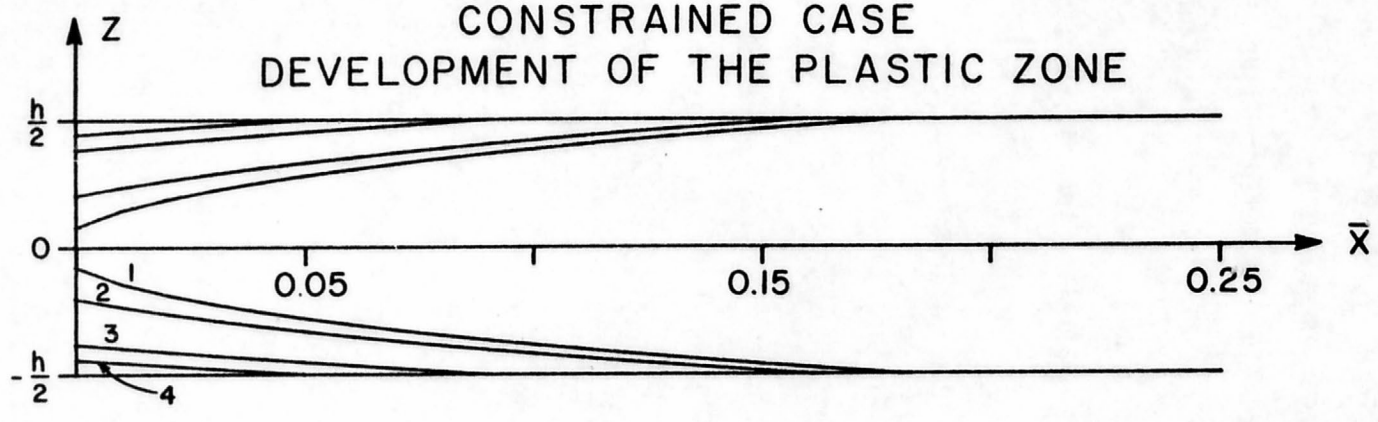

Figure 13. Cross-sectional view of the development of the plastic zone for the constrained case. Curves labeled 1, 2, 3, and 4 correspond to $\bar{w}_o$ values of 0.74, 0.70, 0.60, and 0.55 respectively. The plastic zone is symmetric about the $\bar{x}$ axis.

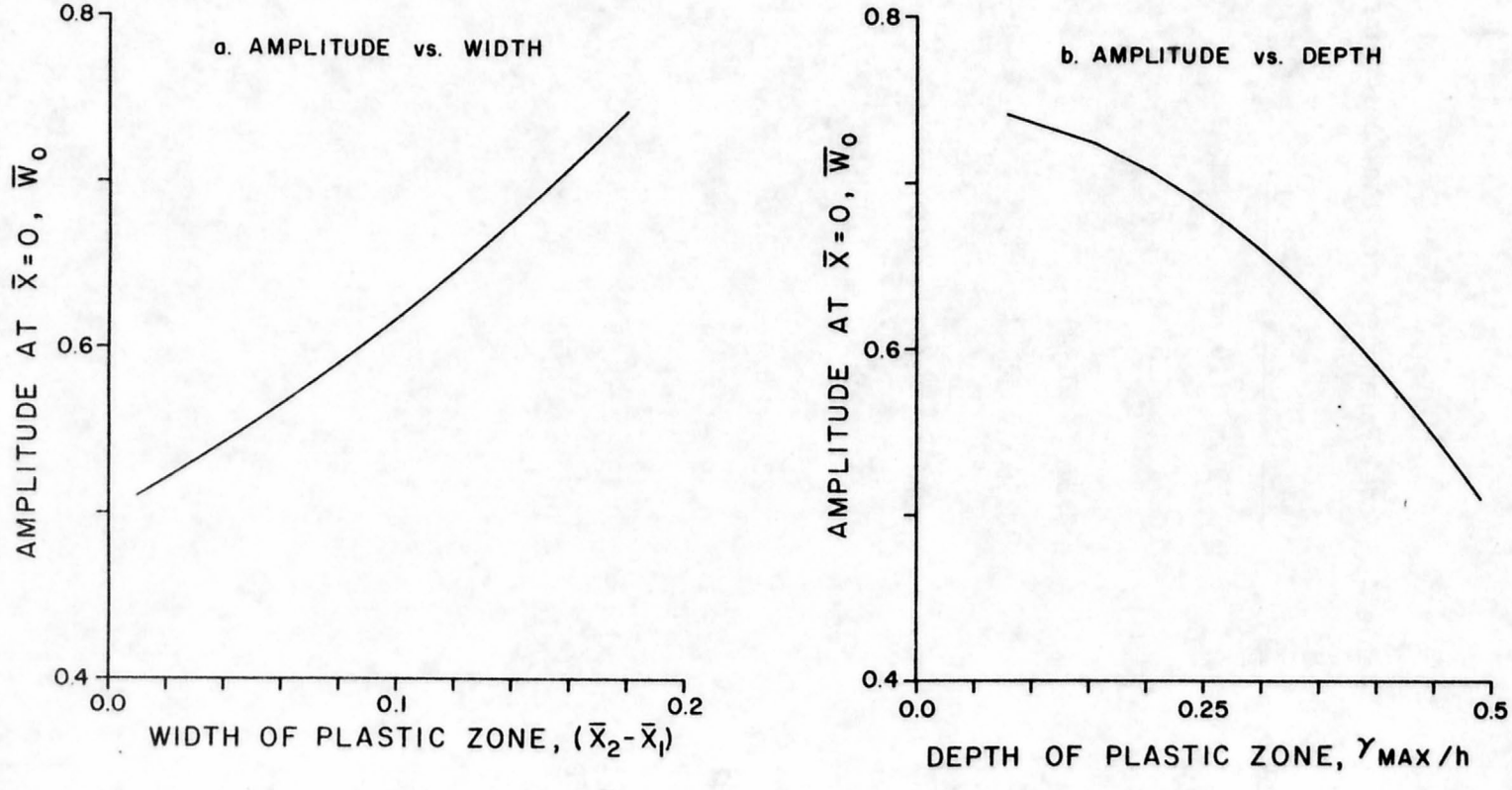

Figure 14. Relationships of the flexural amplitude at the fault to the depth and width extent of the plastic zone in the constrained case.

Table 4. Model Parameters for the Constrained Case

α(km)	σ_o =	1	2	3 kb	Maximum Extent of Failure Zone (km)
30	w_o	0.50 km	1.0 km	1.5 km	0 - 5.4
	w_{max}	0.74	1.5	2.2	
35	w_o	0.37	0.74	1.1	0 - 6.3
	w_{max}	0.55	1.1	1.7	
40	w_o	0.30	0.60	0.89	0 - 7.2
	w_{max}	0.44	0.88	1.3	
45	w_o	0.23	0.47	0.70	0 - 8.1
	w_{max}	0.35	0.69	1.0	
50	w_o	0.19	0.38	0.57	0 - 9.0
	w_{max}	0.28	0.56	0.84	

Zandt and Owens (1980). However, use of these simple models as earthquake prediction tools would be an oversimplification. The implications of these models on the relationship between flexure and seismicity are an important starting point, but flexure is but one factor influencing the occurrence of major earthquakes. The interaction over time of the forces causing the flexure with regional forces and friction on the fault must be considered in studies of earthquake cycles in this region.

DISCUSSION

This chapter is devoted to a discussion of the implications this study has generated concerning both the mechanics of deformation in the Wasatch Front region and the directions in which further related studies should procede. Several sources of error will be considered. The effects of those errors that can be quantified will be evaluated, while possible errors that cannot be quantified will be viewed as areas of further research. Finally the results of recent studies concerning flexure of oceanic lithosphere as constrained by both experimental rock mechanics and studies of the thermal regime of the lithosphere will be reviewed to determine possible applications to Wasatch Front models.

The theoretical values of the flexure and extent of failure presented in the last chapter were shown to be comparable, at least in the unconstrained case, to the observations along the Wasatch Front. However, the predicted values given in that chapter were obtained only after several assumptions and approximations were made. The first of these is that the earth can be modeled by a strong layer overlying a fluid substratum. Although the lower lithosphere undoubtedly does not behave as a perfect fluid on all time scales, the studies cited in the introduction indicate that this is a good approximation of its long term behavior. Problems associated with the assumption that the mechanical layer is of constant thickness

while geophysical evidence (Smith et al., 1975) indicates a thickening of the upper lithosphere about 75 km east of the Wasatch Front are hard to assess since the relationship of the long-term effective mechanical thickness of the lithosphere to other geophysical parameters is not known. The relationship of the effective mechanical thickness of the lithosphere and the thickness of the lithosphere determined by seismic methods appears to be highly temperature dependent (Watts et al., 1980). This indicates that the transition in the thermal regime may be the most important factor in analyzing the thickening problem. If it should be shown that the effective mechanical thickness of the lithosphere does thicken to the east of the Wasatch, the effect would be to increase the flexure close to the fault where the lithosphere is thin, although the magnitude of this increase is unknown.

Another critical assumption is modeling the Wasatch fault as a throughgoing normal fault. This assumption is also hard to test. McDonald (1976) presented evidence that some faults in the eastern Basin and Range are listric normal faults, that is the dip of the fault decreases with depth. The reality of this phenomenon for the Wasatch fault is unknown at present. However, if it is shown that the Wasatch fault is to some extent listric, the geometry of the fault would become a factor in further modeling. The relationship between the depth of the fault when the decrease in dip becomes significant and the mechanical thickness of the lithosphere would be critical to the validity of these models.

The acceptance of the basic model led to the use of the theory of thin plates to solve for the theoretical flexure of an elastic-perfectly plastic plate. This required some approximations to simplify the mathematics of the problem. The most significant of these is neglecting shearing stresses in determining the yield point. Chapple and Forsyth (1979) found that for a given displacement the actual yield stress of the plate could be a maximum of 25% higher if a one kilobar yield stress was assumed, while for a yield stress of 6 kb the maximum error is less than 1%. Since these errors cause an underestimation of the true yield strength, the predicted amplitudes should be considered upper bounds at low yield stress values. The only other potentially problematical mathematical assumption is that the displacements must be small compared to the thickness of the plate. As the displacement increases error is introduced in the predicted stresses so that at some point a more accurate mathematical theory would be required. In similar models using thin plate theory Timoshenko and Woinowsky-Krieger (1959) showed that as the displacement approached half the thickness of the plate the error in stress estimates approached 20%. In this study the maximum displacement is about one-fifth the assumed thickness of the plate, so that the thin plate assumption appears to introduce negligible error. However, should it be shown that the true mechanical thickness of the lithosphere along the Wasatch Front is much thinner than 20 km, a more thorough evaluation of this approximation would be recommended.

The magnitudes of the errors are not large enough to change the conclusion that the predictions for the case of unconstrained flexure

along the Wasatch Front (Table 3) compare favorably with the observed seismicity and uplift data. The major advantage of the elastic-perfectly plastic rheology over the elastic case described by Zandt and Owens (1980) is that large displacements on the Wasatch fault do not produce large stresses in the lithosphere. The rheology used in this study may also be more realistic than the viscoelastic model described by Zandt and Owens (1980) if recent studies indicating that oceanic lithosphere can support significant loads for long (>10^7 yrs) time periods (McNutt and Parker, 1980; Watts et al., 1980) can be extrapolated to the continental lithosphere. Studies by Anderson and Minster (1980) indicate that stress relaxation is a strong function of temperature, so that the high temperature at shallow depths in the Wasatch Front region could be a significant factor in determining the influence of viscoelastic behavior.

The models of this study are encouraging when compared to the results of the elastic and viscoelastic results of Zandt and Owens (1980) (see Table 1), however there are some areas where further study is needed. The primary reasons are oversimplifications in the models for some applications and questions raised by recent studies of flexure of oceanic lithosphere. These areas will be discussed by general research area although the topics cannot necessarily be separated from each other. These topics are: 1) Further research into the most appropriate lithospheric rheology for the region. 2) Development of models considered appropriate for studies of short term phenomena such as earthquake cycles on the Wasatch Front.

3) Evaluation of the vertical loading mechanisms which could be responsible for increasing the uplift on the Wasatch Front to 3 to 4 km.

Lithospheric Rheology

The major research need in this area is the evaluation of the implications of recent studies of oceanic lithosphere for mechanical studies along the Wasatch Front and the Basin and Range in general. Particularly, the study by Goetze and Evans (1979) should be discussed. Goetze and Evans (1979) evaluated the flexure of oceanic lithosphere in view of recent results from experimental rock mechanics. Their study indicates that the yield strength of the lithosphere is a strong function of both temperature and strain rate, two parameters notably absent from flexural studies to date. Goetze and Evans (1979) were able to calculate predicted geotherms which correlated well with calculated geotherms in the regions studied. The conclusion that can be drawn from the work is that temperature considerations may be quite important in flexural studies. This is further developed in the work of Watts et al. (1980) who determined that the effective mechanical thickness (EMT) of the oceanic lithosphere was 2 to 3 times smaller than the seismic thickness. They predicted that the EMT should be between the depths defined by the 300°C and 600°C geotherms in the lithosphere.

This information indicates that the thermal effects on the Wasatch Front models could be significant since, based on normal Basin and Range heat flow values of 0.09 Wm^{-2}, the 300°-600°C geotherms range occurs at about 10 to 20 km depth. However, the incorporation of

these data into models of this region requires that several factors be considered. First, the applicability of oceanic data to Basin and Range models must be established. Assuming this can be done, testing of long-term models will require further data constraints. If the seismicity pattern is considered a time-dependent parameter as is discussed below, then the total uplift on the fault is the only parameter available. Other possible data constraints are topographic and gravity data, seismic moment information, and depth-focal mechanism relationships. Topography and gravity data would require corrections for erosion, sediment loading and preexisting topography to be useful. However, gravity data is an important parameter in oceanic studies and isolation of the topographic effects of the flexure is also essential. Chapple and Forsyth (1979) use a theoretical seismic moment-curvature relationship to establish whether the model adequately predicts the total seismic moment associated with the flexural seismic events. However, their relationship includes a subduction velocity term so an equivalent relationship for the Wasatch Front needs to be established. Finally, although a depth-focal mechanism relationship based on observed data would be useful, it is doubtful that such a relationship could be developed using available data.

Earthquake Studies

The models presented here and by Zandt and Owens (1980) present a good framework for studies of earthquake cycles on the Wasatch Front. As pointed out by Zandt and Owens (1980), the suggestion of a

causal relationship between earthquakes on the main Wasatch fault and current microearthquake activity is an important concept. Further development of this idea requires consideration of some other factors as well. The interaction of regional forces and friction on the fault need to be considered along with a vertical loading mechanism. Under these conditions, one would hope to map some change over time in the seismicity pattern as the likelihood of movement on the main fault increased. Observing this change in seismicity patterns would probably be very difficult, however establishing the positions on the theoretical seismic cycle that various fault segments are in could be an important contribution. Other possible influences on this study would be studies of local strain measurements on the Wasatch Front (Prescott et al., 1979) and time-dependent behavior of the lower lithosphere as a means of loading a fault (Thatcher and Rundle, 1979), as well as the reality of a listric fault geometry for the Wasatch fault. Incorporating all of these features into an earthquake cycle process would be extremely difficult. On the other hand, the establishment of a reasonable theoretical framework based on these concepts would be an important step in the earthquake hazards evaluation of the Wasatch Front area.

Vertical Loading Mechanism

The models presented in this study were all based on the assumption that 3 to 4 km of uplift has occurred on the Wasatch Front. The question of the cause of that uplift should be addressed in future studies. One possible cause, sediment loading, could be evaluated

through the use of geologic data on erosion rates and analysis of isostatic gravity anomalies. As material is eroded from the Wasatch Mountains further uplift must occur to maintain isostatic equilibrium. Gravity studies discussed by Thompson and Burke (1974) and Eaton et al. (1978) indicate that the Basin and Range is almost in a state of complete isostatic equilibrium on a regional scale. On a local scale the relationship between small isostatic anomalies and fault loading should be evaluated. The details of this relationship could shed some light on the question of the significance of sedimentation and erosion as loading mechanisms for the Wasatch fault. There also appears to be a relationship between the effective mechanical thickness of the lithosphere and the depth of isostatic compensation (see Watts et al., 1980) so a study of isostatic anomalies is also related to the previous research topics.

CONCLUSIONS

An elastic-perfectly plastic plate flexure model has been developed and applied to the Wasatch Front region of Utah. The major advantage of the assumption of elastic-perfectly plastic rheology is that it allows for an increase in the total flexure while allowing no increase in stress beyond a specified yield stress. The question that motivated this study, "Accepting the existence of large displacements on the Wasatch fault, what constraints does the assumption of an elastic perfectly plastic lithospheric rheology impose on the model parameters?", has been satisfactorily answered. In order to match both the observed uplift and seismicity data, the lithospheric layer must have a low elastic modulus (0.8 to 1.5 x 10^{10} n/m^2), a low yield strength (1 to 2 kb) and, as a long-term approximation, be essentially unconstrained at the fault. These mechanical properties are consistent with the concept that the lithosphere in the eastern Basan and Range is weak. In addition, the case of constrained flexure presented here and also considered by Zandt and Owens (1980) generated some interesting observations of possible time-varying properties of the seismicity pattern in the region that may be important in earthquake cycle studies.

With the framework of contributing to a modeling process designed to evaluate the dominant tectonic mechanisms active in the Wasatch Front region, this study has been useful in that it answered the

question outlined above and also generated new questions to be addressed later. This study and recent studies on the related problems of oceanic flexure and experimental rock mechanics cited earlier highlight the need for further research in three basic areas: 1) lithospheric rheology, 2) earthquake related studies, 3) vertical loading mechanisms.

It is felt that the third topic, analysis of possible vertical mechanisms, is perhaps the most logical next step since it addresses the fundamental tectonic question of how the Wasatch Mountains developed. This question is critical to earthquake hazards evaluation in the region and could also provide valuable constraints on the rheologic model of the lithosphere.

APPENDIX

Zandt and Owens (1980) presented elastic and viscoelastic flexure models of the Wasatch Front. In this Appendix, the mathematics of their models is derived within the framework developed in this study. Their results were presented in Table 1 of this thesis.

The fundamentals of thin plate models (Equations (1), (2), and (3) in main text) can be easily applied to derive Zandt and Owens' (1980) elastic equations. We know in this case that the stress varies linearly with depth (see Figure 6a). Also, the elastic stress-strain law for this case is (Nadai, 1963, pg. 250):

$$\sigma_x = \frac{E}{1-\nu^2}\,\varepsilon_x \qquad \text{(A-1)}$$

Equations (A-1) and (3) can be used to derive a stress curvature relationship:

$$\sigma_x = \frac{E_z}{1-\nu^2}\,\frac{d^2w}{dx^2}. \qquad \text{(A-2)}$$

Now using (A-2) and (2) we obtain the bending moment-curvature relationship for the elastic case:

$$M = \frac{Eh^3}{12(1-\nu^2)}\,\frac{d^2w}{dx^2} \qquad \text{(A-3)}$$

or defining $N = \dfrac{Eh^3}{12(1-\nu^2)}$, we have

$$M = N \frac{d^2w}{dx^2} \qquad (A\text{-}4)$$

N is called the flexural rigidity of the plate, E, h, and ν are the Young's Modulus, thickness, and Poisson's ratio of the thin layer. Using (A-1) and (1) we are now able to derive the differential equation which Zandt and Owens (1980) solved in the elastic case:

$$N\frac{d^4w}{dx^4} + \rho_s g w = 0 \qquad (A\text{-}5)$$

The general solution is,

$$w = e^{\frac{x}{\alpha}} (A \cos \frac{x}{\alpha} + B \sin \frac{x}{\alpha}) + e^{-\frac{x}{\alpha}}(C \cos \frac{x}{\alpha} + D \sin \frac{x}{\alpha}) \qquad (A\text{-}6)$$

where $\alpha^4 = \frac{4N}{\rho_s g}$, the flexural parameter (Walcott, 1970b). Since $w \to 0$ as $x \to \infty$, the coefficients of the growing exponential are zero and the solution is rewritten:

$$w = w_o e^{-\frac{x}{\alpha}} \cos(\frac{x}{\alpha} + \phi). \qquad (A\text{-}7)$$

Equations (A-7) and (A-4) define the bending moment.

$$M = \frac{2w_o}{\alpha^2} e^{-\frac{x}{\alpha}} \sin(\frac{x}{\alpha} + \phi). \qquad (A\text{-}8)$$

These expressions, (A-7) and (A-8), define the bending moment and amplitude of an elastic plate flexure in terms of the material properties and the integration constants, w_o and ϕ. ϕ can be chosen to obtain the desired moment condition at the fault ($x = 0$). Zandt and Owens (1980) considered two such conditions, that of zero moment at the fault ($\phi = 0$) and that of significant moment at the fault ($\phi = -\frac{\pi}{4}$). These two conditions are discussed further in the text.

The value of w_o was determined by Zandt and Owens (1980) by considering the isostatic forces, P, acting on the plate after the formation of the fault. From Heiskanen and Veining Meinesz, 1958.

$$P = \frac{1}{2} \frac{\rho_c}{\rho_s} (\rho_s - \rho_c)\, g h^2 \tan \theta \qquad \text{(A-9)}$$

where ρ_c is the density of the thin layer and θ is the hade of the fault. Since the isostatic force at any point is proportional to the displacement at that point, we have:

$$P = \rho_s g \int_0^\infty w \, dx \qquad \text{(A-10)}$$

(A-10) and (A-9) define w_o as follows,

$$w_o = \frac{2P}{\rho_s g\, \alpha(\cos \phi - \sin \phi)}. \qquad \text{(A-11)}$$

In addition to the flexure and bending moment, Zandt and Owens (1980) calculated theoretical stresses for their elastic model. This can be easily done by writing the linear stress-depth distribution in the plate as

$$\sigma_x = \sigma_{max} \left[\frac{2z}{h}\right] \qquad \text{(A-12)}$$

Substituting (A-12) into equation (3) of the text defines σ_{max} in terms of the known bending moment (from (A-8)),

$$\sigma_{max} = \frac{6M}{h^2}. \qquad \text{(A-13)}$$

The stresses are equal and opposite in sign at the top and bottom of any cross section of the plate and go to zero at z = 0, the neutral

surface. The model predictions for the elastic case of Zandt and Owens (1980) are presented in Table 1 of the text.

The viscoelastic solution used by Zandt and Owens (1980) was obtained in a much more extensive derivation which will not be presented here. A viscoelastic rheology is characterized by an instantaneous elastic response to rapid loading and a viscous response to long-term loads. Walcott (1970b) suggested that the lithosphere in the Eastern Basin and Range might behave in this manner based on Lake Bonneville rebound data. The introduction of viscoelastic behavior allowed for an increase in the amplitude of the flexure without the large increase in stress required in the elastic case. It also introduces a time-dependency into the analysis which Zandt and Owens (1980) thought was a realistic improvement.

The transition from dominantly elastic to dominantly viscous behavior is controlled by the Maxwell time constant, $\tau = \frac{3\mu}{E}$, of the plate (μ is the viscosity coefficient). The governing differential equation of the simple viscoelastic plate model used by Zandt and Owens (1980) is (Nadai, 1963, pg. 285):

$$N\frac{\partial \dot{w}^4}{\partial x^4} + \rho_s g(\dot{w} + \frac{w}{\tau}) = 0 \qquad \text{(A-14)}$$

where $\dot{w}$ is the time derivative of w. The general solution contains terms representing permanent and elastic deformations. Under a constant load, this solution is:

$$w = w_0 e^{-\frac{x}{\lambda_o}} \cos\left(\frac{x}{\lambda_o} + \phi\right) + \qquad \text{(A-15)}$$

$$w_o \left[\frac{\lambda_o}{2x} \left\{ e^{-\frac{x}{\lambda}} \left(\sin\left(\frac{x}{\lambda} + \phi\right) - \cos\left(\frac{x}{\lambda} + \phi\right)\right) - e^{-\frac{x}{\lambda_o}} \left(\sin\left(\frac{x}{\lambda_o} + \phi\right) - \cos\left(\frac{x}{\lambda_o} + \phi\right)\right) \right\} - e^{-\frac{x}{\lambda_o}} \cos\left(\frac{x}{\lambda_o}\right) \ln\frac{\lambda}{\lambda_o} \right]$$

In this expression $\lambda_o = \alpha$, the flexural parameter at time zero and λ is the time-dependent flexural parameter. Its behavior is defined by:

$$\frac{t}{\tau} = \frac{1}{4}\left[\left(\frac{\lambda_o}{\lambda}\right)^4 - 1 - \ln\left(\frac{\lambda_o}{\lambda}\right)^4\right] \qquad \text{(A-16)}$$

The viscoelastic flexure varies with time under constant load in a manner which increases the amplitude at the fault and decreases the wavelength of the flexure (see Figure 5 in Zandt and Owens, 1980). The results of assuming this model by Zandt and Owens (1980) are given in Table 1 of the text.

REFERENCES

Anderson, D. L. and J. B. Minster, Seismic velocity, attenuation, and rheology of the upper mantle, Physics Earth and Planet. Inter., in press, 1980.

Arabasz, W. J., R. B. Smith, and W. D. Richins, Earthquake studies along the Wasatch Front, Utah: Network monitoring, seismicity, and seismic hazards, in Earthquake Studies in Utah 1850 to 1978, W. J. Arabasz, R. B. Smith, and W. D. Richins, editors, Salt Lake City, Utah, 253-286, 1979.

Bodine, J. H. and A. B. Watts, On lithospheric flexure seaward of the Bonin and Mariana trenches, Earth Planet. Sci. Lett., 43, 132-148, 1979.

Bott, M. H. P., Formation of sedimentary basins of graben type by extension of the continental crust, Tectonophysics, 36, 77-86.

Caldwell, J. G., W. F. Haxby, D. E. Karig, and D. L. Turcotte, On the applicability of a universal elastic trench profile, Earth and Planet, Sci. Lett., 31, 239-246, 1976.

Chapple, W. M. and D. W. Forsyth, Earthquakes and bending of plates at trenches, J. Geophys. Res., 84, 6729-6749, 1979.

Cook, K. L. and J. W. Berg, Jr., Regional gravity survey along the central and southern Wasatch Front, Utah, USGS Profess. Paper 316E, 75-89, 1961.

Eardley, A. J., Geology of the north-central Wasatch Mountains, Utah Bull. Geol. Soc. Am., 55, 819-894, 1933.

Eaton, G. P., R. R. Wahl, H. J. Prostka, D. R. Mabey, and M. D. Kleinkopf, Regional gravity and tectonic patterns: Their relation to late Cenozoic epeirogeny and lateral spreading in the western Cordillera, in Smith, R. B. and G. P. Eaton, eds., Geol. Soc. Am. Mem. 152, 51-91, 1978.

Forsyth, D. W., Comparison of Mechanical Models of the Oceanic Lithosphere, in Proc. of Conf. on Magnitude of Deviatoric Stresses in the Earth's Crust and Upper Mantle, USGS Open file Report 80-625, 550-568, 1980.

Goetze, C. and B. Evans, Stress and temperature in the bending lithosphere as constrained by experimental rock mechanics, Geophys. J. R. astr. Soc., 59, 463-476, 1979.

Griggs, D. T., F. J. Turner, and H. C. Heard, Deformation of rocks at 500° to 800°C, Geol. Soc. Am. Mem., 79, 39-104, 1960.

Heiskanen, W. A. and F. A. Vening Meinesz, The Earth and Its Gravity Field, McGraw-Hill Book Co., Inc., New York, 470 pp, 1958.

Hetényi, M., Beams on an Elastic Foundation, Univ. Michigan Press, Ann Arbor, 255 pp., 1946.

Hill, R., The Mathematical Theory of Plasticity, Oxford Univ. Press, New York, 355 pp., 1950.

Kachanov, L. M., Foundations of the Theory of Plasticity, Elsevier Publ. Co., Inc., New York, 482 pp., 1971.

McDonald, R. E., Tertiary tectonics and sedimentary rocks along the transition, Basin and Range Province to plateau and thrust belt province, Utah, in Rocky Mtn. Assoc. of Geologists, 1976, Sym. on Geology of the Cordilleran Hingeline, J. G. Hill, editor, 281-318, 1976.

McNutt, M. and H. W. Menard, Lithospheric flexure and uplifted atolls, J. Geophys. Res., 83, 12-6-1212, 1978.

McNutt, M. and R. L. Parker, Implications of Regional Gravity for State of Stress in the Earth's Crust and Upper Mantle. in Proc. of Conf. on Magnitude of Deviatoric Stresses in the Earth's Crust and Upper Mantle, USGS Open-File Report 80-625, 895-938, 1980.

Murrell, S. A. F., Rheology of the Lithosphere-Experimental Indications, Tectonophysics, 36, 5-24, 1976.

Nadai, A., Theory of Flow and Fracture of Solids, Vol. II, McGraw-Hill Book, Co., Inc., New York, 348 pp., 1963.

Naeser, C. W., R. B. Bryant, M. D. Crittenden, Jr., and M. L. Sorenson, Fission-track dating in the Wasatch Mountains, Utah: an uplift study, in Proc. of Conf. on Earthquake Hazards along the Wasatch and Sierra Nevada Frontal Fault Zones, USGS Open-File Report 80-801, 634-647, 1980.

Parsons, B. and P. Molnar, The origin of outer topographic rises associated with trenches, Geophys. J. R. astr. Soc., 45, 707, 1976.

Prager, W. and P. G. Hodge, Jr., Theory of Perfectly Plastic Solids, Wiley, New York, 264 pp., 1951.

Prescott, W. H., J. C. Savage and W. T. Kinoshita, Strain accumulation rates in the western United States between 1970 and 1978, J. Geophys. Res., 84, 5423-5435, 1979.

Priestley, K. and J. Brune, Surface waves and the structure of the Great Basin of Nevada and Western Utah, J. Geophys. Res., 83, 2265-2272, 1978.

Sbar, M. L., M. Beranzangi, J. Dorman, C. H. Scholz, and R. B. Smith, Tectonics of the Intermountain seismic belt, western United States: microearthquake seismicity and composite fault plane solutions, Bull. Geol. Soc. Am., 83, 13-28, 1972.

Schwartz, D. P., F. H. Swan, III, K. L. Hanson, P. L. Kneupfer, and L. S. Cluff, Recurrence of surface faulting and large magnitude earthquakes along the Wasatch fault zone near Provo, Utah, (abstract), Geol. Soc. Am. Abstracts with Programs, 11, 301, 1979.

Smith, R. B., L. W. Braile, and G. R. Keller, Upper crust low-velocity layers: Possible effect of high temperatures over a mantle upwarp at the Basin Range-Colorado Plateau Transition, Earth and Planet. Sci. Lett., 28, 197-204, 1975.

Smith, R. B. and M. L. Sbar, Contemporary tectonics and seismicity of the western United States with emphasis on the Intermountain seismic belt, Bull. Geol. Soc. Am., 85, 1205-1218, 1974.

Swan, F. H., III, D. P. Schwartz, K. L. Hanson, P. L. Kneupfer, and L. S. Cluff, Recurrence of surface faulting and large magnitude earthquakes along the Wasatch fault, Utah (abstract), EOS, Trans. Am. Geophys. Union, 59, 1126, 1978.

Thatcher, W. and J. B. Rundle, A model for the earthquake cycle in underthrust zones, J. Geophys. Res., 84, 5540-5556, 1979.

Thompson, G. A. and Burke, D. B., Regional Geophysics of the Basin and Range Province, Earth and Planet. Sci. Ann. Rev., 2, 213-238, 1974.

Timoshenko, S. and S. Woinowsky-Krieger, Theory of Plates and Shells McGraw-Hill Book Co., Inc. New York, 580 pp., 1959.

Turcotte, D. L., D. C. McAdoo, and J. G. Caldwell, An elastic-perfectly plastic analysis of the bending of the lithosphere at a trench, Tectonophysics, 47, 193-205, 1978.

Walcott, R. I., Flexure of the lithosphere at Hawaii, Tectonophysics, 9, 435-466, 1970a.

Walcott, R. I. Flexural rigidity, thickness, and viscosity of the lithosphere, J. Geophys. Res., 75, 3941-3954, 1970b.

Watts, A. B. and J. R. Cochran, Gravity anomalies and flexure of the lithosphere along the Hawaiian-Emperor Seamount Chain, Geophys. J. R. astr. Soc., 38, 119-141, 1974.

Watts, A. B., J. H. Bodine, and M. S. Steckler, Observations of flexure and the state of stress in the oceanic lithosphere in Proc. of Conf. on Magnitudes of Deviatoric Stresses in the Earth's Crust and Upper Mantle, USGS Open-File Report 80-625, 519-549, 1980.

Zandt, G., Seismicity and Earthquake-Generating Stress along the Wasatch Front, Utah (abstract), EOS, Trans. Am. Geophys. Union, 60, 936, 1979.

Zandt, G and T. J. Owens, Crustal flexure associated with normal faulting and implications for seismicity along the Wasatch Front, Utah, Bull. Seis. Soc. Am., 70, 1501-1520, 1980.

VITA

Name	Thomas Joseph Owens
Birthdate	February 4, 1956
Birthplace	Louisville, Kentucky
High School	Terre Haute North Vigo High School Terre Haute, Indiana
University 1974-1978	Purdue University West Lafayette, Indiana
Degree 1977	B.S. in Geophysics Purdue University West Lafayette, Indiana
Professional Organizations	American Geophysical Union
Publications	Zandt, G. and T. J. Owens, Crustal Flexure Associated with Normal Faulting and Implications for Seismicity Along the Wasatch Front, Utah, Bull. Seis. Soc. Am., 70, 1501-1520, 1980.

DISTRIBUTION OF FINAL TECHNICAL REPORT

		No. of Copies
1.	Gordon W. Greene Technical Officer U. S. Geological Survey OES External Research Program, MS 83 345 Middlefield Road Menlo Park, California 94025	10
2.	Dr. Robert B. Smith Co-Principal Investigator	1
3.	Dr. Walter J. Arabasz Co-Principal Investigator	1
4.	Dr. George Zandt Co-Investigator	1
5.	William D. Richins Co-Investigator	1
6.	Department of Geology and Geophyiscs Business Office University of Utah	1
7.	Office of Research Administration University of Utah	1
8.	University Archives Marriott Library University of Utah	1
7.	File Copies Donna Thomas Administraitve Assistant University of Utah Seismograph Stations	2